Mikhail Khadyko

Experimental and Numerical Study of Yielding, Work-Hardening and Anisotropy in Textured AA6xxx Alloys Using Crystal Plasticity Models

Thesis for the degree of Philosophiae Doctor

Trondheim, January 2015

Norwegian University of Science and Technology
Faculty of Engineering Science and Technology
Department of Structural Engineering

NTNU – Trondheim
Norwegian University of
Science and Technology

NTNU
Norwegian University of Science and Technology

Thesis for the degree of Philosophiae Doctor

Faculty of Engineering Science and Technology
Department of Structural Engineering

ISBN 978-82-326-0724-2 (printed ver.)
ISBN 978-82-326-0725-9 (electronic ver.)
ISSN 1503-8181

Doctoral theses at NTNU, 2015:28

Printed by NTNU-trykk

Preface

This thesis was submitted in partial fulfilment of the requirements for the doctor of philosophy at the Norwegian University of Science and Technology (NTNU). The work has been carried out at the Department of Structural Engineering from August 2010 to November 2014. It was funded by the Centre for Research-based Innovation SIMLab. Professor Odd Sture Hopperstad was the main supervisor and Dr. Stéphane Dumoulin from SINTEF Materials and Chemistry was the co-supervisor. The thesis is divided into two parts. The first part is a synopsis and includes an introduction, a literature study and a summary of the work. The second part contains the articles, which were published, submitted or prepared by the candidate during the PhD study.

Articles are included in the thesis:

1. Khadyko, M., Dumoulin, S., Børvik, T., & Hopperstad, O. S. (2014). An experimental-numerical method to determine the work-hardening of anisotropic ductile materials at large strains. International Journal of Mechanical Sciences, 88, 25–36.

2. Khadyko, M., Myhr, O.R., Dumoulin, S. & Hopperstad, O. S. (2014). A microstructure based yield and work-hardening model for textured 6xxx aluminium alloys. Submitted for publication.

3. Khadyko, M., Dumoulin, S., Cailletaud, G. & Hopperstad, O.S. (2014). Latent hardening and plastic anisotropy evolution in AA6060 aluminium alloy. To be submitted for publication.

4. Khadyko, M., Dumoulin, S., Børvik, T., & Hopperstad, O. S. (2014). Simulation of large-strain behaviour of AA6060 under tensile loading using anisotropic plasticity models. Submitted for publication.

Article included in the Appendix:

5. Khadyko, M., Dumoulin, S., & Hopperstad, O. S. (2014). Slip system interaction matrix and its influence on the macroscopic response of Al alloys. Materials Science Forum, 794, 566–571.

Abstract

The present work examines various aspects of the plastic behaviour of the 6000 series of aluminium alloys, including yield, work-hardening, diffuse necking, flow stress anisotropy and plastic flow anisotropy. The alloys were investigated experimentally, using tensile tests, and their behaviour was modelled using the finite element method (FEM). The material in the finite element simulations was described either by anisotropic phenomenological plasticity or crystal plasticity models. The aim of the work was to study the cases in which crystal plasticity models may improve the predictions compared to the phenomenological plasticity models or predict new aspects of the material's behaviour. The first part of the thesis is a literature study on crystal plasticity theory and phenomenological plasticity and a synopsis of the articles, which are included in the second part.

In Article 1 a method for finding the equivalent stress-strain curve from a uniaxial tensile test for a material with anisotropic plastic behaviour after necking is proposed. The force and cross-section diameter measurements in such test produce a true stress-strain curve until fracture, but this curve includes a triaxial stress field, which develops in the neck. To remove the influence of this triaxial field and obtain the equivalent stress-strain curve the reverse engineering method was utilized. A set of specimens produced from the AA6060 and AA6082 alloys with different heat treatments was tested under uniaxial tension condition. These tests were modelled using the FEM, with an anisotropic phenomenological plasticity material model. The work-hardening parameters of this model (which define its equivalent stress-strain curve) were set as the variables in the optimisation procedure. The anisotropic yield surfaces used in the phenomenological model were found using the crystal plasticity model and the crystallographic texture data obtained for the examined alloys. It was found that the equivalent stress-strain curves obtained with this anisotropic plasticity model differ from the curves obtained with an isotropic plasticity model, i.e. this method allows to account for the material's plastic anisotropy. The anisotropic yield surfaces obtained with the crystal plasticity model

allowed to predict the plastic flow anisotropy reasonably well.

In Article 2 the precipitation, yield stress and work-hardening model developed by Myhr et al.[1] is combined with a crystal plasticity model with Taylor type homogenisation. The same alloys as in Article 1 were used. The precipitation model provides the information about the solid solution and precipitate particles formed in the alloy, depending on its thermal history and chemical composition. This information is then transformed into the parameters of the yield and work-hardening model, which predicts the global equivalent stress-strain curve of the alloy. In this work an alternative work-hardening rule was proposed, which also uses the information about solid solution and precipitate particle data from the precipitation model. However, unlike the rule proposed by Myhr et al. it is acting on the slip system level. The global equivalent stress-strain is then calculated using the full constraint Taylor homogenisation model. In this case the influence of crystallographic texture and its evolution on the yield strength and work hardening is naturally accounted for. The results obtained by the two approaches were compared to these experimental data. The comparison showed that while some features of the alloys' plastic behaviour were captured somewhat better by the new approach, the overall improvement was not large and the results were influenced to a greater extent by the precipitation model than by the crystallographic texture.

In Article 3 the latent hardening and its influence on the plastic anisotropy of the aluminium alloys was studied. Phenomenological and physically based crystal plasticity hardening models use different descriptions of the latent hardening. The exact values of the latent hardening matrix is a long-standing problem, which has been attempted to be solved both experimentally and numerically. These efforts produced quite a few different results. Some typical latent hardening matrices found in the literature were tested. The experimental study consisted of uniaxial tensile tests in different material directions on an AA6060 alloy. These test were simulated using the FEM with crystal plasticity. The results of the simulation were compared to the experimental data. In the experiments, the material demonstrated an evolution of the anisotropy of both flow stress and plastic flow. It was shown that while models with different latent hardening matrices all reproduced the main tendencies of the alloy's behaviour, there were noticeable differences in the responses.

In Article 4 an AA6060 alloy sample is studied, in which an extremely sharp cube texture

---

[1] Myhr, O. R., Grong, Ø., and Pedersen, K. O. (2010). A combined precipitation, yield strength, and work hardening model for Al–Mg–Si alloys. Metallurgical and Materials Transactions A, 41(9), 2276–2289.

is observed. The material demonstrated an anomalous rhomboid shape of the fracture surface in the tensile test with a notched cylindrical specimen. The test was modelled using the FEM, with material described by the anisotropic phenomenological plasticity model and a crystal plasticity model. The finite element model represented the specimen geometry and boundary conditions realistically, with the average size of the constituent grains in the model close to the real one. The combination of the realistic geometry and crystal plasticity model allowed predicting the rhomboid shape of the notched specimen's cross-section at larger strains, while the phenomenological FEM failed to do so.

Acknowledgements

First, I want to thank professor Odd Sture Hopperstad, the strategist, and Dr. Stéphane Dumoulin, the tactician, for the excellent supervision of this project. Odd Sture made sure that I always had a clear goal ahead and Stéphane made sure that I could find a path to this goal.

I want to also thank my co-authors: professor Ole Runar Myhr, professor Tore Børvik and professor Georges Cailletaud. It is always exciting to work with the professionals of such calibre.

The work has been financially supported by the Structural Impact Laboratory, Centre for Research-based Innovation (SIMLab), at the Department of Structural Engineering, Norwegian University of Science and Technology, so my gratitude goes to professor Magnus Langseth, the Centre director.

This work would be impossible without a lot of help from many different people. Ida Westermann, the adept metallurgist, provided me with the microstructural data. Torodd Berstad, the computer wizard, helped me to solve the soft- and hardware issues numerous times. Trond Auestad and Tore Wisth, the masters of the lab, gave this work two feet firmly standing on the experimental ground. Egil Fagerholt, Gaute Gruben, David Morin and Afaf Saai provided me with all kinds of help during the project, from an expert piece of advice to a useful software bit. Lots of other people were directly involved in the multitude of activities which resulted in this thesis, and even though I may not know all of them personally I want to express my gratitude for their work.

I highly appreciate the friendly and comfortable, yet stimulating environment of the Department of Structural Engineering, created by its administrative crew, the academic team and my fellow PhD candidates.

On a more personal note, I want to thank the people who may not have been involved directly with the thesis, but have been providing moral support during all these years: Ma and Dad, Grandma and Granddad and my three awesome brothers: Artemy, Igor and Lev. And, last

but not least, Dmitry, Giedrius and a certain Siberian designer.

Contents

Journal articles:

Article 1 M. Khadyko, S. Dumoulin, T. Børvik, O.S. Hopperstad. An experimental-numerical method to determine the work hardening of anisotropic ductile materials at large strains. *International Journal of Mechanical Sciences,* vol. 88, pp. 25–36, 2014

Article 2 M. Khadyko, O. R. Myhr, S. Dumoulin, O.S. Hopperstad. A microstructure based yield and work-hardening model for textured 6xxx aluminium alloys. *Submitted for possible journal publication.*

Article 3 M. Khadyko, S. Dumoulin, G. Cailletaud, O.S. Hopperstad. Latent hardening and plastic anisotropy evolution in AA6060 aluminium alloy. *To be submitted for journal publication.*

Article 4 M. Khadyko, S. Dumoulin, T. Børvik, O.S. Hopperstad. Simulation of large-strain behaviour of AA6060 under tensile loading using anisotropic plasticity models. *Submitted for possible journal publication.*

Appendix

Article 5 M. Khadyko, S. Dumoulin, O.S. Hopperstad. Slip system interaction matrix and its influence on the macroscopic response of Al alloys. *Materials Science Forum,* Vols. 794-796, pp. 566-571, 2014

Chapter 1

Introduction

1.1 Background, motivation and goals

Aluminium alloys have been used extensively as structural material in various branches of industry (building, offshore, automotive, aerospace and more) for decades. The low density, relatively high strength and high corrosion resistance are very attractive advantages that often outweigh the higher cost (compared to other materials). Aluminium alloys are well suited for forming by extrusion (especially the 6000 series), deep drawing, welding and other production techniques. In addition, their mechanical properties may be controlled within certain boundaries by thermal processing. It is not surprising that all aspects of this material are subjected to extended research.

One of these aspects is the mechanical properties of aluminium alloys. Being a typical metal, aluminium demonstrates quite small elastic strains and much larger plastic strains. The engineering field tends to use a solution as simple and cheap as possible for design purposes, but it has been understood in the last decades that the isotropic and linear models are not quite enough, if one aims to achieve maximum efficiency of the production, reliability in operation and controllability of possible failure. The precise knowledge of the plastic deformation properties is necessary for this.

Aluminium alloys do not make this an easy task. They demonstrate all sorts of plastic behaviour, including anisotropic yield and flow potentials and non-linear isotropic and kinematic work hardening. Advanced phenomenological models can describe these features if they are properly calibrated. While calibration of a simpler model requires just a few experimental tests (typically uniaxial tension tests), these advanced models require a larger set of tests, including shear and plane strain tests, if one wishes to obtain models as accurate as possible. Metaphorically speaking the plastic behaviour of an aluminium alloy is an elephant and the tests are the blind men trying to describe it by touching just one of its sides. The problem is exacerbated if we recall that the elephant is multidimensional (e.g. the anisotropic flow potential has five dimensions in general case) and each new blind man costs a hefty sum of money.

On the other hand these complex plastic properties of the alloys are not random, but are a result of their internal structure. Metallic alloys are polycrystals, and the regularities in the statistical distribution of the orientations of the constituent crystals are a source of yield and flow stress anisotropy. The precipitate and solid solution contents in the alloy strongly influence the work-hardening rate. Solid particles also control the kinematic hardening and ductile fracture. Finding the exact nature of the link between the microstructure and the plastic properties is of course a difficult task, and establishing reliable quantitative models is even more difficult.

One of the links between the microstructure and the macroscopic properties is given by the crystal plasticity theory. It describes the plastic properties of crystals on the lattice level, using only the crystal orientation and the slip system work-hardening as input. For example, when it is applied to polycrystals, the 5-dimensional anisotropic flow potential surface of an alloy may be derived from this limited input in detail, instead of being an experimentally calibrated approximation (how well this result corresponds to the real yield surface is another question). The great setback of the crystal plasticity models is their computational cost, which is huge, compared to the phenomenological models. The computer technology needs to make a lot of progress before we can try to replace phenomenological plasticity with the more physically rooted crystal plasticity in technical applications. For now the two approaches can be used side by side, complementing each other in this field. The crystal plasticity may provide some of the calibration data for the phenomenological models. Another application of the crystal plasticity is the study of phenomena that the present day phenomenological models are incapable of predicting, because they lack the description of some important physical mechanisms of the plastic flow.

The objectives set in this thesis are the following:

- To study the use of yield surfaces predicted by crystal plasticity based on texture at large plastic strains (Article 1).
- To study the influence of the crystallographic texture and its evolution on the anisotropy and work-hardening at large plastic strains of textured 6000 series alloys (Article 2).

- To implement the influence of precipitate particles in crystal plasticity in a simple way and study their influence on the 6000 series alloy mechanical behaviour (Article 2).

- To study and numerically predict the distortion hardening in the 6000 series alloys in a broad range of plastic strains and reveal the connection between the results and the structure of the crystal plasticity model (Article 3).

- To compare the predictions of the crystal plasticity and phenomenological plasticity models for necking in aluminium alloys with very sharp textures (Article 4).

The present thesis tries to cover these grounds. The overarching goal is to try and test the crystal plasticity models in some context where the phenomenological models reach their limits in their present form and oversimplify things or lack vital information. Every time the results are compared to the experimental test results, some of which are also not the standard run of the mill type. The results may be largely positive or sometimes less convincing, but in any case they deepen our understanding of the behaviour of the aluminium alloys and its link to the microstructure and underline the numerous problems that still remain.

1.2 Scope and limitations

The experiments were performed on the 6000 family of alloys (6060 and 6082). The uniaxial tension test with an in-house laser gauge was the main test type. Tests were performed in different material directions and on alloys with different tempers (thermal histories) on cast and homogenised materials and extruded materials. The microstructural information was obtained by scanning electron microscopy (SEM). The tests were performed at very low strain rates, so that the strain-rate and dynamic effects were negligibly small and the deformation could be considered quasistatic. The tests were performed at ambient temperature and slowly enough for the thermal energy in plastic deformation to dissipate, so that the thermal effects in the material were negligibly small.

Correspondingly the numerical models ignored dynamic, strain rate and thermal effects. The flow potential of the phenomenological plasticity model was expanding isotropically, kinematic hardening was not considered. The two-term Voce hardening rule was used. The crystal plasticity models used the rate-dependent formulation with a low value of the rate sensitivity parameter, making it a rate-insensitive formulation. A local plasticity model was used; when the geometrically necessary dislocations and strain gradients were of interest, they were modelled in a simplified way with a characteristic length parameter and an additional state variable. No special measures were taken to model the grain boundaries or the microstructure inside the grain (dislocation patterns, particles etc.): the global response of the polycrystal, rather than the local one was usually sought after. The grain size effect was also not included in the models. The initial slip resistance was usually assumed equal on all slip systems, except one instance when this subject is specifically studied. Therefore the texture is the only source of the plastic anisotropy in most simulations.

The deformation was studied until and after necking, but a fracture criterion was not implemented and fracture was not studied experimentally.

Chapter 2

Literature overview

2.1 First observations and experiments

The first purely experimental works that discovered a connection between the plastic deformation of a metal and the evolution of its microstructure were two consecutive articles by J. A. Ewing and W. Rosenhaim: the preliminary one [1] and the main one [2]. First the metal specimens were prepared by either polishing a surface of a metal piece and etching it or pouring melted metal onto a glass or other smooth surface. Then a microscope was used to reveal the microstructure of the specimens. It was found that all observed metals had a crystalline grain structure. By lighting them from different angles, the orientations of the grains were found to be different. Some of the specimens were also annealed and studied again. From the transformations of grains under thermal treatment and their shape, a conclusion was made about how the differently oriented grains appear in metals.

Next the specimens were subjected to plastic tensile, compressive and torsion deformation. The specimens were studied under the microscope, and for deformation above the elastic limit straight parallel lines were observed on what was previously a smooth surface. The lines had different directions in each grain. The lines appeared in different grains as the load increased and sometimes another set of lines appeared in the same grain at an angle to the first ones at higher loads. The compression test produced a set of lines that was indistinguishable from the tension one. The torsion test also showed lines, although their orientation was somewhat different. These lines were proved to be slips — the lines along which part of a grain sheared relative to the rest of the grain, forming a slip step. These lines are consequently the lines of intersection between atomic planes of the crystal lattice and faces of the grains. The shape of

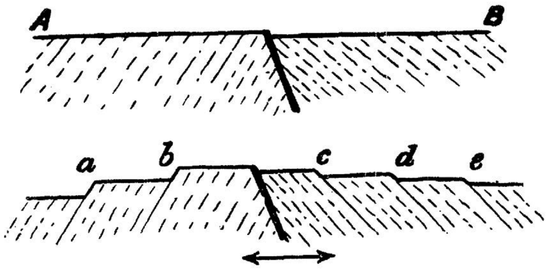

Figure 2.1: Schematic diagram taken from [1] showing slip steps on the surface of a metal near the boundary between two grains, A and B, before and after plastic straining. Dashed lines show the trace of crystallographic planes of slip.

the grains was changing with deformation, but their crystalline structure still remained intact and the slip lines appeared in the same manner, when the specimen was deformed and then polished again.

These observations allowed a conclusion to be made about how the plastic deformation in metals develops. Plastic deformation is due to slip of part of the crystal relative to the rest of the crystal along the gliding crystallographic surfaces. Parts of each grain slip at finite intervals throughout its volume along specific planes in specific directions, and this allows the regular lattice structure to accommodate to the arbitrary distortion of the grain without losing the regularity. Parts of grain between the slip lines were assumed to remain plastically undeformed. So plastic deformation was best described not by homogeneous shearing but rather by a series of discrete finite slips. An illustration of slip steps is shown in Figure 2.1. This was only a reasonable assumption, left to be proved experimentally. Other observations made in [2] considered another possible mechanism for plastic deformation in metals — twinning — and also the time dependency of slip and irreversibility of plastic work under slip, but this was only briefly mentioned.

2.2 Kinematics and kinetics of plastic slip

Ewing and Rosenhaim carried out their experiments before the invention of X-ray crystallography and their assumptions, though reasonable, were only based on indirect observations. By the 1920s X-ray diffraction was first used to determine the crystal structure of various metals and their conclusions were proved by direct measurements. In 1923 G. I. Taylor and C. F. Elam used the new advances in technology to develop those results further and published a preliminary study [3] and a more detailed article [4].

Advances in metallurgy made it possible to produce single crystals of aluminium instead of usual crystal aggregates and machine them into specimens. Markings on the sides of specimens allowed the measurement of deformations and X-ray spectrometry allowed measuring the orientation of crystallographic planes. Then the specimens were subjected to uniaxial tension. Force measurements in combination with X-ray spectrometry and markings' tracking revealed the connection between the stress, the specimen distortion and the orientations of the crystallographic planes.

One of the first observations was made about the preservation of cubic symmetry of the crystal during the whole deformation process up to fracture. Taylor made a conclusion that this must mean that the atoms of the lattice can only move in finite steps proportional to lattice spacing.

The measurements showed that the plastic deformation of the specimens could indeed be represented by shearing. The total displacement consisted of shear strains in the lattice and rotations of the lattice. In this process some planes in the lattice were distorted and some remained undistorted. The orientations of these undistorted planes were found from the deformation measurements and after comparing their positions with the X-ray spectrometry results, these planes were identified as the family of octahedral $\{111\}$ planes. The aforementioned slip was always happening on these planes. The direction of slip was identified as one of the $\langle 110\rangle$ directions. The accurate correspondence between the planes found by two different methods confirmed the idea of plastic deformation as slip on specific crystallographic planes in specific directions. The combination of plane and direction was called slip system. The $\{111\}\langle 110\rangle$ slip systems are shown in Figure 2.2.

When the total stress was decomposed and the shear component, lying in each slip plane along the corresponding slip direction (called resolved shear stress), was found for all slip systems, it turned out to be highest for the slip system that was actually slipping (the active one), and was correspondingly lower for the inactive slip systems. Rotation of the crystal accommodating this shearing mode of deformation to the uniaxial elongation of the specimen was observed. It rotated in such a way that the resolved shear stress on the active system increased. On the other hand the resolved shear stress increased independent of rotations because of the

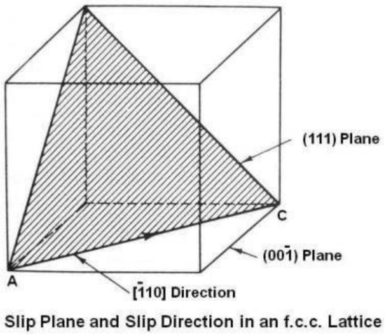

Figure 2.2: A schematic lattice cell of an FCC crystal with one of the possible $\{111\}$ slip planes and possible $\langle 110 \rangle$ directions forming one of 12 possible slip systems [5].

hardening on this slip system (the self-hardening). Taylor assumed that all slip systems in the crystal harden at the same rate even if only one of them is actually slipping. Hardening of non-active systems was called latent hardening. If it was so, the crystal was expected to rotate in slip towards a certain orientation, at which the resolved shear stresses on two slip systems would become equal. Then the slip on a second (conjugate) system would also start and double slip would be observed. The rotation of the crystal would stop as the two rotations, from each of the slips, would be equal and cancel each other. But instead the crystal continued to rotate in single slip beyond this direction (this behaviour was named "overshoot"), see Figure 2.3. The resolved shear stress on the conjugate system was higher than the resolved shear stress on the active system but it was not activated yet. It was an indication that latent hardening was greater than self-hardening.

A series of experiments on single crystals was performed by E. Schmid in 1924 and published in [6]. The experiments showed that at given conditions, for the same aluminium alloy, the highest resolved shear stress at yield in the crystals was a constant, independent of the orientation of the lattice in the specimen and which slip system it was reached on. Those results were used to formulate a plastic criterion for metal single crystals: plastic deformation (or slip on a slip system) starts when the resolved shear stress on one or more of the slip systems is not lower than some value, called critical resolved shear stress (CRSS). This criterion, which was named Schmid's Law, became one of the foundations of the rate-independent crystal plasticity theory. Both Schmid and Taylor stated that the stress components other than the resolved shear stress did not influence the slip (although non-Schmid effects exist, it was a reasonable assumption for the time being).

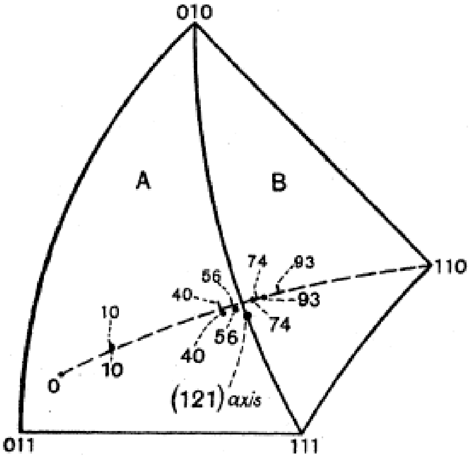

Figure 2.3: Projection of the tensile axis position in the lattice coordinates. The dashed line shows the calculated rotation of axis in single slip. Dots show the measured rotation. If latent hardening was equal to self hardening then the axis should rotate to the (121) symmetry axis and stop, because the rotation from slips on two systems would be equal and cancel each other. Taken from [4].

In [4] more experiments were performed and with greater accuracy, but they only confirmed the results from [3]. This time the crystallographic plane along which the slip would start was predicted before the experiment. When the resolved shear stress was followed through the process of deformation, the hardening was observed and a load-deformation curve was obtained for the slip. Taylor used a quadratic polynomial function to approximate it. Finally some comments about influence of hardening on the stability of plastic flow and an attempt to formulate a fracture criterion were made.

These results were further developed theoretically by Taylor in [7]. He considered a crystal under an arbitrary strain and attempted to develop a method for finding the slip systems which this strain would activate and their respective slips. Taylor used the virtual work principle to choose the active systems. First he showed, that while a strain tensor in general case has 6 independent components, for plastic deformation this number reduces to 5, because of the plastic incompressibility. This means that from the 12 slip systems only 5 are needed to be activated to accommodate this deformation. 792 possible combinations of 5 slip systems may be chosen out of 12 slip systems. Then by some geometrical arguments he reduced the number of combinations to choose between to 24. Later Bishop and Hill showed in [8] that a mistake was made and the number is 92, but this mistake cancelled itself and did not affect the calculations. Then the actual active slip systems were found numerically. The second idea originating in [7] was the model for crystalline aggregate deformation. Taylor assumed that when a polycrystal deforms, the local strains in all constituent crystals are the same and equal to the global strain. He then used this assumption and the method for finding the active slip systems to construct a load-displacement curve for an aggregate of crystals from the stress-strain curve of one slip system. The yield stress obtained this way is the upper bound of the solution of a boundary value problem of a polycrystal. He also used this method to calculate the rotations of the crystals during deformation. The results were in good accordance with the experimental data.

So by the 1940s most vital components of the kinematics (slip systems, single and multiple slip, crystal rotation and texture evolution) and kinetics of crystal plasticity (critical resolved shear stress, self and latent hardening, choice of active slip systems, Taylor model) were formulated.

2.3 The dislocation theory

While the phenomenology of plastic slip was described, its physical mechanisms were still unknown. Why would the crystals slip along these specific planes, how can a crystal lattice be slipped, and what is the reason for hardening? Simple calculations showed that to shift a perfect crystal lattice would require a stress comparable to the elastic shear modulus, which was certainly not the case. Still some theories tried to prove that a perfect lattice must slip easily, and hardening was explained by some irregularities which "lock" it. Taylor in [9] used a different approach and assumed that a perfect lattice is very hard to slip, but some imperfections in it make the necessary force much lower. The possible atomic structure of such imperfections was proposed. As Figure 2.4 shows, this imperfection (or dislocation) may be represented as an additional plane inserted into the lattice. As a result, instead of the stable equilibrium of the perfect lattice, an unstable equilibrium of the new configuration arises. The dashed line in Figure 2.4 b and e represents the atomic plane along which slip occurs. If a force (the resolved shear stress) is applied along this line, then the unstable equilibrium is disturbed and the atom at the end of the line will "jump" into a more stable position. This process will repeat itself until the perfect lattice is recovered (Figure 2.4 c and f). It is obvious that this mode of deformation will preserve the crystal structure globally. The dislocations would move through the crystal and disappear on the boundary, leaving the whole crystal sheared. This propagation would happen in finite time. Microscopic observations of a strained rock salt crystal showed some sort of lines propagating through the crystal. This is mentioned as a positive evidence supporting the theory. Taylor also tried to evaluate energies involved in the equilibrium configurations of the atoms, though he admitted that this two-dimensional simplified picture cannot be very close to the real crystal interior. The influence of temperature was explained, as high temperatures would raise the energy of the atoms and help them overcome the potential barriers so reducing the force necessary to start slipping. Similar types of crystal defects were proposed by Orowan [10] and Polanyi [11] in the same year.

The dislocation in Figure 2.4 is not the only possible type of lattice defect. This type is called the edge dislocation, and its characteristic is that the dislocation line is normal to the plane of Figure 2.4 and the slip direction is in this plane. The direction and distance at which a part of the crystal is displaced by dislocation is called the Burgers vector. Its magnitude is usually equal to the lattice spacing (a perfect lattice vector). Therefore, for the edge dislocation the Burgers vector is normal to the dislocation line. Burgers proposed another type of dislocation

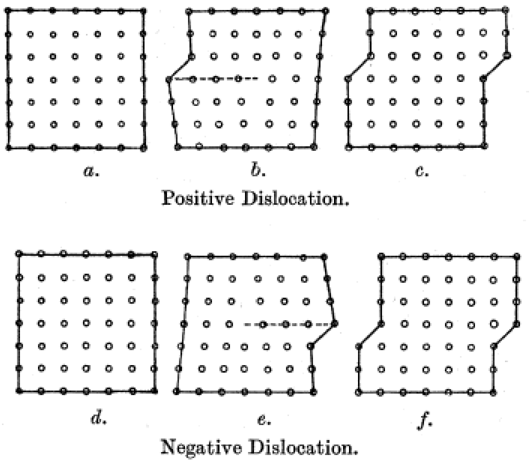

Figure 2.4: Two types of edge dislocations, proposed by Taylor. Taken from [9].

in [12] in 1939, for which this vector is parallel to the dislocation line, a screw dislocation.

In 1907 Volterra [13] analysed how a class of finite deformations in an elastic medium create stress-strain fields by representing any such deformation as a combination of elementary cuts and welds of parts of the medium. This description appeared to fit perfectly for the analysis of dislocations, where the lattice can be imagined cut, stretched and then welded back along the line of the dislocation. Taylor used this analysis to find the elastic stress and strain fields of a dislocation. Figure 2.4 shows two types of dislocations, called positive and negative by Taylor. The difference is the direction of the Burgers vector. The analysis of their elastic fields showed that dislocations will attract or repel each other depending on their "sign". Parallel dislocations of opposite signs would cancel each other if they collide (dislocation annihilation). Dislocations would move if a resolved shear stress is applied and also produce a stress field of their own. Dislocations will also be produced at the crystal boundary. Taylor analysed some simple arrangements of parallel dislocations at equilibrium and found the mean shear stress produced. He found that a crystal with dislocations would have a finite shear strength and that the production of dislocations would lead to hardening. Though he did not manage to verify this theory against experimental data, he founded a field of dislocation dynamics which made big progress later.

In the 1950 – 70s the early simplified models of Taylor were developed further. Dislocations were found to dissociate into partial dislocations and stacking faults in some materials. Many features of real dislocations were analysed: movement of dislocations between slip systems (cross slip), dislocations in elastically anisotropic medium, elastic fields of complex dislocation arrays. Lomer [14] proposed a model for interaction of dislocations on conjugate slip planes that would produce hardening and latent hardening. Frank and Read [15] proposed a mechanism for a possible source of dislocations in a strained crystal, that could play an important role in maintaining plastic flow.

Another important concept introduced in [16] is the geometrically necessary dislocation. If the crystal is strained non-homogeneously (in bending or torsion), the lattice becomes plastically distorted, which would be impossible for a lattice with a sum of Burgers vectors of all dislocations equal to zero. This distortion is made possible by a set of dislocations with non-zero sum of Burgers vectors, which occupy a certain configuration within the crystal, so that the stresses caused by the lattice distortion are minimized. The dislocation density associated with this set will remain as long as this lattice distortion is present. These dislocations are thus called "geometrically necessary dislocations" (GND) to differentiate from the "statistically stored dislocations", which provide the homogeneous plastic deformation. The GNDs play an important role in the non-local crystal plasticity models [17].

2.4 Development of rate-independent crystal plasticity theory

The next important development for rate-independent crystal plasticity was made by J.F.W. Bishop and R. Hill and published in [8]. They introduced the principle of maximum plastic work, which made finding the active slip systems for an arbitrary straining much easier. The essence of this principle can be illustrated as follows.

The face centered cubic (FCC) crystal has 12 slip systems, for each of which a Schmid criterion can be formulated. The Schmid criterion is an inequality $|\tau_\alpha| \leq \tau_{cr}$ where τ_α is the resolved shear stress on slip system α and τ_{cr} is the critical resolved shear stress assumed identical on all slip systems. This inequality defines a hyperplane in the stress space. For an FCC crystal there are 12 such inequalities and 24 hyperplanes. An inner envelope of these hyperplanes forms a hyperpolyhedron, which is the yield surface of a single crystal, each facet of the hyperpolyhedron corresponding to a slip system. As was shown in [8] plastic flow in crystals is associated and obeys the normality rule, i.e. the plastic strain increment vector is always normal to the yield surface. It leads to some interesting consequences. In the general

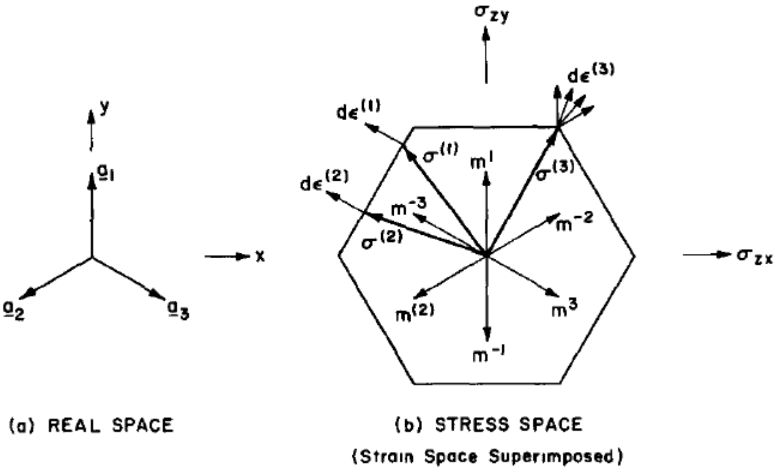

Figure 2.5: Illustration of a projection of a single crystal yield surface (hexagonal crystal, projection on the basal plane for simplicity). Stresses $\sigma^{(1)}$ and $\sigma^{(2)}$ will lead to the same plastic strain, for any strain $\mathrm{d}\varepsilon^{(3)}$ only one stress $\sigma^{(3)}$ is necessary. Taken from [18].

case, a stress state which fulfils Schmid's law will lie on the facet of the hyperpolyhedron and will produce a certain plastic strain increment, normal to this facet. This situation corresponds to single slip, in which only the slip system corresponding to this facet is activated. For some other stress state, it will be at an edge or a vertex of a hyperpolyhedron (which corresponds to the activation of two or more corresponding slip systems and thus multiple slip). Then the direction of the produced plastic strain increment becomes undefined. It is only possible to say that this direction lies between the normals to the adjacent facets at this edge or vertex (so called cone of normals) but any direction in between is possible, because the normal at the sharp vertex is undefined. This is illustrated in Figure 2.5.

If the deformation of the crystal is strain controlled, then in most cases its plastic strain increment will originate in one of the vertices and its stress state will correspond to one of the vertex stress states.

Now we look back at the problem that Taylor tried to solve in 1938. Which slip systems will activate in an arbitrarily strained crystal and what stress will arise? Taylor compared the problem to a problem of a non-conservative mechanical system with friction and applied the virtual work principle. His hypothesis (which was only proven later by Bishop and Hill in [8]) was that the sum of slips in the actually active slip systems will be the least of all sums of slips

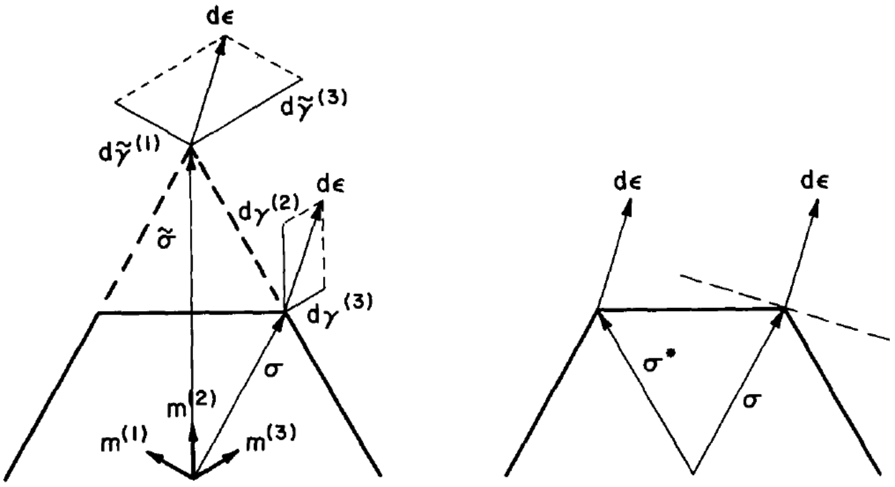

(a) TAYLOR (b) BISHOP & HILL

Figure 2.6: Geometrical interpretation of Taylor and Bishop-Hill methods. a) Trying to put the plastic strain increment in any other vertex than the actual one will lead to larger slips $d\tilde{\gamma}$, violate the yield condition and correspond to higher work than the actual one. b) The given plastic strain increment can only be found within the cone of normals of the right vertex. Putting it in the wrong vertex will correspond to a lower plastic work. Taken from [18].

of the possible slip systems. Hardening was assumed to develop similarly on all systems. He approached this problem directly, found all combinations of slip systems which could produce the given strain, found the sums of slips in them and chose the smallest one. As already said this solution was so cumbersome that Taylor himself made a mistake in it. Another shortcoming of his method was that it had not been proven that a stress could always be found to operate any geometrically possible set of slips without exceeding the CRSS in non-active slip systems. Bishop and Hill worked this out analytically, but their method becomes rather obvious from the geometrical representation in Figure 2.6.

They started from two assumptions: i) the slip and the resolved shear stress have the same direction and ii) the Schmid criterion is fulfilled (this criterion is ignored in Taylor's method). From this standpoint they proved that the plastic work of the actual stress corresponding to the actual plastic strain will be larger than the plastic work from any other vertex stress. They also showed how Taylor's minimum shear principle could be derived from the same assumptions and generalized for arbitrary hardening (Taylor assumed isotropic hardening equal on all slip systems). Instead of minimizing the sum of slips, the plastic work should be maximized. They also found and tabulated all vertex stresses (53 of them), so the problem of finding the right one was greatly reduced. This model of a rate-independent polycrystal was consequently called the Taylor-Bishop-Hill (TBH) model and it was proven later that the two approaches are mathematically equivalent [19].

The problem which Bishop and Hill tried to solve in [8] and [20] was finding the yield surface of a polycrystal from the single crystal properties. By this time several models of polycrystalline aggregates were known. In [21] and [22] a model was proposed where each grain is subjected to a uniaxial stress parallel to the specimen axis. In [23] each grain was supposed to undergo the same extension as the specimen. All these models were criticized for the lack of compatibility between deforming grains. The Taylor model assumed uniform strain and thus avoided this problem but was criticized for lack of stress equilibrium between grains. Still the Taylor model was preferred as more realistic. After developing the maximum work principle, Bishop and Hill showed how it could be applied to the polycrystal to find its yield surface.

In [20] the yield surface was found and compared to the von Mises, Tresca and to experimental yield surfaces. The resulting yield surface lay between the von Mises and Tresca ones, but not very close to the experiment. The stress-strain curve found with the new method was the same as Taylor had found earlier.

In [24] the TBH model was used to analyse the texture evolution, analogously to [7]. Despite all the simplifications and unclear issues of the model, the general trends of tensile and compressive textures were captured in a qualitative sense. The importance of the hardening law and the latent hardening for texture evolution was also analysed. One of the problems of the TBH model discussed in [24] is the ambiguity of the choice of the active slip systems, when the critical resolved shear stress is reached on more than 5 slip systems simultaneously. This corresponds to the vertex where 6 or 8 facets intersect on the yield surface of a crystal. In this case a range of slip systems combinations, satisfying the maximum work principle, could be found, which would provide the same strain but different rotations. Bishop calculated the possible ranges of rotations in these ambiguous situations and compared them with the actual texture evolution, but provided no means to choose a definite one.

One of the big shortcomings of the TBH model, mentioned in [24], was the lack of elasticity in the crystal description. In rigid plastic crystals the stress was developing instantly at all slip systems, activating them simultaneously, while in reality the development of stress is controlled by development of elastic strains and slip systems can activate consecutively. In [25] Lin proposed a model, where elasticity was accounted for. Two main components of the model were the elastic relation — a simple linear Hooke's law $\delta\tau = G\delta\gamma$ (where $\delta\tau$ is an increment of resolved shear stress and $\delta\gamma$ is an increment in elastic resolved shear strain) and an arbitrary hardening law as a functional relation between resolved shear stress and sum of plastic shears. Lin discussed how the consecutive activation of slip systems under load would proceed, how different hardening laws would lead to different activation sequences and different grain rotations (and different texture evolution as a result). The last point discussed was how elasticity reduced the range of possible slip combinations in ambiguous cases, but still did not rule out all of them. The isotropic elasticity of crystals in [25] was a simplification, though elastic strains are small and this simplification is reasonable. The lattice structure of aluminium crystals leads to elastic anisotropy. The experimental measurements of elastic moduli of aluminium were performed in [26]. In more advanced models developed later for the finite element method, an anisotropic elastic potential function was introduced [27].

A convenient formulation of crystal plasticity in terms of finite deformation measures was introduced in [28]. The total deformation of the medium was described by the deformation gradient tensor. This tensor was multiplicatively decomposed into two tensor components — elastic and plastic.

Though the finite deformations were introduced into crystal plasticity, the TBH model was formulated using a small strain measure not defined exactly by the authors. The validity of the established models of crystals for an arbitrary finite strain measure was not strictly proven. In [29], [30] and [31], R. Hill considered the most basic elastic-plastic properties of polycrystalline aggregates (and metals in general) from a mechanical standpoint (without delving into thermodynamics). An arbitrary strain (and corresponding conjugate stress) was used, so that all derivations were independent of the strain measure chosen. Quantitative description of local stress-strain fields was not attempted. Instead a global qualitative response as the relations between macroscopic strain and stress rates in incremental isothermal deformation was studied. A polycrystal is a heterogeneous mixture of crystals and its macroscopic properties are a reflection of the microscopic ones. Hill wanted to reveal which features of the microstructure are "transmitted upwards through the hierarchy of observational levels". Hill showed that if the crystal obeys Schmid's law, then the polycrystal's yield surface will always be convex and the

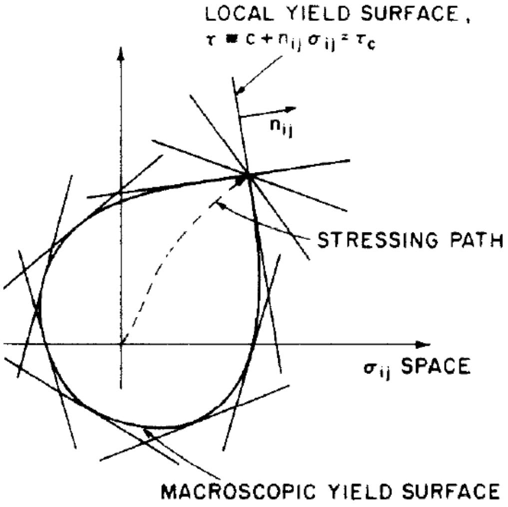

Figure 2.7: In rate-independent plasticity the polycrystal yield surface is the inner envelope of all slip systems' yield planes. When the critical shear stress is reached somewhere in the polycrystal, all planes corresponding to the active systems must contain the current stress state, and hence a vertex develops. Taken from [32].

plastic strain rate will be normal to it. He proved that in elastically isotropic rate-independent crystal plasticity a vertex will form on the yield surface at the point where the stress vector touches the yield surface (see Figure 2.7). The yield surfaces of metals found experimentally were smooth and thus the existence of sharp vertices was doubtable. Hill though showed that anisotropy of elasticity will smoothen the vertex.

Still in this description elastic strains were assumed small. In [33] another level of generalization was applied to the plastic properties of polycrystals. Rice approached the polycrystal as a thermodynamic system. Its inelastic behaviour is caused by different kinds of structural rearrangements (slip, twinning, phase transformations etc.). The extent of this rearrangement at different points of a body is described by a finite number of internal variables. Together with stress, strain and temperature they define the state of the body (state variables). The inelastic deformation is viewed as a sequence of constrained equilibrium states and equilibrium thermodynamics is used. No restrictions were made on the finiteness of elastic or plastic deformations, as well as rate dependency — rate-independent plasticity is a special case of this general framework. Rice showed that if the rate of progression of the structural rearrangements only depends on the current stress state through a conjugate thermodynamic force, then there exists a scalar potential function of the macroscopic stress state at each instant in the history of deformation. The plastic strain rate is a gradient to this potential (in the stress space). In the rate-independent case this reduces to the usual normality rule. Rice also showed how these results could be applied to metals, where the slip on a given system (internal variable) depends on the global stress through the resolved shear stress (conjugate thermodynamic force). The internal variables at separate points for this case are replaced by field-like internal variables. In [34] R. Hill and J. R. Rice developed a more detailed model of a general rate-independent polycrystal within the framework of both [29] and [33]. They addressed the problem of uniqueness of slip system combination and found the condition for unique slip as a requirement to the hardening law. It turned out that uniqueness depends on hardening rates, the stress state and the number and orientation of active systems and is generally not guaranteed for the rate-independent model.

Hardening on different slip systems was an issue first considered in the earliest works of Taylor. As said earlier the overshoot of the tensile axis over the symmetry position indicated that hardening on the inactive systems was higher than on the active one. Accurate measurement of the overshoot could indicate how much higher it was. This method of measuring the latent hardening ratio (LHR) — a ratio between critical resolved shear stress on active and latent systems — is the simplest one but also the most inaccurate. Another method consists in making a big sample of single crystal, straining it in single slip, then cutting smaller samples out of it with different tensile axis orientations (i.e. different slip systems activated in consecutive tensile test). This method is much more difficult and only several works were performed in this way. The difference between the two methods also lies in strain history. In the first one two slips are acting simultaneously and in the second one they act separately.

In [35] the second method is used. The results as summed up in [18] show that the latent hardening is almost always higher than the self-hardening. For coplanar slip systems the LHR was found close to 1. For other systems it varied from 1.15 to 1.4. A later and more thorough investigation was performed in [36]. The same general trend was found, although the coplanar systems were found to have LHR higher than 1. The development of the LHR in the course of straining was investigated. It was found that the LHR grows quickly from 1 to some higher value and then slowly decreases to a constant value. This was approximated with a second order polynomial law. These and some other works are analysed by R.J. Asaro in [37]. Two problems common for all of them mentioned by Asaro is the lack of strain rate influence and inconsistency of results with each other (which may be due to strain rate effects).

2.5 Rate-dependent crystal plasticity theory

Rate independence of plastic flow was a reasonable assumption, but not entirely physically valid. The dislocation dynamics predicted some sort of rate dependency or rate sensitivity. To characterize this sensitivity a parameter m is defined by the following relation

$$m \equiv \frac{\partial ln \dot{\gamma}}{\partial ln \tau} \tag{2.1}$$

In 1981 Chiem and Duffy [38] performed accurate measurements of τ versus γ relations, coupled with observations of dislocation structures with electronic microscopy. They reported different behaviour of dislocations at different strain rates. The value of m was measured at different strain rates, it varied between 70 and 100. They found that it tends to decrease at larger strain rates (meaning aluminium is more strain rate sensitive at higher strain rates) but at quasistatic loading the material behaved as rather strain rate insensitive.

It was not clear whether there is a perceptible difference between a truly rate-independent (described by Schmid law) and rate-insensitive (described by a viscoplastic constitutive relation but with a very low strain rate sensitivity $\frac{1}{m}$) material. J.R. Rice analysed the difference between the two in [32]. He used a relation between τ and $\dot{\gamma}$ of a slip system in the form proposed by Hutchinson in [39]

$$\dot{\gamma}^{\alpha} = \dot{\gamma}_0 \left(\frac{|\tau^{\alpha}|}{\tau_c^{\alpha}} \right)^{\frac{1}{m}} \mathsf{sgn}(\tau^{\alpha}) \tag{2.2}$$

where $\dot{\gamma}_0$ was a reference strain rate and τ_c^{α} was the rate-dependent analogue of the critical shear stress value. In this relation m is equivalent to the strain rate sensitivity in Equation (2.1). Unlike the case of Schmid's law, a non-zero plastic strain rate is present at all stress values different from zero, but at large m its value is negligibly small. The yield surface of such rate-dependent single crystal would not have sharp edges or vertices, but will have smooth transitions between the facets, the radius of the transition curves depending on m. If m approaches infinity, the radius will approach zero and the overall form will be infinitely close to the rate-independent yield surface. Still, according to the analysis [33] the normality of plastic flow would be present as in Schmid's law case. This leads to several important consequences. The rate-independent theory predicts sharp vertices on the yield surface. They were searched experimentally ever since their prediction but were not found. They would not appear in the rate-dependent case, even if the rate sensitivity parameter is very high. Secondly, the ambiguity of slip system choice disappears. Geometrically it can be illustrated by the fact that a normal vector can now be found at all points of the yield surface, no sharp vertex with undefined normal is present. Physically it means that when the stress approaches the corner of the yield surface, slip will gradually begin on the conjugate systems, although at a much lower rate and slip on the primary system will start to decrease and at some point in the middle of the yield surface's corner it will be equal for the two systems. Another difference between the rate-dependent and rate-independent cases is the relation between stress and strain rate: in rate-independent theory $\dot{\gamma}$ is a function of $\dot{\tau}$ while in rate-dependent theory $\dot{\gamma}$ is a function of τ. In [32] Rice also demonstrates that calculations with high m in rate-dependent theory give results practically indistinguishable from the rate-independent ones for problems where both theories can be used.

The rate-independent approach was not abandoned though and a number of attempts to improve it were made. In numerical models in the rate-dependent case if m is high the time step becomes very small and calculation time grows considerably. Gambin in [40] also points out that the reference shear rate in Equation (2.2) is arbitrarily chosen.

2.6 Finite element analysis

The finite element method (FEM) is a way of solving numerically the equations of equilibrium in a continuum using the principle of virtual work. The method can be used with any kind of constitutive relation. In the crystal plasticity field it may be used in combination with Taylor or any other homogenisation model or with the single crystal constitutive relation directly. When we talk about CP-FEM (crystal plasticity finite element method) here, it is implied that the constitutive relation of a single crystal is used in the integration points, so that each element models a grain or part of a grain. The advantage of CP-FEM is that it naturally satisfies both compatibility and equilibrium conditions and allows representing the stress and strain gradients at aggregate and grain levels, unlike Taylor and other such models. It is also usually the only way of solving problems with complex boundary conditions and loading histories. It also allows a natural introduction of some physical phenomena and parameters into the models, like grain boundary effects or shear bands.

The FEM was developed in the 1940s, but was not used with crystal plasticity until the 1980s. The first CP-FEM simulations utilized simplified (two dimensional, three slip systems) crystal model by Rice [32]. In a number of articles ([41], [42], [43], [44], [27]) the FEM and this model were successfully used to analyse the global response and the local behaviour of single crystals and polycrystals. In [45] a 3D aluminium crystal with all 12 slip systems was simulated for the first time.

To accurately describe the lattice rotation and large plastic deformations the finite Lagrangian description of kinematics and kinetics was utilised. The basic formulation is the standard Taylor expansion of the virtual work principle equation about the known state. Both implicit and explicit schemes may be used, depending on the given problem. In [46] the schemes are classified into three types: implicit based on deformation gradient and implicit and explicit based on the slip rates. In [47] an explicit scheme based on deformation gradient is proposed. If an implicit scheme is used, then to update any parameter in the crystalline solid, the value of slip increment $\Delta\gamma^{(\alpha)}$ on the slip system α is necessary. In the aforementioned articles $\Delta\gamma^{(\alpha)}$ is found (after some derivations) from a system of linear equations (see e.g. Equation (3.10) in [27]). For the limit $m \to 0$ (the rate-independent case) the system becomes unsolvable for some combinations of slips on active slip systems, while for the finite positive values of m a unique solution may always be obtained by choosing a small enough time step.

2.7 Strain localization

2.7.1 Necking

Experimental studies of single crystals and polycrystals of metals universally show that homogeneous deformation (in tensile, plane strain and other tests) can only develop until a certain limit. Then the deformation becomes non-homogeneous, with some regions of the material sample deforming much more than the rest. Fast accumulation of plastic strains in these regions (localization of deformation) usually leads to fracture. One type of localization is necking — a quick reduction of thickness (in case of plates) or diameter (in case of cylindrical specimens). If the thickness reduction region is large compared to the thickness, then necking is called diffuse; if this region is comparable in size to the thickness it is called localized.

The first analysis of necking in uniaxial tension was performed in [48] and a simple criterion was derived, which stated that necking starts when the decrease of the force because of reduction of cross section (which reduces to accommodate for plastic incompressibility) cannot be compensated by hardening. In any other more complex stress-strain situation than uniaxial tension, the criterion of necking is much more difficult to derive. For sheets or plates under general biaxial load a number of models exist. Swift [49] derived a criterion for diffuse necking by expanding the Considère [48] approach to the biaxial stress situation. In the same year Hill analysed localized necking in [50]. He considered discontinuities in the stress and velocity fields and the corresponding hyperbolic equations, and found that velocity discontinuities are an idealised mathematical description of localized necking. The neck would lie along the characteristics of the corresponding equations, which are the lines of zero rate of extension (i.e. all straining is due to thinning of the sheet). The model had some problems, notably it predicted no necking in biaxial stretching. To overcome these difficulties models by Marciniak and Kuczynski [51] and Hutchinson and Neale [52] assumed that the localized necking is initiated by some kind of inhomogeneity in the sheet. To simplify the calculations they assumed a thickness variation in a rectangular region in the sheet. The finite element method was used with relative success to predict the initiation and orientation of localized necks, e.g. [53].

2.7.2 Shear bands

Another type of strain localization which may occur in a strained solid is a shear band. A shear band is a narrow band or slice of a material which undergoes much stronger straining than the surrounding material. The shear bands were commonly observed in specimens strained until high strains before fracture. A comprehensive experimental study of the phenomenon was performed by Price and Kelly [54]. One of the first mathematical treatments of the problem may be found in [55] and the development of these ideas in [56].

Hill [55] analysed what he called "waves" in solids. By a wave he meant a geometric surface in the solid across which some of the field variables are discontinuous, like the gradient of velocity, while other variables remain continuous, like the velocity itself. Generally the fields in a solid body can be described by a set of partial differential equations and their boundary conditions (so called Dirichlet problem). The equations may be classified into three types [57]: hyperbolic, parabolic and elliptic. The usual elasticity problem which has smooth solutions in the whole domain regardless of the boundary conditions is an example of elliptic type. When, depending on the boundary conditions, the solution allows discontinuities in some fields, like in the wave propagation problem, it becomes hyperbolic. Hill analysed a solid with a generalized relation between the stress rate and strain rate expressed by an instantaneous modulus (which he assumed symmetric) and normality in plastic deformation. He showed that under some conditions the elliptic solution for this solid's Dirichlet problem may become hyperbolic. He then showed that a stationary discontinuity of the velocity gradient may exist and identified it as a mathematical description of a shear band. The initiation of the shear band (transition from elliptic to hyperbolic solution) and its orientation is defined by the equation system

$$(n_i L_{ijkl} n_l) g_k = 0 \tag{2.3}$$

where L_{ijkl} is the material modulus, n_i is the normal unit vector to the shear band plane and g_k is a vector defining the jump in corresponding field quantity across the shear band border. A non-trivial solution of this equation corresponds to the transition into the hyperbolic regime and the appearance of a shear band. This solution exists if the determinant of $n_i L_{ijkl} n_l$ is equal to zero:

$$det(n_i L_{ijkl} n_l) = 0 \tag{2.4}$$

The initiation of necking is in a way similar to the initiation of a shear band, but in the case of necking the initiation conditions depend on the geometry of the body and boundary constraints. The shear bands may initiate even in a part of the body with all around boundary conditions that prevent other types of localization. Its initiation only depends on the history of field quantities in the body. Thus the shear band formation is a material instability and necking is a geometrical one (though for some problems the border is not so clear, see [58]).

In [56] Rice used the results of Hill to analyse a number of common constitutive relations including the crystal plasticity model. The common conclusion was that the materials with positive hardening, smooth yield surface and normality are very resistant to the formation of shear bands and bands form when the hardening rate drops to or below zero or the stress reaches values of the order of the elastic modulus. For the crystals, some deviation from the Schmid law (normality) was promoting shear band formation at much more realistic conditions. Other factors promoting shear band formation include the yield surface vertices [53], void nucleation and growth [58] and other softening mechanisms and geometrical imperfections. The analysis by Hill and Rice was limited to the rate-independent case. The rate-dependent extension in [58] shows that rate-dependent materials are even more resistant to shear band formation and no loss of ellipticity is possible in Equation (2.3), but the imperfections may cause a transition to the shear band regime anyway.

In [59] Asaro considered another trigger for shear band formation — geometrical softening. It was mentioned above that, as a result of accommodation of shearing along the slip systems to the boundary conditions of the solid, the slip systems tend to rotate from the original orientations. Asaro used a two-dimensional simplified model of a crystal with three slip systems in single/double slip with consideration of slip system kinematics and found that a slip system in tension or compression situation may rotate in such a way that the resolved shear stress on it will increase for just this geometrical reason alone. Despite the fact that the physical hardening rate on slip systems at any point of the system will remain positive, the effect of these rotations may be so large that the total load on the body will decrease as if it softened. This softening may be the vital factor for the band formation.

Several works used this idea to try and simulate the shear band formation numerically. In [41] a rate-independent single crystal model was used, while [42] and [27] used a rate-dependent model and [44] used compression instead of tension. The rate-independent model as usual proved a limited usefulness and provided no solution for higher latent hardening and slip on several slip systems. The rate-dependent model, even approaching the rate-independent case with high values of m, gave solutions for all cases. The difference between the two was that the shear bands in the rate-dependent case formed later in the strain history. The experimental observations were in good agreement with the results of the finite element simulations. Influence of different factors on the formation and characteristics of the shear bands was studied. Mostly the bands were either early and sharp, linear in form (for the alloys with lower hardening rate and ductility), or formed later, more diffuse and could be rather curved, especially near the interfaces (for the softer alloys with higher hardening rate).

The geometrical softening predicted a certain structure of the shear bands. This structure was observed both in the experiments and the simulations, thus supporting this idea. The band was a narrow region where the lattice orientation was rotated several degrees relative to the surrounding lattice in such a direction that the resolved shear stress on the active slip systems was higher. The band itself was not aligned with any of the slip systems, but was close in orientation to the one with the highest resolved shear stress. The material inside the band was heavily deformed, with strains reaching over 1, but still positively hardening. These geometrical features were at least qualitatively reproduced in the simulations. Certainly some features of the bands could not be reproduced. The formation of shear bands was preceded by the formation of so-called coarse slip bands, which then would coalesce into shear bands and the shear bands themselves consisted of thin layers with varying strain. The finite element model of shear band development was limited by the size of the elements. The shape of the elements and the density of the mesh had to be specially tuned to promote shear banding, and the breadth of the band was usually one element (it could not naturally be smaller).

Recently the hardening models utilizing GND density and plastic strain gradients as parameters were used in localization process simulations in [60]. The results did not differ much from the results of simulations with phenomenological hardening models.

2.8 Polycrystal models

2.8.1 General remarks

Metallic alloys are aggregates of a large number of single crystals which grew in similar conditions and are usually assumed to have similar properties. The properties of an alloy will be defined by the properties of these crystals (grains) but also by how these grains are arranged to form this alloy. The size and shape of constituent grains is called the morphology of the alloy and depends on crystal growth and processing conditions, i.e. the thermomechanical history of the sample. The crystal lattice within each grain will be oriented in some way relative to the reference coordinate system connected to the alloy sample. The grain may be defined as a domain within the sample where the lattice orientation remains approximately constant. The grain boundary is the surface across which the lattice orientation makes a significant jump. Some smaller variations of orientations within grains are possible, see [61]. The texture of a polycrystal statistically describes the orientations of grains in this polycrystal. Because of a large number of grains in any reasonable sample of aluminium, describing each individual orientation is practically impossible. But if the orientations of a large enough number of grains (a representative sample) is known, then it is assumed that in the rest of the polycrystal they have the same statistical distribution. This is more or less true for situations where the stress-strain history of the sample is mostly homogeneous, as in rolling, extrusion or wire drawing, but e.g. in deep drawing the stresses and strains are not homogeneous and different parts of the sample may have different texture evolution.

The first quantitative measurements of grain orientations in large enough samples of metals (i.e. of textures of these metals) were performed by Decker et al. in [62] by X-ray diffraction. In [63] the use of the electron backscatter method is developed. The convenient method of working with orientation data was pioneered by Bunge in [64]. To describe the statistical distribution of orientations in the sample the orientation distribution function (ODF) $f(Q)$ is used, which defines the probability that an infinitely small volume fraction of polycrystal is taken up by the lattice having its orientation in an infinitely small neighbourhood of orientation

Q. To describe the orientations the Euler angles are used, which operate sequentially to rotate the global reference system axes to the local crystal axes. The usual problem then is choosing a limited number of orientations for a model, which will represent best the texture of the material (the ODF). There are different ways to approach the task, like dividing the larger sets of measured orientations into smaller sets and assigning a weight to them [65] or approximating the ODF by a random background and several texture components with varying weights [66].

The texture of an alloy (in comparison to alloys with random distribution of orientations which are sometimes said to have no texture) should lead to anisotropy of the plastic properties of this alloy. Yield surfaces of single crystals are polyhedra; when combined in a non-textured aggregate they are averaged to a smooth isotropic yield surface, but when some orientations are more prominent than others (as in the textured aggregate) the features of the corresponding single crystals' yield surfaces emerge in the aggregate's yield surface. Crystal plasticity can capture these features. In [67] such calculations were performed and compared with experimental observations. Although for part of them the correspondence was found very good, for others it was not. Another possible source of anisotropy is the grain morphology. In many cases after extrusion, compression or rolling the grains tend to be elongated along one of the axes. In [68] the Taylor model is used together with the Hall-Petch relation [69] [70] to account for the grain shape in texture evolution under straining. In [71] the influence of grain shape in a polycrystal is studied by three different models and is found rather noticeable. In [72] it is shown how the columnar grain shape can strongly influence the plastic strain ratio and how this can be modelled by considering the geometrically necessary dislocation density.

Another possible source of anisotropy of a polycrystal is the dislocation structures that form in grains during the straining history prior to testing. In [73] a model is developed where the dislocation structures inside a grain (geometrically necessary boundaries) which may have different orientations in the material, are used in a Hall-Petch like relation to find the CRSS in different directions. In [74] a model is developed which incorporates both texture and intragranular dislocation structure evolution into the usual rate-dependent crystal plasticity model.

The slip hardening is most commonly described by a convenient phenomenological function, like e.g. the Voce law [75]. This approach provided many results but incorporating the size and load path effects is not very convenient. On the other hand, physically based models which use the dislocation population as the main characteristic of the material do this incorporation naturally, like [76], where CRSS and slip rates are found from the dislocation densities and these densities are the parameters evolving during the loading history. The basis for these models was developed in [77] and [78]. The statistically stored dislocation density evolution was expressed by a simple differential equation, integration of which gave a law similar to the Voce law. In both phenomenological and dislocation based models the stress-strain history in a point of a solid is defined by the evolution of parameters in this point. These models are called local. It was mentioned that heterogeneous plastic strain leads to emergence of geometrically necessary dislocations. Increase in their density may lead to pile-ups of mobile dislocations and increased slip resistance. Usually the plastic deformation in a polycrystal is non-homogeneous near grain boundaries, and if the grain size is decreased, the volume fraction of heterogeneous plastic strain increases, influencing the response of the polycrystal considerably. If a model is supposed to take these effects into account, it must include the numerical value of inhomogeneity of plastic strain, i.e. the plastic strain gradient. To calculate a gradient, it is necessary to know the plastic strain in points neighbouring the one under consideration, so the stress-strain history in a point is defined not only by the evolution of parameters in this point, but also by its neighbourhood. Thus these models are called non-local. Application of these concepts to the crystal plasticity framework in [79] or [80] allows to reproduce some length scale effects but is computationally costly.

Aluminium alloys contain other components (usually magnesium and silicon), making them in principle multiphase systems. These components (phases) may be present in different forms: solid solution or particles (precipitates) of different coherency. The size, form, orientation and spacing of these particles may influence considerably the plastic properties of the alloy, like initial yield stress, anisotropy of plastic flow and hardening. In [81] some of these influences are investigated with a focus on the kinematic hardening and the physical explanation of the precipitate hardening mechanism. The precipitates harden the alloy and may cause Bauschinger effect not observed in pure aluminium; if the configuration is right they may reduce the anisotropy of the alloy caused by texture [82], [83]. These effects may be modelled in different ways. A theory where the precipitates are treated as elastic inclusions, based on [84], determines the backstresses which arise due to different elastic properties of the precipitate and the matrix [82], [85]. For higher stresses and strains in the precipitates the plastic inclusion theory, that treats the precipitates as plastically deforming, is more accurate. Since 1948 and Orowan's expression for a dislocation overcoming a particle obstacle [86] models accounting for precipitate-dislocation interactions were proposed and tested, [87] and [88].

2.8.2 Taylor-type polycrystal model

If the texture of a polycrystal is not random, some grain orientations will be more prominent than others, and it will ultimately lead to the anisotropy of the plastic properties of the polycrystal. Single crystals rotate under plastic strains as explained above, so the rotations of grains under plastic loading will lead to texture evolution. The models of polycrystals, which use the properties of single crystals, texture and morphology as input and predict the plastic anisotropy and the texture evolution, were developed early on. In [7] Taylor suggested a model where it is assumed that all grains undergo the same homogeneous strain as the sample. The stresses for each grain would also be homogeneous within the grain and found from resolved shear stresses on active systems. The total stress in the sample is then found as a volume average of the stresses in the grains.

Relaxed Taylor models While in the real polycrystal the grains interact and become both compatible and in stress equilibrium, the original Taylor model (also called Full Constraint (FC) Taylor model) ignored half of the process. It seemed that by sacrificing some aspects of compatibility, some equilibrium could be established and the predictions of the theory will be closer to the experiment. These types of polycrystal models are called the Relaxed Constraint (RC) models.

Honeff and Mecking in [89] proposed a model for alloys with elongated flat grains (lath type) and flat grains with breadth and width of comparable magnitude (pancake type) which are typical for rolling. For lath type, one of the shear strain rate components was not forced onto the grain (relaxed) and for the pancake type two of the shear strain rates (both of which did not distort the plane of the pancake) were relaxed. This means that these components in the global strain rate tensor and the local one were different. Van Houtte in [90] analyses the equations for slip rates in the grain in this case and shows that it is equivalent to introducing another virtual slip system, the critical resolved shear stress for which is usually chosen to be zero. This virtual slip system will always be active and take on one of the 5 independent components of the strain rate tensor, and only 4 real slip systems will be active in lath grains (in case of pancake grains it will be two virtual slip systems and 3 active real slip systems). Then he shows that this kind of relaxation implies a stress condition and the stress tensor components corresponding to the relaxed strain rate components will be zero (and consequently in equilibrium).

In [91] this type of model is developed further. The grain is divided into zones as shown

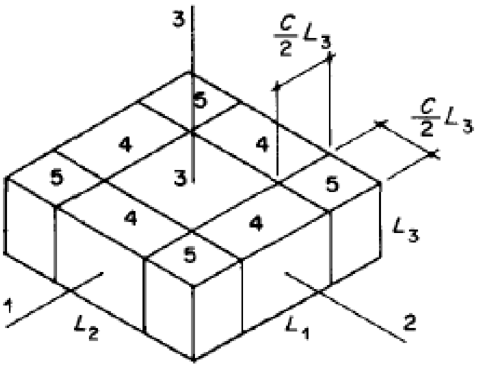

Figure 2.8: The pancake type grain is divided into three zones, where different number of strain rates are relaxed. Taken from [91].

in Figure 2.8, so that the corners (5) are fully strained, the sides (4) are relaxed once (have one virtual slip system) and the center (3) is relaxed twice (has two virtual slip systems). The lath model is similar but consists only of the 4 and 5 type zones. The modified model can also be used for equiaxed grains under rolling or tension, then the FC Taylor model is used up to some strain and is gradually replaced by the RC Taylor model. This approach had some advantages. The predictions for texture evolution were somewhat improved compared to the FC Taylor model. The grain morphology and its evolution also became a part of the model. But the shortcoming were also considerable. The results were not much better than the ones obtained with the FC Taylor model, and the model was limited to rolled/stretched cases of morphology. The strict compatibility of grain deformations from the FC Taylor model was lost. It could be tolerable if the average incompatibility in the polycrystal would be zero, but it was so only for a special case of textures with symmetry around the normal direction.

An attempt to overcome the shortcomings of the first RC Taylor models was made in [92]. The suggested LAMEL model is also specific for rolling and flat elongated grains, but the method is rather different. Instead of one grain as in the previous RC Taylor model, two brick-formed grains stacked on one another lying along the rolling direction are considered, so that they have one common boundary plane. The orientations for these grains are chosen at random from the ODF data. Then two shear components (which do not lie in the interface plane) are allowed to deviate from the global shear, in such a way that they are equal but have opposite sign. This automatically leads to zero volume average of these relaxed shears, incompatible with the other grains, and equality of volume average of all local strain rates and global strain rate. The same additional slip system formalism may be used to construct the equations and find the slip rates. This time the shear stresses on the interface are also in equilibrium but they are not zero. The LAMEL model allows some more accurate predictions of rolling textures but is limited to the rolling case.

A more general model called GIA (grain interaction) was suggested in [93]. Instead of 2, a cluster of 8 brick shaped grains is considered, with 12 interfaces between them. Thus, a total of 24 shears in all grains are relaxed. The method is then similar to the LAMEL model, but to keep the misfits of strain rates on inner interfaces and outer boundaries with the rest of the polycrystal within reasonable limits, a penalty factor is introduced into the equations.

All these models assume homogeneous stress and strain inside the grains, which is not true in real polycrystals. Also the boundaries between the grains in the cluster in the LAMEL and GIA models and the outer grains are treated differently. The model called ALAMEL (advanced LAMEL) [90] assumes a different approach. Instead of using grain centres as the sampling points for stress and strain it uses the boundary between two neighbouring grains and the regions of grain adjacent to the boundary as a basic unit for homogenisation. The orientations of grains are taken from the ODF and the orientation of the grain boundary is found from the microscopy data on grain morphology. Then the process similar to LAMEL is used on them to find slip rates and stresses. The stresses must be in equilibrium on the boundary and the average strain rate of the regions equal to the global strain rate. The orientations after deformation are taken in the regions to construct the deformed texture. The ALAMEL model is generally applicable and showed rather good results. It is also more physically feasible than the FC Taylor model by allowing the jumps in strain rate between grains while keeping equilibrium and compatibility.

2.8.3 Self consistent models

In the self consistent approach each grain is viewed as an ellipsoid surrounded by an elastic-plastic medium, subjected to an external strain history. Then the stress and strain in the grain are calculated from these conditions. The elastic-plastic properties of the medium are in their turn found by averaging the response of all the grains, thus it is called self consistent. The method is based on the work by Eshelby [84] on ellipsoidal inclusions into the elastic medium, which showed that strains in the ellipsoid may be assumed homogeneous and found in an easy and convenient way. Then Hill [94] developed the formulation in the plastic domain. It was further improved to include rate dependence and finite deformations in [95]. The results obtained by this approach in plastic anisotropy and texture evolution predictions are sometimes better than those from the FC Taylor model.

2.8.4 Finite element polycrystal modeling

Most of what was said about single crystal FEM simulations is also valid for polycrystals. There are also some special features. Now the domain consists of a number of grains with a specific morphology, so a number of approaches may be utilized to model them. If only the global response is of interest and some simpler hardening laws are used, then the grains may be represented by cubes, truncated octahedra etc. (or in 2D by regular polygons) and meshed by hexahedral elements. If the morphology should be represented more accurately, then grains are represented by polyhedra (generated as a Voronoi tessellation) and tetrahedral elements may be used, so that the grain boundary is flat and coincide with the element boundary — or smaller hexahedral elements may be used, but the grain boundary is not represented realistically in this case. The influence of element shape and mesh density on the solution, particularly in the localization problems are studied in [96],[97], [98] and [99]. The results show that hexahedral (brick) elements exhibit better performance than tetrahedra, the element size is a defining parameter in the shear banding process, the local stress-strain gradients are sensitive to the element type and size but the global stress-strain response is not.

2.8.5 Texture evolution modelling

The rotation of a single crystal in the course of plastic deformation by slip was described above. The grains in the polycrystal are also constrained by the neighbouring grains and the global boundary conditions, and rotate to accommodate their deformation thus changing the texture. As the texture is a major source of plastic anisotropy, predicting the texture evolution during different loading histories is one of the important tasks of CP theory. The first attempts were made with the FC Taylor model and a limited number of evenly distributed grain orientations [43]. This approach was developed in [100] and [101]. The FC Taylor model and rate-dependent crystal plasticity with a phenomenological hardening law were utilized on a set of several hundred orientations, first randomly distributed and then arranged to represent a texture of a processed alloy (rolled or compressed). The results were compared to the experimental textures. In qualitative sense the predictions were mostly right, but it was noticed that the textures predicted by the FC Taylor model were sharper than the experimental ones (the peak intensities of major texture components were over-predicted) and some weaker and less stable components of the real texture did not appear in the simulations.

The direct finite element modelling of grains was also attempted. In [102] the results from an FC Taylor type model and an FE model, where each element represented one grain, were compared and showed CP-FEM superiority even with this coarse simplified mesh. The factor that prevented CP-FEM from wider use was the high computational cost of the method, which increased drastically for larger and more detailed polycrystal models. For this reason the other variations of the Taylor model were still developed, despite the shortcomings of such homogenisation methods. In [103] different CP-FEM meshes representing the same polycrystal were compared in performance with the FC Taylor model of this polycrystal. Higher resolution meshes performed better as expected and the 3D meshes gave texture evolution closer to the experimental one than the 2D meshes. The study of the deformation throughout the mesh showed that unlike the FC Taylor model, CP-FEM of appropriate resolution always produced strain gradients, which arise as a result of grains adapting to each others deformation. An important difference was the emergence of the shear component of the deformation in some grains while the total deformation did not include shear. This shearing in some grains lead to the development of secondary texture components. These components could not be captured in the Taylor model at all.

In [97] the influence of mesh resolution was studied more in-depth, by making detailed models of a polycrystal with each grain divided into almost 200 elements. Large number of elements inside each grain allowed for inhomogeneous rotations of the lattice in the grains. Different areas rotated differently, depending on their local boundary conditions and formed cells with misorientations smaller than those between different grains, but large enough to improve the obtained deformation textures. In [90] and [104] predictions from different CP models are again compared to the experimental textures. The authors point towards another possible difference between the Taylor type models and CP-FEM — the grains with the same orientations but different surrounding grains will experience different stress-strain history and rotate differently. Another notable result is that the relaxed Taylor models showed the worst results of all tested models. Despite some success, overall the predictions of texture evolution made by any model are still not accurate and reliable enough to be really quantitative predictions.

2.8.6 Shear bands in polycrystals

Most of what has been said about the mechanisms and processes of shear banding in single crystals is true also for polycrystals. The rotation of grains during plastic deformation leads to increased resolved shear stress on some slip systems and overall softening of the grain for shearing. Shear bands develop in some favourably oriented grains and propagate through the grain boundaries into the neighbouring grains. Rotation of neighbouring grains may reduce misorientation between them and make the band propagation easier. The term "geometrical softening" for single crystals is somewhat analogous to the "textural softening" of polycrystals. Under loading the texture may evolve in such a way that the Taylor factor (see e.g. [8] for the definition) for this polycrystal decreases, thus reducing the total force.

Numerical studies of localisation in polycrystals were started with phenomenological material models [53]. As soon as crystal plasticity was introduced into simulations in the 1980s it was used to study the localisation processes in [44]. The polycrystal was modelled as a 2D set of regular polygons. Random orientations were used and formation of bands of high strain were observed in the simulations. A similar investigation was performed in [105]. In these early works the number of grains was limited and the elements used were usually triangles combined into quadrilaterals, which were introduced in [53] and chosen for their ability to represent well shear along diagonals. The elements were usually oriented in such a way as to promote the anticipated shear band. In [106] the influence of element type and mesh density on the shear band formation was investigated. Triangular and rectangular elements of different order and integration type were tested. It was shown that triangular elements of lower order may even prevent the band formation, while no such problems were encountered while using quadrilaterals. An improvement over the older simulations was the use of Voronoi tesselation to create realistic irregular shaped grains. The influence of other parameters, like rate sensitivity, were also investigated.

In [107] and [108] the FC Taylor model was used to model thin polycrystalline sheets instead of modelling grains. Although the conditions for propagation of shear bands in such approach is quite different from direct grain modelling, the results agreed reasonably well with CP-FEM simulations and experimental data.

The influence of texture of a polycrystal on the development of the shear bands in it was investigated in [109]. A Taylor type model was also used, but this time each integration point was assigned 8 orientations, so that the material as a whole represented statistically the texture and was heterogeneous. Different textures gave different patterns of shear bands and cube texture enhanced resistance to shear localization.

The more advanced hardening theory based on GND densities and plastic strain gradients was applied to the localization problem in uniaxial tension in [110]. The influence of different mesh configurations was studied. The model gave mostly the same results as the simpler phenomenological models.

2.8.7 Texture gradients

A homogeneous texture throughout a sample is often a simplification. In processes such as rolling and extrusion, the boundary conditions lead to inhomogeneous strains and as a result to variation of the texture. The texture often has one strongest component at the surface, which gradually changes to another component at the center, so this variation is called the texture gradient. In [111] and [112] the texture gradients are measured in rolled sheets. The Taylor type simulations of rolling gave a reasonably good correspondence with the measurements. In [113] the influence of different parameters of the rolling process on the evolution of texture and texture gradient was studied. In [114] a method of representing the texture gradient through the thickness of a sheet by interpolation functions was developed.

The influence of texture gradients on yield surfaces and forming limit diagrams of aluminium alloys is studied in [115]. The Taylor type model is used to find the yield surfaces of different layers in an aluminium sheet, with a specific focus on the vertex like shapes on the surfaces. The experimental data has a large spread and the results are not conclusive, though some influence of the texture gradient was observed. In [116] strain localization in the sheets with through thickness texture gradient is simulated. Both the FC Taylor model and a CP-FEM model with regular quadrilateral grains are used. The results are compared to the results obtained for the homogeneous texture distribution. For the homogeneous texture the bands were multiple and similar in intensity. In contrast, when the models with texture gradient were used, the FC Taylor type model produced two bands, with a main band and a weaker secondary band. In case of the CP-FEM model only one band was observed. The strong texture gradient clearly influences the properties of the aluminium sheets but this influence is not highlighted in existing literature.

2.9 Phenomenological plasticity models

The phenomenological plasticity models are used in parts of this thesis, so a brief review of this area is necessary. Before the crystalline nature of metals and the physical mechanism of their plastic deformation became known, plasticity was studied and described by constructing some constitutive equations, that connected stress and plastic strains. The phenomenological plasticity models include a yield function, which defines the stress state at which the plastic deformation starts, a flow rule, which defines the direction of the plastic flow, and the hardening rule, which defines the evolution of the flow stress. For metals the associated flow rule is usually assumed, which means that the plastic strains are normal to the yield surface in the stress space. The hardening rule is usually chosen out of convenience. Therefore the yield functions will be mostly discussed further.

The yield function is some norm of the stress tensor (usually the deviatoric stress tensor, as the hydrostatic pressure does not affect the plastic flow in metals [117]), which turns it into a scalar stress. Tresca proposed the first yield function in the middle of the 19th century. He assumed that the yield starts as the maximum shear stress reaches a critical value. Later von Mises proposed a quadratic form, which is until now the most popular yield function. This function was generalised to a non-quadratic form in [118] and [119]. It was shown that the exponent of the yield function depends on the crystalline structure of the metal, being 8 for FCC and 6 for BCC metals. Hill proposed a generalisation of the von Mises function which made it suitable for plastically anisotropic materials in [120]. It was further generalized by making it non-quadratic and adding other terms in [121] and [122]. The Hershey's isotropic yield function was adapted for anisotropic plasticity by Barlat and co-authors in the YLD series of yield functions [123], [124] and by Banabic et al. in BBC series of functions [125], [126].

Karafillis and Boyce proposed a way to account for anisotropy by a linear transformation of the deviatoric stress tensor in [127]. A class of yield functions based on this linear transformation was developed by Barlat et al in [128] and [129].

These phenomenological functions are very flexible and can describe all sorts of plastic behaviour but at a price of a large number of experimental tests, necessary to properly calibrate them. Some of the tests could be replaced by the crystal plasticity simulations, as discussed in [130], [131], [132] and [133].

Chapter 3

Summary and remarks

3.1 Summary

The topic of the present thesis is the plastic properties of aluminium alloys, specifically the 6000 series, and the numerical models which describe these properties. The aspects of the plastic behaviour studied in this work are the yield and work hardening, flow stress and plastic flow anisotropy and their connection with the material's microstructure and the influence of these features on strain localisation in diffuse necking. The numerical models include anisotropic phenomenological plasticity models and crystal plasticity models with various slip system hardening rules, implemented as user subroutines in the finite element simulations. The experimental data is obtained from uniaxial tensile tests on cylindrical specimens. The accurate measurement of diameters of the specimen in two directions, appropriately coinciding with the local axes of material symmetry, allowed to estimate the average true stress in the post-necking regime and the development of the plastic strain anisotropy. Consequently, the application of the phenomenological and the crystal plasticity models to the anisotropic AA6000 alloys with strong crystallographic textures at large plastic strains was tested in different contexts in all the included articles.

Article 1 deals with estimating the equivalent stress-strain curve of the corresponding alloy from the data provided by this experimental set-up. The true stress-strain curve may be calculated easily from the measurement results, if the cross section of the specimen is assumed to remain elliptical at all times. This is a reasonable assumptions for a material with an orthotropic symmetry. But this true stress will include a considerable contribution of a triaxial stress field, that arises in the neck of the specimen. This field is due to the geometrical constraint of the specimen, as well as the material properties. The work-hardening of the material itself, especially in the large strain range after necking, is therefore very difficult to estimate from the true stress-strain data. The existing analytical solutions assume an isotropic material. In the present case, a number of specimens was produced from AA6060 and AA6082 alloys with different heat treatments, corresponding to T4, T6, T6x, T7 and O tempers. The microstructures of the two alloys were investigated and their crystallographic textures were procured. Both alloys were found to possess a strong texture, which indicates a yield surface different from an isotropic one. The texture data was used to obtain the anisotropic yield surfaces, used in the anisotropic phenomenological yield surface Yld2004-18p [128]. This plasticity model, implemented in a FEM code in previous work, was used to simulate the uniaxial tensile tests. The true stress-strain curve from the simulation contains the contributions from the material model (equivalent stress-strain curve) and the geometrical constraint of the neck (triaxial stress field). An optimization program used the work-hardening parameters of the equivalent stress-strain curve as variables and the difference between the simulated and experimental true stress-strain curve as residual that needs to be minimized. This allowed obtaining the work-hardening model parameters (equivalent stress-strain curve) for all the tested alloy and heat treatment combinations. The validity of these results depends on the accuracy of the FEM model in describing the stress-strain fields in the specimen, especially in the necking zone. The same optimisation procedure was performed with the same experimental data and an isotropic J2 plasticity model. The comparison showed that the material anisotropy noticeably influences the stress and work-hardening rate determined in the optimisation procedure. The yield surface estimated with the crystal plasticity theory was evaluated by comparing the strains in the directions normal to the tensile direction (the plastic strain ratio) in the simulation and the experiment. They were found reasonably similar and quite different from unity (which was the case for the isotropic material).

This experimental-numerical procedure was used in Article 2, 3 and 4 as well. In case of Article 2, the same results from Article 1 were used as the experimental basis. Article 2 deals with an existing nanoscale model, which uses the information about the chemical composition of the alloy and its heat treatment to predict its yield strength and work-hardening. It uses the dislocation density in the crystals of the alloy as the hardening parameter and predicts its evolution depending on the solid solution concentration and precipitate particles size and average distance. The transition from the local crystal level to the global level is made in a very simplified way, by using the Taylor factor, and the model was calibrated and tested on the non-textured alloys only. In Article 2 it is proposed to make the local-global transition more realistic by using a crystal plasticity model. The new formulation automatically includes the texture and texture evolution influence on the yield and work-hardening properties of the alloy in case of an arbitrary crystallographic texture. The proposed crystal plasticity model also uses dislocation density as the work-hardening parameter on slip system level and includes the hardening caused by the precipitate particles via the characteristic distance between them. The full constraint Taylor model is used as the homogenisation method. The textured AA6060 and AA6082 alloys in different tempers from Article 1 were used as a case study. Their precipitation particle and solid solution content were predicted by the precipitate model and used together with their texture data to find their yield stress and equivalent stress-strain curves. The results showed that the texture has a noticeable influence on the yield stress and initial work-hardening rate and texture evolution has some influence on the work-hardening rates at large plastic strains. But the stress-strain curves obtained with the new method were only marginally closer to the experimental ones. The influence of the precipitation model was found to be much stronger than the influence of the crystallographic texture.

Article 5 from the Appendix contains some preliminary studies of the concepts, that were later extensively examined in Article 3. Article 3 uses alloy AA6060 in T4 temper again, but in this study the axes of the tensile specimens, cut from the extruded profile, are oriented in different directions: from 0° to 90° at 22.5° intervals. The procedures developed in Article 1 are applied to these specimens and consequently the equivalent stress-strain curves until fracture are obtained for this material in different material directions. The results reveal that the anisotropy of the flow stress and the plastic flow for this material evolves considerably during the deformation. The test is modelled by the FEM with the crystal plasticity material model. Besides a phenomenological slip system hardening model (Voce), a class of work-hardening models that use the dislocation densities on the slip systems as the hardening parameter was used. These models describe the latent hardening using an interaction matrix, which is physically the relative strength of interaction between the dislocations on different slip systems. Finding the correct values of this matrix is a long-standing problem in material science. A number of values were found for it by different experimental and numerical methods. In Article 3 some typical values are evaluated for this particular test type (uniaxial tension). It is demonstrated that the values of the interaction matrix affect some features of the evolving plastic anisotropy and have even stronger effect on the local behaviour of the constituent crystals. Some other features of the plastic anisotropy could not be reproduced by the crystal plasticity model, namely the higher yield stress and hardening rate in 0° direction. It could nevertheless be reproduced if the initial dislocation density was assumed to be different on different slip systems and if certain values of the interaction matrix were used. While estimating the values of the interaction matrix from this sort of experimental data does not seem feasible, it could be used to evaluate the values found by other methods.

Article 4 once again uses the experimental and numerical set-up from Article 1, but this time on another AA6060 alloys in cast and homogenised and extruded states. The specimens this time are either smooth as in Articles 1 and 3 or notched, with a 2 *mm* or 0.8 *mm* notch radius. The extruded material is particularly interesting, because it demonstrates an extremely sharp cube texture under the EBSD investigation and unusual rhomboid shapes of the fracture surfaces of the notched specimens and almost rectangular shape of the fracture surfaces of the smooth specimens. The cast and homogenised material demonstrates the circular fracture surfaces, typical for an plastically isotropic material. The procedures described in Article 1 are used again to obtain the hardening parameters of the materials, though in this case the non-elliptic cross-section of the extruded material specimens is likely to introduce an error. Crystal plasticity and anisotropic phenomenological plasticity models were used with the same FEM mesh to model the tensile tests. Unlike Articles 1–3, where crystal plasticity was used with a representative volume element, the mesh used in crystal plasticity simulations in Article 4 was based on realistic specimen geometry, with the average size of the grain in the model approximately equal to the average size of the grain in the tested alloy. For the cast and homogenized material the results were similar: both plasticity models and specimen geometries produced the same circular cross sections, as expected, and the force-displacement was predicted accurately by both models as well. For the extruded material the results were more varied. The phenomenological model failed to predict the unusual cross section shapes of the notched specimens, while the crystal plasticity succeeded in this. For the smooth specimens the results were less conclusive, both phenomenological and crystal plasticity models captured some features of the experimental cross-section but failed at others. The force-displacement predictions were off for both models, probably due to the error in the material parameters identification introduced by the non-elliptic shape of the cross sections. The results demonstrated that in some cases only a combination of a physically based material model (crystal plasticity) and a realistic geometry and boundary conditions (leading to an accurate description of the stress-strain field) can reproduce the experimental results.

3.2 Suggestions for future work

- A number of simplifications were made in Article 1, that could introduce some error (most likely insignificant) in the results. The full 3D yield surface could be obtained from the crystal plasticity simulations, instead of a reduced one in the article and using CP-FEM instead of the full constraint Taylor model.

- In Article 2 the main problem seems to be with the precipitation model. In terms of its crystal plasticity part, a better homogenisation technique could be used, like relaxed constraint, self-consistent or CP-FEM.

- The main weakness of the method in Article 3 is the use of full constraint Taylor for material parameter identification. In that case the use of CP-FEM instead is problematic, because of the high computational cost. But some other homogenisation methods could be tested, their influence on the response for models with different interaction matrices could be studied and eventually a more accurate material parameter identification could be performed.

- In Article 4 a more advanced crystal plasticity hardening model could be used instead of the Voce rule. The mesh could be more refined, to the point of representing each grain with several elements.

References

[1] J. A. Ewing and W. Rosenhain, "Experiments in micro-metallurgy: effects of strain. Preliminary notice," *Proceedings of the Royal Society of London*, vol. 65, no. 413-422, pp. 85–90, 1899.

[2] J. A. Ewing and W. Rosenhain, "The crystalline structure of metals. Second paper," *Proceedings of the Royal Society of London*, vol. 67, no. 435-441, pp. 112–117, 1900.

[3] G. I. Taylor and C. F. Elam, "Bakerian lecture. The distortion of an aluminium crystal during a tensile test," *Proceedings of the Royal Society of London. Series A*, vol. 102, no. 719, pp. 643–667, 1923.

[4] G. Taylor and C. Elam, "The plastic extension and fracture of aluminium crystals," *Proceedings of the Royal Society of London. Series A, Containing Papers of a Mathematical and Physical Character*, pp. 28–51, 1925.

[5] K. P. Shah, "http://practicalmaintenance.net/?p=1135."

[6] E. Schmid, "Yield point of crystals. Critical shear stress law," in *Proceedings of the First International Congress for Applied Mechanics, Delft*, 1924.

[7] G. I. Taylor and H. Quinney, "The plastic distortion of metals," *Philosophical Transactions of the Royal Society of London. Series A, Containing Papers of a Mathematical or Physical Character*, pp. 323–362, 1932.

[8] J. Bishop and R. Hill, "XLVI. A theory of the plastic distortion of a polycrystalline aggregate under combined stresses," *Philosophical Magazine*, vol. 42, no. 327, pp. 414–427, 1951.

[9] G. I. Taylor, “The mechanism of plastic deformation of crystals. Part I. Theoretical,” *Proceedings of the Royal Society of London. Series A, Containing Papers of a Mathematical and Physical Character*, pp. 362–387, 1934.

[10] E. Orowan, “Plasticity of crystals,” *Zeitschrift für Physik*, vol. 89, no. 9-10, pp. 605–659, 1934.

[11] M. Polanyi, “Lattice distortion which originates plastic flow,” *Zeitschrift für Physik*, vol. 89, no. 9-10, pp. 660–662, 1934.

[12] J. M. Burgers, *Some considerations on the fields of stress connected with dislocations in a regular crystal lattice. I.* Koninklijke Nederlandse Akademie van Wetenschappen, 1939.

[13] V. Volterra, “Sur l’équilibre des corps élastiques multiplement connexes,” in *Annales Scientifiques de l’Ecole Normale Superieure*, vol. 24, pp. 401–517, Société mathématique de France, 1907.

[14] W. Lomer, “A dislocation reaction in the face-centred cubic lattice,” *Philosophical Magazine Series 7*, vol. 42, no. 334, pp. 1327–1331, 1951.

[15] F. Frank and W. Read Jr, “Multiplication processes for slow moving dislocations,” *Physical Review*, vol. 79, no. 4, p. 722, 1950.

[16] J. Nye, “Some geometrical relations in dislocated crystals,” *Acta Metallurgica*, vol. 1, no. 2, pp. 153–162, 1953.

[17] H. Gao and Y. Huang, “Geometrically necessary dislocation and size-dependent plasticity,” *Scripta Materialia*, vol. 48, no. 2, pp. 113–118, 2003.

[18] U. Kocks, “The relation between polycrystal deformation and single-crystal deformation,” *Metallurgical and Materials Transactions*, vol. 1, no. 5, pp. 1121–1143, 1970.

[19] P. Van Houtte, “On the equivalence of the relaxed Taylor theory and the Bishop-Hill theory for partially constrained plastic deformation of crystals,” *Materials Science and Engineering*, vol. 55, no. 1, pp. 69–77, 1982.

[20] J. Bishop and R. Hill, “CXXVIII. A theoretical derivation of the plastic properties of a polycrystalline face-centred metal,” *Philosophical Magazine Series 7*, vol. 42, no. 334, pp. 1298–1307, 1951.

[21] G. Sachs, “Plasticity problems in metals,” *Transactions of the Faraday Society*, vol. 24, pp. 84–92, 1928.

[22] H. Cox and D. Sopwith, “The effect of orientation on stresses in single crystals and of random orientation on strength of polycrystalline aggregates,” *Proceedings of the Physical Society*, vol. 49, no. 2, p. 134, 1937.

[23] E. Calnan and C. Clews, “XCVII. Deformation textures in face-centred cubic metals,” *Philosophical Magazine*, vol. 41, no. 322, pp. 1085–1100, 1950.

[24] J. Bishop, “A theory of the tensile and compressive textures of face-centred cubic metals,” *Journal of the Mechanics and Physics of Solids*, vol. 3, no. 2, pp. 130–142, 1955.

[25] T. Lin, “Analysis of elastic and plastic strains of a face-centred cubic crystal,” *Journal of the Mechanics and Physics of Solids*, vol. 5, no. 2, pp. 143–149, 1957.

[26] J. F. Thomas Jr, “Third-order elastic constants of aluminum,” *Physical Review*, vol. 175, no. 3, p. 955, 1968.

[27] A. Needleman, R. Asaro, J. Lemonds, and D. Peirce, “Finite element analysis of crystalline solids,” *Computer Methods in Applied Mechanics and Engineering*, vol. 52, no. 1, pp. 689–708, 1985.

[28] E. Lee and D. Liu, “Finite-strain elastic—plastic theory with application to plane-wave analysis,” *Journal of Applied Physics*, vol. 38, no. 1, pp. 19–27, 1967.

[29] R. Hill, “The essential structure of constitutive laws for metal composites and polycrystals,” *Journal of the Mechanics and Physics of Solids*, vol. 15, no. 2, pp. 79–95, 1967.

[30] R. Hill, “On constitutive inequalities for simple materials - I,” *Journal of the Mechanics and Physics of Solids*, vol. 16, no. 4, pp. 229–242, 1968.

[31] R. Hill, “On constitutive inequalities for simple materials - II,” *Journal of the Mechanics and Physics of Solids*, vol. 16, no. 5, pp. 315–322, 1968.

[32] J. Pan and J. R. Rice, “Rate sensitivity of plastic flow and implications for yield-surface vertices,” *International Journal of Solids and Structures*, vol. 19, no. 11, pp. 973–987, 1983.

[33] J. R. Rice, “Inelastic constitutive relations for solids: an internal-variable theory and its application to metal plasticity,” *Journal of the Mechanics and Physics of Solids*, vol. 19, no. 6, pp. 433–455, 1971.

[34] R. Hill and J. Rice, “Constitutive analysis of elastic-plastic crystals at arbitrary strain,” *Journal of the Mechanics and Physics of Solids*, vol. 20, no. 6, pp. 401–413, 1972.

[35] U. Kocks and T. Brown, “Latent hardening in aluminum,” *Acta Metallurgica*, vol. 14, no. 2, pp. 87–98, 1966.

[36] P. Franciosi, M. Berveiller, and A. Zaoui, “Latent hardening in copper and aluminium single crystals,” *Acta Metallurgica*, vol. 28, no. 3, pp. 273–283, 1980.

[37] R. J. Asaro, “Micromechanics of crystals and polycrystals,” *Advances in Applied Mechanics*, vol. 23, pp. 1–115, 1983.

[38] C. Chiem and J. Duffy, “Strain rate history effects and observations of dislocation substructure in aluminum single crystals following dynamic deformation,” *Materials Science and Engineering*, vol. 57, no. 2, pp. 233–247, 1983.

[39] J. Hutchinson, “Bounds and self-consistent estimates for creep of polycrystalline materials,” *Proceedings of the Royal Society of London. A. Mathematical and Physical Sciences*, vol. 348, no. 1652, pp. 101–127, 1976.

[40] W. Gambin, “Refined analysis of elastic-plastic crystals,” *International Journal of Solids and Structures*, vol. 29, no. 16, pp. 2013–2021, 1992.

[41] D. Peirce, R. Asaro, and A. Needleman, “An analysis of nonuniform and localized deformation in ductile single crystals,” *Acta Metallurgica*, vol. 30, no. 6, pp. 1087–1119, 1982.

[42] D. Peirce, R. J. Asaro, and A. Needleman, “Material rate dependence and localized deformation in crystalline solids,” *Acta Metallurgica*, vol. 31, no. 12, pp. 1951–1976, 1983.

[43] R. J. Asaro and A. Needleman, “Overview no. 42: Texture development and strain hardening in rate dependent polycrystals,” *Acta Metallurgica*, vol. 33, no. 6, pp. 923–953, 1985.

[44] S. Harren, H. Deve, and R. Asaro, “Shear band formation in plane strain compression,” *Acta Metallurgica*, vol. 36, no. 9, pp. 2435–2480, 1988.

[45] R. Becker, J. Butler, H. Hu, and L. Lalli, “Analysis of an aluminum single crystal with unstable initial orientation (001)[110] in channel die compression,” *Metallurgical Transactions A*, vol. 22, no. 1, pp. 45–58, 1991.

[46] X. Ling, M. Horstemeyer, and G. Potirniche, “On the numerical implementation of 3D rate-dependent single crystal plasticity formulations,” *International Journal for Numerical Methods in Engineering*, vol. 63, no. 4, pp. 548–568, 2005.

[47] M. Grujicic and S. Batchu, “Crystal plasticity analysis of earing in deep-drawn ofhc copper cups,” *Journal of Materials Science*, vol. 37, no. 4, pp. 753–764, 2002.

[48] M. Considère, *Memoire sur l’emploi du fer et de l’acier dans les constructions*. Dunod, 1885.

[49] H. Swift, “Plastic instability under plane stress,” *Journal of the Mechanics and Physics of Solids*, vol. 1, no. 1, pp. 1–18, 1952.

[50] R. Hill, “On discontinuous plastic states, with special reference to localized necking in thin sheets,” *Journal of the Mechanics and Physics of Solids*, vol. 1, no. 1, pp. 19–30, 1952.

[51] Z. Marciniak and K. Kuczyński, “Limit strains in the processes of stretch-forming sheet metal,” *International Journal of Mechanical Sciences*, vol. 9, no. 9, pp. 609–620, 1967.

[52] J. Hutchinson, K. Neale, and A. Needleman, “Mechanics of sheet metal forming,” *Plenum Press, New York*, p. 269, 1978.

[53] V. Tvergaard, A. Needleman, and K. K. Lo, “Flow localization in the plane strain tensile test,” *Journal of the Mechanics and Physics of Solids*, vol. 29, no. 2, pp. 115–142, 1981.

[54] R. Price and A. Kelly, “Deformation of age-hardened aluminium alloy crystals—II. Fracture,” *Acta Metallurgica*, vol. 12, no. 9, pp. 979–992, 1964.

[55] R. Hill, “Acceleration waves in solids,” *Journal of the Mechanics and Physics of Solids*, vol. 10, no. 1, pp. 1–16, 1962.

[56] J. R. Rice, *The localization of plastic deformation*. Division of Engineering, Brown University, 1976.

[57] T. Belytschko, W. K. Liu, B. Moran, and K. Elkhodary, *Nonlinear finite elements for continua and structures*. John Wiley & Sons, 2013.

[58] A. Needleman and V. Tvergaard, “Analyses of plastic flow localization in metals,” *Applied Mechanics Reviews*, vol. 45, no. 3S, pp. S3–S18, 1992.

[59] R. J. Asaro, “Geometrical effects in the inhomogeneous deformation of ductile single crystals,” *Acta Metallurgica*, vol. 27, no. 3, pp. 445–453, 1979.

[60] N. Jia, P. Eisenlohr, F. Roters, D. Raabe, and X. Zhao, “Orientation dependence of shear banding in face-centered-cubic single crystals,” *Acta Materialia*, vol. 60, no. 8, pp. 3415–3434, 2012.

[61] L. Delannay, O. Mishin, D. J. Jensen, and P. Van Houtte, “Quantitative analysis of grain subdivision in cold rolled aluminium,” *Acta Materialia*, vol. 49, no. 13, pp. 2441–2451, 2001.

[62] B. Decker, E. Asp, and D. Harker, “Preferred orientation determination using a Geiger counter X-ray diffraction goniometer,” *Journal of Applied Physics*, vol. 19, no. 4, pp. 388–392, 1948.

[63] D. J. Dingley and V. Randle, “Microtexture determination by electron back-scatter diffraction,” *Journal of Materials Science*, vol. 27, no. 17, pp. 4545–4566, 1992.

[64] H. Bunge, *Texture analysis in materials science: mathematical methods*. Butterworths, 1982.

[65] M. A. Melchior and L. Delannay, “A texture discretization technique adapted to polycrystalline aggregates with non-uniform grain size,” *Computational Materials Science*, vol. 37, no. 4, pp. 557–564, 2006.

[66] T. Böhlke, U.-U. Haus, and V. Schulze, “Crystallographic texture approximation by quadratic programming,” *Acta Materialia*, vol. 54, no. 5, pp. 1359–1368, 2006.

[67] F. Barlat, Y. Maeda, K. Chung, M. Yanagawa, J. Brem, Y. Hayashida, D. Lege, K. Matsui, S. Murtha, S. Hattori, *et al.*, "Yield function development for aluminum alloy sheets," *Journal of the Mechanics and Physics of Solids*, vol. 45, no. 11, pp. 1727–1763, 1997.

[68] H. Bunge, F. Wagner, and P. Van Houtte, "A new way to include the grain shape in texture simulations with the Taylor model," *Journal de Physique Lettres*, vol. 46, no. 23, pp. 1109–1113, 1985.

[69] W. Sylwestrowicz and E. Hall, "The deformation and ageing of mild steel," *Proceedings of the Physical Society. Section B*, vol. 64, no. 6, p. 495, 1951.

[70] N. J. Petch, "The cleavage strength of polycrystals," *Journal of Iron Steel Institute*, 1953.

[71] L. Delannay, M. Melchior, J. Signorelli, J.-F. Remacle, and T. Kuwabara, "Influence of grain shape on the planar anisotropy of rolled steel sheets–evaluation of three models," *Computational Materials Science*, vol. 45, no. 3, pp. 739–743, 2009.

[72] L. Delannay and M. R. Barnett, "Modelling the combined effect of grain size and grain shape on plastic anisotropy of metals," *International Journal of Plasticity*, vol. 32, pp. 70–84, 2012.

[73] N. Hansen and D. J. Jensen, "Flow stress anisotropy caused by geometrically necessary boundaries," *Acta Metallurgica et Materialia*, vol. 40, no. 12, pp. 3265–3275, 1992.

[74] B. Peeters, M. Seefeldt, C. Teodosiu, S. R. Kalidindi, P. Van Houtte, and E. Aernoudt, "Work-hardening/softening behaviour of bcc polycrystals during changing strain paths: I. An integrated model based on substructure and texture evolution, and its prediction of the stress–strain behaviour of an if steel during two-stage strain paths," *Acta Materialia*, vol. 49, no. 9, pp. 1607–1619, 2001.

[75] E. Voce, "A practical strain-hardening function," *Acta Metallurgica*, vol. 51, pp. 219–226, 1955.

[76] A. Ma and F. Roters, "A constitutive model for FCC single crystals based on dislocation densities and its application to uniaxial compression of aluminium single crystals," *Acta Materialia*, vol. 52, no. 12, pp. 3603–3612, 2004.

[77] U. Kocks, “Laws for work-hardening and low-temperature creep,” *Journal of Engineering Materials and Technology*, vol. 98, no. 1, pp. 76–85, 1976.

[78] H. Mecking and U. Kocks, “Kinetics of flow and strain-hardening,” *Acta Metallurgica*, vol. 29, no. 11, pp. 1865–1875, 1981.

[79] J. Y. Shu and N. A. Fleck, “Strain gradient crystal plasticity: size-dependent deformation of bicrystals,” *Journal of the Mechanics and Physics of Solids*, vol. 47, no. 2, pp. 297–324, 1999.

[80] Y. Aoyagi and K. Shizawa, “Multiscale crystal plasticity modeling based on geometrically necessary crystal defects and simulation on fine-graining for polycrystal,” *International Journal of Plasticity*, vol. 23, no. 6, pp. 1022–1040, 2007.

[81] A. Abel and R. Ham, “The cyclic strain behaviour of crystals of aluminum-4 wt.% copper—I. The Bauschinger effect,” *Acta Metallurgica*, vol. 14, no. 11, pp. 1489–1494, 1966.

[82] P. Bate, W. Roberts, and D. Wilson, “The plastic anisotropy of two-phase aluminium alloys—I. Anisotropy in unidirectional deformation,” *Acta Metallurgica*, vol. 29, no. 11, pp. 1797–1814, 1981.

[83] H. Sehitoglu, T. Foglesong, and H. Maier, “Precipitate effects on the mechanical behavior of aluminum copper alloys: Part II. Modeling,” *Metallurgical and Materials Transactions A*, vol. 36, no. 13, pp. 763–770, 2005.

[84] J. D. Eshelby, “The determination of the elastic field of an ellipsoidal inclusion, and related problems,” *Proceedings of the Royal Society of London. Series A. Mathematical and Physical Sciences*, vol. 241, no. 1226, pp. 376–396, 1957.

[85] C.-S. Han, R. Wagoner, and F. Barlat, “On precipitate induced hardening in crystal plasticity: theory,” *International Journal of Plasticity*, vol. 20, no. 3, pp. 477–494, 2004.

[86] E. Orowan, “Problems of plastic gliding,” *Proceedings of the Physical Society*, vol. 52, no. 1, p. 8, 1940.

[87] F. Fazeli, W. Poole, and C. Sinclair, “Modeling the effect of AlSc precipitates on the yield stress and work hardening of an Al–Mg–Sc alloy,” *Acta Materialia*, vol. 56, no. 9, pp. 1909–1918, 2008.

[88] O. R. Myhr, Ø. Grong, and K. O. Pedersen, “A combined precipitation, yield strength, and work hardening model for al-mg-si alloys,” *Metallurgical and Materials Transactions A*, vol. 41, no. 9, pp. 2276–2289, 2010.

[89] H. Honneff and H. Mecking, “Analysis of the deformation texture at different rolling conditions,” in *Proceedings of ICOTOM*, vol. 6, pp. 347–355, 1981.

[90] P. Van Houtte, S. Li, M. Seefeldt, and L. Delannay, “Deformation texture prediction: from the Taylor model to the advanced LAMEL model,” *International Journal of Plasticity*, vol. 21, no. 3, pp. 589–624, 2005.

[91] C. Tome, G. Canova, U. Kocks, N. Christodoulou, and J. Jonas, “The relation between macroscopic and microscopic strain hardening in FCC polycrystals,” *Acta Metallurgica*, vol. 32, no. 10, pp. 1637–1653, 1984.

[92] P. Van Houtte, L. Delannay, and I. Samajdar, “Quantitative prediction of cold rolling textures in low-carbon steel by means of the LAMEL model,” *Texture, Stress, and Microstructure*, vol. 31, no. 3, pp. 109–149, 1999.

[93] M. Crumbach, G. Pomana, P. Wagner, and G. Gottstein, “A Taylor type deformation texture model considering grain interaction and material properties. Part II–experimental validation and coupling to FEM,” in *Recrystallization and Grain Growth, Proceedings of the First Joint International Confernce, Springer-Verlag*, 2001.

[94] R. Hill, “Continuum micro-mechanics of elastoplastic polycrystals,” *Journal of the Mechanics and Physics of Solids*, vol. 13, no. 2, pp. 89–101, 1965.

[95] A. Molinari, G. Canova, and S. Ahzi, “A self consistent approach of the large deformation polycrystal viscoplasticity,” *Acta Metallurgica*, vol. 35, no. 12, pp. 2983–2994, 1987.

[96] O. Diard, S. Leclercq, G. Rousselier, and G. Cailletaud, “Evaluation of finite element based analysis of 3D multicrystalline aggregates plasticity: Application to crystal plas-

ticity model identification and the study of stress and strain fields near grain boundaries," *International Journal of Plasticity*, vol. 21, no. 4, pp. 691–722, 2005.

[97] Z. Zhao, S. Kuchnicki, R. Radovitzky, and A. Cuitino, "Influence of in-grain mesh resolution on the prediction of deformation textures in FCC polycrystals by crystal plasticity FEM," *Acta Materialia*, vol. 55, no. 7, pp. 2361–2373, 2007.

[98] F. Harewood and P. McHugh, "Investigation of finite element mesh independence in rate dependent materials," *Computational Materials Science*, vol. 37, no. 4, pp. 442–453, 2006.

[99] I. Simonovski, L. Cizelj, and N. Jakšić, "The influence of finite element meshes on the results of a spatial polycrystalline aggregate model," *Nuclear Engineering and Design*, vol. 241, no. 4, pp. 1184–1190, 2011.

[100] S. R. Kalidindi, C. A. Bronkhorst, and L. Anand, "Crystallographic texture evolution in bulk deformation processing of FCC metals," *Journal of the Mechanics and Physics of Solids*, vol. 40, no. 3, pp. 537–569, 1992.

[101] S. Kalidindi and L. Anand, "Macroscopic shape change and evolution of crystallographic texture in pre-textured FCC metals," *Journal of the Mechanics and Physics of Solids*, vol. 42, no. 3, pp. 459–490, 1994.

[102] C. Bronkhorst, S. Kalidindi, and L. Anand, "Polycrystalline plasticity and the evolution of crystallographic texture in FCC metals," *Philosophical Transactions of the Royal Society of London. Series A: Physical and Engineering Sciences*, vol. 341, no. 1662, pp. 443–477, 1992.

[103] V. Bachu and S. R. Kalidindi, "On the accuracy of the predictions of texture evolution by the finite element technique for FCC polycrystals," *Materials Science and Engineering: A*, vol. 257, no. 1, pp. 108–117, 1998.

[104] L. Delannay, S. Kalidindi, and P. Van Houtte, "Quantitative prediction of textures in aluminium cold rolled to moderate strains," *Materials Science and Engineering: A*, vol. 336, no. 1, pp. 233–244, 2002.

[105] L. Anand and S. Kalidindi, “The process of shear band formation in plane strain compression of FCC metals: effects of crystallographic texture,” *Mechanics of Materials*, vol. 17, no. 2, pp. 223–243, 1994.

[106] O. Watanabe, H. M. Zbib, and E. Takenouchi, “Crystal plasticity: micro-shear banding in polycrystals using Voronoi tessellation,” *International Journal of Plasticity*, vol. 14, no. 8, pp. 771–788, 1998.

[107] K. Inal, P. Wu, and K. Neale, “Instability and localized deformation in polycrystalline solids under plane-strain tension,” *International Journal of Solids and Structures*, vol. 39, no. 4, pp. 983–1002, 2002.

[108] K. Inal, P. Wu, and K. Neale, “Finite element analysis of localization in FCC polycrystalline sheets under plane stress tension,” *International Journal of Solids and Structures*, vol. 39, no. 13, pp. 3469–3486, 2002.

[109] M. Kuroda and V. Tvergaard, “Effects of texture on shear band formation in plane strain tension/compression and bending,” *International Journal of Plasticity*, vol. 23, no. 2, pp. 244–272, 2007.

[110] M. Kuroda, “On large-strain finite element solutions of higher-order gradient crystal plasticity,” *International Journal of Solids and Structures*, vol. 48, no. 24, pp. 3382–3394, 2011.

[111] S. Li, F. Sun, and H. Li, “Observation and modeling of the through-thickness texture gradient in commercial-purity aluminum sheets processed by accumulative roll-bonding,” *Acta Materialia*, vol. 58, no. 4, pp. 1317–1331, 2010.

[112] X. Zeng, M. Ahmad, and O. Engler, “Texture gradient, average texture, and plastic anisotropy in various Al–Li sheet alloys,” *Materials Science and Technology*, vol. 10, no. 7, pp. 581–591, 1994.

[113] M. Chen, J. Li, Y. Zhao, H. Yuan, and W. Liu, “Comparison of texture evolution between different thickness layers in cold rolled Al–Mg alloy,” *Materials Characterization*, vol. 62, no. 12, pp. 1188–1195, 2011.

[114] M. Miller and T. Turner, “A methodology for measuring and modeling crystallographic texture gradients in processed alloys,” *International Journal of Plasticity*, vol. 17, no. 6, pp. 783–805, 2001.

[115] X.-H. Zeng and F. Barlat, “Effects of texture gradients on yield loci and forming limit diagrams in various aluminum-lithium sheet alloys,” *Metallurgical and Materials Transactions A*, vol. 25, no. 12, pp. 2783–2795, 1994.

[116] K. Neale, K. Inal, and P. Wu, “Effects of texture gradients and strain paths on localization phenomena in polycrystals,” *International Journal of Mechanical Sciences*, vol. 45, no. 10, pp. 1671–1686, 2003.

[117] P. W. Bridgman, “The stress distribution at the neck of a tension specimen,” *Transactions of American Society of Metals*, 1944.

[118] A. Hershey, “The plasticity of an isotropic aggregate of anisotropic face centered cubic crystals,” *Journal of Applied Mechanics*, 1954.

[119] W. Hosford, “A generalized isotropic yield criterion,” *Journal of Applied Mechanics*, vol. 39, no. 2, pp. 607–609, 1972.

[120] R. Hill, “A theory of the yielding and plastic flow of anisotropic metals,” *Proceedings of the Royal Society of London. Series A. Mathematical and Physical Sciences*, vol. 193, no. 1033, pp. 281–297, 1948.

[121] R. Hill, “Theoretical plasticity of textured aggregates,” vol. 85, no. 01, pp. 179–191, 1979.

[122] R. Hill, “Constitutive modelling of orthotropic plasticity in sheet metals,” *Journal of the Mechanics and Physics of Solids*, vol. 38, no. 3, pp. 405–417, 1990.

[123] F. Barlat and K. Lian, “Plastic behavior and stretchability of sheet metals. Part I: A yield function for orthotropic sheets under plane stress conditions,” *International Journal of Plasticity*, vol. 5, no. 1, pp. 51–66, 1989.

[124] F. Barlat, D. J. Lege, and J. C. Brem, “A six-component yield function for anisotropic materials,” *International Journal of Plasticity*, vol. 7, no. 7, pp. 693–712, 1991.

[125] D. Banabic, T. Kuwabara, T. Balan, D. Comsa, and D. Julean, “Non-quadratic yield criterion for orthotropic sheet metals under plane-stress conditions,” *International Journal of Mechanical Sciences*, vol. 45, no. 5, pp. 797–811, 2003.

[126] D. Banabic, H. Aretz, D. Comsa, and L. Paraianu, “An improved analytical description of orthotropy in metallic sheets,” *International Journal of Plasticity*, vol. 21, no. 3, pp. 493–512, 2005.

[127] A. Karafillis and M. Boyce, “A general anisotropic yield criterion using bounds and a transformation weighting tensor,” *Journal of the Mechanics and Physics of Solids*, vol. 41, no. 12, pp. 1859–1886, 1993.

[128] F. Barlat, H. Aretz, J. Yoon, M. Karabin, J. Brem, and R. Dick, “Linear transfomation-based anisotropic yield functions,” *International Journal of Plasticity*, vol. 21, no. 5, pp. 1009–1039, 2005.

[129] H. Aretz and F. Barlat, “New convex yield functions for orthotropic metal plasticity,” *International Journal of Non-Linear Mechanics*, vol. 51, pp. 97–111, 2013.

[130] F. Barlat and O. Richmond, “Prediction of tricomponent plane stress yield surfaces and associated flow and failure behavior of strongly textured fcc polycrystalline sheets,” *Materials Science and Engineering*, vol. 95, pp. 15–29, 1987.

[131] P. Zattarin, P. Lipinski, and A. Rosochowski, “Numerical study of the influence of microstructure on subsequent yield surfaces of polycrystalline materials,” *International Journal of Mechanical Sciences*, vol. 46, no. 9, pp. 1377–1398, 2004.

[132] A. Saai, S. Dumoulin, O. Hopperstad, and O.-G. Lademo, “Simulation of yield surfaces for aluminium sheets with rolling and recrystallization textures,” *Computational Materials Science*, vol. 67, pp. 424–433, 2013.

[133] F. Grytten, B. Holmedal, O. S. Hopperstad, and T. Børvik, “Evaluation of identification methods for YLD2004-18p,” *International Journal of Plasticity*, vol. 24, no. 12, pp. 2248–2277, 2008.

Article 1

M. Khadyko, S. Dumoulin, T. Børvik, O.S. Hopperstad

An experimental-numerical method to determine the work hardening of anisotropic ductile materials at large strains

International Journal of Mechanical Sciences 88 (2014) 25–36

International Journal of Mechanical Sciences 88 (2014) 25–36

Contents lists available at ScienceDirect

International Journal of Mechanical Sciences

journal homepage: www.elsevier.com/locate/ijmecsci

An experimental–numerical method to determine the work-hardening of anisotropic ductile materials at large strains

M. Khadyko [a],*, S. Dumoulin [b], T. Børvik [a], O.S. Hopperstad [a]

[a] Structural Impact Laboratory (SIMLab), Centre for Research-based Innovation, Department of Structural Engineering, Norwegian University of Science and Technology, NO-7491 Trondheim, Norway
[b] SINTEF Materials & Chemistry, NO-7465 Trondheim, Norway

A R T I C L E I N F O

Article history:
Received 19 December 2013
Received in revised form
26 June 2014
Accepted 1 July 2014
Available online 8 July 2014

Keywords:
Tensile tests
Plastic anisotropy
Strain localisation
Finite element method
Crystal plasticity

A B S T R A C T

The determination of work-hardening for ductile materials at large strains is difficult to perform in the framework of usual tensile tests because of the geometrical instability and necking in the specimen at relatively low strains. In this study, we propose a combination of experimental and numerical techniques to overcome this difficulty. Extruded aluminium alloys are used as a case since they exhibit marked plastic anisotropy. In the experiments, the minimum diameters of the axisymmetric tensile specimen in two normal directions are measured at high frequency by a laser gauge in the necking area together with the corresponding force, and the true stress–strain curve is found. The anisotropy of the material is determined from its crystallographic texture using the crystal plasticity theory. This data is used to represent the specimen by a 3D finite element model with phenomenological anisotropic plasticity. The experimental true stress–strain curve is then used as a target curve in an optimisation procedure for calibrating the hardening parameters of the material model. As a result, the equivalent stress–strain curve of the material up to fracture is obtained.

1. Introduction

One of the basic and most important experimental tests in material science is the uniaxial tension test. A great variety of ways to perform the test on a given material exists, with different sizes and shapes of the specimens and different methods to apply the tensile load and measure the resulting displacements and forces. All these variations have a common core, defined by the way the material (or in our case an aluminium alloy) deforms plastically. At small strains, in the elastic and early plastic regime, the deformation of the specimen may be safely considered homogeneous throughout the cross-section. Consequently the stress may be calculated as the ratio of the total force and cross-section area (either initial or current). In this regime of deformation the specimen may also be assumed, without much loss of accuracy, to deform homogeneously along its length, at least on some considerable length span in the centre. It allows for a convenient way to measure and calculate strains with strain gauges, extensometers, digital image correlation or other techniques. The problems arise when the strain reaches some critical value and the specimen goes into another regime of deformation – diffuse necking [1]. The critical strain for necking is much lower than the ultimate strain at fracture for most important aluminium alloys. In the diffuse necking regime the deformation concentrates in some area of the specimen and the strain becomes highly heterogeneous. Moreover, the stress situation in the necking area becomes much more complex. In the homogeneous regime the component of the stress along the tensile axis is the only component of the stress tensor and is therefore equal to the equivalent stress, provided that the material is isotropic. If the material is anisotropic, the latter holds only in the reference direction. But in the necking area the heterogeneous deformation field produces a complex stress field with triaxiality deviating from the initial value. It is still possible to find the average true stress component in the tensile direction as well as the average true strain in the necking area, but this true stress component will noticeably deviate from the equivalent stress [2]. The conceptual difficulty here is that we are seeking the properties of the material, but we measure the response of a specimen with all its constraints and instabilities. While the material continues to work-harden up until very large strains, we only have reliable information about its behaviour in a relatively small strain range, where the specimen is still geometrically stable.

The first attempt to overcome this problem was made by Bridgman [3]. His approach was analytical and consisted of finding the stress field in the neck region of a tensile specimen with circular cross-section and isotropic plastic behaviour of the material. The result was a parameter which transformed the true stress

---

* Corresponding author.
E-mail address: mikhail.khadyko@ntnu.no (M. Khadyko).

http://dx.doi.org/10.1016/j.ijmecsci.2014.07.001
0020-7403/

in the neck of the specimen (the smallest cross section) into the equivalent stress. Later other researchers tried to improve the initial solution aiming for better accuracy [4] or other specimen geometries [5], but after all the Bridgman correction for the true stress remains the most popular analytical method.

The main shortcomings of this solution are the much idealised assumed properties of the material and the specimen. The material must be isotropic, which makes the application of this method to highly anisotropic textured aluminium alloys very dubious. The correction in its initial form depends on the curvature of the neck region which is hard to measure, and the existing phenomenological methods, which avoid this measurement, sacrifice some accuracy [6]. Thus, extracting the equivalent stress as a function of strain from the tensile test after the onset of necking remains an important problem.

We propose a method of extracting this information from a specimen of arbitrary axisymmetric geometry and made of an orthotropic material. Instead of an analytical solution we use a numerical approach based on the finite element method (FEM). Already in the 1970s, FEM was used to find stress–strain fields in the necking area [7,8]. It has since then been used successfully to model localisation up until fracture in uniaxial tension [9] and plane strain [10], as well as for anisotropic textured aluminium alloys [11]. Other examples of recent works, where FEM solutions of localisation problems are validated by experimental data, include [12,13].

The plastic anisotropy of the tested material is described by an anisotropic yield function. This kind of yield function is also well established. Since the early work of Hill [14], different formulations have been proposed [15,16]. This sort of functions was found to be an adequate representation of the plastic anisotropy of aluminium alloys, when fitted to experimental data [17]. A class of non-quadratic yield functions based on linear transformations of the stress deviator was proposed in [18] and discussed more generally in [19]. These yield functions typically use a large number of parameters to describe the shape of the yield surface of the material with high flexibility and accuracy. The drawback is the correspondingly high number of material tests necessary to identify these parameters.

To reduce the required number of tests in the parameter identification procedure, the tests may be complemented by numerical simulations utilising the crystal plasticity theory. Knowledge of the crystallographic texture and the plastic behaviour of the slip systems in the individual crystals of the material, allows us to substitute some of the tests with simulations. This method was first used in [20,21]. By now it is used by many researchers with relative success, especially in predicting the plastic strain anisotropy of metals and alloys [22]. Though crystal plasticity simulations may ignore some important physical mechanisms playing a role in the plastic response, they are in general cheaper than physical testing. The limits of this method are discussed in [23]. Crystal plasticity is used to find the yield surface of textured alloys in [24–26].

The method we propose is based on these techniques, well established theoretically and validated by experiments. We use 3D FEM simulations of a tensile specimen, with an anisotropic yield surface, found from crystal plasticity simulations. The true stress–strain response of the simulated specimen is then fitted to the response of the real specimen by optimising the properties of the simulated material – its yield strength and hardening parameters. When these characteristics are found we can directly obtain the equivalent stress–strain response of the material.

In recent years several researchers have approached the problem using a similar framework. Zhano and Li [27] used an optimisation procedure to extrapolate the stress after necking. Cabezas and Celentano [28] used FEM to find correction factors for cylindrical and plane steel specimens. Bogusz et al. [29] used digital image correlation and FEM simulations to compare correction factors from different analytical models. Ling [30] extrapolated the hardening from before necking and validated it with an FEM simulation of the post-necking deformation. Westermann et al. [31] used the same laser gauge measurement and a similar numerical simulation method as in this work, but for isotropic aluminium alloys. However, to the authors' best knowledge, the proposed combination of crystal plasticity, anisotropic material model and optimisation technique to obtain the equivalent stress–strain curve all the way to failure for a ductile aluminium alloy has not been used before.

2. Experiments

2.1. Materials

Two aluminium alloys were used in the tests: AA6060 and AA6082. The chemical composition of the alloys is given in Table 1. The specimens were obtained from 10 mm thick and 90 mm wide extruded flat profiles at 90° to the extrusion direction and heat treated to five different tempers: T4, T6x, T6, T7 and O. The various heat treatments are described in Table 2. The alloys were analysed in the scanning electron microscope using electron back-scattering diffraction (EBSD) and EDAX TSL OIM software to provide grain morphology and texture. The orientation distribution functions (ODF) for the two alloys are shown in Figs. 1 and 2. The EBSD measurements were carried out in the plane defined by the extrusion and normal directions of the profile, using 10 μm steps on a square grid for the AA6060 alloy and 5 μm steps for the AA6082 alloy. The ODFs were calculated from the pole figures in the EDAX TSL OIM software using a harmonic series expansion and triclinic sample symmetry [32]. The total number of measured orientations (or grains/subgrains) is 2611 and 25512 for AA6060 and AA6082, respectively. The grain structure of the alloys is presented in Fig. 3. The textures and grain structures are typical for recrystallised alloys (AA6060) and non-recrystallised, extruded alloys (AA6082), respectively. The AA6060 alloy has an equi-axed, recrystallised grain structure, whereas the AA6082 alloy has a non-recrystallised structure with flat, pancake-shaped grains. The most prominent texture component in both alloys is a cube component, but the other orientations differ strongly between AA6060 and AA6082. The texture of the AA6060 alloy is comprised of a strong cube texture with a minor Goss component, while the AA6082 alloy has a cube texture with orientations along the β-fibre, which runs from the Copper to the Brass orientation, through the S component.

2.2. Mechanical testing

Tensile tests were performed at room temperature on three specimens for each temper of each alloy, giving a total of 30 tests. The geometry of the specimen is shown in Fig. 4. The cross-head velocity of the universal tensile testing machine was 1.2 mm/min, which corresponds to an initial strain rate of $5 \times 10^{-4}\,\mathrm{s}^{-1}$. The force and the minimum diameter of the cross section in two normal directions were measured during the whole test until

Table 1
Chemical composition of the alloys in wt%.

Alloy	Fe	Si	Mg	Mn	Cr	Cu	Zn	Ti
AA6060	0.193	0.422	0.468	0.015	0.000	0.002	0.005	0.008
AA6082	0.180	0.880	0.600	0.530	0.150	0.020	0.005	0.011

Table 2
Heat treatment of the specimens to different tempers.

Temper	Stage 1	Stage 2	Stage 3	Stage 4	Stage 5
T4	540 °C in salt bath for 15 min	Fast water cooling	One week at room temperature	–	–
T6x	540 °C in salt bath for 15 min	Fast water cooling	15 min at room temperature	185 °C in oil bath for one hour	Air cooling
T6	540 °C in salt bath for 15 min	Fast water cooling	15 min at room temperature	185 °C in oil bath for five hours	Air cooling
T7	540 °C in salt bath for 15 min	Fast water cooling	15 min at room temperature	185 °C in oil bath for one week	Air cooling
O	540 °C in salt bath for 15 min	Fast water cooling	15 min at room temperature	350 °C in salt bath for twenty four hours	Air cooling

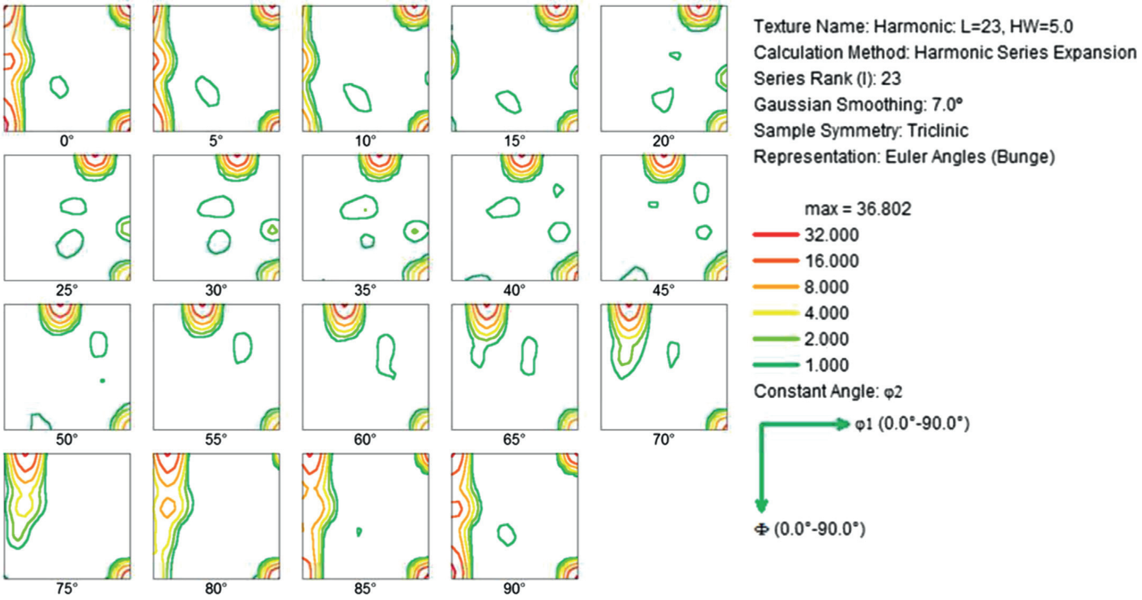

Fig. 1. Orientation distribution function for the AA6060 alloy.

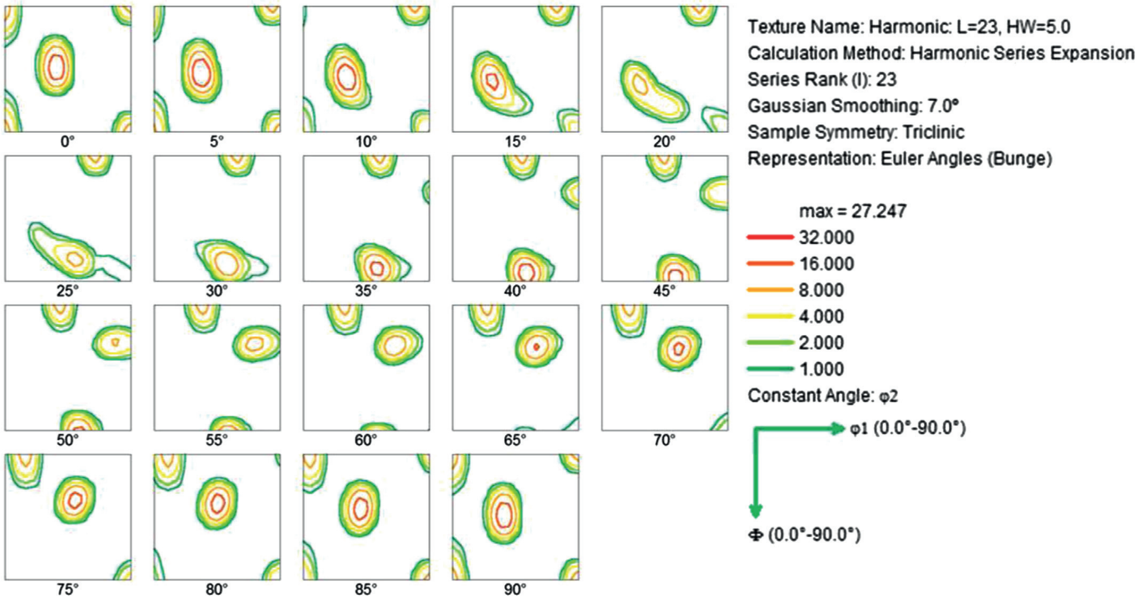

Fig. 2. Orientation distribution function for the AA6082 alloy.

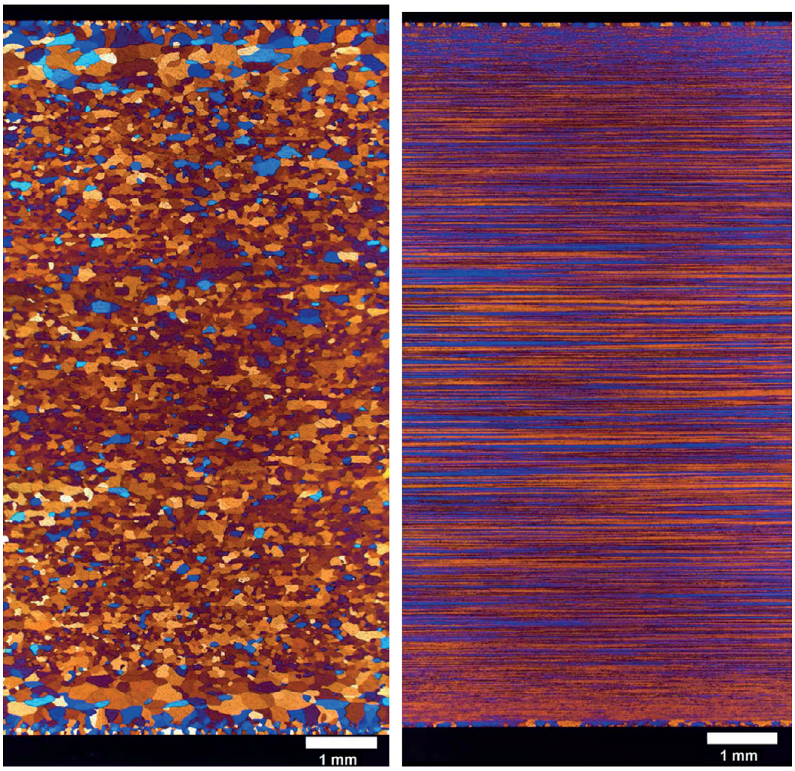

Fig. 3. Grain structure of the AA6060 (left) and AA6082 (right) alloys, where the extrusion direction is horizontal and the normal (or thickness) direction is vertical.

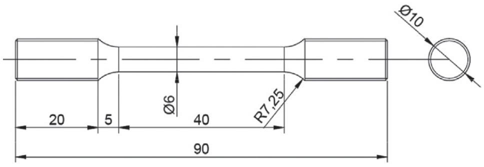

Fig. 4. Tensile specimen geometry.

fracture. The measurements of the minimum diameter were performed with an in-house measuring rig. It consists of two lasers mounted normally to each other and to the tensile axis of the specimen. The lasers project light beams with dimensions $13 \times 0.1\ \text{mm}^2$ across the specimen and on the detectors at the opposite side of the rig. The system uses a high-speed, contact-less AEROEL XLS13XY laser gauge with 1 μm resolution, which is installed on a mobile frame. The sample was scanned at a frequency of 1200 Hz during the test and the measured data were transferred by the built-in electronics to the remote computer via fast Ethernet. This setup ensured that the minimum diameters of the specimen in two normal directions were accurately measured throughout the whole test.

We introduce a Cartesian coordinate system x,y,z, where x is the extrusion direction, y is the transverse direction in the flat profile and z is the normal direction (i.e. in the thickness direction of the profile). The tensile direction is then always in the y direction. If we denote the measured diameters D_x and D_z, and assume that the deformed cross section is elliptical in shape (which is a reasonable assumption for orthotropic material), then we can find the current cross-section area as

$$A = \frac{\pi}{4} D_x D_z \tag{1}$$

The true (Cauchy) stress is found as

$$\sigma_y = \frac{F}{A} \tag{2}$$

where F is the measured tensile force. If we also assume plastic incompressibility, the true logarithmic strain can be expressed as

$$\varepsilon_y = \ln\left(\frac{A_0}{A}\right) \tag{3}$$

where A_0 is the initial cross-section area of the specimen. These measures only express the average response of the specimen after necking starts. Similarly when equivalent strains are discussed, logarithmic strain is used. It should be noted that the plastic incompressibility assumption may not hold at strains near fracture because of void nucleation and growth.

The strain ratio, denoted r_y, is here defined as

$$r_y = \frac{d\varepsilon_x}{d\varepsilon_z} \tag{4}$$

where $\varepsilon_x = \ln(D_x/D_0)$ and $\varepsilon_z = \ln(D_z/D_0)$ are the logarithmic strains in the extrusion and normal directions, respectively. The ratio r_y equals unity for isotropic materials, while values different from unity indicates anisotropic plastic flow. If the texture evolves significantly with plastic deformation, r_y is also expected to change.

3. Material modelling

3.1. Crystal plasticity

To establish a yield surface to be used in the phenomenological yield function, the crystal plasticity theory is utilised. It is implemented numerically in a rate-dependent form with the Kalidindi hardening model [33,34] and a Taylor-type polycrystal homogenisation [35].

3.1.1. Single crystal kinematics and kinetics

A finite deformation formulation is used. The total deformation gradient is multiplicatively decomposed into elastic and plastic parts [36]

$$\boldsymbol{F} = \boldsymbol{F}^e \boldsymbol{F}^p \tag{5}$$

The plastic part $\boldsymbol{F}^p$ transforms the body from the initial configuration Ω_0 into the intermediate plastically deformed configuration $\overline{\Omega}$. The elastic component $\boldsymbol{F}^e$ transforms the body from intermediate into the current configuration Ω with elastic deformation and rigid body rotation. The first transformation is due to slip on the slip systems, which are here represented by couples of vectors connected to the lattice. The lattice remains undeformed during this transformation. During the second transformation the lattice deforms and rotates together with the material. The intermediate configuration is thus unaffected by rigid body rotations, so the constitutive relations formulated in this configuration are objective. The following relations are based on [33]. The vectors $\boldsymbol{m}_0^\alpha$ and $\boldsymbol{n}_0^\alpha$ are the slip direction and slip plane normal vectors, respectively, for a slip system α in the initial and intermediate configuration, whereas $\boldsymbol{m}^\alpha$ and $\boldsymbol{n}^\alpha$ are the slip system vectors in the current configuration, rotated and stretched by the elastic deformation gradient $\boldsymbol{F}^e$. These vectors are normal to each other in any configuration by definition. The plastic velocity gradient $\overline{\boldsymbol{L}}^p$ in the intermediate configuration then has these vectors as a basis

$$\overline{\boldsymbol{L}}^p = \dot{\boldsymbol{F}}^p (\boldsymbol{F}^p)^{-1} = \sum_{\alpha=1}^{n} \dot{\gamma}^\alpha \boldsymbol{m}_0^\alpha \otimes \boldsymbol{n}_0^\alpha \tag{6}$$

where $\dot{\gamma}^\alpha$ is the slip rate on slip system α in the intermediate configuration and n is the total number of slip systems. The elastic Green strain tensor $\overline{\boldsymbol{E}}^e$ in the intermediate configuration may be defined as

$$\overline{\boldsymbol{E}}^e = \frac{1}{2}[(\boldsymbol{F}^e)^T \boldsymbol{F}^e - \boldsymbol{I}] = \frac{1}{2}(\overline{\boldsymbol{C}}^e - \boldsymbol{I}), \quad \overline{\boldsymbol{C}}^e = (\boldsymbol{F}^e)^T \boldsymbol{F}^e \tag{7}$$

where $\overline{\boldsymbol{C}}^e$ is the elastic right Cauchy–Green deformation tensor and $\boldsymbol{I}$ is the unity tensor. The second Piola–Kirchhoff stress tensor $\overline{\boldsymbol{S}}$ in the intermediate configuration is obtained by pulling back the Cauchy stress tensor $\boldsymbol{\sigma}$ into this configuration

$$\overline{\boldsymbol{S}} = det\boldsymbol{F}(\boldsymbol{F}^e)^{-1} \boldsymbol{\sigma}\, (\boldsymbol{F}^e)^{-T} \tag{8}$$

This stress is power conjugate to the elastic Green strain and is found from the hyperelastic law

$$\overline{\boldsymbol{S}} = \mathbf{C}_{el}^{\overline{S}} : \overline{\boldsymbol{E}}^e \tag{9}$$

where $\mathbf{C}_{el}^{\overline{S}}$ is the fourth order tensor of elastic moduli. It has 3 independent components and hence describes the crystal anisotropy. The total power per unit volume $\dot{w}$ produced by the crystal consists of elastic (stored) and plastic (dissipated) parts

$$\dot{w} = \dot{w}^e + \dot{w}^p = \overline{\boldsymbol{S}} : \dot{\overline{\boldsymbol{E}}}^e + \overline{\boldsymbol{C}}^e \overline{\boldsymbol{S}} : \overline{\boldsymbol{L}}^p \tag{10}$$

The plastic part of the total power may be also expressed through the power spent on every slip system if the resolved shear stress τ^α is introduced

$$\dot{w}^p = \sum_{\alpha=1}^{n} \tau^\alpha \dot{\gamma}^\alpha \tag{11}$$

where τ^α is connected to the second Piola–Kirchhoff stress through the slip system vector basis

$$\tau^\alpha = \overline{\boldsymbol{C}}^e \overline{\boldsymbol{S}} : (\boldsymbol{m}_0^\alpha \otimes \boldsymbol{n}_0^\alpha) \tag{12}$$

3.1.2. Flow and hardening rules

The plastic flow is described by a widely used rate-dependent rule proposed in [37] as

$$\dot{\gamma}^\alpha = \dot{\gamma}_0 \left(\frac{|\tau^\alpha|}{\tau_c^\alpha} \right)^{1/m} \operatorname{sgn}(\tau^\alpha) \tag{13}$$

where $\dot{\gamma}_0$ is the reference slip rate, m is the instantaneous strain rate sensitivity and τ_c^α is the history dependent yield strength of slip system α. The hardening rate of each slip system is defined by

$$\dot{\tau}_c^\alpha = \sum_{\beta=1}^{n} h^{\alpha\beta} |\dot{\gamma}^\beta| \tag{14}$$

where $h^{\alpha\beta}$ are the slip hardening rates developing on slip system α because of slip on system β. They may be decomposed into

$$h^{\alpha\beta} = q^{\alpha\beta} h^\beta \tag{15}$$

where $q^{\alpha\beta}$ is a matrix of self-hardening and latent-hardening coefficients and h^β may be defined as proposed in [34]

$$h^\beta = h_0 \left(1 - \frac{\tau_c^\beta}{\tau_s} \right)^a \tag{16}$$

here h_0 is the initial hardening rate, τ_s is the resolved shear stress saturation value and a is the power law parameter. The initial slip resistance τ_{c0}^α is assumed equal for all slip systems.

3.1.3. Polycrystal modelling

The material sample includes too many orientations to be represented numerically as it is, so we represent it with a reduced number of orientations, chosen by analysing its texture. It has been shown that this reduced number is enough to accurately represent the properties of the material in numerical simulations [26]. Each grain is represented by its orientation and volume fraction. We assume the volume fraction to be equal for all grains.

The Taylor model [35] assumes that all grains undergo the same strain as the whole specimen. Stress equilibrium between the grains is then not satisfied. The stress in the specimen is found as an average, i.e.

$$\boldsymbol{\sigma} = \frac{1}{n} \sum_{g=1}^{n} \boldsymbol{\sigma}_g \tag{17}$$

where $\boldsymbol{\sigma}_g$ is the Cauchy stress in grain g and n is the total number of grains. The use of the Taylor model (here the so-called full-constraint variant is used) against a FEM model of a polycrystal and various relaxed constraint models is discussed in [23,38]. The conclusion is that no method is universally good at describing the polycrystal response, while the Taylor model has the advantage of simplicity and computational efficiency.

Some common assumptions are made about the material. The initial value of the slip resistance is the same on all slip systems, as well as the other material parameters; i.e., the material has no history of prior deformation. The influence of precipitates, inclusions, dispersoids or any other factors is ignored; just pure Schmid slip is considered, so that crystallographic texture is the only source of plastic anisotropy. This assumption may seem crude, but including these other factors is a very difficult task and for most cases texture is by far the main source of anisotropy [39].

3.2. Continuum plasticity

The behaviour of the material in the tensile tests is modelled by an anisotropic hypoelastic–plastic continuum model. The main features of this model are small elastic and finite plastic strains, isotropic elasticity and orthotropic yield surface, associated plastic flow and isotropic strain hardening. The corotational formulation is used to simplify the description of plastic anisotropy. The principal directions of the plastic anisotropy are aligned with the coordinate system, connected to the un-rotated configuration. The axes of this system are assumed to remain orthogonal during deformation. The corotational Cauchy stress is also defined in this system.

The corotational stress and rate-of-deformation tensors are defined [40] as

$$\hat{\boldsymbol{\sigma}} = \boldsymbol{R}^T \boldsymbol{\sigma} R \tag{18}$$

$$\hat{\boldsymbol{D}} = \boldsymbol{R}^T \boldsymbol{D} \boldsymbol{R} \tag{19}$$

where $\boldsymbol{D}$ is the rate-of-deformation tensor in the current configuration, $\boldsymbol{\sigma}$ is the Cauchy stress tensor and $\boldsymbol{R}$ is the rotation tensor found from the polar decomposition of the deformation gradient tensor

$$\boldsymbol{F} = \boldsymbol{R}\boldsymbol{U} \tag{20}$$

The corotational rate-of-deformation tensor is decomposed into a sum of elastic and plastic parts

$$\hat{\boldsymbol{D}} = \hat{\boldsymbol{D}}^e + \hat{\boldsymbol{D}}^p \tag{21}$$

In the hypoelastic formulation the corotational stress rate is connected to the corotational deformation rate

$$\dot{\hat{\boldsymbol{\sigma}}} = \hat{\boldsymbol{C}}_{el}^{\sigma} : \hat{\boldsymbol{D}}^e \tag{22}$$

where $\hat{\boldsymbol{C}}_{el}^{\sigma}$ is the fourth order tensor of elastic moduli. Elastic isotropy is assumed for the material, so only two independent parameters are enough to define this tensor, i.e. the Young modulus E and the Poisson ratio ν.

The yield function is formulated as

$$f(\hat{\boldsymbol{\sigma}}, \overline{\varepsilon}) = \overline{\sigma}(\hat{\boldsymbol{\sigma}}) - \kappa(\overline{\varepsilon}) \tag{23}$$

where $\overline{\varepsilon}$ is the equivalent plastic strain, $\overline{\sigma}$ is the equivalent stress and κ is the flow stress in uniaxial tension in the reference direction. The evolution of the flow stress κ is described by a two-term Voce rule [41]

$$\kappa(\overline{\varepsilon}) = \kappa_0 + \sum_{i=1}^{2} Q_i \left(1 - \exp\left(-\frac{\theta_i}{Q_i}\overline{\varepsilon}\right)\right) \tag{24}$$

where κ_0 is the yield stress, and Q_i and θ_i are model parameters governing the work-hardening.

The corotational plastic rate-of-deformation tensor evolves according to the associated flow rule

$$\hat{\boldsymbol{D}}^p = \dot{\lambda}\frac{\partial f}{\partial \hat{\boldsymbol{\sigma}}} \tag{25}$$

where $\dot{\lambda}$ is the plastic multiplier, which satisfies the loading–unloading conditions, written in Kuhn–Tucker form as

$$\dot{\lambda} \geq 0, \quad f \leq 0, \quad f\dot{\lambda} = 0 \tag{26}$$

The form of the equivalent stress used here, called Yld2004-18p by the authors, was developed in [19] to represent complex shapes of anisotropic yield surfaces, viz.

$$\overline{\sigma} = \left(\frac{1}{4}\phi\right)^{1/m} \tag{27}$$

where

$$\phi = \phi(\tilde{\boldsymbol{S}}', \tilde{\boldsymbol{S}}'') = \sum_{i=1}^{3}\sum_{j=1}^{3} |\tilde{S}_i' - \tilde{S}_j''|^m \tag{28}$$

In this equation m is the shape parameter while $\tilde{\boldsymbol{S}}'$ and $\tilde{\boldsymbol{S}}''$ represent the principal values of the stress tensors $\tilde{\boldsymbol{s}}'$ and $\tilde{\boldsymbol{s}}''$. These stress tensors are in turn produced by linear transformations of the corotational stress tensor

$$\tilde{\boldsymbol{s}}' = \mathbf{C}' : \hat{\boldsymbol{s}} = \mathbf{C}' : \mathbf{T} : \hat{\boldsymbol{\sigma}} \tag{29}$$

$$\tilde{\boldsymbol{s}}'' = \mathbf{C}'' : \hat{\boldsymbol{s}} = \mathbf{C}'' : \mathbf{T} : \hat{\boldsymbol{\sigma}} \tag{30}$$

where the fourth order tensor $\mathbf{T}$ transforms the corotational stress $\hat{\boldsymbol{\sigma}}$ into its deviatoric part $\hat{\boldsymbol{s}}$ and the fourth order tensors $\mathbf{C}'$ and $\mathbf{C}''$ contain the coefficients describing the anisotropy of the material. In the orthotropic case 9 independent coefficients are enough to define each of them, and on matrix form in Voigt notation they read

$$\begin{bmatrix} \tilde{s}_x' \\ \tilde{s}_y' \\ \tilde{s}_z' \\ \tilde{s}_{xy}' \\ \tilde{s}_{yz}' \\ \tilde{s}_{xz}' \end{bmatrix} = \begin{bmatrix} 0 & -c_{12}' & -c_{13}' & 0 & 0 & 0 \\ -c_{21}' & 0 & -c_{23}' & 0 & 0 & 0 \\ -c_{31}' & -c_{32}' & 0 & 0 & 0 & 0 \\ 0 & 0 & 0 & c_{44}' & 0 & 0 \\ 0 & 0 & 0 & 0 & c_{55}' & 0 \\ 0 & 0 & 0 & 0 & 0 & c_{66}' \end{bmatrix} \begin{bmatrix} \hat{s}_x \\ \hat{s}_y \\ \hat{s}_z \\ \hat{s}_{xy} \\ \hat{s}_{yz} \\ \hat{s}_{xz} \end{bmatrix} \tag{31}$$

$$\begin{bmatrix} \tilde{s}_x'' \\ \tilde{s}_y'' \\ \tilde{s}_z'' \\ \tilde{s}_{xy}'' \\ \tilde{s}_{yz}'' \\ \tilde{s}_{xz}'' \end{bmatrix} = \begin{bmatrix} 0 & -c_{12}'' & -c_{13}'' & 0 & 0 & 0 \\ -c_{21}'' & 0 & -c_{23}'' & 0 & 0 & 0 \\ -c_{31}'' & -c_{32}'' & 0 & 0 & 0 & 0 \\ 0 & 0 & 0 & c_{44}'' & 0 & 0 \\ 0 & 0 & 0 & 0 & c_{55}'' & 0 \\ 0 & 0 & 0 & 0 & 0 & c_{66}'' \end{bmatrix} \begin{bmatrix} \hat{s}_x \\ \hat{s}_y \\ \hat{s}_z \\ \hat{s}_{xy} \\ \hat{s}_{yz} \\ \hat{s}_{xz} \end{bmatrix} \tag{32}$$

If all the non-zero anisotropy coefficients c_{ij}' and c_{ij}'' are set to unity, this yield function will reduce to an isotropic high-exponent yield function. The total number of parameters to identify in the continuum plasticity model is 26: two elasticity coefficients, E and ν; the initial yield stress, κ_0; the hardening parameters, Q_i and θ_i, $i = 1, 2$; the shape parameter, m; and the 18 anisotropy coefficients, c_{ij}' and c_{ij}''.

4. Parameter identification

4.1. Slip system level

The initial step of the method is to obtain an estimate of the yield surface shape from the crystal plasticity (CP) simulations. The microstructural study provided information about the orientations of the grains in the alloys and allowed to build the corresponding ODF. To run the CP model this information needs to be transformed into a convenient set of orientations which accurately represents the texture. Different methods of doing this exist, e.g. [42,43]. The one used in this work is the following. A total of 1000 grain orientations were taken randomly from the whole set of measured orientations. The number is small enough to provide reasonable computation times and big enough to represent the influence of all texture components on the shape of the yield surface [44]. The representativeness of this random set in relation to the components of the real texture was checked by making several random choices of 1000 orientations, calculating the ODFs of those reduced sets and comparing them with the ODF of the real texture. The differences were insubstantial, so this method was used for both alloys.

The initial shape of the yield surface, i.e. the initial plastic anisotropy, is commonly believed to depend mostly on the texture, and in the utilised CP model it depends solely on the texture. Hardening is assumed isotropic in the continuum model, meaning that this shape stays the same throughout the deformation. The factor that defines the shape of the yield surface of the polycrystal is which slip systems in the constituent crystals activate and which do not. Thus, the shape of the yield surface calculated for alloys with different hardening parameters should be the same – as for example in [45,46] the calculated yield surfaces for two different AA6063 alloy specimens are the same. In addition, when the yield surfaces were calculated with the same texture, but different sets of hardening parameters, the results were also identical.

In our case we deal with two yield surfaces, corresponding to two different textures. The same yield surface is used for all tempers of the same alloy. The hardening parameters we used are given in Table 3.

It should be mentioned that there may be some factors influencing the crystallographic slip, which may lead to anisotropic hardening or a different yield surface than the one found on the basis of our assumptions, but accounting for them is a difficult task and outside the scope of this article.

The crystal plasticity model is implemented into a user material subroutine for LS-DYNA. The subroutine utilises an explicit integration scheme by Grujicic and Batchu [47]. Explicit time integration of the momentum equations is used. The material is represented by a single eight-node element with one Gauss point (reduced integration). Using more elements in the Taylor model increases the computation time significantly, without substantial improvement of accuracy. The yield surface is calculated as follows. The element is subjected to a range of tensile and shear strain combinations, creating a cloud of points in the strain space. The straining stops each time the specific plastic work of deformation reaches a value of 0.5 MPa approximately corresponding to incipient yielding. The resulting stress responses are also represented by points in stress space, lying on the yield surface, which corresponds to this value of plastic work. Then an optimisation script uses these stress points and the anisotropic yield criterion defined by Eq. (23) to find the components of the transformation tensors in Eqs. (31) and (32), see Table 4 for the obtained values. The resulting yield surfaces are shown in Fig. 5, where σ_x is the normal stress in the reference direction, which is here the extrusion direction, σ_y is the normal stress in the transverse direction of the flat profile, and $\sigma_0 \equiv \kappa_0$ is the initial yield stress in the reference direction. The contours represent lines of constant shear stresses σ_{xy} in the plane of the flat profile. The calculated yield surfaces fit well with the ones found for alloys with similar texture/microstructure in [45]. The shear stresses σ_{yz} and σ_{zx} are not applied to the model and the coefficients for these stresses in Table 4 are equal to unity, i.e. they are assumed isotropic. It is a reasonable assumption for a specimen made of a flat extruded profile and deformed in tension, and these stresses in the simulations are considerably lower than the other components of the stress tensor. Therefore an improvement in the equivalent stress predictions would most likely be minor, while the number of the Taylor model runs will increase by an order of magnitude.

4.2. Continuum level

The next step is the application of these results to the continuum plasticity model and fitting of the model to the experimental data. The mesh of the FE model of the tensile specimen is shown in Fig. 6. Owing to the orthotropic symmetry and to reduce computation time only 1/8th of the specimen is modelled. The dimensions of the smallest elements used in the necking area are $0.3 \times 0.3 \times 0.07\ \text{mm}^3$. Several test simulations with larger and smaller elements were run to ensure that at this element size the mesh does not affect the solution. Symmetrical boundary conditions are utilised and constant velocity is applied to the upper plane, where the specimen is fixed to the test machine. It should be noted that in the experiments necking occurs at a point determined by the imperfections of the specimen, while in the simulation the mesh is made without imperfections and the specimens necks in the centre (at the corresponding edge of the mesh). The eight-node solid element with full integration and formulation for elements with poor aspect ratio available in LS-DYNA was used in the simulations. Explicit time integration was chosen, since some initial test runs showed that implicit integration for this model does not provide any considerable advantage in speed, stability or accuracy. Mass scaling (by increasing the density of the material) was used to reduce the simulation time. It was then checked that the kinetic energy was still very small compared with the total energy of the specimen, to ensure quasi-static loading conditions.

The elastic–plastic behaviour of the material is modelled as described in Section 3.2. The 18 coefficients of the two linear transformations of the stress tensor used to describe the plastic anisotropy were determined as described in Section 4.1. The elastic constants were set to nominal values for aluminium alloys. It thus remains to determine the parameters κ_0, Q_i and θ_i of the two-term Voce hardening rule. This is done using LS-OPT [48]

Table 4
Coefficients of the YLD2004-18p yield function.

Coefficients	AA6060	AA6082
c'_{12}	0.3050	0.8178
c'_{13}	0.8051	1.3225
c'_{21}	−0.3320	0.9947
c'_{23}	0.5246	1.3271
c'_{31}	−0.4386	0.2568
c'_{32}	0.6322	0.5350
c'_{44}	0.9768	1.2029
c'_{55}	1.0000	1.0000
c'_{66}	1.0000	1.0000
c''_{12}	0.8578	−0.1288
c''_{13}	−0.2922	0.7223
c''_{21}	1.0911	1.1617
c''_{23}	0.8548	1.3056
c''_{31}	1.1442	0.9130
c''_{32}	0.6040	0.6049
c''_{44}	−0.2170	0.8661
c''_{55}	1.0000	1.0000
c''_{66}	1.0000	1.0000

Table 3
Crystal plasticity model parameters used in the yield surface calculations.

c_{11} (MPa)	c_{12} (MPa)	c_{44} (MPa)	$\dot{\gamma}_0$ (s^{-1})	m	$q^{\alpha\beta}$, $\alpha=\beta$ $\alpha\neq\beta$	h_0 (MPa)	a	τ_s (MPa)	τ^{α}_{c0} (MPa)
106,430	60,350	28,210	0.010	0.005	1.00 1.40	411.25	1.354	104.02	46.70

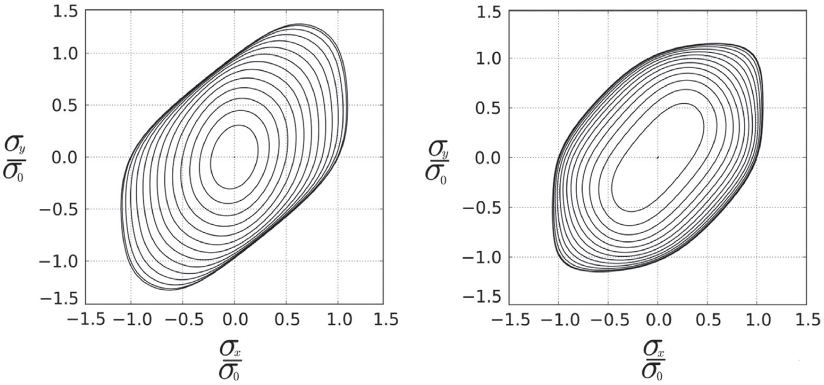

Fig. 5. Generated yield surfaces for alloys AA6060 (left) and AA6082 (right). Maximum value of σ_{xy}/σ_0 is 0.88 for AA6060 and 0.52 for AA6082.

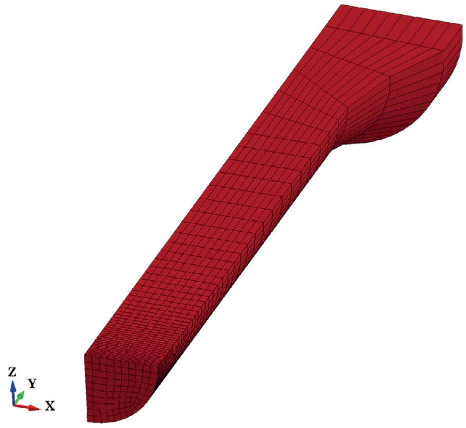

Fig. 6. Finite element mesh of the tensile specimen.

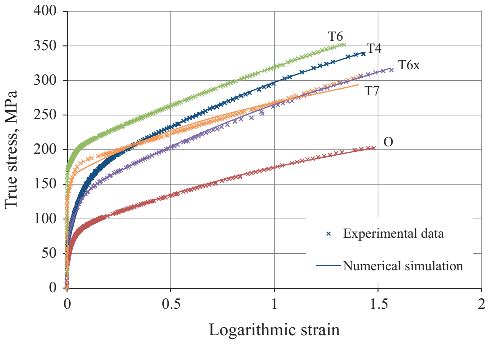

Fig. 7. True stress versus logarithmic strain curves for the AA6060 alloy.

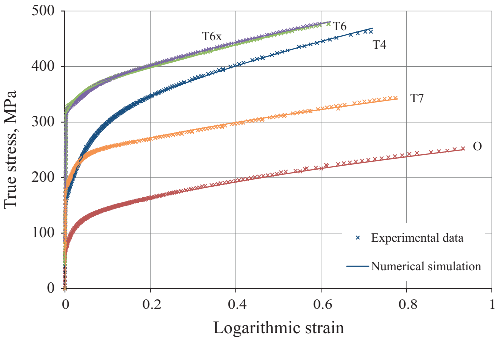

Fig. 8. True stress versus logarithmic strain curves for the AA6082 alloy.

– an optimisation tool that interacts with LS-DYNA. Within each iteration LS-OPT runs 10 simulations with LS-DYNA varying these parameters within prescribed intervals. A true stress–strain curve for the central cross-section area (where necking occurs) is calculated at the end of each simulation. These curves are compared to the true stress–strain curves found from the experiments for the corresponding alloy. LS-OPT compares the experimental curve with the simulated one, calculates the mean squared error and varies the hardening parameters in such a way that in the next iteration the mean squared error is reduced. After usually 15–20 iterations the mean squared error reduces from the range of 1–100 to around 10^{-5} and more iterations do not further reduce it.

5. Results

5.1. Continuum plasticity model calibration

The results of the optimisation procedure described in the previous section are presented in Figs. 7 and 8 for the two alloys in terms of the true stress–strain curves for the five tempers. The measured true stress–strain curves, obtained for three specimens of each alloy–temper combination, are in good agreement with each other, so only one typical curve is shown. In general, the two-term Voce hardening rule led to very good fits with small errors for most of the simulations. The largest error is observed for AA6060-T7, where the overall shape of the curve could not be accurately reproduced. A better fit for this case would have been obtained by using a three-term Voce hardening rule.

The simulation model accounts for plastic anisotropy, and the correspondence of the anisotropy in plastic flow in the simulations and experiments was also checked. This is done by comparing the strain ratio r_y obtained in experiments and simulations. The results are shown in Figs. 9 and 10, where r_y is the slope of the curves. The experimental and simulated values of r_y are reasonably close for both alloys. A point of interest is that in the case of the AA6060 alloy we observe significant change in the r_y value throughout the test. The most obvious reason for this is an evolution of the texture

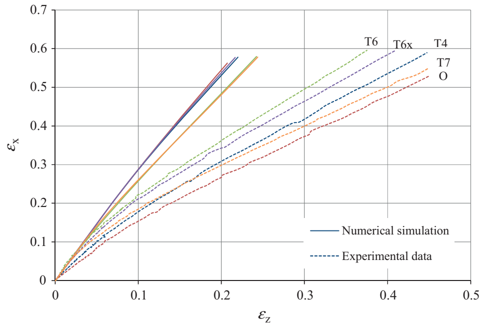

Fig. 9. Logarithmic strain in extrusion direction (ε_x) versus logarithmic strain in normal direction (ε_z) for the AA6060 alloy.

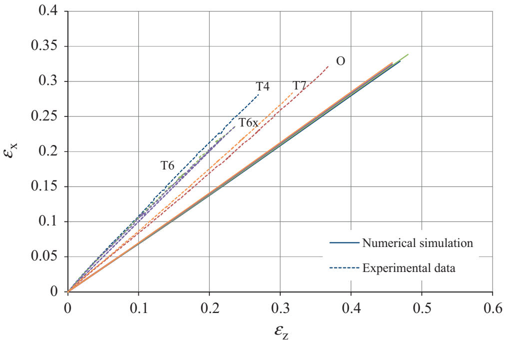

Fig. 10. Logarithmic strain in extrusion direction (ε_x) versus logarithmic strain in normal direction (ε_z) for the AA6082 alloy.

with deformation. This means that the shape of the yield surface also evolves and our assumption of isotropic hardening is reasonable, but not generally correct. The AA6082 alloy demonstrates much less evolution of r_y, so at least for this alloy the assumption of isotropic hardening holds with reasonable accuracy.

A comparison between the necking zones of the specimens at fracture as observed in the experiments and predicted by the finite element model is presented for two different alloys and tempers in Fig. 11. In the figure, the experimental and numerical results have been superimposed. Considering the discrepancy in the r_y ratio between the model and the experiment, the curvature of the necking zone is well reproduced in both cases.

5.2. Equivalent stress–strain curves

The main result of the model calibration is the parameters in the Voce hardening rule defining the equivalent stress–strain curves of the materials. The results are compiled in Figs. 12 and 13. The equivalent stress–strain curves are plotted until the point of fracture in the experiments. For most alloy/temper combinations the equivalent stress–strain curves obtained for the three specimens tested are in very good agreement with each other. Therefore only the averaged equivalent stress–strain curve is shown in the figures. In Table 5 the numerical values of the hardening parameters for typical specimens are presented.

The first notable result is the profound effect of the heat treatment on the initial strength and work-hardening of the two alloys. A detailed discussion of the physical mechanisms responsible for the observed behaviour will be presented elsewhere. The second observation is the large difference in ductility between the alloys. For the AA6060 alloy even the usually less ductile T6 and T7 tempers fracture at more than 120% strain.

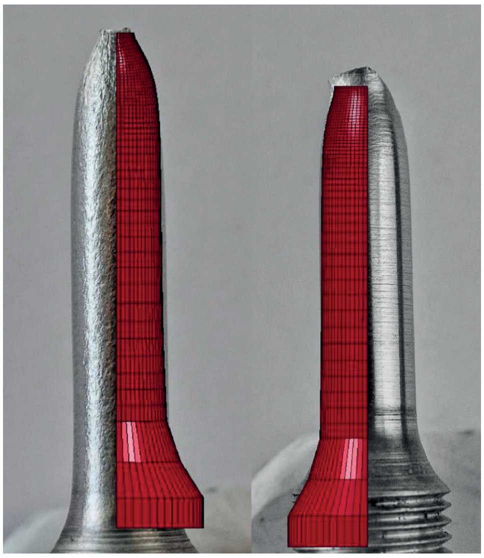

Fig. 11. Necking in FEM model and real specimen in AA6060-T4 (left) and AA6082-T6x (right).

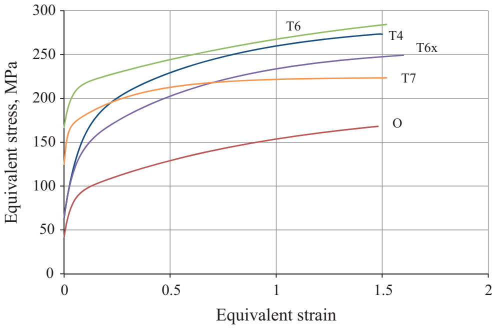

Fig. 12. Equivalent stress–strain curves for the AA6060 alloy.

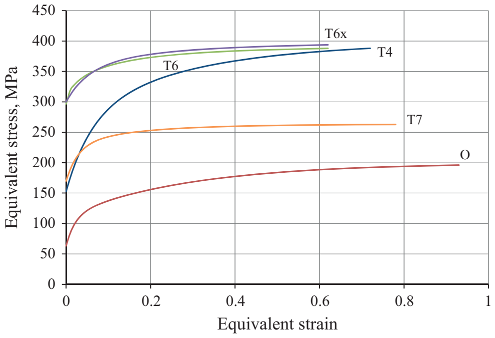

Fig. 13. Equivalent stress–strain curves for the AA6082 alloy.

The “apparent hardening rate” at large strains is much higher for the true stress–strain curves than for the equivalent stress–strain curves, see Fig. 14 for two examples. The reason for this is obviously the contribution of the triaxial stress field to the true stress measured after necking. The hydrostatic stress does not contribute to the equivalent stress, which is based on linear transformations of the stress deviator. Fig. 14 shows another difference: the equivalent stress may be either higher or lower than the true stress even before necking. The reason for this is that the specimens are oriented at 90° to the extrusion direction, which was taken here as the reference direction, and the stress in any direction other than the extrusion direction depends on the anisotropy of the yield surface. In this case, the 90° flow stress is either lower (AA6060) or higher (AA6082) than the 0° flow stress.

The method of using an anisotropic plasticity model to find the equivalent stress was compared to two simpler methods using either an isotropic plasticity model or the modified Bridgman correction method, as it is formulated in [6]. The T4 temper of both alloys was used in the comparison. First, the numerical optimisation procedure was performed with the isotropic von Mises yield surface instead of the anisotropic Yld2004-18p surface. The resulting values of the hardening parameters are given in Table 6, while the parameter set obtained with the anisotropic plasticity model is given in Table 5. The calibrated values of the hardening parameters for the isotropic and anisotropic criteria differ considerably, from 15% to 20% to almost twofold in case of the parameter θ_2. A comparison of the equivalent stress–strain curves obtained with the three different methods is presented in Fig. 15. The results are noticeably different. The Bridgman correction may over- or underestimate the equivalent stress, depending on the plastic anisotropy of the material. The von Mises yield function model gives predictions very similar to the Bridgman method, but only until a certain strain level (around 75%). However, compared with the true stress–strain curve, the three equivalent stress–strain curves are in reasonable agreement, especially considering the work-hardening rate.

Table 5
The obtained parameters for the two-term Voce hardening rule.

Alloy/temper	κ_0 (MPa)	Q_1 (MPa)	θ_1 (MPa)	Q_2 (MPa)	θ_2 (MPa)
AA6060-T4	65.00	97.69	1499.74	122.00	195.70
AA6060-T6x	65.00	67.41	1502.52	126.26	204.68
AA6060-T6	167.00	44.30	1489.83	111.66	78.20
AA6060-T7	125.00	39.17	3117.43	59.65	202.50
AA6060-O	42.00	46.36	1480.37	102.99	103.53
AA6082-T4	157.00	143.03	1961.54	105.74	269.89
AA6082-T6x	300.00	66.13	1296.66	59.76	104.59
AA6082-T6	305.00	46.59	1344.37	54.13	107.42
AA6082-T7	170.00	44.35	1515.79	45.51	460.98
AA6082-O	65.00	45.88	2179.59	87.46	319.21

6. Discussion and conclusions

While it is hard to evaluate how accurately we predicted the equivalent stress–strain curves, it is possible to re-evaluate the accuracy of the initial assumptions in light of the results.

The first issue is the yield function. The full-constraint Taylor simulations predicted the yield function rather well for both alloys, as judged based on the measured strain ratio r_y. The assumption of isotropic hardening seems to be fulfilled with good accuracy for the AA6082 alloy, but not for the AA6060 alloy. The yield surface defines the direction of the plastic strain rate, and this direction was gradually changing according to Fig. 9. However the initial value of the strain ratio r_y, and ergo the yield surface shape, was predicted quite well by the full-constraint Taylor model for the AA6060 alloy. Thus, the evolution of the r_y ratio is most probably due to evolution of the texture.

A possible improvement could be made by using more advanced implementation of the crystal plasticity model. In [49] the predictions of the yield surface of a similar alloy (AA6063)

Table 6
The obtained parameters for the two-term Voce hardening rule, when an isotropic von Mises yield surface is used.

Alloy/temper	κ_0 (MPa)	Q_1 (MPa)	θ_1 (MPa)	Q_2 (MPa)	θ_2 (MPa)
AA6060-T4	64.00	115.20	1263.85	148.96	95.66
AA6082-T4	159.00	110.58	2164.29	150.58	599.61

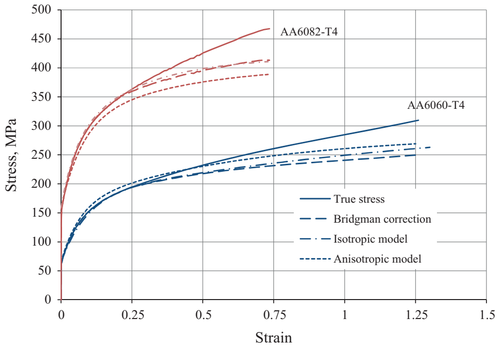

Fig. 15. Comparison between different methods of estimating the equivalent stress–strain curve in reference direction based on measured true stress–strain curve in transverse direction for the AA6060 and AA6082 alloys in temper T4.

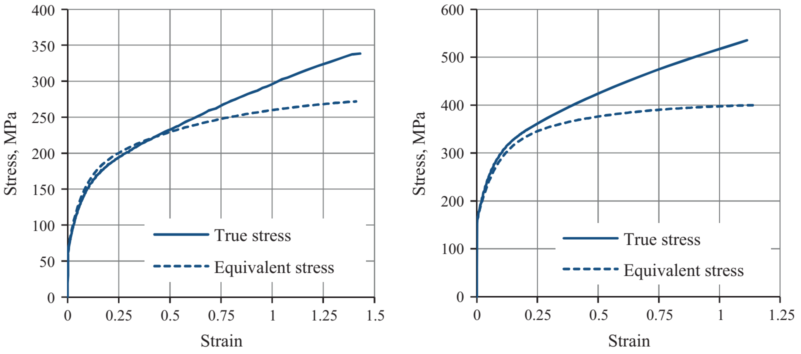

Fig. 14. Comparison between equivalent and true stress versus logarithmic strain curves for AA6060-T4 (left) and AA6082-T4 (right).

were performed with full-constraint Taylor, self-consistent and CP-FEM models. All of them gave rather good estimates of the strain ratio r_y in the 90° direction and each one had difficulties predicting the yield surface in the area of the biaxial stress. The most accurate yield surface shape may for now only be obtained by a costly combination of several uniaxial tensile tests in different directions in combination with shear and plane strain tests [50]. So the use of CP-FEM or self-consistent models would most probably improve results only marginally.

An improvement could come from using a full 3D stress field in the yield surface calibration procedure, as already discussed in Section 4.1. Overall, the improvement resulted from the use of anisotropic criterion instead of an isotropic is quite substantial, while further improvements in the anisotropic yield function are difficult and give a considerably less effect on the final result.

Another issue is the two-term Voce hardening rule. It is rather flexible and fits to most of the 6xxx alloys hardening curves well, but in some cases, like AA6060-T7, it was likely not flexible enough to reproduce some of the features of the true stress–strain curve. A better result could have been obtained by using a three-term Voce hardening rule.

Some improvements could be done in FEM implementation of the methods too. An accurate description of the necking zone requires a dense mesh. In addition very high local strains distort the elements immensely. To prevent the elements from too much of shape distortion and associated problems, they are initially not cubic but flatted. Re-meshing the geometry at least partly after a certain strain is reached may be a better way to handle this issue. The main problem with all kinds of measures that makes the model more accurate, but more complicated, is that it is run not once but sometimes hundreds of times by LS-OPT to optimise the hardening parameters, meaning that any increase in computation time for one simulation leads to a much larger increase in the total optimisation time.

The equivalent stress–strain curves were found for deformation after necking and large strain values until fracture. It should be remembered though that what was really found is the equivalent stress–strain curves in an isotropically hardened two-term Voce material with Yld2004-18p yield criterion implemented in an FEM mesh. How well the predicted equivalent stress–strain curves correspond to the real curves depends on how accurate the assumptions and the models are. For practical applications the accuracy of the results is determined by how well they predict the forces and displacements in various problems, so at least for the problem of necking in a cylindrical rod it is very accurate. The comparison in Fig. 15 indicates that this approach is the next step towards a more accurate estimate of the equivalent stress–strain curves at large strains.

Acknowledgements

We want to thank Norsk Hydro ASA for the material used to produce the specimens. The work done by Dr. Ida Westermann at SINTEF Materials and Chemistry on heat treatment and texture and microstructure investigation of the specimens is also much appreciated.

References

[1] Considère M. Memoire sur l'emploi du fer et de l'acier dans les constructions. Dunod; 1885.
[2] Mirone G. Role of stress triaxiality in elastoplastic characterization and ductile failure prediction. Eng Fract Mech 2007;74:1203–21.
[3] Bridgman P. The stress distribution at the neck of a tension specimen. Trans Am Soc Met 1944;32:553–74.
[4] Davidenkov N, Spiridonova N. Analysis of the state of stress in the neck of a tension test specimen. Proc Am Soc Test Mater 1946;46:1147–58.
[5] Aronofsky J. Evaluation of stress distribution in the symmetrical neck of flat tensile bars. J Appl Mech 1951:75–84.
[6] Le Roy G, Embury J, Edwards G, Ashby M. A model of ductile fracture based on the nucleation and growth of voids. Acta Metall Mater 1981;29:1509–22.
[7] Needleman A. A numerical study of necking in circular cylindrical bar. J Mech Phys Solids 1972;20:111–27.
[8] Norris Jr. D, Moran B, Scudder J, Quinones D. A computer simulation of the tension test. J Mech Phys Solids 1978;26:1–19.
[9] Tvergaard V, Needleman A. Analysis of the cup-cone fracture in a round tensile bar. Acta Metall Mater 1984;32:157–69.
[10] Tvergaard V, Needleman A, Lo KK. Flow localization in the plane strain tensile test. J Mech Phys Solids 1981;29:115–42.
[11] Fourmeau M, Børvik T, Benallal A, Lademo O, Hopperstad O. On the plastic anisotropy of an aluminium alloy and its influence on constrained multiaxial flow. Int J Plast 2011;27:2005–25.
[12] Dunand M, Mohr D. On the predictive capabilities of the shear modified Gurson and the modified Mohr–Coulomb fracture models over a wide range of stress triaxialities and Lode angles. J Mech Phys Solids 2011;59:1374–94.
[13] Nam AW, Choung J. Prediction of failure strain according to stress triaxiality of a high strength marine structural steel. Collision and Grounding of Ships Offshore. Taylor & Francis group; 2013 p. 69.
[14] Hill R. A theory of the yielding and plastic flow of anisotropic metals. Proc R Soc Lond A: Math Phys Eng Sci 1948;193:281–97.
[15] Hosford W. A generalized isotropic yield criterion. J Appl Mech 1972;39:607.
[16] Bron F, Besson J. A yield function for anisotropic materials application to aluminum alloys. Int J Plast 2004;20:937–63.
[17] Barlat F, Maeda Y, Chung K, Yanagawa M, Brem J, Hayashida Y, et al. Yield function development for aluminum alloy sheets. J Mech Phys Solids 1997;45:1727–63.
[18] Aretz H, Barlat F. General orthotropic yield functions based on linear stress deviator transformations. AIP Conf Proc 2004;712:147.
[19] Barlat F, Aretz H, Yoon J, Karabin M, Brem J, Dick R. Linear transfomation-based anisotropic yield functions. Int J Plast 2005;21:1009–39.
[20] Barlat F. Crystallographic texture, anisotropic yield surfaces and forming limits of sheet metals. Mater Sci Eng 1987;91:55–72.
[21] Barlat F, Richmond O. Prediction of tricomponent plane stress yield surfaces and associated flow and failure behavior of strongly textured FCC polycrystalline sheets. Mater Sci Eng 1987;95:15–29.
[22] Choi S-H, Brem J, Barlat F, Oh K. Macroscopic anisotropy in AA5019A sheets. Acta Mater 2000;48:1853–63.
[23] Grytten F, Holmedal B, Hopperstad OS, Børvik T. Evaluation of identification methods for YLD2004-18p. Int J Plast 2008;24:2248–77.
[24] Beradai C, Berveiller M, Lipinski P. Plasticity of metallic polycrystals under complex loading paths. Int J Plast 1987;3:143–62.
[25] Zattarin P, Lipinski P, Rosochowski A. Numerical study of the influence of microstructure on subsequent yield surfaces of polycrystalline materials. Int J Mech Sci 2004;46:1377–98.
[26] Saai A, Dumoulin S, Hopperstad O. Influence of texture and grain shape on the yield surface in aluminium sheet material subjected to large deformations. AIP Conf Proc 2011;1353:85.
[27] Zhano K, Li Z. Numerical analysis of the stress–strain curve and fracture initiation for ductile material. Eng Fract Mech 1994;49:235–41.
[28] Cabezas EE, Celentano DJ. Experimental and numerical analysis of the tensile test using sheet specimens. Finite Elem Anal Des 2004;40:555–75.
[29] Bogusz P, Popławski A, Morka A, Niezgoda T. Evaluation of true stress in engineering materials using optical deformation measurement methods. J KONES Powertrain Transp 2012;19:53–64.
[30] Ling Y. Uniaxial true stress–strain after necking. AMP J Tech 1996;5:37–48.
[31] Westermann I, Pedersen K, Furu T, Børvik T, Hopperstad OS. Effects of particles and solutes on the strength, work-hardening and ductile fracture of aluminium alloys; 2014 [submitted for publication].
[32] Engler O, Randle V. Introduction to texture analysis: macrotexture, microtexture, and orientation mapping. Boca Raton, Florida, USA: CRC Press,; 2010.
[33] Needleman A, Asaro R, Lemonds J, Peirce D. Finite element analysis of crystalline solids. Comput Methods Appl Mech Eng 1985;52:689–708.
[34] Kalidindi SR, Bronkhorst CA, Anand L. Crystallographic texture evolution in bulk deformation processing of FCC metals. J Mech Phys Solids 1992;40:537–69.
[35] Taylor GI. The mechanism of plastic deformation of crystals. Part I. Theoretical. Proc R Soc Lond A: Math Phys Eng Sci 1934;145:362–87.
[36] Lee E, Liu D. Finite-strain elastic – plastic theory with application to plane-wave analysis. J Appl Phys 1967;38:19–27.
[37] Hutchinson J. Bounds and self-consistent estimates for creep of polycrystalline materials. Proc R Soc Lond A: Math Phys Eng Sci 1976;348:101–27.
[38] Li S, Engler O, Van Houtte P. Plastic anisotropy and texture evolution during tensile testing of extruded aluminium profiles. Model Simul Mater Sci 2005;13:783–95.
[39] Kocks UF, Tomé CN, Wenk H-R. Texture and anisotropy: preferred orientations in polycrystals and their effect on materials properties. Cambridge, UK: Cambridge University Press; 2000.
[40] Belytschko T, Liu WK, Moran B. Nonlinear finite elements for continua and structures. Chichester, New York: John Wiley; 2000.
[41] Voce E. The relationship between stress and strain for homogeneous deformation. J Inst Met 1948;74:537–62.

[42] Melchior MA, Delannay L. A texture discretization technique adapted to polycrystalline aggregates with non-uniform grain size. Comput Mater Sci 2006;37:557–64.
[43] Böhlke T, Haus U-U, Schulze V. Crystallographic texture approximation by quadratic programming. Acta Mater 2006;54:1359–68.
[44] Lequeu P, Gilormini P, Montheillet F, Bacroix B, Jonas J. Yield surfaces for textured polycrystals – I. Crystallographic approach. Acta Metall Mater 1987;35:439–51.
[45] Achani D, Hopperstad OS, Lademo OG. Behaviour of extruded aluminium alloys under proportional and non-proportional strain paths. J Mater Process Technol 2009;209:4750–64.
[46] Pedersen KO, Lademo OG, Berstad T, Furu T, Hopperstad OS. Influence of texture and grain structure on strain localisation and formability for AlMgSi alloys. J Mater Process Technol 2008;200:77–93.
[47] Grujicic M, Batchu S. Crystal plasticity analysis of earing in deep-drawn OFHC copper cups. J Mater Sci 2002;37:753–64.
[48] Stander N, Roux W, Goel T, Eggleston T, Craig K. LS-OPT user's manual. Livermore, California, USA: Livermore Software Technology Corporation; 2008.
[49] Dumoulin S, Engler O, Hopperstad O, Lademo O. Description of plastic anisotropy in AA6063-T6 using the crystal plasticity finite element method. Model Simul Mater Sci 2012;20:055008.
[50] Zhang K, Holmedal B, Manik T, Zhao Q. Crystal plasticity calculations of mechanical anisotropy of aluminium compared to experiments and to yield criterion fittings. In: Proceedings of the ICAA13 13th international conference on aluminum alloys; 2012. p. 915–20.

Article 2

M. Khadyko, O. R. Myhr, S. Dumoulin, O.S. Hopperstad

A microstructure based yield and work-hardening model for textured 6xxx aluminium alloys.

Submitted for possible journal publication.

A microstructure based yield and work-hardening model for textured 6xxx aluminium alloys

M. Khadyko[1,*], Ole Runar Myhr[1, 3], S. Dumoulin[2] and O.S. Hopperstad[1]

[1] Structural Impact Laboratory (SIMLab), Centre for Research-based Innovation, Department of Structural Engineering,
Norwegian University of Science and Technology, NO-7491 Trondheim, Norway
[2]SINTEF Materials & Chemistry, NO-7465 Trondheim, Norway
[3]Hydro Aluminium, Research and Technology Development (RTD), Romsdalveien 1
NO-6601 Sunndalsøra, Norway

Abstract

The plastic properties of an aluminium alloy are defined by its microstructure. The most important factors are the presence of alloying elements in form of solid solution and precipitates of various sizes, and the crystallographic texture. A nanoscale model that predicts the work hardening curves of 6xxx aluminium alloys was proposed by Myhr et al. [1]. The model predicts the solid solution concentration and the particle size distribution from the chemical composition and thermal history of the alloy. The yield stress and the work hardening of the alloy are then determined from dislocation mechanics. The model was largely used for non-textured materials in previous studies. In this work, a crystal plasticity based approach is proposed for the work hardening part of the nanoscale model, which allows including the influence of the crystallographic texture. The model is evaluated by comparison with experimental data from uniaxial tensile tests on two textured 6xxx alloys in five temper conditions.

Keywords: aluminium alloys; solutes; precipitates; dislocations; work-hardening; crystal plasticity.

---

[*] Corresponding author: Mikhail Khadyko (mikhail.khadyko@ntnu.no)

1. Introduction

Aluminium alloys are the second most important metallic structural materials after steel and are used in the broadest range of products. The variety of their applications is mirrored by the variety of properties they exhibit. The yield strength, work-hardening and fracture strain of two aluminium alloys may differ by an order of magnitude. Age-hardening may dramatically change these parameters even for the same alloy. In addition some aluminium products, including extruded and rolled sheets, possess considerable plastic anisotropy. Such variety of properties has quite often some common underlying physical mechanism, which just manifests itself differently in different conditions. An important task of the material science is to uncover these physical mechanisms and to express them through quantitative models, which can be used in practical applications.

The plastic anisotropy was the first characteristic feature of aluminium which was explained by such quantitative physical models. In [2, 3] Taylor developed a theory of plastic deformation of crystals and polycrystals using aluminium for experimental validation. The crystals deform plastically by slip on certain slip systems, defined by crystallographic planes and directions. Therefore the crystalline grains of any metal are intrinsically plastically anisotropic. Polycrystals containing a multitude of grains may be plastically isotropic if the constituent grains are oriented randomly. If some grain orientations are more prominent, or in other words if the polycrystal has a non-random crystallographic texture, the grains with these orientations will have a pronounced contribution to the anisotropy of the whole sample. If the texture of the polycrystal is known, a variety of methods is available to determine the plastic anisotropy, including the full-constraint Taylor model, relaxed-constraint Taylor models, the self-consistent viscoplastic model and finite element models [4-10].

The next aspect of the plastic behaviour of aluminium alloys is their work-hardening. Taylor in [11] and Orowan in [12] introduced the key concept of a dislocation as a defect of the crystal lattice which propagates through the crystal, transfers plastic deformation, carries elastic energy and interacts with other dislocations. Taylor analysed the dislocation structure in the crystal and connected the flow stress in the crystal with its dislocation density. The problem that remained was to determine the evolution of the dislocation density during plastic deformation. Kocks and Mecking [13, 14] proposed an evolution law which consists of two terms. The first term describes the accumulation of dislocations with plastic deformation and is inversely proportional to the mean free path of the dislocation before it is stopped by interaction with another (immobile) dislocation. The second term describes the annihilation of dislocations during straining (dynamic recovery) and is proportional to the distance between two dislocations with opposite Burgers vector at which they annihilate each other. Different improvements and modifications have been proposed for this basic model including kinematic hardening [15] and influence of grain size [16, 17]. The original model was formulated with the very simplified assumptions of homogeneous dislocation density inside the material. Nevertheless, even after a more rigorous analysis, when the dislocation structures inside the grain (dislocation cells) are taken into consideration, the general evolution rule still holds [18, 19].

Aluminium alloys usually contain particles of varying size and chemical composition, such as precipitates, dispersoids and constituent particles. Their influence on the work-hardening was analysed from the point of view of dislocation theory by Ashby in [20, 21]. It was demonstrated that the dislocation density associated with non-homogeneous plastic deformation around non-shearable particles (geometrically necessary dislocations, as opposed to the statistically stored dislocations) is inversely proportional to the average distance between the particles. Estrin [22, 23] proposed a generalization of the Kocks-Mecking model where different dislocation accumulation (and consequently work-hardening) mechanisms were represented by their characteristic distances and linearly added together. This approach was used to build the models which account for the precipitate particles in [24-26].

The two aspects of aluminium alloys – anisotropy and dislocation density based work-hardening – were combined in a crystal plasticity model in [27] and developed further in [28]. The hardening in this model has the same form as in the Kocks-Mecking model, but acts on each slip system controlling the critical resolved shear stress instead of the global stress. This model only includes the evolution of statistically stored dislocations, but it may be generalized in the same manner as the Kocks-Mecking model with terms for other factors contributing to work-hardening added linearly. These terms will again be inversely proportional to the characteristic distance of the corresponding work-hardening mechanism. A crystal plasticity model which includes grain size influence is developed in [29] while twinning is included by its characteristic distance in [30].

Even if the mechanical properties of an aluminium alloy are closely related with its microstructure, the experimental determination of the microstructure of an alloy is a difficult and tedious task. In [31] and [1] an attempt is made to derive the microstructure from the chemical composition and the thermal history of the alloy. In [1] a complete model for this is proposed, which combines a precipitation model and dislocation based initial yield strength and work-hardening models for the 6xxx family of alloys. It is referred in this article as the Nanostructural Model (NaMo). The theory behind the model is developed by Myhr and co-workers in [32-34]. The work-hardening model is a version of the Kocks-Mecking equation formulated in terms of global stress and strain. In [35] the NaMo precipitation model was used together with a crystal plasticity model to study the influence of precipitates on the work-hardening and anisotropy of the aluminium alloys.

NaMo, as formulated in [1], is treating the polycrystalline nature of aluminium in a very simplified manner, reducing the texture and grain rotation effects to one constant parameter. Furthermore, it was calibrated and tested on aluminium alloys with random texture. In the present work, the effects of crystallographic texture are implemented into NaMo more properly using the crystal plasticity theory. Thus, the plastic anisotropy and the influence of texture and grain rotations on the initial yield stress and work-hardening are included in the model. A series of experiments was conducted on different temper conditions of the AA6060 and AA6082 alloys with pronounced texture and the results were compared to the predictions of NaMo with and without the crystal plasticity modification. This allows estimating how well NaMo works for textured aluminium alloys and to which extent the deviations between predictions and experimental data are caused by crystallographic texture effects or the underlying precipitation model.

2. Experiments

A series of quasi-static tensile tests were performed on cylindrical specimens made of the aluminium alloys AA6060 and AA6082. The compositions of the two alloys are given in Table 1. The specimens were taken from 10 mm thick and 90 mm wide extruded flat profiles at 90° to the extrusion direction and were given a separate solution heat treatment at 540° C for 15 minutes before they were quenched to room temperature and subsequently aged to tempers T4, T6x, T6, T7 and O, where the T4 temper corresponds to one week room temperature storage. The heat treatment is described in more detail in Table 2 (see also [36]).

The uniaxial tensile tests were performed in a testing machine with laser gauges, allowing precise measurements of the specimen’s minimum diameter at high frequency. The test set-up made it possible to obtain the true stress-strain curve until fracture for all specimens. The crystallographic texture of the alloys was measured with a scanning electron microscope using electron back-scattering diffraction. The results were processed using harmonic series expansion to find the orientation distribution function (ODF) for the alloys. These ODFs were used in a crystal plasticity model to calculate the yield surface of the alloys.

Table 1: Chemical composition of the alloys, wt%.

Alloy	Fe	Si	Mg	Mn	Cr	Cu	Zn	Ti
AA6060	0.193	0.422	0.468	0.015	0.000	0.002	0.005	0.008
AA6082	0.180	0.880	0.600	0.530	0.150	0.020	0.005	0.011

Table 2: Heat treatment of the alloys.

Temper	Stage 1	Stage 2	Stage 3	Stage 4	Stage 5
T4	540°C in salt bath for 15 min	Water quenching	One week at room temperature	___	___
T6x	540°C in salt bath for 15 min	Water quenching	15 min at room temperature	185°C in oil bath for one hour	Air cooling
T6	540°C in salt bath for 15 min	Water quenching	15 min at room temperature	185°C in oil bath for five hours	Air cooling
T7	540°C in salt bath for 15 min	Water quenching	15 min at room temperature	185°C in oil bath for one week	Air cooling
O	540°C in salt bath for 15 min	Water quenching	15 min at room temperature	350°C in salt bath for twenty four hours	Air cooling

A finite element model of the tensile specimen was built, with the material described by an anisotropic plasticity model using a two-term Voce work-hardening rule. The tensile test was simulated and the true stress-strain curve from the simulation was fitted to the true stress-strain curve from the experiments by optimizing the parameters of the two-term Voce work-hardening rule. Thus the equivalent stress-strain curve until fracture was obtained for each material. It should be noted that the equivalent stress-strain curves were determined by using the extrusion direction as the reference direction; i.e., the obtained equivalent stress-strain curves are consistent with true stress vs. logarithmic plastic strain curves from uniaxial tension tests in the extrusion direction. The test specimens on the other hand were cut at 90° to the extrusion direction, because the results from tension tests in the in-plane transverse direction tend to be more consistent and reliable. The results are presented in Figure 1.

Further details on the experimental set-up and procedures, the numerical modelling and optimization, and the results are given in [37].

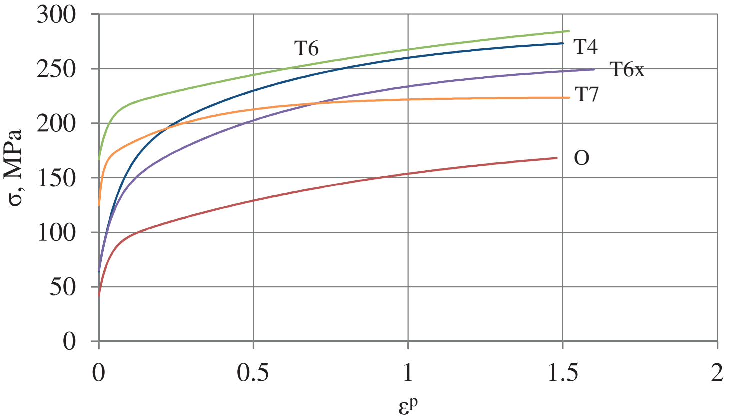

a)

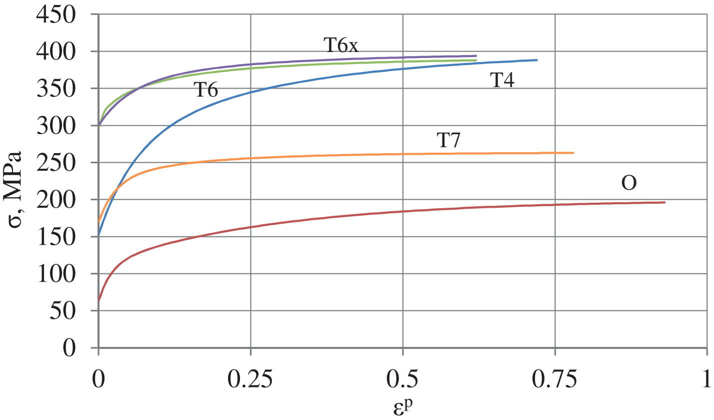

b)

Figure 1: Equivalent stress-strain curves for a) AA6060 and b) AA6082, using the extrusion direction as the reference direction [37]

3. Theoretical foundation

3.1. Nanostructural model (NaMo).

A detailed outline of the theory and assumptions lying in the foundation of NaMo is given elsewhere [1, 32-34], therefore only a review of the key ideas and equations will be given here. The model consists of three parts: a precipitation model, a yield strength model and a work-hardening model.

3.1.1. Precipitation model

The chemical composition of the alloy and the thermal history are used as an input for the precipitation model. Time is discretized into small steps. The first component of the model is the nucleation law. It predicts the number of stable nuclei, which form at every time step. The incubation period is neglected and the steady state nucleation rate j calculated according to

$$j = j_0 \exp\left[-\left(\frac{A_0}{\mathrm{R}T}\right)^3 \left(\frac{1}{\ln\left(\bar{C}/C_e\right)}\right)^2\right] \exp\left(-\frac{Q_d}{\mathrm{R}T}\right) \qquad (1)$$

where the first exponential term expresses the energy barrier against heterogeneous nucleation, and the second accounts for the temperature dependency of the diffusion coefficient. Further, T is the temperature, R is the universal gas constant, $\bar{C}$ is the mean solute concentration in the matrix, C_e is the equilibrium solute concentration at the particle/matrix interface, A_0 is a parameter related to the energy barrier for nucleation, Q_d is the activation energy for diffusion and j_0 is a pre-exponential term. The nucleated particles are idealized as spherical and are characterized by their radius r, solute concentration C_p and an interface energy. These particles may either dissolve or grow as described by the second component of the model – the particle radius rate law

$$\frac{dr}{dt} = \frac{\bar{C} - C_i}{C_p - C_i}\frac{D}{r} \qquad (2)$$

where C_i is the solute concentration at the particle/matrix interface and D is the diffusion coefficient. The Gibbs-Thomson equation [32] is used to relate C_i to the equilibrium concentration C_e. When this equation is combined with Equation (2), an expression for the critical radius r_0 for a particle that neither dissolves nor grows can be derived. At a certain time step during a heat treatment, particles smaller than r_0 dissolve while particles larger than r_0 grow, which leads to the evolution of a distribution of particles of various size, i.e. a discrete particle size distribution (PSD) with a defined number of particles within each size class $r \pm (\Delta r / 2)$ (if $\Delta r \to 0$ then the function becomes continuous).

A range of different particles may form in 6xxx alloys depending on the chemical composition and the heat treatment, but the ones that are of main interest here are the nanometre scale hardening particles consisting of Mg and Si (e.g. β'' and β' particles), as well as clusters and GP-zones, which may form at room temperature. Each of these classes or groups of particles is represented by a separate PSD in the model, i.e. one PSD for β'' and β' particles and one for clusters and GP-zones.

The third component of the model is the continuity equation. It is used to find the mean solute concentration $\bar{C}$ in the matrix, and is based on the fact that even though there may be a transition between elements in solid solution and in the particles comprising the two PSDs during a heat treatment, the overall content of each alloying element remains constant. The continuity equation reads [36]

$$\bar{C} = \frac{C_0 - \left(C_{p1} \sum_i \frac{4}{3} \pi r_i^3 N_i + C_{p2} \sum_j \frac{4}{3} \pi r_j^3 N_j \right)}{1 - \left(\sum_i \frac{4}{3} \pi r_i^3 N_i + \sum_j \frac{4}{3} \pi r_j^3 N_j \right)} \tag{3}$$

where C_0 is the initial solute concentration in the alloy, C_{p1} and C_{p2} are the concentration of alloying element in particles which belong to each of the two size distributions. N_i and N_j are the number of particles per unit volume within the discrete radius intervals $r_i \pm (\Delta r / 2)$ and $r_j \pm (\Delta r / 2)$ corresponding to each of the distributions.

3.1.2. Yield strength model

The yield strength model uses dislocation theory to convert the results from the precipitation model, i.e. the mean solute concentration and the PSD, into a corresponding room temperature yield stress. It considers two kinds of contributions: precipitation strengthening σ_p and solid solution strengthening σ_{ss}, in addition to the intrinsic strength of the pure aluminium σ_i.

The precipitation strengthening contribution σ_p corresponds to the difference in yield stress between a material containing particles, and an identical material without particles. For the former material, σ_p can be attributed to the extra stress needed for a dislocation to break away from particles acting as obstacles along the dislocation line when the dislocation starts to move. A reasonable expression for σ_p can be obtained by calculating the mean obstacle strength of particles that interact with a bowing dislocation along the entire dislocation line by considering the specific strength of each individual particle according to the two governing mechanisms, i.e. shearing of small, and Orowan bypassing of larger particles that exceed a critical radius. In addition, the mean effective particle spacing must be calculated from the particle size distribution using the Friedel formalism [38] before σ_p can be obtained as described in [39].

The solid solution contribution is due to individual atoms of Si, Mg, Mn and Cu that are present in the aluminium matrix. These atoms serve as weak obstacles for the dislocations and their overall strength contribution is calculated using the framework outlined in [32,37]. When several strengthening mechanisms are operating simultaneously, it is assumed that their contributions may be added linearly. Thus the total initial yield strength of the material is calculated as

$$\sigma_y = \sigma_i + \sigma_{ss} + \sigma_p \tag{4}$$

3.1.3. Work-hardening model

The work-hardening model is based on the assumption that the total dislocation density may be decomposed into two parts: the statistically stored and geometrically necessary dislocation densities ρ_s and ρ_g, respectively, which evolve independently from each other. These two contributions to the dislocation density may be added linearly and applied in the Taylor equation to obtain the work-hardening as [11]

$$\Delta\sigma_d \equiv \sigma - \sigma_y = \alpha M \mu b \sqrt{\rho_s + \rho_g} \tag{5}$$

where α is a constant, M is the Taylor factor, μ is the shear modulus and b is the magnitude of the Burgers vector. The evolution of ρ_s is described by the Kocks-Mecking equation [14]

$$d\rho_s = \left(k_1\rho_s^{1/2} - k_2\rho_s\right)d\varepsilon^p \tag{6}$$

where k_1 characterizes the generation of dislocations and is assumed constant for the 6xxx family of alloys, k_2 is the recovery term which depends on the solid solution concentration and ε^p is the equivalent plastic strain. This expression may be integrated analytically which gives

$$\rho_s = \left(\frac{k_1}{k_2}\right)^2 \left(1 - \exp\left(-\frac{k_2\varepsilon^p}{2}\right)\right)^2 \tag{7}$$

The dependence of k_2 on the concentration of elements in solid solution arises from several mechanisms [13, 14] and is described by

$$k_2 = k_1 \frac{\alpha M \mu b}{k_3\left(\hat{C}_{Mg}\right)^{3/4}} \tag{8}$$

Here k_3 is a parameter, determined by calibration against experimental data, and $\hat{C}_{Mg}$ is the equivalent magnesium concentration, which is a parameter that accounts for the different alloying elements contribution to dynamic recovery. For Al-Mg-Si alloys, a reasonable estimate is the following [1]: $\hat{C}_{Mg} = \bar{C} + 0.5C_{Si}^{eff}$, where C_{Si}^{eff} is the effective silicon concentration, which is obtained through a correction for the amount of Si being tied up as coarse particles [33]. Note that $\bar{C}$ is taken as the mean concentration of Mg in solid solution for AlMgSi alloys.

The evolution of the geometrically necessary dislocation density is a variation of the Ashby equation [21], adapted for the global plastic strain

$$\rho_g = \frac{k_4}{b\lambda_{g,o}}\varepsilon^p \tag{9}$$

where k_4 is a parameter, determined by calibration to tests and $\lambda_{g,o}$ is the characteristic geometric slip distance associated with the Orowan particles. The geometrically necessary dislocation density only increases up to a certain value, at which recovery mechanisms are triggered. The critical plastic strain ε_c at which this occurs depends on the volume fraction of the Orowan particles f_o, namely

$$\varepsilon_c = \left(\frac{f_o^{ref}}{f_o} \right) \varepsilon_c^{ref} \tag{10}$$

where f_o^{ref} and ε_c^{ref} are the corresponding values of a reference alloy. The precipitation model provides information about both the geometric slip distance $\lambda_{g,o}$ and the volume fraction of the Orowan particles f_o [36], i.e.

$$\lambda_{g,o} = \left(8 \sum_i r_i^2 N_i \right)^{-1} \quad \text{for } r_i > r_c \tag{11}$$

$$f_o = \sum_i \frac{4}{3} \pi r_i^3 N_i \quad \text{for } r_i > r_c \tag{12}$$

where r_c is the particle radius defining the transition between shearable and non-shearable particles. Note that $\lambda_{g,o}$ and f_o are calculated from just one of the two PSDs, i.e. the PSD representing β'' and β' particles, since for the other distribution representing clusters and GP-zones, all particles are less than the critical radius (i.e. $r_i < r_c$).

3.2. Crystal plasticity model

3.2.1. Single crystal kinematics and kinetics

The finite deformation formulation is used. The deformation gradient $\boldsymbol{F}$ is multiplicatively decomposed into an elastic part $\boldsymbol{F}^e$ and a plastic part $\boldsymbol{F}^p$

$$\boldsymbol{F} = \boldsymbol{F}^e \boldsymbol{F}^p \tag{13}$$

Here $\boldsymbol{F}^p$ accounts for plastic slip and transforms the crystal from the initial configuration Ω_0 into the intermediate plastically deformed configuration $\bar{\Omega}$ while $\boldsymbol{F}^e$ accounts for the elastic deformations and rigid body rotations and transforms the crystal from the intermediate configuration $\bar{\Omega}$ into the current configuration Ω. The slip systems are defined by the slip direction vector $\boldsymbol{m}_0^\alpha$ and the slip plane normal vector $\boldsymbol{n}_0^\alpha$ in the initial configuration. They stay the same in the intermediate configuration and transform into vectors $\boldsymbol{m}^\alpha$ and $\boldsymbol{n}^\alpha$, respectively, in the current configuration. These vectors may be used as a basis of the plastic velocity gradient $\bar{\boldsymbol{L}}^p$ in the intermediate configuration

$$\bar{\boldsymbol{L}}^p = \dot{\boldsymbol{F}}^p \left(\boldsymbol{F}^p\right)^{-1} = \sum_{\alpha=1}^{n} \dot{\gamma}^\alpha \boldsymbol{m}_0^\alpha \otimes \boldsymbol{n}_0^\alpha \tag{14}$$

where $\dot{\gamma}^\alpha$ is the slip rate on slip system α in the intermediate configuration and n is the total number of slip systems.

The elastic Green strain tensor $\bar{\boldsymbol{E}}^e$ in the intermediate configuration may be defined as

$$\bar{\boldsymbol{E}}^e = \frac{1}{2}\left[\left(\boldsymbol{F}^e\right)^T \boldsymbol{F}^e - \boldsymbol{I}\right] = \frac{1}{2}\left(\bar{\boldsymbol{C}}^e - \boldsymbol{I}\right), \quad \bar{\boldsymbol{C}}^e = \left(\boldsymbol{F}^e\right)^T \boldsymbol{F}^e \tag{15}$$

where $\bar{\boldsymbol{C}}^e$ is the elastic right Cauchy-Green deformation tensor and $\boldsymbol{I}$ is the unity tensor. If the Cauchy stress tensor $\boldsymbol{\sigma}$ is pulled back into this configuration, the second Piola-Kirchhoff stress tensor $\bar{\boldsymbol{S}}$ is obtained

$$\bar{\boldsymbol{S}} = \det\boldsymbol{F} \left(\boldsymbol{F}^e\right)^{-1} \boldsymbol{\sigma} \left(\boldsymbol{F}^e\right)^{-T} \tag{16}$$

By assuming small elastic deformations, it is reasonable to adopt a linear hyperelastic model to describe the elastic behaviour

$$\bar{\boldsymbol{S}} = \mathbf{C}_{el}^{\bar{S}} : \bar{\boldsymbol{E}}^e \tag{17}$$

where $\mathbf{C}_{el}^{\bar{S}}$ is the fourth order tensor of elastic moduli. The total power per unit volume $\dot{w}$ consists of elastic and plastic parts

$$\dot{w} = \dot{w}^e + \dot{w}^p = \bar{\boldsymbol{S}} : \dot{\bar{\boldsymbol{E}}}^e + \bar{\boldsymbol{C}}^e \bar{\boldsymbol{S}} : \bar{\boldsymbol{L}}^p \tag{18}$$

The plastic power may be rewritten as a sum of powers spent on all the slip systems

$$\dot{w}^p = \sum_{\alpha=1}^{n} \tau^\alpha \dot{\gamma}^\alpha \tag{19}$$

where τ^{α} is the resolved shear stress on slip system α, power conjugate to the slip rate $\dot{\gamma}^{\alpha}$. It may be found from the second Piola-Kirchhoff stress tensor as

$$\tau^{\alpha}=\bar{\boldsymbol{C}}^{e}\bar{\boldsymbol{S}}:\left(\boldsymbol{m}_{0}^{\alpha}\otimes\boldsymbol{n}_{0}^{\alpha}\right) \tag{20}$$

3.2.2. Flow and work-hardening rules

The plastic flow is described by a rate-dependent rule

$$\dot{\gamma}^{\alpha}=\dot{\gamma}_{0}\left(\frac{\left|\tau^{\alpha}\right|}{\tau_{c}^{\alpha}}\right)^{\frac{1}{m}}\operatorname{sgn}\left(\tau^{\alpha}\right) \tag{21}$$

where $\dot{\gamma}_0$ is the reference slip rate, m is the instantaneous strain rate sensitivity and τ_c^{α} is the history dependent critical resolved shear stress of slip system α. The initial value of yield strength is equal to $\tau_c^{\alpha}=\tau_y$ for all slip systems.

We introduce work-hardening by connecting the critical resolved shear stress rate $\dot{\tau}_c^{\alpha}$ to the slip rates on the slip systems

$$\dot{\tau}_{c}^{\alpha}=\theta\sum_{\beta=1}^{n}q_{\alpha\beta}\left|\dot{\gamma}^{\beta}\right| \tag{22}$$

where $\theta\equiv d\tau_c/d\Gamma$ is the hardening rate defined by a master curve, and $q_{\alpha\beta}$ is the matrix of self-hardening and latent-hardening coefficients. The accumulated slip Γ is defined by the evolution equation

$$\dot{\Gamma}=\sum_{\alpha=1}^{n}\left|\dot{\gamma}^{\alpha}\right| \tag{23}$$

and the master hardening curve is given by

$$\tau_{c}=\tau_{y}+\alpha\mu b\sqrt{\rho_{s}+\rho_{g}} \tag{24}$$

where ρ_s and ρ_g are the average densities of statistically stored and geometrically necessary dislocations, respectively. Similarly to NaMo, it is assumed that the two dislocation densities may be added linearly and used in the Taylor equation to obtain the work-hardening. The dislocation density evolutions are connected to the accumulated slip by

$$d\rho_s = \left(k_1^{cp}\sqrt{\rho_s} - k_2^{cp}\rho_s\right)d\Gamma \tag{25}$$

$$d\rho_g = \frac{1}{bL}\left(1-\left(\frac{\rho_g}{\rho_g^{sat}}\right)^a\right)d\Gamma \tag{26}$$

where k_1^{cp} and k_2^{cp} are correspondingly the accumulation and annihilation terms for statistically stored dislocations, L is a parameter proportional to the characteristic distance between the Orowan particles and ρ_g^{sat} is the density of geometrically necessary dislocations at saturation. The evolution of the geometrically necessary dislocation density is formulated in a slightly different manner than in NaMo, while keeping the behaviour of linear increase and fast saturation at some critical value. The value of parameter a may be chosen high enough to approach Equation (9) as closely as necessary. The work-hardening rate θ is the derivative of the master curve τ_c with respect to the accumulated slip Γ, viz.

$$\theta \equiv \frac{d\tau_c}{d\Gamma} = \frac{\partial \tau_c}{\partial \rho_s}\frac{d\rho_s}{d\Gamma} + \frac{\partial \tau_c}{\partial \rho_g}\frac{d\rho_g}{d\Gamma} \tag{27}$$

which by use of Equations (25) and (26) may be rewritten as

$$\theta = \frac{\alpha\mu b}{2\sqrt{\rho_s + \rho_g}}\left(k_1^{cp}\sqrt{\rho_s} - k_2^{cp}\rho_s + \frac{1}{bL}\left(1-\left(\frac{\rho_g}{\rho_g^{sat}}\right)^a\right)\right) \tag{28}$$

3.2.3. Polycrystal modelling

The behaviour of the polycrystal is modelled using the assumption of a constant deformation gradient in all grains – i.e. the full-constraint Taylor model. This model does not provide stress equilibrium between the grains and usually slightly overestimates the global stress. Nevertheless, it is still fairly accurate and computationally efficient. The use of this model for predicting the yield stress anisotropy against other models (relaxed constraint, self-consistent and finite element models) is discussed in [4] and [40].

The deformation gradient is equal to the global deformation gradient for all constituent grains and the global Cauchy stress $\boldsymbol{\sigma}$ is found as an average of the local Cauchy stresses $\boldsymbol{\sigma}_k$ in the grains

$$\boldsymbol{\sigma} = \frac{1}{n_g} \sum_{k=1}^{n_g} \boldsymbol{\sigma}_k \tag{29}$$

where n_g is the number of grains. The contribution of all grains to the total stress is the same, meaning it is assumed they all have equal volume.

The plastic rate-of-deformation tensor $\bar{\boldsymbol{D}}_k^p$ for grain k may be found as the symmetric part of $\bar{\boldsymbol{L}}_k^p$, i.e.

$$\bar{\boldsymbol{D}}_k^p = \frac{1}{2}\left(\bar{\boldsymbol{L}}_k^p + \left(\bar{\boldsymbol{L}}_k^p\right)^T\right) \tag{30}$$

and is used to define the equivalent plastic strain rate in grain k by

$$\dot{\varepsilon}_k^p = \sqrt{\frac{2}{3}\bar{\boldsymbol{D}}_k^p : \bar{\boldsymbol{D}}_k^p} \tag{31}$$

The Taylor factor for grain k is then defined as

$$M_k = \frac{\dot{\Gamma}_k}{\dot{\varepsilon}_k^p} \tag{32}$$

where $\dot{\Gamma}_k$ is the accumulated slip rate of the same grain. The Taylor factor for the polycrystal is then defined in the form

$$M = \frac{\frac{1}{n_g}\sum_{k=1}^{n_g}\dot{\Gamma}_k}{\frac{1}{n_g}\sum_{g=1}^{n_g}\dot{\varepsilon}_k^p} \tag{33}$$

where it was used that all grains are assumed to have equal volume in the full-constraint Taylor model.

4. Parameter identification

Before NaMo may be used to calculate the stress-strain curve of a 6xxx aluminium alloy, it must be calibrated against experimental data. The parameters that need to be calibrated are:

- the dislocation accumulation coefficient, k_1
- the coefficient connecting equivalent Mg concentration and recovery, k_3
- the coefficient connecting characteristic slip distance and geometrically necessary dislocation accumulation, k_4
- the reference critical strain, ε_c^{ref}
- the reference particle volume fraction, f_o^{ref}

The parameters k_1 and k_2 are found by fitting the Equation (5) for work hardening and Equation (7) for statistically stored dislocation density to the experimental stress-strain curves for two alloys with no considerable particle influence; k_3 is then found from the obtained k_2. The remaining parameters k_4, ε_c^{ref} and f_o^{ref} are found by fitting the same equations and in addition Equation (9) for the geometrically necessary dislocation density to the experimental stress-strain curve of an alloy with considerable influence of precipitate particles on the response. The details of the calibration and the parameter values for 6xxx alloys may be found in [1].

To use the crystal plasticity version of the hardening model (CP-NaMo), it is necessary to find out how the output of the precipitation model of NaMo is connected to the parameters of CP-NaMo. The accumulation coefficient k_1^{cp} is assumed constant for the 6xxx family of alloys, in the same way as k_1. The recovery coefficient k_2^{cp} is assumed to depend on the equivalent magnesium concentration in the same form as k_2, i.e.

$$k_2^{cp} = k_1^{cp} \frac{\alpha \mu b}{k_3^{cp} \left(\hat{C}_{Mg}\right)^{3/4}} \tag{34}$$

The parameter L is proportional to the slip distance $\lambda_{g,o}$, viz.

$$L = k_4^{cp} \lambda_{g,o} \tag{35}$$

where k_4^{cp} is a parameter. It should be noted that $\lambda_{g,o}$ is calculated from the precipitation model and has a direct physical meaning of slip distance, while L is a parameter proportional to it, but also including the contribution of the calibration procedure. The geometrically necessary dislocation density increases until saturation value ρ_g^{sat}; that happens when the accumulated slip reaches its critical value Γ_c. This value in turn depends on the volume fraction of Orowan particles f_o analogously to Equation (10), i.e.

$$\Gamma_c = \left(\frac{f_o^{ref}}{f_o} \right) \Gamma_c^{ref} \tag{36}$$

Provided that parameter a in Equation (26) is sufficiently large, the saturation value for the geometrically necessary dislocation density may be estimated without much loss of accuracy as

$$\rho_g^{sat} = \frac{k_5^{cp}}{f_o bL} \tag{37}$$

where k_5^{cp} is a parameter. Therefore the set of constants, which must be found for CP-NaMo is the following

- the dislocation accumulation coefficient, k_1^{cp}
- the coefficient connecting equivalent Mg concentration and recovery, k_3^{cp}
- the coefficient connecting slip distance and geometrically necessary dislocation accumulation, k_4^{cp}
- the coefficient defining the saturation density of the geometrically necessary dislocations, k_5^{cp}

The initial slip resistance τ_y is found directly from the initial yield stress part of NaMo. NaMo uses the stress relations formulated on slip system level and multiplies the result by the Taylor factor to transform them to global stresses. If this multiplication is left out, we obtain

$$\tau_y = \tau_i + \tau_p + \tau_{ss} \tag{38}$$

where the contribution to the yield stress of the intrinsic strength of aluminium, the particles and the solid solution are denoted τ_i, τ_p and τ_{ss}, respectively.

The numerical set up of CP-NaMo consists of an 8-node element with reduced integration (i.e. only a single integration point), using full-constraint Taylor type homogenization in the integration point. The explicit solver of the nonlinear finite element program LS-DYNA was used. The crystal plasticity material model is implemented as a user material subroutine. This subroutine utilizes the explicit integration scheme by Grujicic and Batchu [41]. The single integration point, full-constraint Taylor method may seem rather crude, but comparison of the experimental tests with the explicit finite element modelling (either one or more elements per grain) showed that it predicts the stress rather accurately, only several percent higher than a much more complex and time consuming finite element model.

The goal of the calibration was to find a set of parameters k_i^{cp} that would result in the same stress-strain response from CP-NaMo and NaMo for the reference materials. The first two reference materials are AA6060 and AA6082 in T4 temper. They were chosen because the geometric slip distance for these materials is very high, meaning that their stress-strain response is not influenced by the precipitates. Therefore the k_1^{cp} and k_2^{cp} coefficients may be isolated and used to find the coefficient k_3^{cp}. The calibration was performed with LS-OPT [42], which is an optimization program that runs several LS-DYNA simulations with different values of material parameters and compares the results of the simulations with some reference data. The mean squared error is calculated for each set of values and new values are chosen in such a way that the mean squared error is reduced. Usually after 15-20 iterations an optimal set of values is found. This procedure was used for the two aforementioned materials, utilizing the same k_1^{cp} and two different k_2^{cp} as the parameters varied by LS-OPT. When the two k_2^{cp} were found, they were used in Equation (34), together with the equivalent Mg concentration, known from the precipitation model, to find k_3^{cp}.

The second step was to find the precipitate related constants. For this the AA6060 alloy in T6 temper was chosen. The geometrical slip distance for this material was small enough to show a considerable influence on the stress-strain response. The coefficient k_2^{cp} for this alloy is found from the already determined coefficient k_3^{cp}, whereas k_1^{cp} is the same for all alloys. The parameters L and ρ_g^{sat} (and thereby k_4^{cp} and k_5^{cp}), were found by adjusting them in such a way that ρ_g would grow at the same rate and saturate at the same value compared to ρ_s in CP-NaMo as in NaMo, i.e.

$$\left(\frac{\rho_g^{sat}}{\rho_s^{sat}}\right)_{CP-NaMo} = \left(\frac{\rho_g^{sat}}{\rho_s^{sat}}\right)_{NaMo} \tag{39}$$

and

$$\left(\frac{\Gamma_g^{sat}}{\Gamma_s^{sat}}\right)_{CP-NaMo} = \left(\frac{\varepsilon_g^{sat}}{\varepsilon_s^{sat}}\right)_{NaMo} \tag{40}$$

where ε_g^{sat} and ε_s^{sat} are plastic strain values at which geometrically necessary and statistical dislocation densities saturate in NaMo, while Γ_g^{sat} and Γ_s^{sat} are the analogous accumulated slip values in CP-NaMo.

The rest of crystal plasticity model parameters were taken from literature (e.g. [7]). Their values are shown in Table 3.

The stress-strain curves from NaMo and CP-NaMo are presented in Figure 2. Because NaMo uses the Taylor factor $M = 3.1$ corresponding to random texture, a set of 1000 random orientations was used as the input into the calculations. In NaMo this value stays the same throughout the deformation, but in CP-NaMo it evolves, as may be seen in Figure 3. The difference in Taylor factor is as high as 15% for large strains, leading to different shape of the stress-strain curve. NaMo has a characteristic saturation of the stress, where the hardening rate falls practically to zero, while CP-NaMo for random texture continues to harden even when the dislocation densities on active slip systems have saturated, because of the evolution of the Taylor factor. Another difference is the latent hardening parameter $q_{\alpha\beta}$ in CP-NaMo, which is not found in NaMo and could hardly be implemented in it in a simple way. So, if this is taken into account, obtaining exactly the same stress-strain curves with CP-NaMo and NaMo is not possible (and probably not desired) in some cases. The data from the precipitation model, used as the input is given in Table 4 and the obtained parameters of CP-NaMo are given in Table 5. The coefficient k_1^{cp}, constant for all materials (i.e. combinations of alloy and temper), is equal to $1.25 \cdot 10^5 \text{ mm}^{-1}$.

We attempted a more direct calibration, where the experimental curves and CP-NaMo were used from the very beginning, but this attempt failed. Remarkably, the stress-strain curves in temper T4 for the two alloys did not fall into the assumed framework in which the work hardening is controlled solely by the equivalent Mg concentration, and the obtained values of k_2^{cp} did not allow to find a reasonable value of k_3^{cp}.

Table 3: Parameters of crystal plasticity model

c_{11}, MPa	c_{12}, MPa	c_{44}, MPa	$\dot{\gamma}_0$, s^{-1}	m	$q_{\alpha\beta}$	μ, MPa	a	b, mm
106430	60350	28210	0.010	0.005	1.4, if $\alpha \neq \beta$ 1.0, if $\alpha = \beta$	24400	0.3	$2.86\cdot10^{-7}$

Table 4: Output of the precipitation and yield strength models of NaMo

Alloy/temper	$\hat{C}_{Mg}$, wt%	$\lambda_{g,o}$, m	f_o	τ_y, MPa
AA6060-T4	0.638	$1.00\cdot10^{9}$	$6.54\cdot10^{-22}$	17.6
AA6060-T6x	0.370	4.19	$6.55\cdot10^{-10}$	45.6
AA6060-T6	0.149	$2.52\cdot10^{-6}$	$1.11\cdot10^{-3}$	61.7
AA6060-T7	0.0450	$6.34\cdot10^{-7}$	$7.52\cdot10^{-3}$	44.9
AA6060-O	0.645	$4.40\cdot10^{3}$	0.00	12.7
AA6082-T4	0.882	$1.25\cdot10^{12}$	$6.54\cdot10^{-22}$	42.9
AA6082-T6x	0.511	$1.25\cdot10^{9}$	$1.04\cdot10^{-20}$	68.6
AA6082-T6	0.265	$1.55\cdot10^{-6}$	$1.82\cdot10^{-3}$	88.2
AA6082-T7	0.189	$4.63\cdot10^{-7}$	$9.71\cdot10^{-3}$	67.3
AA6082-O	0.288	$2.50\cdot10^{-5}$	$8.55\cdot10^{-3}$	22.7

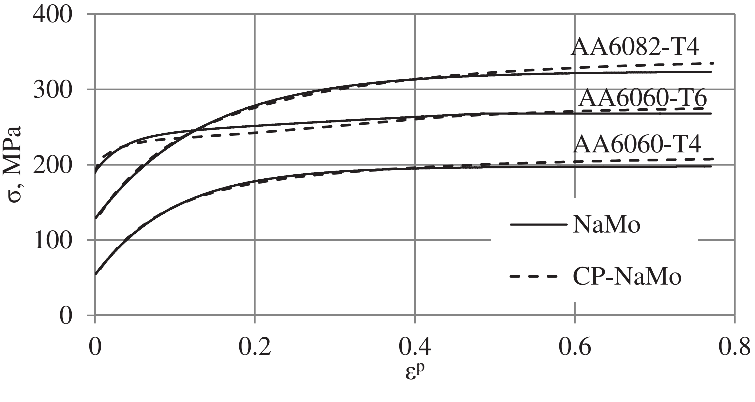

Figure 2: Equivalent stress-strain curves used in the calibration of CP-NaMo.

Table 5: The parameters of CP-NaMo.

Alloy/temper	k_2^{cp}	L, mm	ρ_g^{sat}, mm^{-2}
AA6060-T4	7.47	$4.72\cdot10^{13}$	$1.92\cdot10^{18}$
AA6060-T6x	11.68	$1.99\cdot10^{5}$	$4.49\cdot10^{7}$
AA6060-T6	24.59	$1.20\cdot10^{-1}$	$4.37\cdot10^{7}$
AA6060-T7	65.75	$3.01\cdot10^{-2}$	$2.58\cdot10^{7}$
AA6060-O	7.41	$2.09\cdot10^{8}$	$1.00\cdot10^{20}$
AA6082-T4	5.74	$5.91\cdot10^{16}$	$1.54\cdot10^{15}$
AA6082-T6x	8.98	$5.91\cdot10^{13}$	$9.47\cdot10^{9}$
AA6082-T6	15.36	$7.34\cdot10^{-2}$	$4.37\cdot10^{7}$
AA6082-T7	20.26	$2.20\cdot10^{-2}$	$2.74\cdot10^{7}$
AA6082-O	14.35	1.19	$5.77\cdot10^{5}$

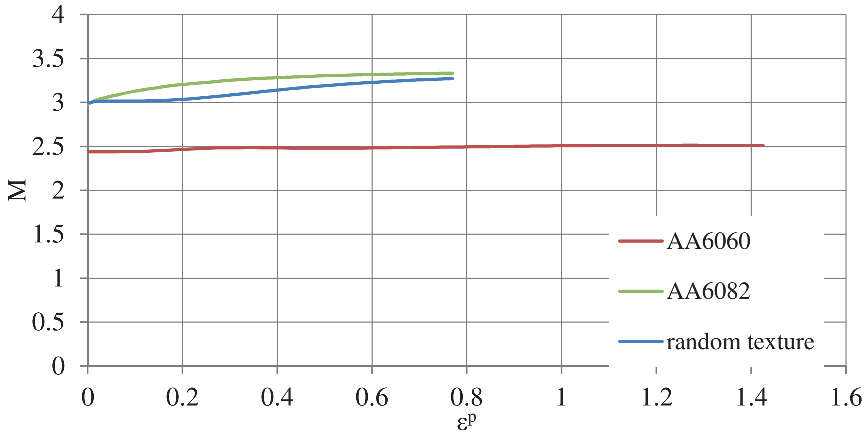

Figure 3: Evolution of Taylor factor M with equivalent plastic strain for different textures.

5. Results

The results of the optimization procedure described in Section 4 were used to find the work-hardening parameters of all the tested alloy/temper combinations. Then an equivalent stress-strain curve was obtained and compared to the experimental data and the basic NaMo. In this procedure the crystallographic texture of the alloy was used. NaMo is formulated in terms of slips and resolved shear stresses, and uses the Taylor factor $M = 3.1$ to find the global stress and strain. This approach is reasonable to use for alloys exhibiting random texture (and perhaps weak texture), but in the case of the present experiments the texture is not random. Instead of a constant Taylor factor we obtain a value relevant for the actual alloy and also its possible evolution, as shown in Section 4.

The equivalent stress-strain curves obtained from NaMo and CP-NaMo are compared with the experimental ones for all alloy/temper combinations in Figure 4 to Figure 8. These figures also present the work-hardening rate as a function of equivalent plastic strain and work-hardening. In these plots the work-hardening rate Θ is defined as

$$\Theta \equiv \frac{d\sigma}{d\varepsilon^p} \tag{41}$$

where σ and ε^p denote the equivalent stress and the equivalent plastic strain, respectively, with the extrusion direction used as reference direction.

With respect to the texture of the AA6060 alloy, the actual Taylor factor is much lower than for a random texture as seen in Figure 3. This gives a large difference between the stress-strain curves obtained by NaMo and CP-NaMo. A second difference between the model predictions may be seen e.g. for tempers T6 and T7. The work-hardening rate predicted by NaMo drops very abruptly when the geometrically necessary dislocations stop to accumulate. This behaviour is not observed in the experiments and is quite unphysical. In CP-NaMo saturation of the density of geometrically necessary dislocations leads to a smooth transition towards lower work-hardening rate. Out of the two alloys considered, the predictions for this alloy are the least accurate. The error is also not systematic for either of the two models. While the hardening rate is predicted with reasonable accuracy for all tempers, except temper O, the predicted stress level is, in general, deviating considerably. The initial work-hardening rate of the CP-NaMo prediction for this alloy is generally lower than the one of NaMo, most probably because of the Taylor factor difference.

The actual Taylor factor for the AA6082 alloy is quite close to the one for the random texture, and, thus, the difference between the stress-strain curves predicted by NaMo and the CP-NaMo is less pronounced. However the evolution of the Taylor factor is more noticeable than for the AA6060 alloy, which leads to better predictions of the work-hardening rate at large strains with CP-NaMo than NaMo. The predictions for the O temper fail again, but for the other tempers the predictions are fairly accurate. The initial yield stress deviates from the experimental one for tempers T6x and T7, but the predictions of the work-hardening are reasonably good for all tempers except the O temper.

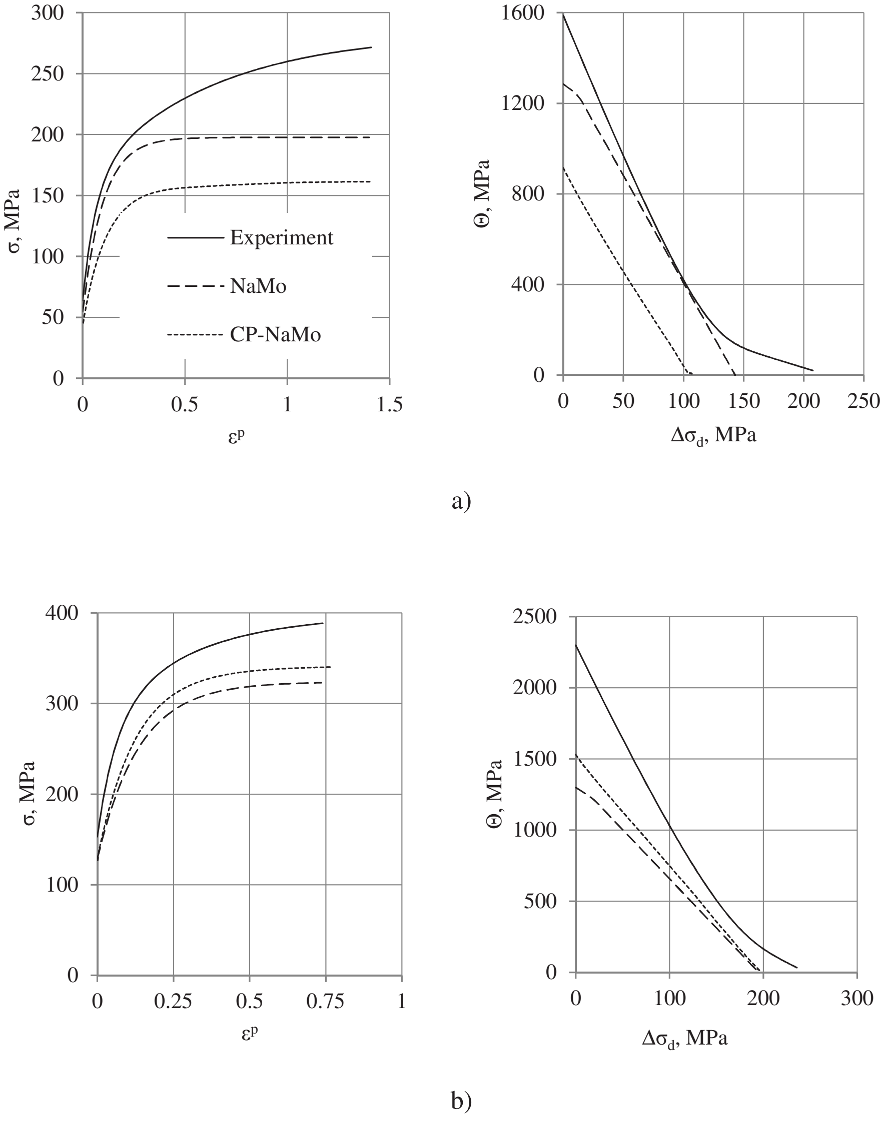

a)

b)

Figure 4: Comparison between NaMo, CP-NaMo and experimental data for the T4 temper of the two alloys in terms of the equivalent stress, σ, vs. the equivalent plastic strain, ε^p, and the work-hardening rate, Θ, vs. the work-hardening, $\Delta\sigma_d \equiv \sigma - \sigma_y$: a) AA6060-T4 and b) AA6082-T4

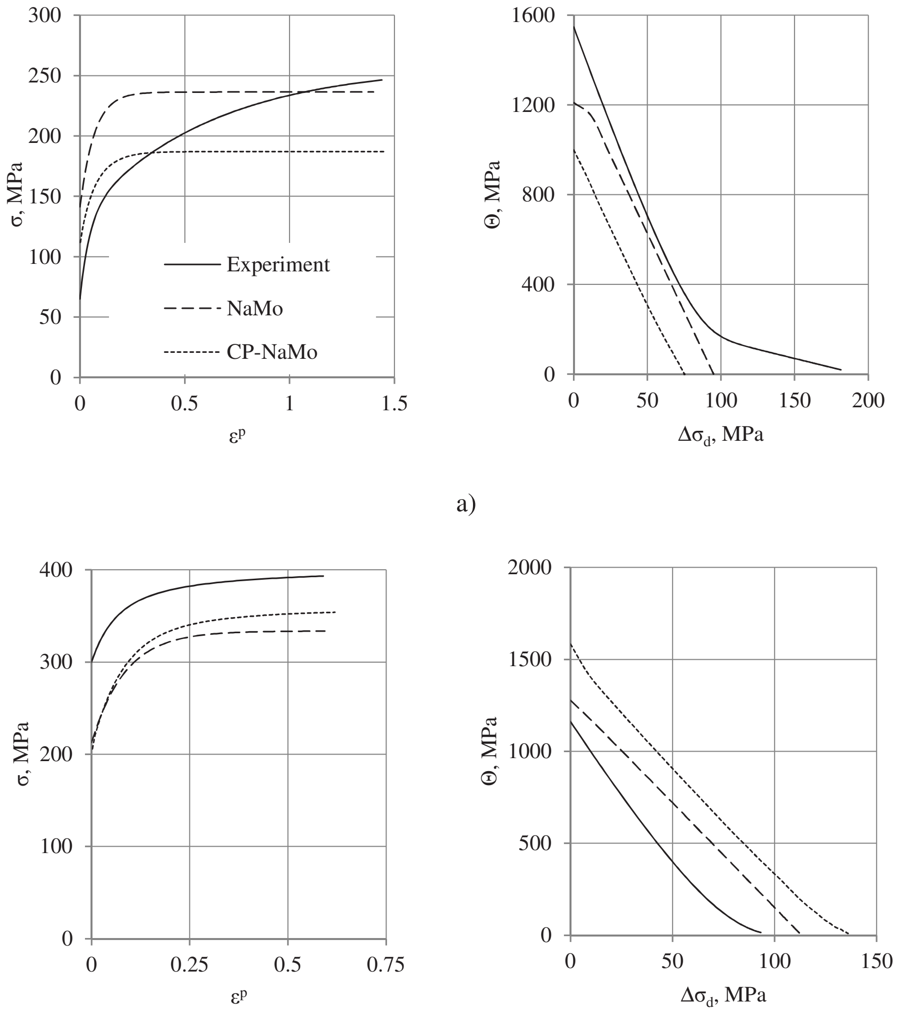

a)

b)

Figure 5: Comparison between NaMo, CP-NaMo and experimental data for the T6x temper of the alloys: a) AA6060-T6x and b) AA6082-T6x

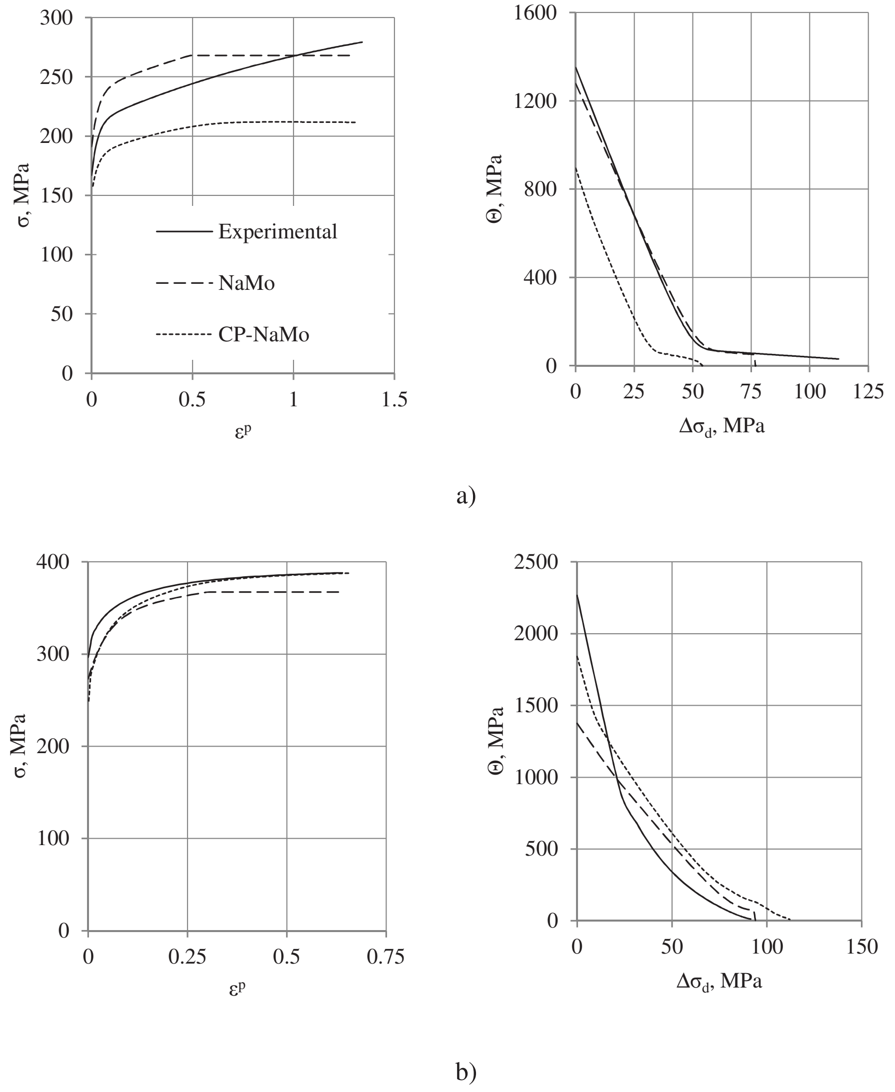

Figure 6: Comparison between NaMo, CP-NaMo and experimental data for the T6 temper of the alloys: a) AA6060-T6 and b) AA6082-T6

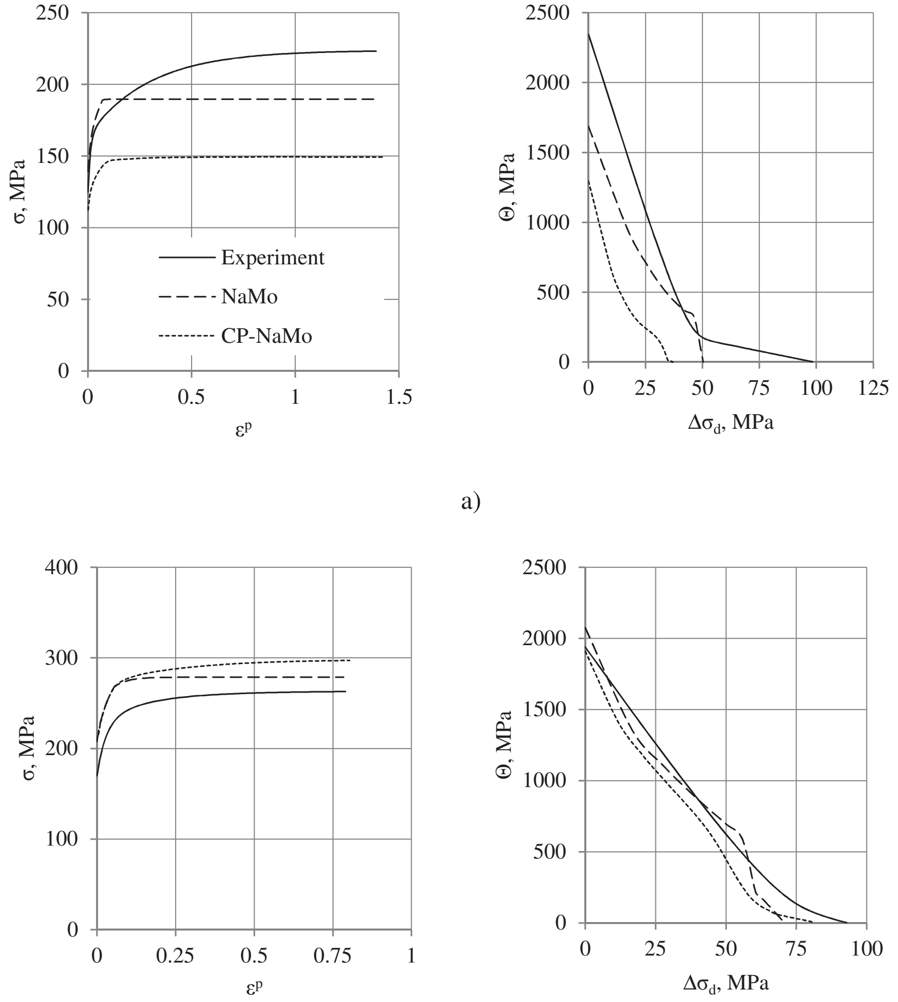

a)

b)

Figure 7: Comparison between NaMo, CP-NaMo and experimental data for the T7 temper of the alloys: a) AA6060-T7 and b) AA6082-T7

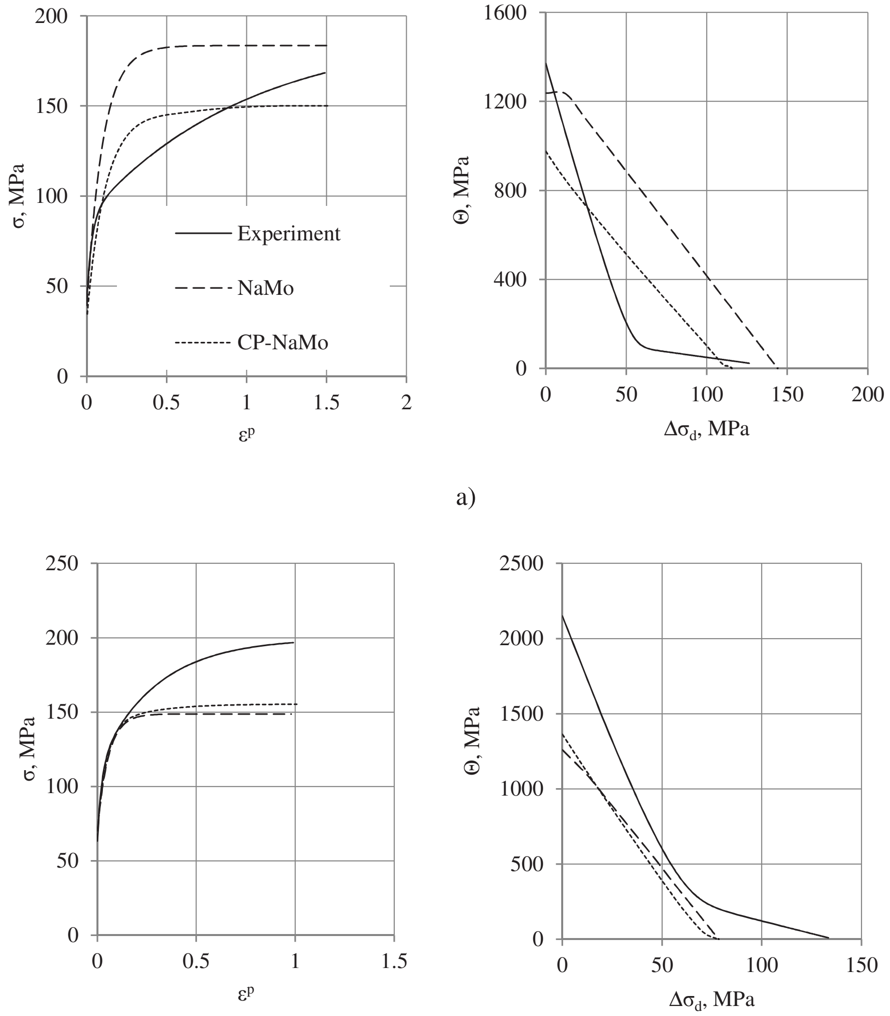

a)

b)

Figure 8: Comparison between NaMo, CP-NaMo and experimental data for the O temper of the alloys: a) AA6060-O and b) AA6082-O

6. Discussion and conclusions

CP-NaMo provided some improvements over the basic NaMo, mainly as a means to account for the texture influence in a better way than by just using a constant Taylor factor, but overall it did not improve the results, which are still dominated by the precipitation and yield strength model. They may be improved by including some other possible dislocation obstacles. For example the Cr dispersoids that are present in the AA6082 alloy may be added as another sort of non-shearable particles. In this alloy the yield strength was underestimated for all but the T7 temper, unlike the other alloy where the stress was either overestimated or underestimated without a preference.

The precipitation model provides input for both the yield stress and the work-hardening model, and is therefore crucial for the accuracy of the predictions of the resulting stress-strain curves. Accordingly, inaccurate predictions of the precipitate structure will inevitably lead to deviations between the predicted and measured initial yield strength as well as work-hardening. There are a number of simplified assumptions both for the nucleation and the growth and dissolution equations which may be violated and cause errors in the predictions.

Inaccurate predictions by the precipitation model is probably a major reason for the deviations between predictions and measurements for the O-temper condition since this particular heat treatment has not been comprehensively investigated and verified for NaMo previously. For the O-temper, the precipitation model predicts almost no formation of particles for the AA6060 alloy, which is an unrealistic result, since there will be precipitation of coarse particles taking place during ageing at 350^{o}C [43], which is not captured by the nucleation law. A more accurate description of the nucleation would have changed the complete stress-strain curve through the introduction of coarse non-shearable Orowan particles and a corresponding increase in the density of geometrically necessary dislocations as well as an associated lowering of the solid solution level, leading to increased dynamic recovery and a decreased density of statistically stored dislocations.

The precipitation model is also a main reason for the deviations between NaMo and measurements for the underaged T6x temper condition. This is a demanding ageing heat treatment to predict since the nucleation rate may be very low for a certain time period at the start of the ageing, known as the “incubation time”. Since the incubation time is not included in the nucleation laws of the precipitation model, NaMo may be somewhat inaccurate for the early stages of ageing. For the present materials, the low composition alloy AA6060 exhibits a distinct incubation period, where the macroscopic yield strength remains almost constant, and where NaMo overestimates the precipitation and the corresponding yield stress significantly, as can be seen in Figure 5 (a). This is in contrast to the AA6082 alloy, which due to its higher alloy content, does not show a pronounced incubation period and for which NaMo tends to underestimate the initial yield stress, as can be seen in Figure 5 (b).

The numerical implementation of CP-NaMo could be made more advanced and a finite element model of a polycrystal with realistic grain shapes modelled with many elements could be used, but the increase of the computation time would be dramatic, while the accuracy of stress predictions would most probably be minor.

A common trend may be noticed for the two alloys. Whenever the strains reach high values, the hardening rate of the experimental stress-strain curve shows two distinct regions. It is especially visible on the Θ - $\Delta\sigma_d$ plots. The work-hardening rate Θ decreases linearly until some point and then the slope changes and starts decreasing at a slower rate. This is certainly a consequence of the two-term Voce hardening rule, which was used to extract the equivalent stress from the after-necking regime of the test samples. However, the two-term Voce rule fits very well to the experimental data, and much better than a one-term Voce rule. The first term describes the initial hardening and saturates quickly, while the second term describes the slower saturating hardening at higher strains. Indeed, real alloys exhibit non-zero work-hardening also at the later deformation stages. It is denoted Stage IV hardening, it has a constant rate and is quite low, yet noticeable. The NaMo and CP-NaMo on the other hand are an approximation for a one-term Voce rule and therefore cannot properly describe hardening at higher strains. It should be noted that the particle-induced hardening is in a way the second term, but it behaves differently than the second term displayed by the experimental data. It saturates at relatively small strains and gives no contribution in the later stages of deformation. For example in [44] the Stage IV hardening is studied experimentally and a model is proposed, which accounts for it. This model connects Stage IV hardening with the dislocation substructure and adds a term to Equation (24) which starts to dominate the hardening rate at large strains. Some similar approach could be used for NaMo.

Out of 10 alloy/temper combinations, NaMo and CP-NaMo failed to predict the behaviour of 5, succeeded for 2 and made a mistake in the initial yield stress for 3. One should remember that these results were obtained without any reference to the actual tensile tests performed on these specimens, just using the chemical composition, the thermal history and texture measurements. Even if all the difficulties encountered in explaining the plastic behaviour of aluminium alloys based on microstructure are considered, this result is not satisfactory and leaves a lot of room for improvement in future work.

References

[1] O. R. Myhr, Ø. Grong, and K. O. Pedersen, "A Combined Precipitation, Yield Strength, and Work Hardening Model for Al-Mg-Si Alloys," *Metallurgical and Materials Transactions A,* vol. 41, pp. 2276-2289, 2010.

[2] G. I. Taylor and C. F. Elam, "Bakerian lecture. the distortion of an aluminium crystal during a tensile test," *Proceedings of the Royal Society of London. Series A,* vol. 102, pp. 643-667, 1923.

[3] G. Taylor and C. Elam, "The plastic extension and fracture of aluminium crystals," *Proceedings of the Royal Society of London. Series A, Containing Papers of a Mathematical and Physical Character,* vol. 108, pp. 28-51, 1925.

[4] F. Grytten, B. Holmedal, O. S. Hopperstad, and T. Børvik, "Evaluation of identification methods for YLD2004-18p," *International Journal of Plasticity,* vol. 24, pp. 2248-2277, 2008.

[5] C. Beradai, M. Berveiller, and P. Lipinski, "Plasticity of metallic polycrystals under complex loading paths," *International Journal of Plasticity,* vol. 3, pp. 143-162, 1987.

[6] P. Zattarin, P. Lipinski, and A. Rosochowski, "Numerical study of the influence of microstructure on subsequent yield surfaces of polycrystalline materials," *International Journal of Mechanical Sciences,* vol. 46, pp. 1377-1398, 2004.

[7] A. Saai, S. Dumoulin, and O. Hopperstad, "Influence of Texture and Grain Shape on the Yield Surface in Aluminium Sheet Material Subjected to Large Deformations," in *AIP Conference Proceedings*, 2011, p. 85.

[8] F. Barlat, "Crystallographic texture, anisotropic yield surfaces and forming limits of sheet metals," *Materials Science and Engineering,* vol. 91, pp. 55-72, 1987.

[9] F. Barlat and O. Richmond, "Prediction of tricomponent plane stress yield surfaces and associated flow and failure behavior of strongly textured FCC polycrystalline sheets," *Materials Science and Engineering,* vol. 95, pp. 15-29, 1987.

[10] S.-H. Choi, J. Brem, F. Barlat, and K. Oh, "Macroscopic anisotropy in AA5019A sheets," *Acta Materialia,* vol. 48, pp. 1853-1863, 2000.

[11] G. I. Taylor, "The Mechanism of Plastic Deformation of Crystals. Part I. Theoretical," *Proceedings of the Royal Society of London. Series A,* vol. 145, pp. 362-387, July 2, 1934 1934.

[12] E. Orowan, "Mechanical strength properties and real structure of crystals," *Zeitschrift für Physik,* vol. 89, pp. 327-343, 1934.

[13] U. Kocks, "Laws for work-hardening and low-temperature creep," *Journal of Engineering Materials and Technology,* vol. 98, p. 76, 1976.

[14] H. Mecking and U. Kocks, "Kinetics of flow and strain-hardening," *Acta Metallurgica,* vol. 29, pp. 1865-1875, 1981.

[15] O. Bouaziz, D. Barbier, J. Embury, and G. Badinier, "An extension of the Kocks–Mecking model of work hardening to include kinematic hardening and its application to solutes in ferrite," *Philosophical Magazine,* vol. 93, pp. 247-255, 2013.

[16] A. Acharya and A. Beaudoin, "Grain-size effect in viscoplastic polycrystals at moderate strains," *Journal of the Mechanics and Physics of Solids,* vol. 48, pp. 2213-2230, 2000.

[17] J. Li and A. Soh, "Modeling of the plastic deformation of nanostructured materials with grain size gradient," *International Journal of Plasticity,* 2012.

[18] D. Kuhlmann-Wilsdorf, "Theory of workhardening 1934-1984," *Metallurgical Transactions A,* vol. 16, pp. 2091-2108, 1985.

[19] S. C. Baik, Y. Estrin, H. S. Kim, and R. J. Hellmig, "Dislocation density-based modeling of deformation behavior of aluminium under equal channel angular pressing," *Materials Science and Engineering: A,* vol. 351, pp. 86-97, 2003.

[20] K. G. Russell and M. Ashby, "Slip in aluminum crystals containing strong, plate-like particles," *Acta Metallurgica,* vol. 18, pp. 891-901, 1970.

[21] M. Ashby, "The deformation of plastically non-homogeneous materials," *Philosophical Magazine,* vol. 21, pp. 399-424, 1970.

[22] Y. Estrin and H. Mecking, "A unified phenomenological description of work hardening and creep based on one-parameter models," *Acta Metallurgica,* vol. 32, pp. 57-70, 1984.

[23] Y. Estrin, "Dislocation theory based constitutive modelling: foundations and applications," *Journal of Materials Processing Technology,* vol. 80, pp. 33-39, 1998.

[24] J. H. Kim, M.-G. Lee, D. Kim, and R. Wagoner, "Micromechanics-based strain hardening model in consideration of dislocation-precipitate interactions," *Metals and Materials International,* vol. 17, pp. 291-300, 2011.

[25] L. Cheng, W. Poole, J. Embury, and D. Lloyd, "The influence of precipitation on the work-hardening behavior of the aluminum alloys AA6111 and AA7030," *Metallurgical and Materials Transactions A,* vol. 34, pp. 2473-2481, 2003.

[26] F. Roters, D. Raabe, and G. Gottstein, "Work hardening in heterogeneous alloys—a microstructural approach based on three internal state variables," *Acta Materialia,* vol. 48, pp. 4181-4189, 2000.

[27] C. Teodosiu and J. L. Raphanel, "Finite element simulations of large elastoplastic deformations of multicrystals," in *Proceedings of the international seminar MECAMAT91*, 1991, pp. 153-168.

[28] L. Tabourot, M. Fivel, and E. Rauch, "Generalised constitutive laws for fcc single crystals," *Materials Science and Engineering: A,* vol. 234, pp. 639-642, 1997.

[29] D. Cédat, O. Fandeur, C. Rey, and D. Raabe, "Polycrystal model of the mechanical behavior of a Mo–TiC 30 vol.% metal–ceramic composite using a three-dimensional microstructure map obtained by dual beam focused ion beam scanning electron microscopy," *Acta Materialia,* vol. 60, pp. 1623-1632, 2012.

[30] M. Shiekhelsouk, V. Favier, K. Inal, and M. Cherkaoui, "Modelling the behaviour of polycrystalline austenitic steel with twinning-induced plasticity effect," *International Journal of Plasticity,* vol. 25, pp. 105-133, 2009.

[31] A. Simar, Y. Bréchet, B. De Meester, A. Denquin, and T. Pardoen, "Microstructure, local and global mechanical properties of friction stir welds in aluminium alloy 6005A-T6," *Materials Science and Engineering: A,* vol. 486, pp. 85-95, 2008.

[32] O. Myhr and Ø. Grong, "Modelling of non-isothermal transformations in alloys containing a particle distribution," *Acta Materialia,* vol. 48, pp. 1605-1615, 2000.

[33] O. Myhr, Ø. Grong, and S. Andersen, "Modelling of the age hardening behaviour of Al–Mg–Si alloys," *Acta Materialia,* vol. 49, pp. 65-75, 2001.

[34] O. Myhr, Ø. Grong, H. Fjaer, and C. Marioara, "Modelling of the microstructure and strength evolution in Al–Mg–Si alloys during multistage thermal processing," *Acta Materialia,* vol. 52, pp. 4997-5008, 2004.

[35] N. Anjabin, A. Karimi Taheri, and H. Kim, "Crystal plasticity modeling of the effect of precipitate states on the work hardening and plastic anisotropy in an Al–Mg–Si alloy," *Computational Materials Science,* vol. 83, pp. 78-85, 2014.

[36] J. Johnsen, J. Holmen, O. Myhr, O. Hopperstad, and T. Børvik, "A nano-scale material model applied in finite element analysis of aluminium plates under impact loading," *Computational Materials Science,* vol. 79, pp. 724-735, 2013.

[37] M. Khadyko, S. Dumoulin, T. Børvik, and O. Hopperstad, "An experimental-numerical method to determine the work-hardening of anisotropic ductile materials at large strains," *International Journal of Mechanical Sciences,* vol. 88, pp. 25-36, 2014.

[38] J. Friedel and L. Vassamillet, *Dislocations* vol. 3: Pergamon Press Oxford, 1964.

[39] A. Deschamps and Y. Brechet, "Influence of predeformation and ageing of an Al–Zn–Mg alloy—II. Modeling of precipitation kinetics and yield stress," *Acta Materialia,* vol. 47, pp. 293-305, 1998.

[40] S. Li, O. Engler, and P. Van Houtte, "Plastic anisotropy and texture evolution during tensile testing of extruded aluminium profiles," *Modelling and Simulation in Materials Science and Engineering,* vol. 13, pp. 783-795, 2005.

[41] M. Grujicic and S. Batchu, "Crystal plasticity analysis of earing in deep-drawn OFHC copper cups," *Journal of Materials Science,* vol. 37, pp. 753-764, 2002.

[42] N. Stander, W. Roux, T. Goel, T. Eggleston, and K. Craig, "LS-OPT user's manual," *Livermore software technology corporation,* 2008.

[43] B. Milkereit, N. Wanderka, C. Schick, and O. Kessler, "Continuous cooling precipitation diagrams of Al–Mg–Si alloys," *Materials Science and Engineering: A,* vol. 550, pp. 87-96, 2012.

[44] Ø. Ryen, H. I. Laukli, B. Holmedal, and E. Nes, "Large strain work hardening of aluminum alloys and the effect of mg in solid solution," *Metallurgical and Materials Transactions A,* vol. 37, pp. 2007-2013, 2006.

Article 3

M. Khadyko, S. Dumoulin, G. Cailletaud, O.S. Hopperstad

Latent hardening and plastic anisotropy evolution in AA6060 aluminium alloy.

To be submitted for journal publication.

Latent hardening and plastic anisotropy evolution in AA6060 aluminium alloy.

M. Khadyko[1,*], S. Dumoulin[2], G. Cailletaud[3] and O.S. Hopperstad[1]

[1] *Structural Impact Laboratory (SIMLab), Centre for Research-based Innovation, Department of Structural Engineering, Norwegian University of Science and Technology, NO-7491 Trondheim, Norway*

[2] *SINTEF Materials & Chemistry, NO-7465 Trondheim, Norway*

[3] *MINES ParisTech, Centre des Matériaux, CNRS UMR 7633, BP 87 91003 Evry Cedex, France*

Abstract

The crystal plasticity theory predicts that hardening on a particular slip system and its corresponding work-hardening rate will depend on the slip activity on both this slip system and all others. The exact form of this dependence is defined by the latent hardening description in form of the latent hardening matrix or the interaction matrix. It has been assumed that this matrix describes the relative strength of various dislocation interactions and is therefore the same for a wide range of alloys with the same lattice structure. Different methods have been used to estimate the values of the interaction matrix components: one is experimental and uses strain-path changes; another simulates the dislocations dynamics in a crystal directly at the microscale and estimates the strength of the forming locks. In this work, the influence of the interaction matrix (and thus latent hardening) on the development of plastic anisotropy is studied. An extruded AA6060 alloy is tested in uniaxial tension in different directions and the anisotropy of the alloy is found to evolve considerably throughout the deformation. A crystal plasticity model is used to simulate the experimental tests, and the use of different interaction matrices is evaluated. A noticeable influence on the predicted evolution of plastic anisotropy as well as the stress-strain field and slip inside the constituent grains is found.

Keywords: crystal plasticity; plastic anisotropy; latent hardening; finite element method; dislocations; interaction matrix.

---

[*] Corresponding author: Mikhail Khadyko (mikhail.khadyko@ntnu.no)

1 Introduction

The mechanisms of plastic deformation of metallic materials at the microscale can be described by the crystal plasticity theory. Metals and alloys are crystalline materials and the basic deformation mechanism in the plastic regime is represented by slip on specific crystallographic planes and directions denoted slip systems. The kinematics of this type of plastic deformation was first described by Taylor in [1, 2]. The plastic deformation accumulating on the slip systems leads to an increase in the resolved shear stress, i.e. the material work-hardens. The work-hardening in a crystal is particularly complex, because the slip resistance increases not only on the active but also on the non-active slip systems. The work-hardening of each slip system is therefore divided into self and latent hardening. The influence of latent hardening on the plastic deformation of a single crystal was observed already in [2], where the slip systems were activated or remained inactive depending not only on the orientation of the crystal but also on its deformation history. The response of a polycrystal depends on the properties of the constituent crystals and will also be affected by latent hardening. Therefore, predicting the properties of a polycrystal depends, among other things, on a good prediction of the latent hardening. This problem has been approached in different ways. The basic assumption that all non-active systems harden similarly was used in phenomenological models [3-5], where the self and latent hardening were described using two independent components. A more complex approach within the phenomenological framework was used in [6].

In [7] Taylor proposed a relationship between the resolved shear stress on the slip systems and the dislocation density in the crystal. It was combined with an equation describing the evolution of the dislocation density in [8] and [9], formulated for global stress and strain in the material. Later in [10] it was modified by accounting for dislocation densities on different slip systems. In this model, the dislocations interact with each other and get pinned on each other, forming different types of dislocation locks [11]. Depending on the relative position of the slip systems, these locks are divided into coplanar, collinear, Hirth (normal), glissile and sessile (Lomer-Cottrel) types. The relative strength of these locks combined together with the self-hardening, constitutes an interaction matrix with 6 independent components. This matrix in principle defines both the flow stress (i.e. the stress which is necessary to overcome the lock and to start the dislocation movement and plastic deformation) and the hardening rate – the stronger the lock, the more easily the dislocations get caught into it, contributing to the work-hardening. Teodosiu [10] used a very simple interaction matrix, based on the assumption that the self-hardening was negligible compared to latent hardening, which was the same on all slip systems (a similar approach was used in [12] for modelling the plastic behaviour of copper).

The interaction between different slip systems and latent hardening were studied experimentally in [13, 14] and [15] on aluminium single crystals and in [16] on copper. The method used consisted in deforming the specimen in order to activate some specific slip systems, followed by a change in deformation path and then measuring the resistance on the other slip systems. The results were not very accurate or consistent with each other, probably due to the complexity of the experimental procedure. However, some general conclusions were made: the interaction matrix was reduced to 4 independent components, corresponding to different types of locks and these components were arranged from strongest to weakest. Coplanar, collinear and Hirth types were united under one value. These results were used in [17-20]. The model used in the latter treated the interaction matrix for flow stress and hardening differently. It was assumed that the flow stress is dominated by the averaged short-range interactions between dislocations and the interaction matrix in the strength expression was reduced to either one common coefficient or two – for self and latent hardening.

A new approach, which uses advances in computational mechanics, has been used to find the values of the interaction matrix components. It uses dislocation dynamics simulations, where the dislocations in a deforming crystal are modelled explicitly as moving, interacting linear defects in the lattice. In [21-23] the components of the interaction matrix were obtained by this method. The results were not consistent with [13]: the collinear interactions were shown to be much stronger than other types and merging coplanar, collinear and Hirth type interactions into one matrix component was shown to be unreasonable. Though these results were obtained under some strict assumptions (small strains, elastic constants and other material parameters for pure copper) they provide a way to estimate the interaction matrix for any face centred-cubic (FCC) metal.

In [24] the strain-path change approach was used again to try to find the interaction matrix of an FCC material in the light of these new results. Copper specimens were subjected to strain-path change (from pure shear to uniaxial tension) and the obtained stress-strain data were used to calibrate a model similar to the one proposed by Teodosiu [10, 25] and a phenomenological model relying on local hardening.

The crystal plasticity models have been known and used in the modelling of single crystals and polycrystals for a long time, thus the latent hardening has been also studied and a large volume of experimental results has been accumulated. However, what the actual latent hardening matrix (or interaction matrix) for any given material is still remains an open question. The results obtained with different experimental and numerical procedures are quite different from each other. On the other hand, the obtained results are not tested on different kinds of loading conditions and materials. As stated above, the latent hardening is an important factor in the plastic deformation of a crystal and its influence should probably express itself in a variety of ways, not limited to the case of changing strain-paths.

In the present work, an experimental study is performed for an extruded aluminium alloy AA6060 in temper T4 with strong cube texture. Tensile tests are carried out in different material directions of the flat profile using cylindrical samples. The average true stress and the average true strain within the minimum cross-section are measured to failure. The experiments show that the anisotropy in flow stress and plastic flow is not constant but evolves considerably throughout the whole deformation process. To evaluate the influence of the interaction matrix (or latent hardening) on the predicted plastic anisotropy, these tests are modelled using the crystal plasticity finite element method (CP-FEM) with different interaction matrices and the predicted global response is compared to the experimental one. The local response at the level of the slip systems obtained in the CP-FEM simulations with different interaction matrices is also discussed.

The article is organised as follows. The mechanical tests on the extruded aluminium alloy AA6060 in temper T4 are described in Section 2. A review of the adopted crystal plasticity models is given in Section 3, while the finite element modelling is described in Section 4. The procedure of the calibration of the crystal plasticity models is presented in Section 5 using corrected data from the mechanical tests. Section 6 presents the results from the experimental and numerical studies and discusses the findings. Conclusions are provided in Section 7.

2 Experimental results

2.1 Choice of the material and its microstructure

The material, which was used as a model material, is the AA6060 aluminium alloy in T4 temper, delivered as an extruded flat profile with 10 mm thickness and 90 mm width. There are several reasons for choosing this alloy and heat treatment for this study. It is a recrystallized material with large equiaxed grains (see Figure 1), so that the influence of grain morphology on the material properties is small. The material is very ductile, so that the stress-strain curve for strains up to 140% may be obtained. The T4 temper corresponds to heating the material at 540°C in salt bath for 15 min, followed by water quenching and storage at room temperature for prolonged time. This makes sure that Mg and Si, which are the primary alloying elements, are present in the alloy in form of solid solution and GP-zones/clusters, while precipitate particles are not formed during natural ageing. Depending on their size, the precipitates may act as a source for geometrically necessary dislocations during plastic deformation, in addition to the statistically stored dislocations [26], which cannot be described by the work-hardening rules adopted in this work.

The chemical composition of the alloy is given in Table 1. The material was analysed in the scanning electron microscope using electron back-scattering diffraction (EBSD) and EDAX TSL OIM software to provide grain morphology and texture. The grain morphology and the Orientation Distribution Function (ODF) are presented in Figure 1 and Figure 2, respectively. The EBSD measurements were carried out in the plane defined by the extrusion and normal directions of the profile, using 10 μm steps on a square grid. The ODF was calculated from the pole figures in the EDAX TSL OIM software using a harmonic series expansion and triclinic sample symmetry [27]. The total number of measured orientations (or grains) in the sample is 2611. The main component of the texture is a strong cube texture with a minor Goss component. Both the texture and the grain morphology are typical for recrystallized alloys.

Table 1: Chemical composition of the alloy in wt%.

Fe	Si	Mg	Mn	Cr	Cu	Zn	Ti
0.193	0.422	0.468	0.015	0.000	0.002	0.005	0.008

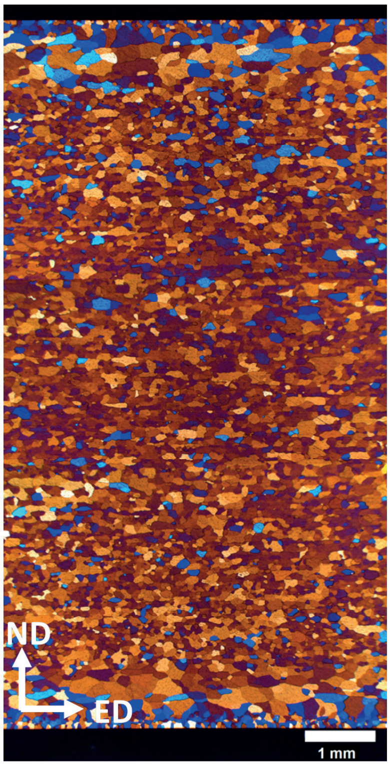

Figure 1: Grain morphology of the AA6060 alloy.

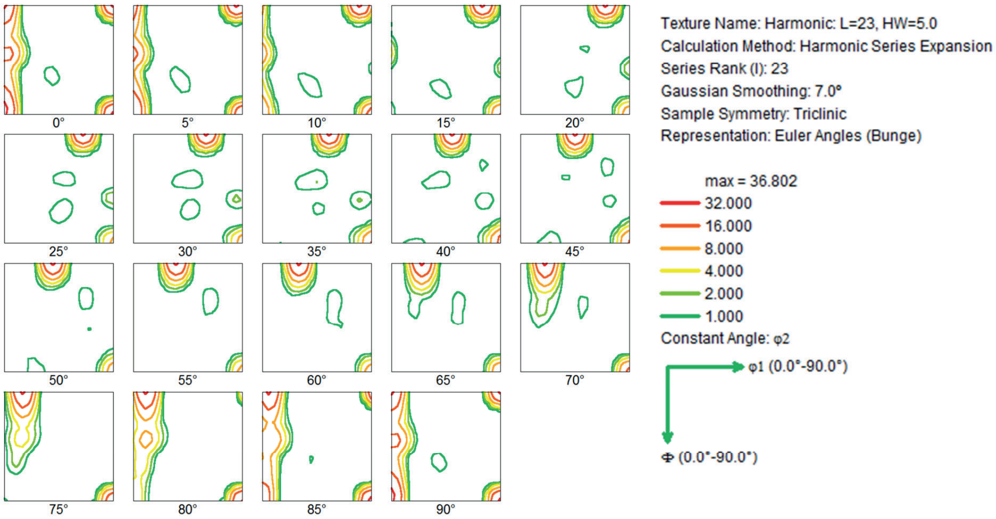

Texture Name: Harmonic: L=23, HW=5.0
Calculation Method: Harmonic Series Expansion
Series Rank (l): 23
Gaussian Smoothing: 7.0°
Sample Symmetry: Triclinic
Representation: Euler Angles (Bunge)

Figure 2: Orientation Distribution Function (ODF) for the AA6060 alloy

2.2 Mechanical tests

The tensile specimens were obtained from the extruded flat profile at different angles θ to the extrusion direction with 22.5° interval (i.e., θ equals 0°, 22.5°, 45°, 67.5° and 90°). Three specimens were tested for each direction, giving a total of 15 tests. The specimen geometry is shown in Figure 3. A rectangular coordinate system xyz is defined such that the x-axis is in the transverse direction and the y-axis is in the longitudinal direction of the specimen, while the z-axis is always in the thickness direction of the extruded profile. Two laser gauges were measuring the diameters of the specimens in the width and thickness directions at high frequency during the tests, so the minimum diameters before and after necking are known with high accuracy. If we denote the measured diameters D_x and D_z, and assume that the deformed cross section is elliptical in shape (which is a reasonable assumption for an orthotropic material), then we may find the current cross-section area as

$$A = \frac{\pi}{4} D_x D_z \tag{1}$$

The true (Cauchy) stress is found as

$$\sigma_y = \frac{F}{A} \tag{2}$$

where F is the measured tensile force. If we also assume plastic incompressibility, the logarithmic strains may be expressed as

$$\varepsilon_x = \ln\left(\frac{D_x}{D_0}\right), \quad \varepsilon_y = \ln\left(\frac{A_0}{A}\right), \quad \varepsilon_z = \ln\left(\frac{D_z}{D_0}\right) \tag{3}$$

where D_0 and $A_0 = \frac{\pi}{4} D_0^2$ are the initial diameter and cross-section area of the specimen, respectively. The logarithmic strain is also used further in this work. The strain ratio is defined as

$$r_y = \frac{d\varepsilon_x}{d\varepsilon_z} \tag{4}$$

which equals unity for isotropic materials.

The results from the tensile tests are presented in Figure 4 and Figure 5. Figure 4 a) presents representative true stress-strain curves to failure, whereas the scatter between parallel tests is displayed in Figure 4 b). These results clearly demonstrate the anisotropic work-hardening of the AA6060 alloy. Figure 5 a) presents the plastic flow in terms of the strain in the transverse direction of the tensile specimen as a function of the thickness strain. The thickness direction of the specimen always coincides with the thickness direction of the profile, while the width direction of the specimen is rotating and coincides with the width direction of the profile for the 0° orientation and with the extrusion direction for the 90° orientation. The strain ratio as function of tensile strain and tensile direction is plotted in Figure 5 b). The anisotropy of the plastic flow is initially very strong but diminishes with tensile straining due to texture evolution. Since the results for the three specimens of each orientation are very close to each other, a representative curve for each orientation is shown and used further.

Table 2: Interaction matrix for FCC crystals as defined by Franciosi [15].

	A2	A3	A6	B2	B4	B5	C1	C3	C5	D1	D4	D6
A2	g_0	g_1	g_1	g_3	g_4	g_4	g_2	g_4	g_5	g_2	g_5	g_4
A3		g_0	g_1	g_4	g_2	g_5	g_4	g_3	g_4	g_5	g_2	g_4
A6			g_0	g_5	g_5	g_2	g_5	g_4	g_2	g_4	g_4	g_3
B2				g_0	g_1	g_1	g_2	g_5	g_4	g_2	g_4	g_5
B4					g_0	g_1	g_5	g_2	g_4	g_4	g_3	g_4
B5						g_0	g_4	g_4	g_3	g_5	g_4	g_2
C1							g_0	g_1	g_1	g_3	g_4	g_4
C3								g_0	g_1	g_4	g_2	g_5
C5									g_0	g_4	g_5	g_2
D1										g_0	g_1	g_1
D4											g_0	g_1
D6												g_0

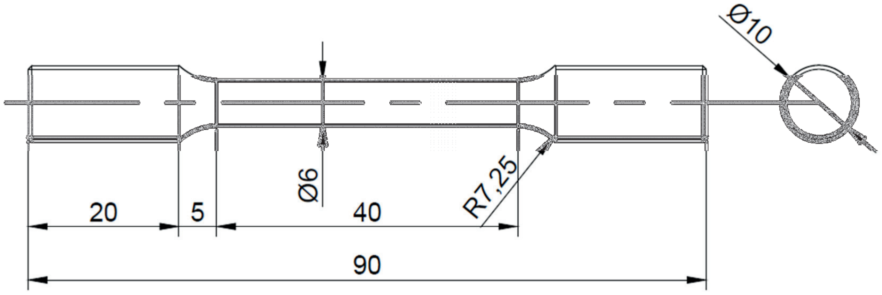

Figure 3: Uniaxial tensile test specimen geometry.

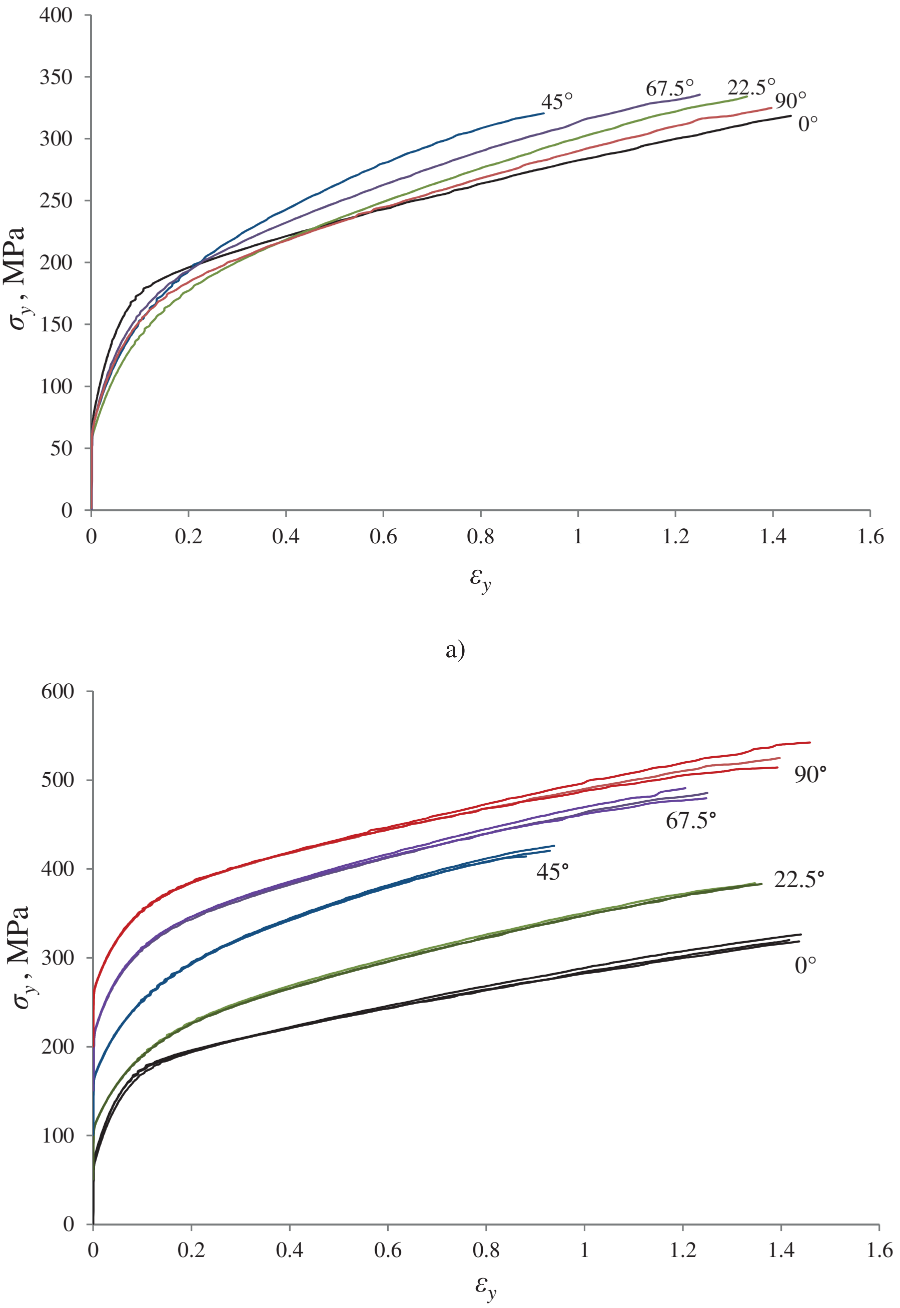

a)

b)

Figure 4: True stress σ_y versus logarithmic strain ε_y curves for specimens with different orientations θ: a) representative curves, b) curves from all three specimens of each orientation with a 50 MPa shift between the orientations.

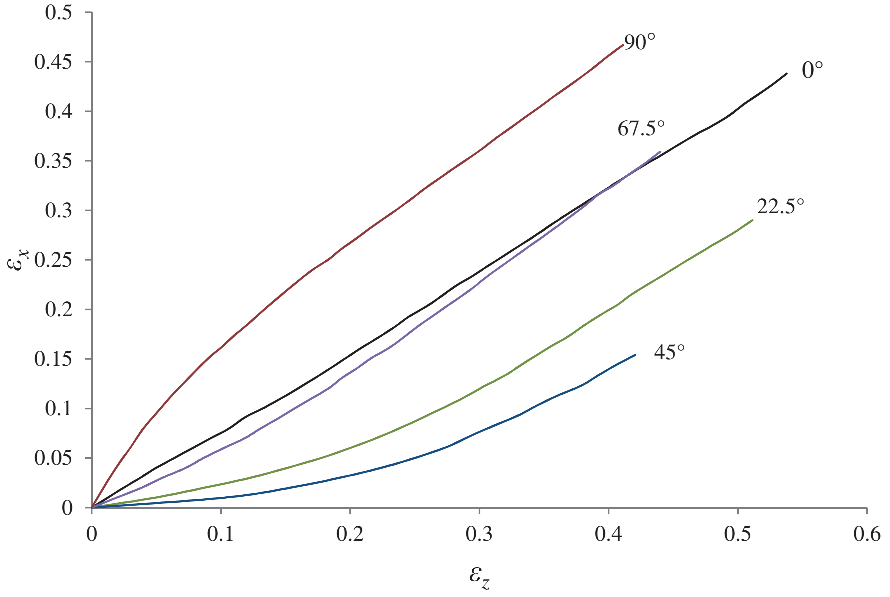

a)

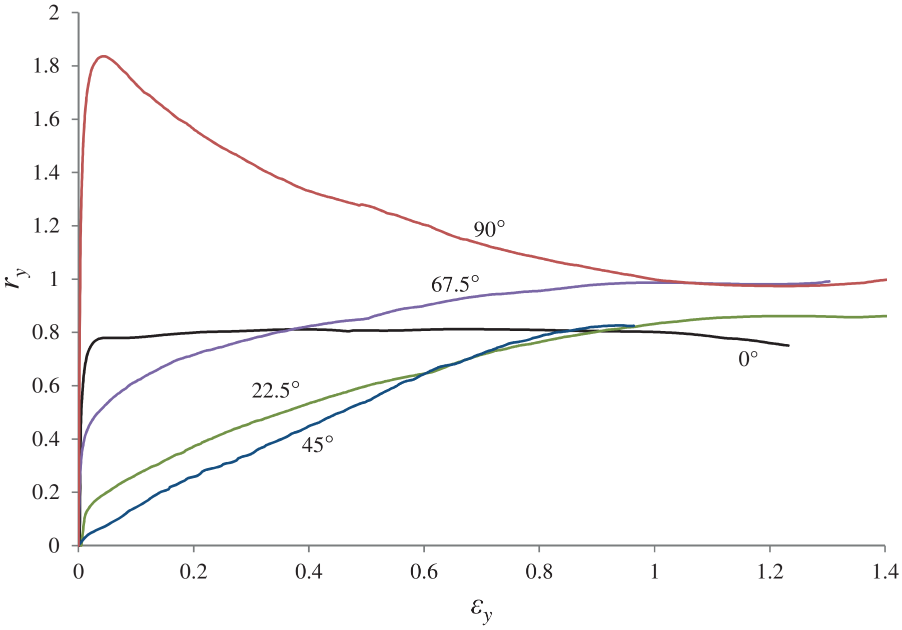

b)

Figure 5: a) Logarithmic width strain ε_x versus logarithmic thickness strain ε_z for the specimens in different directions and b) the strain ratio r_y versus longitudinal logarithmic strain ε_y.

3 Constitutive modelling

3.1 Single crystal kinematics and kinetics

The finite deformation formulation is used. The total deformation of the crystal from the initial configuration Ω_0 to the current configuration Ω is mapped by the deformation gradient tensor $\mathbf{F}$, which may be multiplicatively decomposed into elastic and plastic parts [28]

$$\mathbf{F} = \mathbf{F}^e \mathbf{F}^p \tag{5}$$

where $\mathbf{F}^p$ maps the transformation between the initial configuration Ω_0 and the intermediate plastically deformed configuration $\bar{\Omega}$, and $\mathbf{F}^e$ maps the transformation from $\bar{\Omega}$ to Ω. Thus, $\mathbf{F}^p$ accounts for plastic slip and $\mathbf{F}^e$ accounts for elastic deformations and rigid body rotations. The slip systems in the initial and intermediate configurations are defined by vectors $\mathbf{m}_0^\alpha$ and $\mathbf{n}_0^\alpha$ — the slip direction and slip plane normal, respectively. These vectors are connected to the lattice and remain unchanged by $\mathbf{F}^p$, while $\mathbf{F}^e$ transforms them into current configuration vectors $\mathbf{m}^\alpha$ and $\mathbf{n}^\alpha$. Here α identifies the relevant slip system. The plastic velocity gradient in the intermediate configuration $\bar{\mathbf{L}}^p$ is defined as

$$\bar{\mathbf{L}}^p = \dot{\mathbf{F}}^p \left(\mathbf{F}^p\right)^{-1} = \sum_{\alpha=1}^{n} \dot{\gamma}^\alpha \mathbf{m}_0^\alpha \otimes \mathbf{n}_0^\alpha \tag{6}$$

where $\dot{\gamma}^\alpha$ is the slip rate on slip system α and n is the total number of slip systems (12 in the case of an FCC lattice). The elastic Green strain tensor $\bar{\mathbf{E}}^e$ in the intermediate configuration is defined as

$$\bar{\mathbf{E}}^e = \frac{1}{2}\left(\bar{\mathbf{C}}^e - \mathbf{I}\right), \quad \bar{\mathbf{C}}^e = \left(\mathbf{F}^e\right)^T \mathbf{F}^e \tag{7}$$

where $\bar{\mathbf{C}}^e$ is the elastic right Cauchy-Green deformation tensor and $\mathbf{I}$ is the unity tensor. The second Piola-Kirchhoff stress tensor $\bar{\mathbf{S}}$ in the intermediate configuration may be found from the Cauchy stress tensor $\boldsymbol{\sigma}$ as

$$\bar{\mathbf{S}} = \det \mathbf{F} \left(\mathbf{F}^e\right)^{-1} \boldsymbol{\sigma} \left(\mathbf{F}^e\right)^{-T} \tag{8}$$

This stress is power conjugate with the elastic Green strain tensor $\bar{\mathbf{E}}^e$ and may be found from the hyperelastic law

$$\bar{\mathbf{S}} = \bar{\mathbf{C}}_{el}^{\bar{S}} : \bar{\mathbf{E}}^e \tag{9}$$

where $\bar{\mathbf{C}}_{el}^{\bar{S}}$ is the tensor of elastic moduli. In the case of orthotropic symmetry it is defined by three independent components, describing the elastic anisotropy of the crystal.

The stress acting on the slip systems and power conjugate with the slip rate $\dot{\gamma}^\alpha$ is the resolved shear stress τ^α. It is found from the second Piola-Kirchhoff stress tensor as

$$\tau^\alpha = \bar{\mathbf{C}}^e \bar{\mathbf{S}} : \left(\mathbf{m}_0^\alpha \otimes \mathbf{n}_0^\alpha\right) \tag{10}$$

3.2 Flow and hardening rules

The flow rule used here is the well-known viscoplastic rule [29] which controls the activation of the slip systems

$$\dot{\gamma}^\alpha = \dot{\gamma}_0 \left(\frac{\left|\tau^\alpha\right|}{\tau_c^\alpha} \right)^{\frac{1}{m}} \operatorname{sgn}\left(\tau^\alpha\right) \tag{11}$$

where $\dot{\gamma}_0$ is the reference slip rate, m is the slip rate sensitivity parameter and τ_c^α is the slip resistance of slip system α.

The Teodosiu-type hardening models use the dislocation density as the hardening parameter. Then the hardening of slip system α is described by an equation proposed in [7] and [10]:

$$\tau_c^\alpha = \tau_0 + a\mu b \sqrt{\sum_{\beta=1}^{n} d^{\alpha\beta} \rho^\beta} \tag{12}$$

where a is a dimensionless coefficient, μ is the elastic shear modulus, b is the length of the Burgers vector, ρ^β is the dislocation density on slip system β, and $d^{\alpha\beta}$ is the interaction matrix, showing the relative strength of interaction between the dislocations on slip systems α and β. The initial slip resistance τ_0 is assumed to be the same on all slip systems. The dislocation density ρ^β is assumed to have initially a negligibly small positive value. The dislocation density evolves according to [9, 10]

$$\dot{\rho}^\alpha = \frac{1}{b} \left(\frac{1}{K} \sqrt{\sum_{\beta=1}^{n} g^{\alpha\beta} \rho^\beta} - 2 y_c \rho^\alpha \right) \left|\dot{\gamma}^\alpha\right| \tag{13}$$

where K is a dimensionless parameter that defines the accumulation of dislocations, y_c is the distance at which two dislocations with opposite Burgers vectors annihilate each other. $g^{\alpha\beta}$ is the interaction matrix, similar to $d^{\alpha\beta}$, but in this case the strength of dislocation interaction defines the accumulation of forest dislocations on slip system α depending on the dislocation density on system β. The total number of components in each of the interaction matrices $g^{\alpha\beta}$ and $d^{\alpha\beta}$ matrix is 144. The number of independent components is 6, corresponding to different types of the slip systems mutual orientations. The interaction matrix $g^{\alpha\beta}$ is given explicitly in Table 2 the interaction matrix $d^{\alpha\beta}$ has an analogous structure.

The phenomenological models describe work-hardening on slip systems with some convenient function. The latent hardening description is usually simpler than in the Teodosiu-type models and is limited to one matrix, connecting hardening rate with slip rate. As a typical example of the phenomenological model with this latent hardening description we consider the two-term Voce rule

$$\dot{\tau}_c^{\alpha} = \theta(\Gamma) \sum_{\beta=1}^{n} q_{\alpha\beta} \left| \dot{\gamma}^{\beta} \right| \tag{14}$$

where $q_{\alpha\beta}$ is the matrix of self-hardening and latent-hardening coefficients, and the accumulated slip Γ is defined by the evolution equation

$$\dot{\Gamma} = \sum_{\alpha=1}^{n} \left| \dot{\gamma}^{\alpha} \right| \tag{15}$$

The master hardening rate $\theta(\Gamma)$ is defined as

$$\theta(\Gamma) = \sum_{k=1}^{2} \theta_k \exp\left(-\frac{\theta_k}{\tau_k} \Gamma \right) \tag{16}$$

where θ_k and τ_k are material parameters. The initial slip resistance τ_{c0}^{α} is assumed equal for all slip systems.

In the numerical implementation of the single crystal plasticity model into the finite element method, one element may either represent a part of a grain (or possibly the whole grain) or it may represent many grains. In the latter case, the full-constraint Taylor method is used here to compute the element stresses. The full-constraint Taylor-type homogenisation assumes a constant deformation gradient throughout all the grains of a polycrystal, ignoring stress equilibrium, and the total stress is obtained as a simple average of the stresses in the grains:

$$\boldsymbol{\sigma} = \frac{1}{n_g} \sum_{g=1}^{n_g} \boldsymbol{\sigma}_g \tag{17}$$

where $\boldsymbol{\sigma}_g$ is the Cauchy stress in grain g, and n_g is the total number of grains. The grains are assumed to have equal volume.

4 Finite element modelling

The uniaxial tensile test was modelled using the finite element method. In all simulations the solid linear eight node “brick” elements with selectively reduced integration were used. This type of finite elements is usually avoided in the context of crystal plasticity simulations. The main reason for this is that the actual grains or their representation with Voronoi tessellations are too complex to represent with a mesh consisting of regular hexahedra, so the grain volume and grain boundary shape will be only approximated, while the tetrahedral elements may represent them accurately. Still, as it was found in [30], the use of hexahedral elements in crystal plasticity simulations does not affect the global response of a modelled polycrystal. Considering the local response, the use of tetrahedral elements is necessary if the goal is to approximate a real polycrystal grain morphology as precisely as possible. On the other hand, if the goal is to model some representative polycrystal, e.g. consisting of equiaxed grains with similar volume, then the choice of element type is not as critical. The representation of grain boundaries in such models is usually rather simplified and abstract, and there is no evidence that the smooth grain boundary of tetrahedral mesh is substantially better than the jagged boundary of a hexahedral mesh in predicting the global stress-strain response. The hexahedral element also has an advantage of numerical efficiency. The linear tetrahedral elements give a noticeably stiff solution compared to quadratic tetrahedral or linear hexahedral [31], while the number of degrees of freedom for a linear hexahedral element is lower than for a quadratic tetrahedral (8 nodes against 10). In our case, the polycrystal was represented by cubic “grains” of equal volume, i.e. equal number of elements per grain.

The finite element program LS-DYNA was used for all simulations. The crystal plasticity material model was implemented as a user-material subroutine [32]. The subroutine utilizes an explicit integration scheme by Grujicic and Batchu [33]. Explicit integration of the momentum equations was used with mass scaling to reduce computation time.

The response of the material was studied by using a representative volume element (RVE) with periodic boundary conditions. In some cases the Taylor type homogenisation was used to reduce computation time. In this case, one element was used as an RVE and periodic boundary conditions were applied to its nodes. The tensile tests in different directions were simulated by rotating the texture around the z-axis (i.e. the thickness direction) by the appropriate angle. The texture was represented by a set of 1000 orientations, picked randomly from the total set of 2611 measured orientations. To ensure that this set represents the total texture well, several sets were picked in this way and ODFs were created for them. The difference in ODFs was insubstantial.

Several meshes with different number of elements representing each grain were tested. The corresponding stress-strain curves are shown in Figure 6 using parameters identified below and the interaction matrix of Fivel et al. [18]. If more than 1 element per grain is used, the gradients of the stress-strain fields inside the grains may be modelled. The higher mesh resolution allows for better compatibility of the neighbouring grain deformations, relaxing the resulting local stresses and reducing the global average stress. The difference between the global response of a mesh with 8000 elements and meshes with 27000 or 64000 elements is not very large, while the computation time is roughly proportional to the number of elements. In the following, the Taylor model was used only for the identification of the parameters of the different hardening rules due to its computational efficiency. A mesh with 8000 elements was used for all other simulations where each grain was represented by 8 elements, see Figure 7.

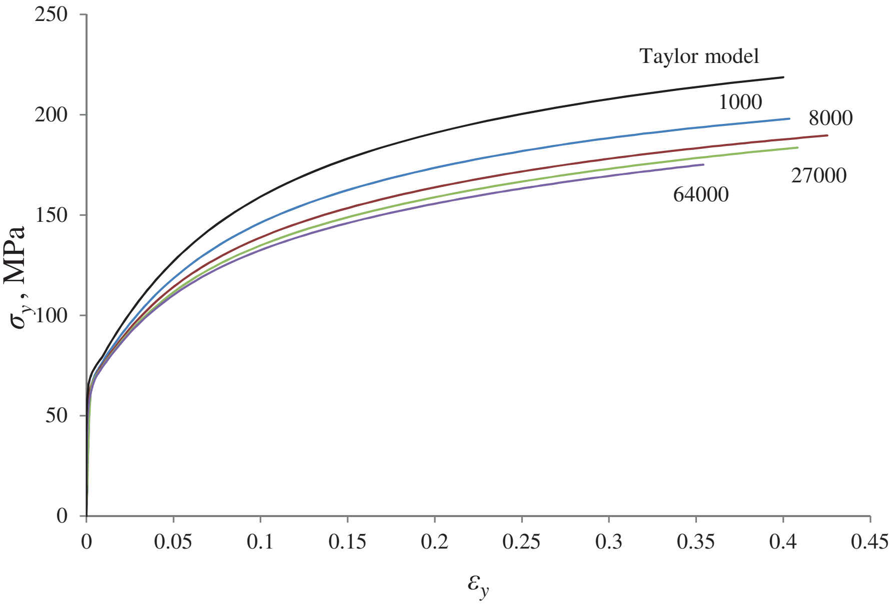

Figure 6: Stress-strain curves from FE models with different mesh resolution.

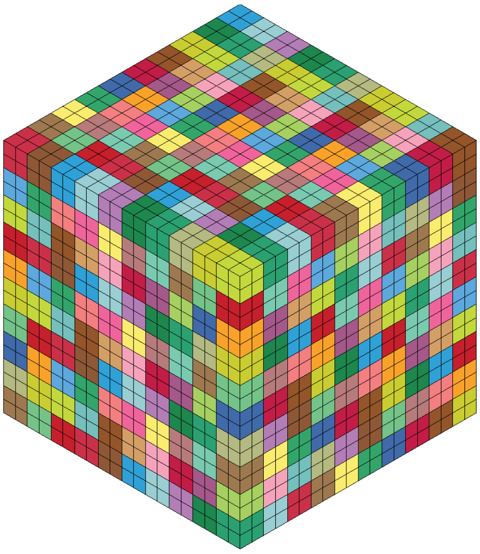

Figure 7: FE mesh with 8000 elements representing 1000 grains.

5 Parameter identification

5.1 Stress correction after necking

The above described numerical setup provides the framework for uniaxial tension, where the only component of the stress tensor is the tensile stress. On the other hand, in the experiments the stress situation becomes complex after necking, with the triaxial stress field contributing to the true stress. To remove this influence and find the corrected stress, the following procedure was used. The specimen was modelled using the finite element method. The material was represented by a phenomenological plasticity model with anisotropic yield function [34] and isotropic hardening, described by a two-term Voce rule. The shape of the yield surface for the AA6060 material was found from the texture data using crystal plasticity and the full-constraint Taylor model [35]. The parameters in the Voce rule were determined through an optimization procedure using the LS-OPT software [36]. Simulation of the tension test was performed with different sets of parameters in the Voce rule. The true stress-strain curve was computed and compared with the experimental one. This was repeated until both curves were coinciding thus providing an optimum set of parameters for the Voce rule. A detailed description of the procedure is given in [37].

.

This procedure was used to find the corrected stress in the 90° orientation, which was taken as the reference direction. Let σ_θ denote the corrected stress at orientation θ and let ε_θ^p be the corresponding logarithmic plastic strain. Since the 90° orientation is chosen as the reference direction, we will define the equivalent stress by $\sigma_{eq} \equiv \sigma_{90}$ and the equivalent plastic strain by $\varepsilon_{eq} \equiv \varepsilon_{90}^p$. The equivalent plastic strain for other orientations is defined from the incremental work relation

$$dw^p \equiv \sigma_\theta d\varepsilon_\theta^p = \sigma_{eq} d\varepsilon_{eq} \tag{18}$$

where σ_θ and σ_{eq} are evaluated at the same level of specific plastic work w^p.

To find the corrected stress σ_θ in other directions, the Bridgman correction [38] was used, viz.

$$\sigma_\theta = \frac{\sigma_y}{(1+2R/a)\cdot\ln(1+a/2R)} \tag{19}$$

where a is the minimum radius and R is the radius of curvature of the neck. The geometry of the neck was estimated by the relation proposed by Le Roy et al. [39], i.e.

$$\frac{a}{R} = k\left(\varepsilon_\theta^p - \varepsilon_{\theta u}^p\right) \tag{20}$$

where $\varepsilon_{\theta u}^p$ is the logarithmic plastic strain at the start of necking at orientation θ and k is a parameter. This parameter was found for the 90° direction by fitting the corrected stress-strain curve found from Equation (19) to the equivalent stress-strain curve found from the optimization procedure described above. The obtained value of $k = 0.45$ was then used for all other orientations, while $\varepsilon_{\theta u}^p$ was found directly from the directional tensile tests. The corrected stress-strain curves are presented in Figure 8.

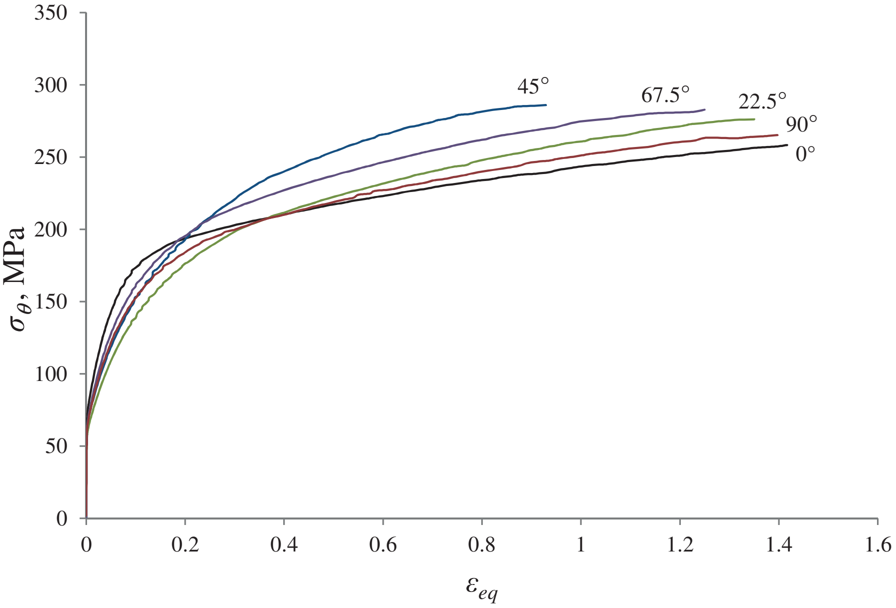

Figure 8: Flow stress (or corrected stress) versus equivalent strain for samples in different directions, where the flow stress σ_{90} at orientation $\theta = 90°$ equals the equivalent stress σ_{eq}.

5.2 Parameters of crystal plasticity model

The second stage of the study was to identify the parameters of the crystal plasticity model. The parameters $\dot{\gamma}_0$, μ, m and b in Equations (11)–(13) may be found in [10] and [19]. However, of principal interest here are the components of the interaction matrices $d^{\alpha\beta}$ and $g^{\alpha\beta}$ in addition to the parameter a. They were taken from different sources and may be divided into three categories. The first one proposed in [10] and [12] assumes that the latent hardening is dominating and equal for all dislocation locks. It was used in simulations of Cu behaviour but the same kind of arguments may be applied to Al as another FCC metal. The second one is the four-component interaction matrix $g^{\alpha\beta}$ in Equation (13) for the dislocation density evolution following the conclusions of Franciosi [13]. They are also usually normalized, so that the coefficient $d_5 = 1$. In both above approaches the interaction matrix in Equation (12) is reduced to one or two components (for self and latent hardening). In the third category, both interaction matrices have six independent components. The values of the used matrices with corresponding references are given in Table 3 and Table 4. In the case of two-term Voce hardening, the self-hardening is assumed equal to unity, while the latent hardening term $q^{\alpha\beta}$, $\alpha \neq \beta$ is equal to 1.4, following the conclusions in [14]. This value is most widely used in the literature.

The remaining parameters are the work-hardening parameters K and y_c, or θ_k and τ_k ($k = 1, 2$) in the case of the two-term Voce rule, which have to be fitted to the experimental data. This was done using the optimization program LS-OPT. As described previously, it fits the output of LS-DYNA (e.g. in form of a stress-strain curve) to a target curve (in this case the experimental equivalent stress-strain curve in the 90° direction) by varying chosen parameters of the LS-DYNA simulations (in this case K and y_c or θ_k and τ_k). After calculating the mean squared error between the simulated and target curves it adjusts the parameters in such a way that the error is reduced at the next iteration. During this procedure LS-DYNA simulations are run many times, so the numerical model needs to be rather efficient, if the optimization process is to be finished in reasonable time. Therefore, the full-constraint Taylor model was used. The use of this homogenisation procedure against others, like the relaxed-constraint Taylor model and the viscoplastic self-consistent model is discussed in [40, 41].

The initial slip resistance τ_0 is assumed to be equal for all the models. It was found through the aforementioned fitting procedure, where τ_0 was the only variable, using the two-term Voce work-hardening rule – it is the most computationally efficient model – and used for all models. For this material $\tau_0 = 27\ \text{MPa}$.

The results of the optimization procedure are presented in Table 5 and Table 6. One may notice that for the interaction matrices with similar structure (i.e. the 6 or 4 component matrix) the K and y_c parameters are also similar. The stress-strain curves obtained with different matrices, compared to the experimental target curve are presented in Figure 9. By varying just two parameters, it was possible to fit the crystal plasticity models to the experimental target curve, with only small discrepancies between the models with different matrices. This provides a common reference point for their comparison. Then uniaxial tension in different material directions was simulated, using these work-hardening parameters and the 8000 element mesh described above.

Table 3: Interaction matrix for strength, Equation (11).

Parameter sets	a	d_0	d_1	d_2	d_3	d_4	d_5
Teodosiu et al. (1991) [10]	1	0.42	0.52	0.52	0.52	0.52	0.52
Delaire et al (2000) [12]	1	0.52	0.72	0.72	0.72	0.72	0.72
Tabourot et al. (1997) [17]	0.3	1	1	1	1	1	1
Fivel et al. (1998) [18]	0.3	1	1	1	1	1	1
Dumoulin et al. (2000) [19]	1	0.3	0.07	0.07	0.07	0.07	0.07
Tabourot et al. (2001) [20]	1	0.16	0.11	0.11	0.11	0.11	0.11
Madec et al. (2003) [22]	1	0.084	0.084	0.051	1.265	0.075	0.084
Devincre et al. (2008) [23]	1	0.122	0.122	0.07	0.625	0.137	0.122
Gérard et al. (2012) [24]	0.38	0.025	0.01	0.04	14.3	0.6	0.5

Table 4: Interaction matrix for dislocation density evolution, Equation (13).

Parameter sets	g_0	g_1	g_2	g_3	g_4	g_5
Teodosiu et al. (1991) [10]	0	1	1	1	1	1
Delaire et al (2000) [12]	0	1	1	1	1	1
Tabourot et al. (1997) [17]	0.2	0.3	0.3	0.3	0.4	1
Fivel et al. (1998) [18]	0.01	0.4	0.4	0.4	0.75	1
Dumoulin et al. (2000) [19]	0.2	0.8	0.8	0.8	0.8	1
Tabourot et al. (2001) [20]	0.96	0.96	0.96	0.96	0.96	1
Madec et al. (2003) [22]	0.084	0.084	0.051	1.265	0.075	0.084
Devincre et al. (2008) [23]	0.122	0.122	0.07	0.625	0.137	0.122
Gérard et al. (2012) [24]	0.025	0.01	0.04	14.3	0.6	0.5

Table 5: Calibration results for the hardening model with different interaction matrices.

Parameter sets	K	y_c [mm]
Teodosiu et al. (1991) [10]	27.755	$6.516 \cdot 10^{-6}$
Delaire et al (2000) [12]	31.767	$6.578 \cdot 10^{-6}$
Tabourot et al. (1997) [17]	7.833	$1.038 \cdot 10^{-5}$
Fivel et al. (1998) [18]	8.827	$1.044 \cdot 10^{-5}$
Dumoulin et al. (2000) [19]	12.756	$9.090 \cdot 10^{-6}$
Tabourot et al. (2001) [20]	17.824	$6.226 \cdot 10^{-6}$
Madec et al. (2003) [22]	3.606	$6.000 \cdot 10^{-6}$
Devincre et al. (2008) [23]	6.014	$5.139 \cdot 10^{-6}$
Gérard et al. (2012) [24]	5.933	$5.244 \cdot 10^{-6}$

Table 6**:** Calibration results for the two-term Voce hardening model.

τ_{c0}^{α}, MPa	τ_1, MPa	θ_1, MPa	τ_2, MPa	θ_2, MPa
27.00	24.85	183.81	29.17	40.95

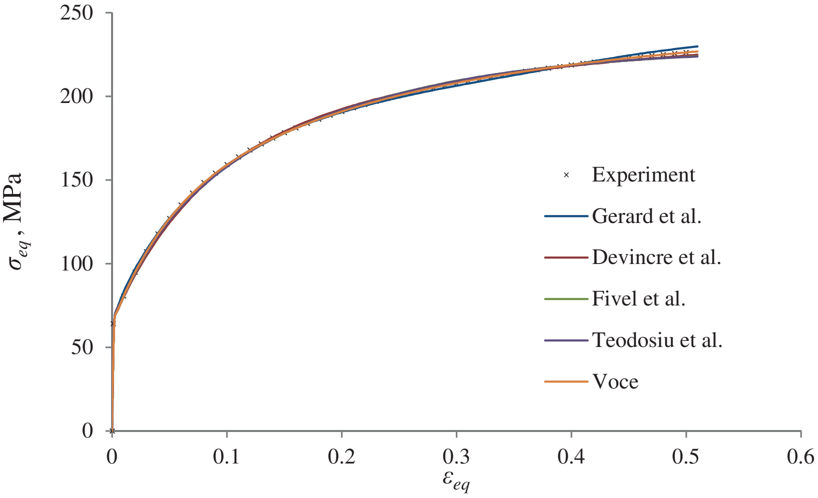

Figure 9: Calibration of the crystal plasticity model with different interaction matrices using the equivalent stress-strain curve in the 90° direction.

6 Results and discussion

To represent the in-plane anisotropy of the material, the flow stress ratio $\sigma_\theta / \sigma_{eq}$ is plotted against the orientation angle θ for given values of the equivalent plastic strain ε_{eq}. It is recalled that $\sigma_{eq} \equiv \sigma_{90}$ and further that the stresses are evaluated at the same value of the specific plastic work $w^p = \int \sigma_\theta d\varepsilon_\theta^p$. The experimental results are shown in Figure 10 for different amounts of plastic work. The plastic anisotropy of the material obviously evolves considerably from the point of yielding to fracture (which happens at strain around 100% for the 45° orientation). The general trend is that the flow stress ratio exhibits a maximum at 0° and a minimum at 22.5° at the early stages of deformation which changes into a maximum at 45° and a minimum at 0° at large deformations. One possible reason for the shift from maximum to minimum at 0° could be high initial values of the dislocation density on the slip systems activated when loading is in this direction.

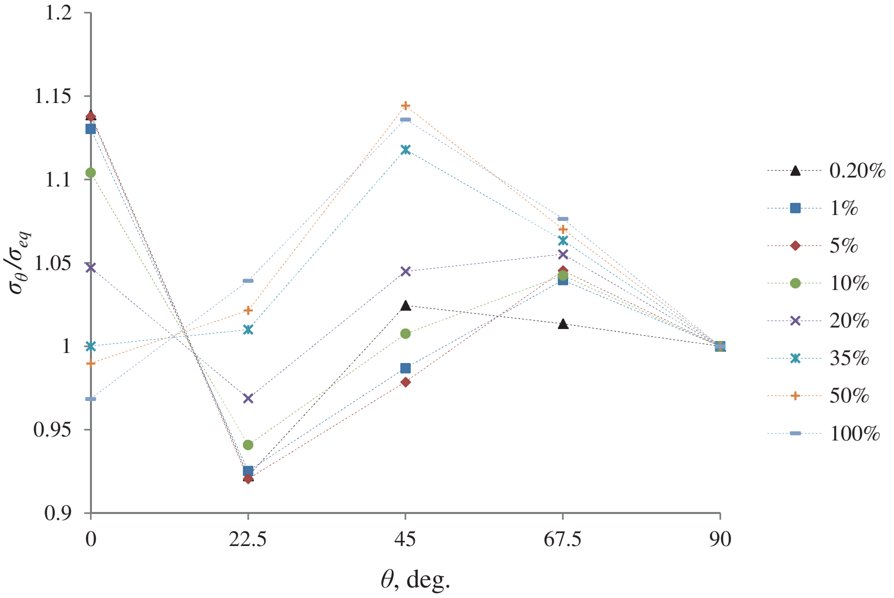

Figure 10: Flow stress ratio $\sigma_\theta / \sigma_{eq}$ from the experiment versus specimen orientation θ. The stress ratio is taken at equal values of plastic work for all directions, corresponding to the plastic strain in the reference direction, given in the legend.

The evolution of the anisotropy in plastic flow may be evaluated from Figure 5a), displaying the logarithmic strain ε_x in the width direction of the specimen against the logarithmic strain ε_z in the thickness direction of the extruded profile, or in Figure 5 b) presenting the strain ratio r_y as function of tensile strain and tensile direction. It is seen that r_y differs between the different orientations at small strains, while at larger strains r_y tends to approximately unity for all orientations. This type of behaviour may be expected from a ductile polycrystal. The slip in the constituent grains has to be kinematically compatible with the extension of the specimen, which leads to grain rotations. The flow of the polycrystal is a combination of the material flow in the constituent grains, so these rotations lead to its evolution. In addition, the rotations change the resolved shear stress on the slip systems, so that new systems may activate, or the old ones may deactivate.

The flow stress ratios $\sigma_\theta / \sigma_{eq}$ obtained with crystal plasticity and different interaction matrices are compared to the experimental data in Figure 11 to Figure 16. The yield stress anisotropy (which in the current approach was assumed to be only texture dependent), i.e. flow stress ratio measured at 0.2% plastic strain, is practically the same for all models (see Figure 11), but the flow stress ratios start diverging already at 1% equivalent plastic strain. The general trend in all the CP models is similar to the experimental one, with a minimum at the 22.5° orientation at smaller strains and a maximum at 45° for larger strains. An important difference between simulations and experiments is that the predictions, which are based on the assumption of equal initial slip resistance and the measured crystallographic texture, generally give a lower flow stress ratio at the 0° direction than observed in the experiments. The minimum at 22.5° disappears completely from the experimental curves, but remains, though reduced, in the CP models. The maximum at 45 ° is quite overestimated by the interaction matrices after Gérard et al. [24] and Devincre et al. [23]. The simple latent hardening matrix of the two-term Voce law gives the same basic trend as the dislocation density based models.

The strain ratio r_y obtained for the different interaction matrices is compared to the experimental data in Figure 17. The variation between the responses for different models here is noticeable, but lower than the variation of the flow stress ratio. The CP models fit quite well with the experimental results both with respect to the initial value of the strain ratio and its evolution. The largest discrepancy between simulations and experiments occurs at the 0° and 45° orientations.

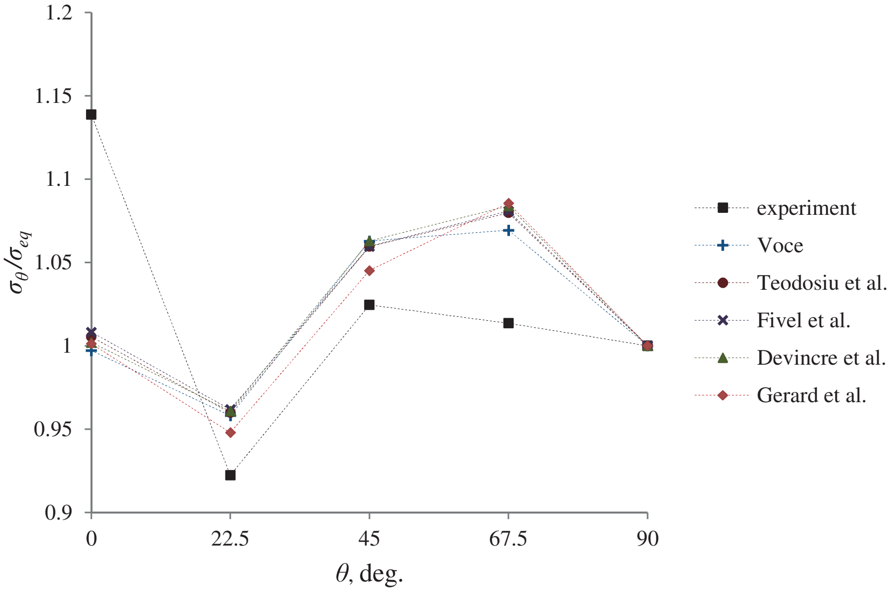

Figure 11: Flow stress ratio $\sigma_\theta / \sigma_{eq}$ at incipient yielding (0.2% plastic strain) versus specimen orientation θ from the experimental tests and simulations.

The results may be explained using the crystal plasticity theory for the constituent crystals of the specimen. For the most part of the aggregate the crystals undergo extension in one direction, which for most orientations may be provided by slip on one or two particular slip systems. The other deformations, namely the accommodation of deformation between different grains, have much smaller magnitude and are provided by slip of lesser magnitude on three other systems. Therefore, most of the time, the majority of slip activity is dependent only on the orientation of the crystals. This gives the resulting general trends in both stress anisotropy and strain ratio evolution which are similar for all models. On the other hand, many grains after some deformation will orient in such a way that several different slip systems may become active (the stress in these grains will reach the vertex of the crystal’s polyhedral yield surface). Then, what system will get activated and what will not, depends on the evolved slip resistances of the slip systems and therefore on the latent hardening of the crystal. The slip systems that provide the accommodation of deformation of different grains may also be not unique to the crystal orientation, and will as well depend on the latent hardening description. Different slip systems activated will give variation in grain rotations and consequently strains and stresses. Therefore the models with different latent hardening matrices demonstrate some noticeable differences in plastic behaviour on the polycrystal level.

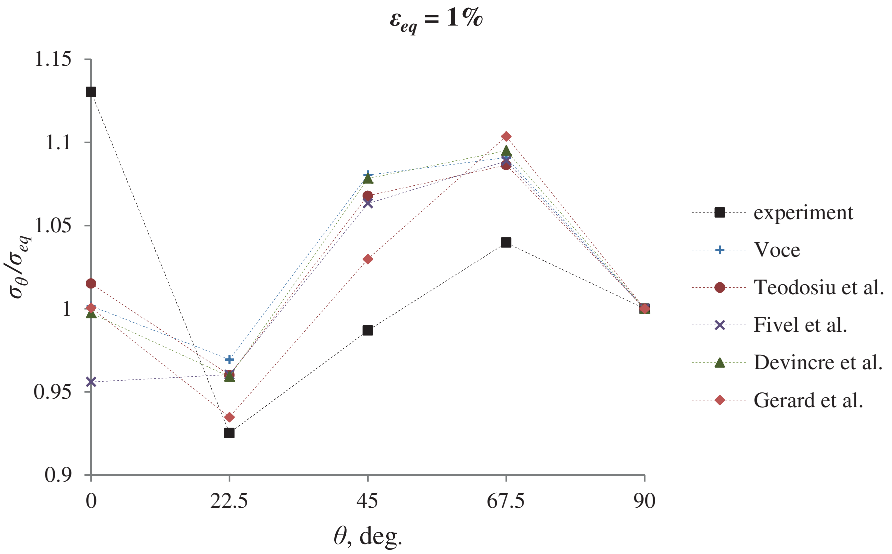

a)

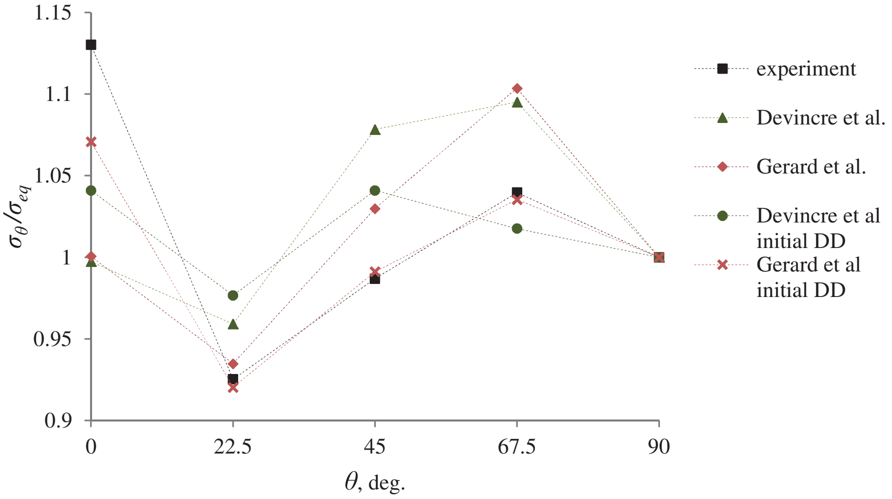

b)

Figure 12: Flow stress ratio $\sigma_\theta / \sigma_{eq}$ against sample orientation θ for different interaction matrices at specific plastic work corresponding to 1 % plastic strain in the 90° direction. In a) the initial dislocation density is equal for all slip systems, in b) it is increased for the A2 slip system.

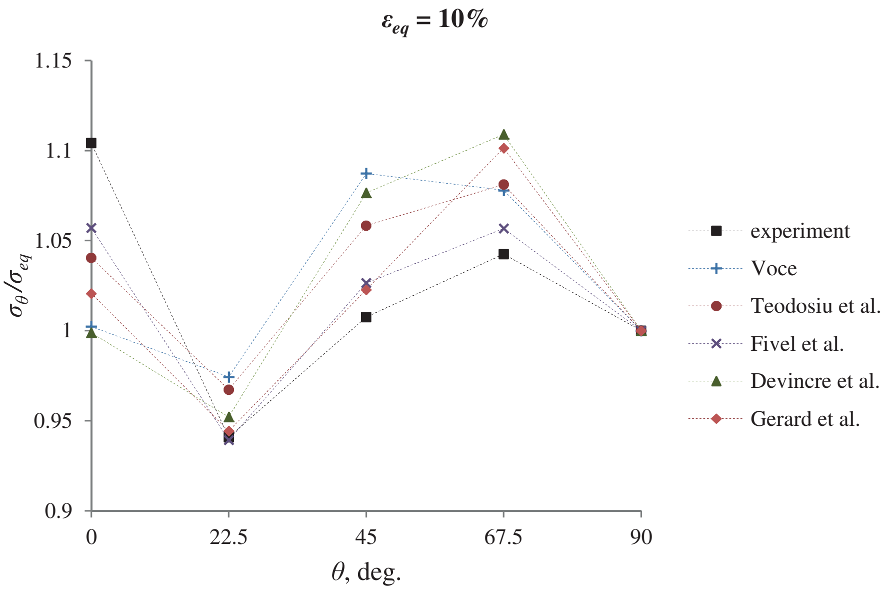

a)

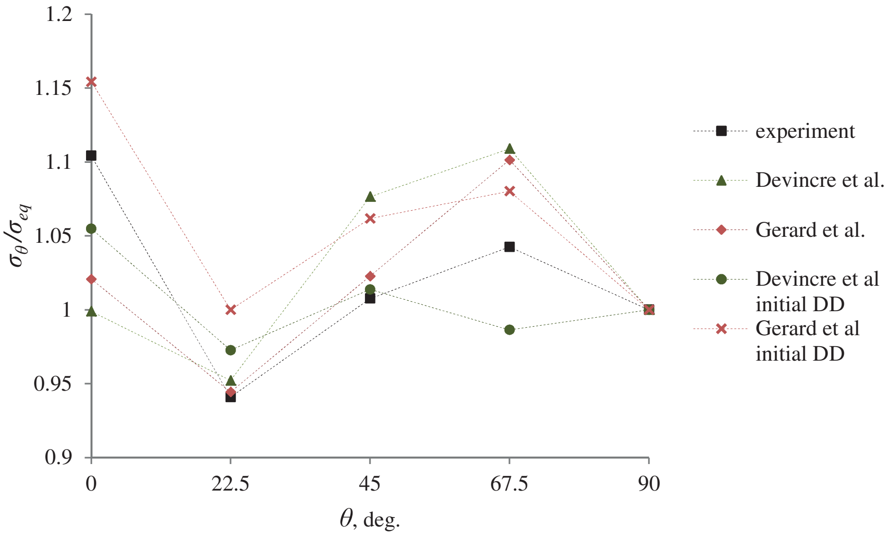

b)

Figure 13: Flow stress ratio $\sigma_\theta / \sigma_{eq}$ against sample orientation θ for different interaction matrices at specific plastic work corresponding to 10 % plastic strain in the 90° direction. In a) the initial dislocation density is equal for all slip systems, in b) it is increased for the A2 slip system.

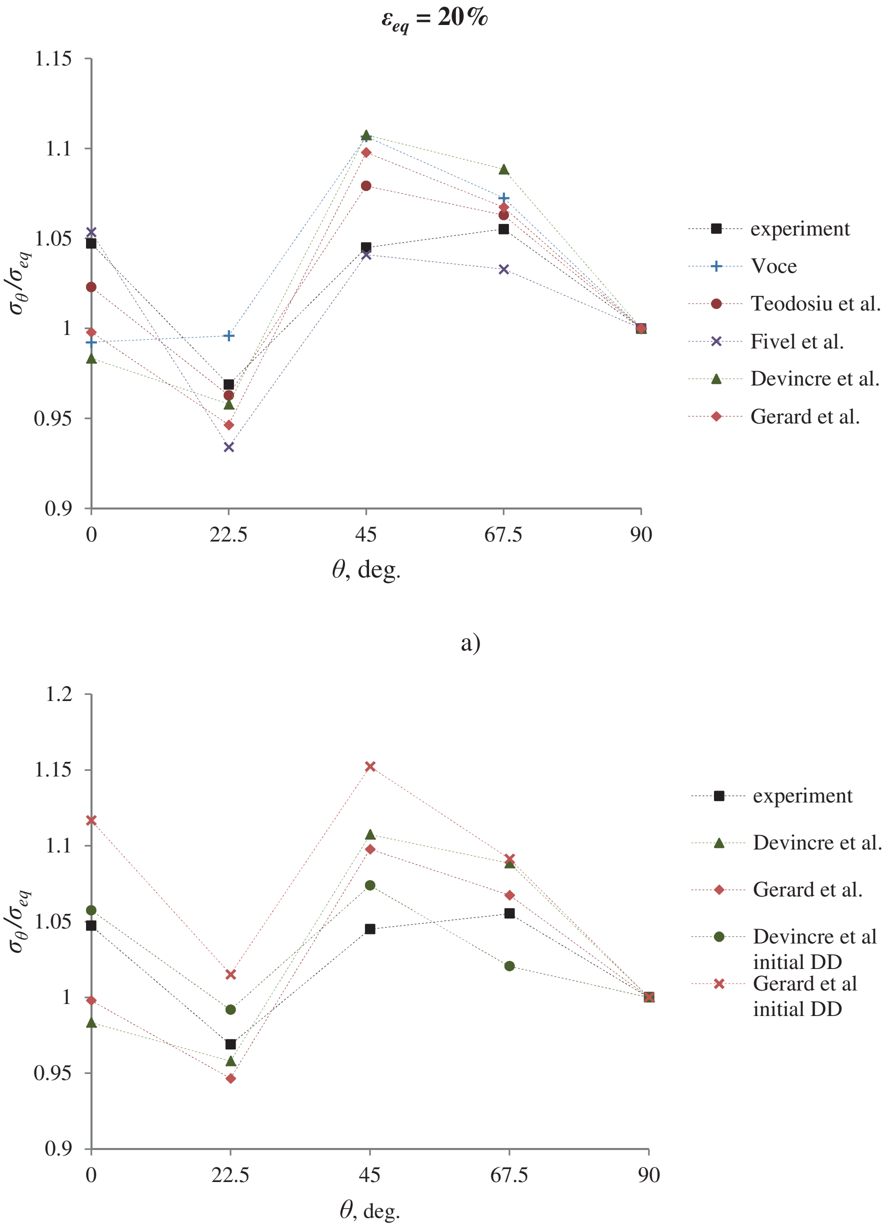

a)

b)

Figure 14: Flow stress ratio $\sigma_\theta / \sigma_{eq}$ against sample orientation θ for different interaction matrices at specific plastic work corresponding to 20 % plastic strain in the 90° direction. In a) the initial dislocation density is equal for all slip systems, in b) it is increased for the A2 slip system.

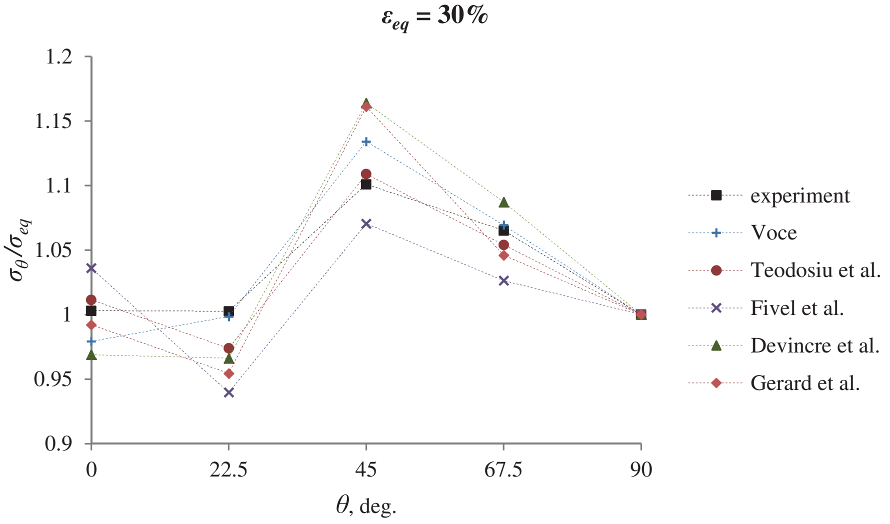

a)

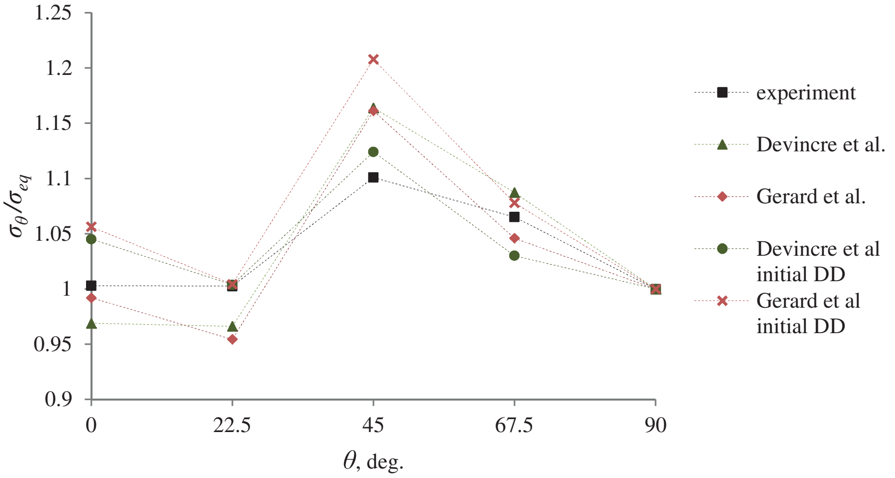

b)

Figure 15: Flow stress ratio $\sigma_\theta / \sigma_{eq}$ against sample orientation θ for different interaction matrices at specific plastic work corresponding to 30 % plastic strain in the 90° direction. In a) the initial dislocation density is equal for all slip systems, in b) it is increased for the A2 slip system.

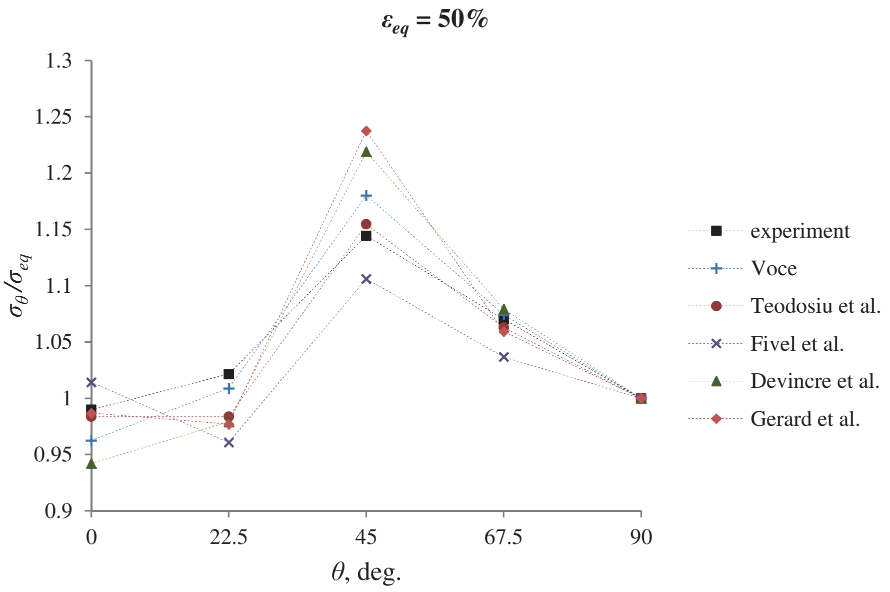

Figure 16: Flow stress ratio $\sigma_\theta / \sigma_{eq}$ against sample orientation θ for different interaction matrices at specific plastic work corresponding to 50 % plastic strain in the 90° direction.

The differences on single crystal level are much more substantial. In the case of the 6-component interaction matrix, and especially the matrix of Gérard et al., the maximum local von Mises stress, at any deformation, was more than twice as high as the global stress, while for the two-term Voce model and the 4-component matrix this difference was around 50%. The high local stresses are a result of the structure of the work-hardening rule. For the two-term Voce rule and the 4-component matrix the slip resistance of a slip system is calculated by averaging the internal variable (dislocation density or master hardening rate) on all other slip systems by lumping them all into the latent hardening category and assigning the same weight: the $d^{\alpha\beta}$ matrix for the 4-component matrix models includes either one or two independent components and $q^{\alpha\beta}$ for the two-term Voce rule includes two – for latent and self-hardening. On the other hand, in the 6-component models the influence of the slip systems on each other is much more complex, because the same 6-component matrix is used both for the dislocation density and the slip resistance calculations ($d^{\alpha\beta}$ and $g^{\alpha\beta}$ for them are assumed to be the same). In addition, for all three 6-component models considered, the proportion between the largest and the smallest component of the interaction matrix is from around 10 for the matrix of Devincre et al. to 1400 for the matrix of Gérard et al. This creates a situation where for some orientations the crystal has to slip on a certain set of slip systems (by geometrical constraint), but this set, through the interaction matrix, is hardening much faster than the same slip system sets in other grains for the same material. This leads to some peculiar behaviour, when similar responses of a polycrystal are provided by very dissimilar local plastic response. A particularly interesting question would be to prove experimentally which type of latent hardening is closer to the physical reality.

To test the validity of the hypothesis that the initial dislocation density may skew the stress anisotropy out of the texture defined pattern, simulations were performed with increased initial density on the slip system A2 for the matrices of Devincre et al. and Gérard et al. The 4-component matrix models were not used, because in these cases, the different initial dislocation densities on different slip system do not play a significant role in the anisotropy of the plastic flow for the already discussed reason of "averaging". The results are presented on Figure 12 to Figure 15. The system A2 was chosen based on some preliminary simple simulations with the full-constraint Taylor model. The initial dislocation density on system A2 was set to $3 \cdot 10^8\ \mathrm{mm}^{-2}$. The results show that indeed the initial dislocation density may increase the stress ratio in the 0° direction towards the experimental values. The interaction matrix though still controls the anisotropy development: the new stress ratios mirror the general trends of the models without the initial dislocation density, e.g. the overshoot at 45° is still present. Therefore the hypothesis that the initial dislocation density affects the anisotropy is physically plausible.

Another difference between different latent hardening descriptions is how they behave in different methods of homogenisation. Namely in this work the full-constraint Taylor model and the CP-FEM were used. Using simple hardening rules in the crystal plasticity model, like the two-terms Voce rule, the full-constraint Taylor model gives rather accurate predictions of the global stress when compared to CP-FEM simulations [42]. However, when adopting the Teodosiu-type crystal plasticity model, the difference between the full-constraint Taylor model and even the simplest CP-FEM simulation with one linear element representing one grain becomes much more substantial, see Figure 6. As a result, the obtained values of K and y_c are not very accurate. A calibration of the material parameters using CP-FEM is possible but the increase of the computation time is large: the simulation with an 8000 element mesh took 40 times as much computer time as a simulation with the full-constraint Taylor model. In principle, the annihilation distance y_c is a physical parameter, defined mainly by the solid solution concentration in the alloy and independent of the interaction matrix. The values of y_c found form calibrations with different interaction matrices (Table 5) are mostly quite similar, but not the same. The consequence is that the hardening properties of the single crystals in the performed simulations may differ. This adds another complication in the use of the dislocation density based CP models. Nevertheless, the main point of this work still stands. When the single crystal simulation was run with different values of K and y_c but the same interaction matrix, the slip system activation pattern was the same. The activation of slip systems, and therefore the evolution of plastic anisotropy, is controlled by the interaction matrix within a broad range of K and y_c .

7 Conclusions

The AA6060 material in T4 temper was used to study the evolution of plastic anisotropy at large strains. To this end, uniaxial tensile tests in different material directions were performed with a test set-up that allowed obtaining the average true stress and the average true strain in the minimum cross-section of the sample at very high strains and until fracture. To investigate the influence of the interaction matrix on the predicted evolution of plastic anisotropy, these tensile tests were simulated with the CP-FEM, using hardening models with different latent hardening descriptions found in the literature, and the results were compared to the experimental data.

The examined material demonstrated a continuous evolution of the anisotropy in flow stress and strain ratio that depended on the tensile direction. The CP-FEM models, using different latent hardening descriptions, all captured the general trends of this evolution quite well. On the other hand, different latent hardening matrices lead to noticeable discrepancies between the produced results, especially in the predicted evolution of the flow stress anisotropy. The discrepancies become even bigger if the local response of the constituent grains is concerned. The latent hardening description was also shown to be important if variations in the initial dislocation density are to be considered. While this type of tensile tests could hardly be used to find the values of the interaction matrix, it could well be used to assess the validity of the values found by other methods.

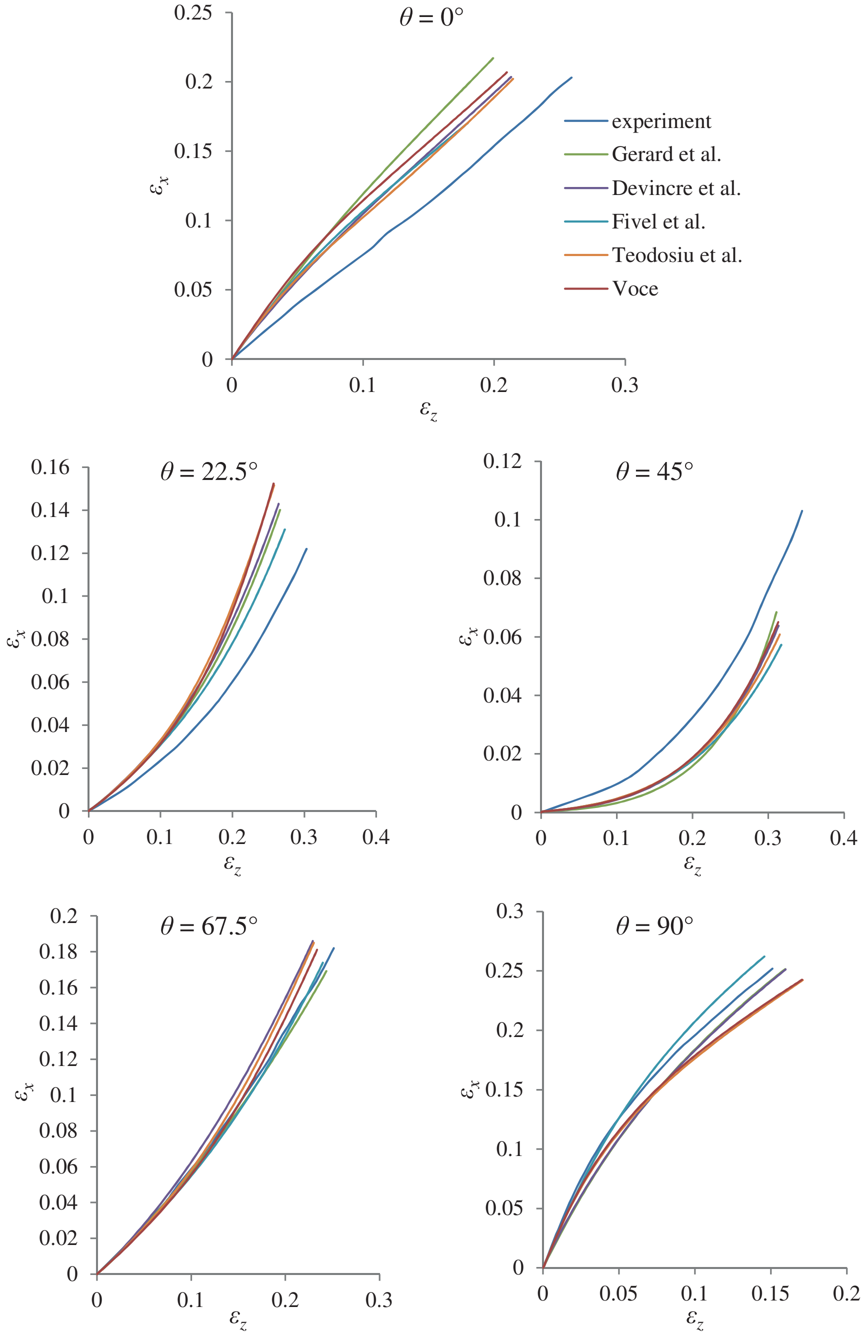

Figure 17: Logarithmic width strain ε_x versus logarithmic thickness strain ε_z for different specimen orientations θ from experiments and simulations with different interaction matrices. The slope of the curves represents the strain ratio r_y.

References

[1] G. I. Taylor and C. F. Elam, "Bakerian lecture. the distortion of an aluminium crystal during a tensile test," *Proceedings of the Royal Society of London. Series A,* vol. 102, pp. 643-667, 1923.

[2] G. Taylor and C. Elam, "The plastic extension and fracture of aluminium crystals," *Proceedings of the Royal Society of London. Series A, Containing Papers of a Mathematical and Physical Character,* vol. 108, pp. 28-51, 1925.

[3] S. R. Kalidindi, C. A. Bronkhorst, and L. Anand, "Crystallographic texture evolution in bulk deformation processing of FCC metals," *Journal of the Mechanics and Physics of Solids,* vol. 40, pp. 537-569, 1992.

[4] D. Peirce, R. Asaro, and A. Needleman, "An analysis of nonuniform and localized deformation in ductile single crystals," *Acta Metallurgica,* vol. 30, pp. 1087-1119, 1982.

[5] C. Tome, G. Canova, U. Kocks, N. Christodoulou, and J. Jonas, "The relation between macroscopic and microscopic strain hardening in FCC polycrystals," *Acta Metallurgica,* vol. 32, pp. 1637-1653, 1984.

[6] G. J. Weng and A. Phillips, "An investigation of yield surfaces based on dislocation mechanics—I: Basic theory," *International Journal of Engineering Science,* vol. 15, pp. 45-59, 1977.

[7] G. I. Taylor, "The Mechanism of Plastic Deformation of Crystals. Part I. Theoretical," *Proceedings of the Royal Society of London. Series A,* vol. 145, pp. 362-387, July 2, 1934 1934.

[8] U. Kocks, "Laws for work-hardening and low-temperature creep," *Journal of Engineering Materials and Technology,* vol. 98, p. 76, 1976.

[9] H. Mecking and U. Kocks, "Kinetics of flow and strain-hardening," *Acta Metallurgica,* vol. 29, pp. 1865-1875, 1981.

[10] C. Teodosiu and J. L. Raphanel, "Finite element simulations of large elastoplastic deformations of multicrystals," in *Proceedings of the international seminar MECAMAT91*, 1991, pp. 153-168.

[11] J. Hirth, "On dislocation interactions in the fcc lattice," *Journal of Applied Physics,* vol. 32, pp. 700-706, 2004.

[12] F. Delaire, J. Raphanel, and C. Rey, "Plastic heterogeneities of a copper multicrystal deformed in uniaxial tension: experimental study and finite element simulations," *Acta Materialia,* vol. 48, pp. 1075-1087, 2000.

[13] P. Franciosi, M. Berveiller, and A. Zaoui, "Latent hardening in copper and aluminium single crystals," *Acta Metallurgica,* vol. 28, pp. 273-283, 1980.

[14] U. Kocks and T. Brown, "Latent hardening in aluminum," *Acta Metallurgica,* vol. 14, pp. 87-98, 1966.

[15] P. Franciosi and A. Zaoui, "Multislip in fcc crystals a theoretical approach compared with experimental data," *Acta Metallurgica,* vol. 30, pp. 1627-1637, 1982.

[16] P. Jackson and Z. Basinski, "Latent hardening and the flow stress in copper single crystals," *Canadian Journal of Physics,* vol. 45, pp. 707-735, 1967.

[17] L. Tabourot, M. Fivel, and E. Rauch, "Generalised constitutive laws for fcc single crystals," *Materials Science and Engineering: A,* vol. 234, pp. 639-642, 1997.

[18] M. Fivel, L. Tabourot, E. Rauch, and G. Canova, "Identification through mesoscopic simulations of macroscopic parameters of physically based constitutive equations for the plastic behaviour of fcc single crystats," *Le Journal de Physique IV,* vol. 8, pp. Pr8-151-Pr8-158, 1998.

[19] S. Dumoulin, L. Tabourot, T. Gradel, M. Fivel, and J. Moreau, "Identification of constitutive laws for Al 99.5," in *Advances in Mechanical Behaviour, Plasticity and Damage: Proceedings of Euromat 2000*, 2000, p. 311.

[20] L. Tabourot, S. Dumoulin, and P. Balland, "An attempt for a unified description from dislocation dynamics to metallic plastic behaviour," *Le Journal de Physique IV,* vol. 11, pp. Pr5-111-Pr5-118, 2001.

[21] B. Devincre, L. Kubin, and T. Hoc, "Physical analyses of crystal plasticity by DD simulations," *Scripta Materialia,* vol. 54, pp. 741-746, 2006.

[22] R. Madec, B. Devincre, L. Kubin, T. Hoc, and D. Rodney, "The role of collinear interaction in dislocation-induced hardening," *Science,* vol. 301, pp. 1879-1882, 2003.

[23] B. Devincre, T. Hoc, and L. Kubin, "Dislocation mean free paths and strain hardening of crystals," *Science,* vol. 320, pp. 1745-1748, 2008.

[24] C. Gérard, G. Cailletaud, and B. Bacroix, "Modeling of latent hardening produced by complex loading paths in FCC alloys," *International Journal of Plasticity,* 2012.

[25] J. Raphanel, C. Rey, and C. Teodosiu, "Finite Element Simulation of the Elastoplastic Deformation of Tricrystals: Comparisons with Experiments and Analytical Solutions," in *Anisotropy and Localization of Plastic Deformation*, ed: Springer, 1991, pp. 168-170.

[26] K. G. Russell and M. Ashby, "Slip in aluminum crystals containing strong, plate-like particles," *Acta Metallurgica,* vol. 18, pp. 891-901, 1970.

[27] O. Engler and V. Randle, *Introduction to texture analysis: macrotexture, microtexture, and orientation mapping*: CRC press, 2010.

[28] E. Lee and D. Liu, "Finite-Strain Elastic—Plastic Theory with Application to Plane-Wave Analysis," *Journal of Applied Physics,* vol. 38, pp. 19-27, 1967.

[29] F. H. Norton, *The creep of steel at high temperatures*: McGraw-Hill Book Company, Incorporated, 1929.

[30] O. Diard, S. Leclercq, G. Rousselier, and G. Cailletaud, "Evaluation of finite element based analysis of 3D multicrystalline aggregates plasticity: Application to crystal plasticity model identification and the study of stress and strain fields near grain boundaries," *International Journal of Plasticity,* vol. 21, pp. 691-722, 2005.

[31] I. Simonovski, L. Cizelj, and N. Jakšić, "The influence of finite element meshes on the results of a spatial polycrystalline aggregate model," *Nuclear Engineering and Design,* vol. 241, pp. 1184-1190, 2011.

[32] S. Dumoulin, O. Hopperstad, and T. Berstad, "Investigation of integration algorithms for rate-dependent crystal plasticity using explicit finite element codes," *Computational Materials Science,* vol. 46, pp. 785-799, 2009.

[33] M. Grujicic and S. Batchu, "Crystal plasticity analysis of earing in deep-drawn OFHC copper cups," *Journal of Materials Science,* vol. 37, pp. 753-764, 2002.

[34] H. Aretz and F. Barlat, "General orthotropic yield functions based on linear stress deviator transformations," in *AIP Conference Proceedings*, 2004, p. 147.

[35] F. Barlat and O. Richmond, "Prediction of tricomponent plane stress yield surfaces and associated flow and failure behavior of strongly textured FCC polycrystalline sheets," *Materials Science and Engineering,* vol. 95, pp. 15-29, 1987.

[36] N. Stander, W. Roux, T. Goel, T. Eggleston, and K. Craig, "LS-OPT user's manual," *Livermore software technology corporation,* 2008.

[37] M. Khadyko, S. Dumoulin, T. Børvik, and O. Hopperstad, "An experimental-numerical method to determine the work-hardening of anisotropic ductile materials at large strains," *International Journal of Mechanical Sciences,* vol. 88, pp. 25-36, 2014.

[38] P. Bridgman, "The stress distribution at the neck of a tension specimen," *Transactions of American Society for Metals,* vol. 32, pp. 553-574, 1944.

[39] G. Le Roy, J. Embury, G. Edwards, and M. Ashby, "A model of ductile fracture based on the nucleation and growth of voids," *Acta Metallurgica,* vol. 29, pp. 1509-1522, 1981.

[40] F. Grytten, B. Holmedal, O. S. Hopperstad, and T. Børvik, "Evaluation of identification methods for YLD2004-18p," *International Journal of Plasticity,* vol. 24, pp. 2248-2277, 2008.

[41] S. Li, O. Engler, and P. Van Houtte, "Plastic anisotropy and texture evolution during tensile testing of extruded aluminium profiles," *Modelling and Simulation in Materials Science and Engineering,* vol. 13, pp. 783-795, 2005.

[42] A. Saai, S. Dumoulin, and O. Hopperstad, "Influence of Texture and Grain Shape on the Yield Surface in Aluminium Sheet Material Subjected to Large Deformations," in *AIP Conference Proceedings*, 2011, p. 85.

Article 4

M. Khadyko, S. Dumoulin, T. Børvik, O.S. Hopperstad

Simulation of large-strain behaviour of AA6060 under tensile loading using anisotropic plasticity models.

Submitted for possible journal publication.

Simulation of large-strain behaviour of AA6060 under tensile loading using anisotropic plasticity models

M. Khadyko[1,*], S. Dumoulin[2], T. Børvik[1] and O.S. Hopperstad[1]

[1] Structural Impact Laboratory (SIMLab), Centre for Research-based Innovation, Department of Structural Engineering,
Norwegian University of Science and Technology, NO-7491 Trondheim, Norway
[2]SINTEF Materials & Chemistry, NO-7465 Trondheim, Norway

Abstract

Cylindrical smooth and notched AA6060 samples were tested in tension. The material was either cast and homogenized or extruded with strong cube texture. The textured specimens demonstrated unusual shapes of the fracture surface that deviated from elliptical and were more rectangular in shape. A phenomenological plasticity model was used in finite element simulations of the tensile tests, together with a crystal plasticity model. The phenomenological plasticity model could not reproduce the evolution of the cross-section of the specimens made from the textured material. The crystal plasticity finite element model on the other hand demonstrated behaviour closer to the experiment.

Keywords: tensile tests; plastic anisotropy; stress triaxiality; finite element method; crystal plasticity

---

[*] Corresponding author: Mikhail Khadyko (mikhail.khadyko@ntnu.no)

1. Introduction

The uniaxial tension test is at first sight a simple problem in mechanical science. The stress tensor has only one component and the strain is practically homogeneous in a large region of the specimen. However, even this simple case turns into a much more complex problem after the onset of necking. The strain field becomes highly heterogeneous and stress heterogeneity follows. The stress field also becomes triaxial. An accurate solution of this problem is very important. The uniaxial tension test is widely used to find the mechanical properties of metallic materials and finding the evolution of these properties after necking depends on the accuracy of this solution. The fracture of ductile materials happens usually after a considerable post-necking deformation, therefore any attempts to predict fracture based on the stresses, strains or deformation energies require a precise knowledge of the mechanical fields within the neck.

The problem of localization in uniaxial tension has been treated analytically since Considère [1] derived a criterion for the onset of necking. It was later analysed more rigorously as a bifurcation problem in [2] and its analytical equations were approached numerically in [3]. In [4] the stress triaxiality was accounted for and the equivalent stress in the smallest cross-section was found for the case of a round specimen made of an isotropic material. In later years this solution was extended to other cross-section geometries [5], and its accuracy was improved [6, 7]. The solution in [4] requires the measurement of the neck curvature, which is hard to perform accurately. A more practical solution which sacrifices some accuracy to avoid this measurement was derived in [8]. The search for new analytical solutions continues practically to present day [9, 10].

An alternative to the analytical solution is the numerical solution obtained by using the finite element method (FEM). The first attempts of analysing the tensile test and localization problems with FEM were made already in the 1970s in [11] and [12]. The FEM has an advantage of not being limited to some specific specimen geometry or material properties. It was used to study localization in smooth and notched cylindrical tensile specimens [13-16], tensile specimens with rectangular cross-section [17], plane-strain tension [18] and metal sheets [19, 20]. It was also used to study the influence of more advanced material models, like strain gradient plasticity, on the necking phenomenon [21-23].

The plastic anisotropy of the material may be described using phenomenological anisotropic yield functions. Anisotropy was introduced into the plastic flow description in [24]. Different ways to implement anisotropy were proposed later [25, 26]. The simulations of anisotropic materials using this type of yield functions, fitted to experimental data, usually produce rather accurate solutions [27]. In [28] a type of yield functions based on linear transformations of the stress deviator was proposed and described more generally in [29]. A large number of free parameters make these yield functions very flexible and able to reproduce complex anisotropic behaviour, but also very hard to calibrate properly.

The more physically based, yet more complex, way to define the material properties in FE simulations is to use the crystal plasticity (CP) theory. It provides a realistic description of the plastic flow as a result of slip on crystallographic planes in the multitude of crystalline grains constituting the metallic specimen. The complex anisotropic plastic behaviour then emerges naturally from the model, as a result of the crystallographic texture and hardening on the slip system level. The CP material model is very computationally heavy, so it is rarely used to model the whole specimen, which consists of millions of grains. It is often used to model the localization in metal sheets, where only a small part of the sheet needs to be represented, with applied plane-strain or plane-stress boundary conditions [30-33]. The CP model allows studying phenomena which are outside the scope of the phenomenological models, like surface roughening [34], and their influence on necking. Other applications of the CP model are localization in thin films [35], tubes under pressure [36] and deep drawing [37]. In [38] and [39], tensile tests on Al and Cu single crystals with rectangular cross-section of the specimen are simulated, but, in general, necking in the uniaxial tension test is not often studied using CP models.

In this work both the CP-FEM and the FEM with phenomenological anisotropic plasticity are used to simulate the tensile test on smooth and notched cylindrical specimens. Two materials of the same AA6060 alloy were studied – the first material was cast and homogenized, while the second material was extruded into a flat profile. As expected, the cast and homogenized material displayed a random distribution of grain orientations, while the extruded material exhibited a peculiar, very sharp crystallographic texture. As the results of the tensile tests show, the texture has a very strong effect on the shape of the cross-section during necking and until fracture. It is in the following attempted to reproduce this behaviour of the real materials in the numerical simulations.

2. Experimental procedures

The aluminium alloy AA6060 was provided as DC-cast extrusion ingots of 100 mm diameter produced in a laboratory casting machine by Hydro Aluminium R&D Sunndal. The chemical composition of the alloy was (in weight %): 0.2 Fe, 0.5 Mg, 0.4 Si and Al balance. The material was homogenized in a laboratory furnace using temperature-time cycles similar to the industrial practice, consisting of a soaking treatment followed by a predetermined cooling rate (see [40] for details). The ingot was subsequently extruded in an 800 tons laboratory press to rectangular profiles with dimensions 10×50 mm^2 using industrial extrusion parameters, i.e., billet temperature of 475°C, container temperature of 435°C and ram speed of 5 mm/s. The profiles were cooled in air after extrusion.

Test specimens were made from the cast and homogenized billet and from the extruded profile and tested after more than one week storage at room temperature to obtain a stable condition. Triplicate tensile tests were performed on axisymmetric smooth and notched samples oriented along the longitudinal axis of the ingot and the extrusion direction of the profile, respectively. The geometry of the test samples is shown in Figure 1.

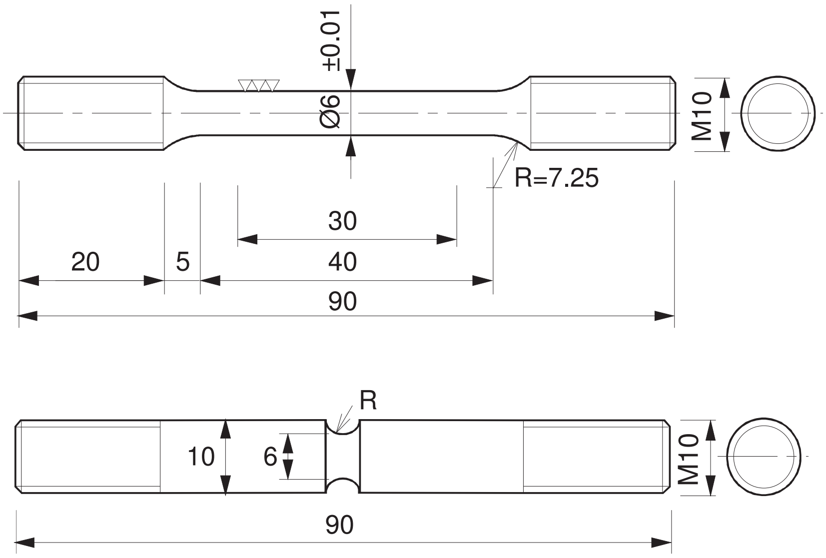

Figure 1: Geometries of the smooth and notched specimens where two values of the notch radius R (2.0 mm and 0.8 mm) were tested.

Optical micrographs of the grain structures of the two materials are shown in Figure 2. The two materials have equiaxed grain structure. Grain sizes of about 66 μm and 59 μm were found for the cast and homogenized and the extruded materials, respectively.

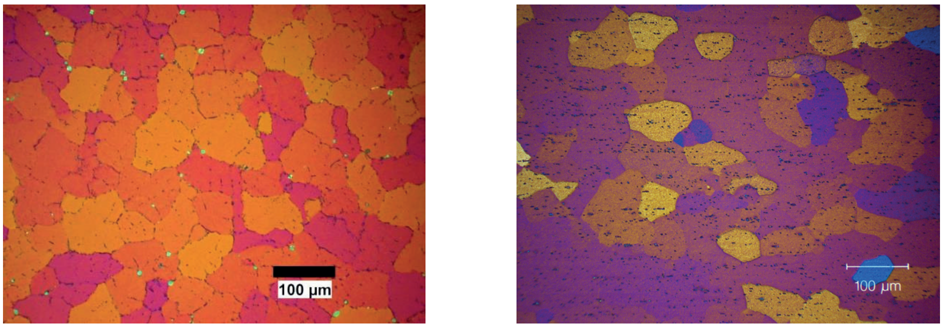

Figure 2: Grain structure for cast and homogenized (left) and extruded (right) materials [40].

The crystallographic textures of the two materials were measured with a scanning electron microscope using electron back-scattering diffraction. The results were processed using harmonic series expansion to find the orientation distribution functions (ODF) presented in Figure 3. The ODFs show that the cast and homogenized material has random texture, as expected, while the extruded material has a strong cube texture with maximum intensity above 100 times random.

The average strain rate before necking was $5 \cdot 10^{-4} \mathrm{s}^{-1}$ for the smooth specimens and the cross-head speed of the testing machine was adjusted to obtain approximately the same strain rate also in the notched specimens. The applied force and diameters aligned with the initial material directions at the minimum cross section of the specimen were measured continuously until fracture, using an in-house measuring rig with two perpendicular lasers [41]. A coordinate system was used, where *x*-direction is the reference direction, coinciding with the extrusion direction or billet direction in case of cast and homogenized material, *y*-direction coincide with the transverse direction of the billet and *z*-direction coinciding with the thickness direction. The Cauchy stress and the logarithmic longitudinal strain were calculated as

$$\sigma = \frac{F}{A} \quad \text{and} \quad \varepsilon = \ln \frac{A_0}{A} \tag{1}$$

where F is the applied force, $A_0 = \frac{\pi}{4} D_0^2$ is the initial cross-section area and D_0 is the initial diameter of the gauge section. The current area of the cross section was estimated as

$$A = \frac{\pi}{4} D_y D_z \tag{2}$$

where D_y and D_z are the diameters measured continuously by the laser-based measuring system. The extruded material was assumed to be orthotropic, and the diameters D_y and D_z were measured in the long and short transverse directions of the profile, respectively. The cast and homogenized material was assumed to be isotropic. The strain ratio r was defined as

$$r = \frac{d\varepsilon_y}{d\varepsilon_z}$$

where the logarithmic strains in the transverse directions are defined by

$$\varepsilon_y = \ln \frac{D_y}{D_0}, \quad \varepsilon_z = \ln \frac{D_z}{D_0} \tag{3}$$

Further details regarding the experimental setup and results can be found in [40].

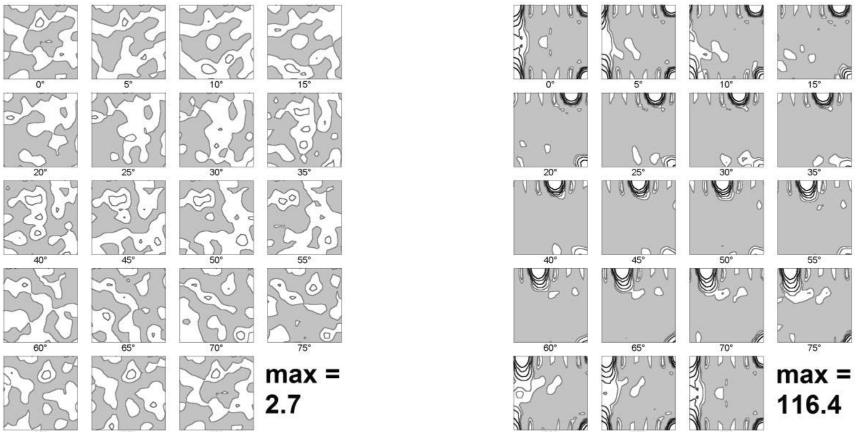

Figure 3: Orientation distribution function for cast and homogenized material (left) and extruded material (right). The sections in Euler angle space $(\varphi_1, \varphi_2, \Phi)$ are presented at $\varphi_2 = 0^\circ, 5^\circ, 10^\circ, ..., 90^\circ$ with φ_1 as abscissa and Φ as ordinate. The level curves are shown at intensities 1, 2, 4, 8, 16, … times random and the maximum intensity is given for each material [40].

3. Material modelling

3.1. *Crystal plasticity*

3.1.1. Single crystal plasticity

The framework for finite deformations is considered in this work where the total deformation gradient is multiplicatively decomposed into elastic and plastic parts [42]

$$\mathbf{F} = \mathbf{F}^e \mathbf{F}^p \tag{4}$$

The plastic part $\mathbf{F}^p$ transforms the body from the initial configuration Ω_0 into the intermediate plastically deformed configuration $\bar{\Omega}$ due to plastic slip, whereas the elastic part $\mathbf{F}^e$ transforms the body from intermediate into the current configuration Ω with elastic deformation and rigid body rotation. The plastic velocity gradient $\bar{\mathbf{L}}^p$ in the intermediate configuration is defined by

$$\bar{\mathbf{L}}^p = \dot{\mathbf{F}}^p \left(\mathbf{F}^p\right)^{-1} = \sum_{\alpha=1}^{n} \dot{\gamma}^\alpha \mathbf{m}_0^\alpha \otimes \mathbf{n}_0^\alpha \tag{5}$$

where the orthonormal vectors $\mathbf{m}_0^\alpha$ and $\mathbf{n}_0^\alpha$ are the slip direction and slip plane normal vectors, respectively, for a slip system α in the initial and intermediate configurations, $\dot{\gamma}^\alpha$ is the slip rate on slip system α, and n is the total number of slip systems.

The elastic Green strain tensor $\bar{\mathbf{E}}^e$ in the intermediate configuration is given by

$$\bar{\mathbf{E}}^e = \frac{1}{2}\left(\bar{\mathbf{C}}^e - \mathbf{I}\right), \quad \bar{\mathbf{C}}^e = \left(\mathbf{F}^e\right)^T \mathbf{F}^e \tag{6}$$

where $\bar{\mathbf{C}}^e$ is the elastic right Cauchy-Green deformation tensor and $\mathbf{I}$ is the unity tensor. The second Piola-Kirchhoff stress tensor $\bar{\mathbf{S}}$ in the intermediate configuration reads as

$$\bar{\mathbf{S}} = \det \mathbf{F} \left(\mathbf{F}^e\right)^{-1} \boldsymbol{\sigma} \left(\mathbf{F}^e\right)^{-T} \tag{7}$$

where $\boldsymbol{\sigma}$ is the Cauchy stress tensor. Since $\bar{\mathbf{E}}^e$ and $\bar{\mathbf{S}}$ constitute a power conjugate pair, a linear hyperelastic relation for small elastic strains is defined by

$$\bar{\mathbf{S}} = \bar{\mathbf{C}}_{el}^{\bar{S}} : \bar{\mathbf{E}}^e \tag{8}$$

where $\bar{\mathbf{C}}_{el}^{\bar{S}}$ is the fourth order tensor of elastic moduli that has three independent components describing the elastic anisotropy of the crystal.

The plastic flow is described by

$$\dot{\gamma}^{\alpha} = \dot{\gamma}_0 \left(\frac{\left|\tau^{\alpha}\right|}{\tau_c^{\alpha}} \right)^{\frac{1}{m}} \operatorname{sgn}\left(\tau^{\alpha}\right) \tag{9}$$

where $\dot{\gamma}_0$ is the reference slip rate, m is the instantaneous strain rate sensitivity, τ_c^{α} is the yield strength of slip system α, and the resolved shear stress τ^{α} is obtained as

$$\tau^{\alpha} = \bar{\mathbf{C}}^{e}\bar{\mathbf{S}} : \left(\mathbf{m}_0^{\alpha} \otimes \mathbf{n}_0^{\alpha}\right) \tag{10}$$

The hardening is defined by

$$\dot{\tau}_c^{\alpha} = \theta\left(\Gamma\right) \sum_{\beta=1}^{n} q_{\alpha\beta} \left|\dot{\gamma}^{\beta}\right| \tag{11}$$

where $\theta\left(\Gamma\right)$ is the master hardening rate, $q_{\alpha\beta}$ is the matrix of self-hardening and latent-hardening coefficients, and the accumulated slip Γ is defined by the evolution equation

$$\dot{\Gamma} = \sum_{\alpha=1}^{n} \left|\dot{\gamma}^{\alpha}\right| \tag{12}$$

The master hardening rate $\theta\left(\Gamma\right)$ is defined as

$$\theta\left(\Gamma\right) = \sum_{k=1}^{2} \theta_k \exp\left(-\frac{\theta_k}{\tau_k} \Gamma \right) \tag{13}$$

where θ_k and τ_k are material parameters. The initial slip resistance τ_{c0}^{α} is assumed equal for all slip systems.

3.1.2. Polycrystal plasticity

In this work the polycrystal is modelled by two homogenisation methods: the full-constraint Taylor model and the crystal plasticity finite element model (CP-FEM).

The full-constraint Taylor model [43] assumes that all grains undergo the same strain as the whole specimen. Stress equilibrium between the grains is then not satisfied. The stress in the specimen is found as an average, i.e.

$$\boldsymbol{\sigma} = \frac{1}{n_g}\sum_{g=1}^{n_g}\boldsymbol{\sigma}_g \tag{14}$$

where $\boldsymbol{\sigma}_g$ is the Cauchy stress in grain g and n_g is the total number of grains and where it is assumed that all grains have the same volume. This model is used when only the global response of the polycrystal is of interest.

When the local behaviour should be properly described, each grain is modelled separately by one element, i.e. using CP-FEM, so that both stress equilibrium and strain compatibility are naturally accounted for, although at the expense of a much higher computational time.

3.2. Continuum plasticity

The corotational stress and rate-of-deformation tensors are defined as

$$\hat{\boldsymbol{\sigma}} = \mathbf{R}^T\boldsymbol{\sigma}\mathbf{R}, \quad \hat{\mathbf{D}} = \mathbf{R}^T\mathbf{D}\mathbf{R} \tag{15}$$

where $\boldsymbol{\sigma}$ is the Cauchy stress tensor, $\mathbf{D}$ is the rate-of-deformation tensor, and $\mathbf{R}$ is the rotation tensor found from the polar decomposition of the deformation gradient tensor. The corotational rate-of-deformation tensor is decomposed into a sum of elastic and plastic parts

$$\hat{\mathbf{D}} = \hat{\mathbf{D}}^e + \hat{\mathbf{D}}^p \tag{16}$$

A hypoelastic relation for small elastic strains is defined by

$$\dot{\hat{\boldsymbol{\sigma}}} = \hat{\mathbf{C}}_{el}^{\sigma} : \hat{\mathbf{D}}^e \tag{17}$$

where $\hat{\mathbf{C}}_{el}^{\sigma}$ is the fourth order tensor of elastic moduli. Elastic isotropy is assumed for the material, so only two independent parameters are enough to define this tensor, i.e. the Young's modulus E and the Poisson ratio ν.

The yield function is formulated as

$$f\left(\hat{\boldsymbol{\sigma}}, \bar{\varepsilon}\right) = \bar{\sigma}\left(\hat{\boldsymbol{\sigma}}\right) - \kappa\left(\bar{\varepsilon}\right) \tag{18}$$

where $\bar{\varepsilon}$ is the equivalent plastic strain, $\bar{\sigma}$ is the equivalent stress and κ is the flow stress in uniaxial tension in the reference direction. The evolution of the flow stress κ is described by a two-term Voce rule

$$\kappa(\bar{\varepsilon}) = \kappa_0 + \sum_{i=1}^{2} Q_i \left(1 - \exp\left(-\frac{\theta_i}{Q_i}\bar{\varepsilon}\right)\right) \tag{19}$$

where κ_0 is the yield stress, and Q_i and θ_i are model parameters governing the work-hardening.

The corotational plastic rate-of-deformation tensor evolves according to the associated flow rule

$$\hat{\mathbf{D}}^p = \dot{\lambda}\frac{\partial f}{\partial \hat{\boldsymbol{\sigma}}} \tag{20}$$

where $\dot{\lambda}$ is the plastic multiplier, which satisfies the loading-unloading conditions, written in Kuhn-Tucker form as

$$\dot{\lambda} \geq 0, \quad f \leq 0, \quad f\dot{\lambda} = 0 \tag{21}$$

The linear transformation-based anisotropic yield criterion Yld2004-18p [28, 29] is adopted here to represent the plastic anisotropy of the two AA6060 materials. The yield function is defined by

$$\phi(\tilde{\mathbf{S}}', \tilde{\mathbf{S}}'') \equiv \sum_{i=1}^{3}\sum_{j=1}^{3} \left|\tilde{S}_i' - \tilde{S}_j''\right|^m = 4\bar{\sigma}^m \tag{22}$$

where m is the shape parameter; $\tilde{\mathbf{S}}'$ and $\tilde{\mathbf{S}}''$ represent the principal values of the stress tensors $\tilde{\mathbf{s}}' = \mathbf{C}' : \hat{\mathbf{s}}$ and $\tilde{\mathbf{s}}'' = \mathbf{C}'' : \hat{\mathbf{s}}$, $\hat{s}$ being the corotational stress deviator. The coefficients describing the orthotropic anisotropy of the material are the components c_{ij}' and c_{ij}'' of the fourth-order transformation tensors $\mathbf{C}'$ and $\mathbf{C}''$, respectively. On matrix form in Voigt notation these stress transformations read as

$$\begin{bmatrix} \tilde{s}'_x \\ \tilde{s}'_y \\ \tilde{s}'_z \\ \tilde{s}'_{xy} \\ \tilde{s}'_{yz} \\ \tilde{s}'_{xz} \end{bmatrix} = \begin{bmatrix} 0 & -c'_{12} & -c'_{13} & 0 & 0 & 0 \\ -c'_{21} & 0 & -c'_{23} & 0 & 0 & 0 \\ -c'_{31} & -c'_{32} & 0 & 0 & 0 & 0 \\ 0 & 0 & 0 & c'_{44} & 0 & 0 \\ 0 & 0 & 0 & 0 & c'_{55} & 0 \\ 0 & 0 & 0 & 0 & 0 & c'_{66} \end{bmatrix} \begin{bmatrix} \hat{s}_x \\ \hat{s}_y \\ \hat{s}_z \\ \hat{s}_{xy} \\ \hat{s}_{yz} \\ \hat{s}_{xz} \end{bmatrix} \tag{23}$$

$$\begin{bmatrix} \tilde{s}''_x \\ \tilde{s}''_y \\ \tilde{s}''_z \\ \tilde{s}''_{xy} \\ \tilde{s}''_{yz} \\ \tilde{s}''_{xz} \end{bmatrix} = \begin{bmatrix} 0 & -c''_{12} & -c''_{13} & 0 & 0 & 0 \\ -c''_{21} & 0 & -c''_{23} & 0 & 0 & 0 \\ -c''_{31} & -c''_{32} & 0 & 0 & 0 & 0 \\ 0 & 0 & 0 & c''_{44} & 0 & 0 \\ 0 & 0 & 0 & 0 & c''_{55} & 0 \\ 0 & 0 & 0 & 0 & 0 & c''_{66} \end{bmatrix} \begin{bmatrix} \hat{s}_x \\ \hat{s}_y \\ \hat{s}_z \\ \hat{s}_{xy} \\ \hat{s}_{yz} \\ \hat{s}_{xz} \end{bmatrix} \tag{24}$$

There are 18 coefficients to describe the plastic anisotropy, while the yield surface exponent m, usually set to 8 for FCC materials, governs the shape (or curvature) of the yield surface. If all the 18 anisotropy coefficients are set to unity, the Yld2004-18p yield function reduces to the isotropic high-exponent Hershey yield function [44]. The total number of model parameters of the continuum plasticity model to identify is 26: two elasticity coefficients, E and ν; the initial yield stress, κ_0; four hardening parameters, Q_i and θ_i, $i = 1, 2$; the shape parameter, m; and the 18 anisotropy coefficients c'_{ij} and c''_{ij}.

All material models used in the study were implemented in the explicit nonlinear FEM code LS-DYNA [45] as user-material subroutines. The explicit integration scheme by Grujicic and Batchu [37] was used for the CP model (both single- and poly- crystal) while the cutting plane algorithm proposed by Ortiz and Simo [46] was used for the continuum plasticity model. Owing to the explicit time integration of the momentum equations, the time steps were very small and the adopted stress-update algorithms were found to be accurate, robust and efficient, even if they are only conditionally stable.

4. Parameter identification

4.1. Continuum level

The experiments produced average Cauchy stress vs. logarithmic strain curves representative for the smallest cross-section of the tensile samples. In order to proceed, it was necessary to determine the equivalent stress-strain curves of the materials based on these results. As already stated, the average Cauchy stress is dependent not only on material properties, but also on the specimen geometry, and is influenced by the triaxial stress field in the necking area. To extract the equivalent stress the following numerical procedure was used.

The smooth tensile specimen was modelled using FEM. To reduce the computation time and considering the orthotropic nature of the material, only 1/8th of the specimen was modelled with symmetric boundary conditions on the appropriate planes. The simulations were carried out using the explicit solver of the nonlinear FEM code LS-DYNA [45]. Mass scaling was used to reduce the CPU time. To ensure a quasi-static solution, it was checked that the kinetic energy remained a small fraction of the internal energy of the sample throughout the simulations. The mesh was built using hexahedral solid elements with full integration (8 integration points) where 10 elements are used across the radius of the cylindrical sample, and is shown in Figure 4. Several meshes with different element sizes were tried to ensure that the mesh resolution did not affect the solution. The material behaviour was represented by the anisotropic plasticity model described in Section 3.2. The anisotropy coefficients c'_{ij} and c''_{ij} may be identified if enough stress points on the yield surface of the material are known from experiments. These experimental data were not available in the present work, so a workaround was used, utilizing the CP theory.

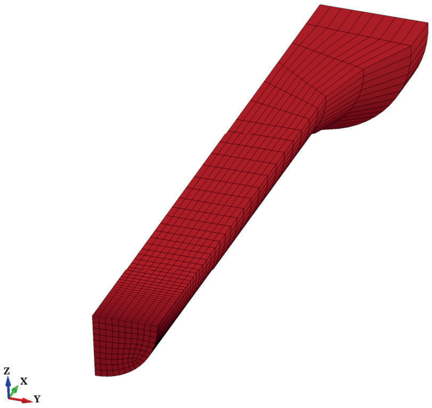

Figure 4: Finite element mesh used in the parameter identification process.

It is commonly assumed that the yield surface of a polycrystal, modelled by the above described CP theory, depends practically solely on the texture [47]. The hardening does not play a significant role in the plastic flow anisotropy at small values of the plastic work, and the grain rotations are negligibly small. Hence, the yield surfaces found for alloys with similar textures are always similar, see e.g. [48] and [49]. It is therefore possible to estimate the yield surfaces of the alloys investigated in this work without prior knowledge of their hardening properties. We can thus use the hardening parameters of a similar alloy from the literature, which are given in Table 1 and Table 2, in combination with the full-constraint Taylor model to find the yield surfaces for the two materials under study. A single element with one integration point was used. A total of 1000 grain orientations were randomly chosen from the measured sets of orientations to represent the texture of the material. Periodic boundary conditions were applied to the nodes and the element was subjected to a wide range of strain paths. The straining stopped when the plastic work reached the prescribed value, corresponding to 0.2% plastic strain in uniaxial tension in the reference direction. This allowed obtaining conforming stress states on the yield surface. Then an optimisation script was used to find a set of anisotropy coefficients c'_{ij} and c''_{ij} corresponding to the obtained yield surface shape. The yield surfaces obtained for the two materials are shown in Figure 5 and the corresponding anisotropy coefficients may be found in Table 3. The reference direction is the longitudinal direction of the extrusion ingot for the cast and homogenized material with random texture and the extrusion direction for the extruded material with strong cube texture.

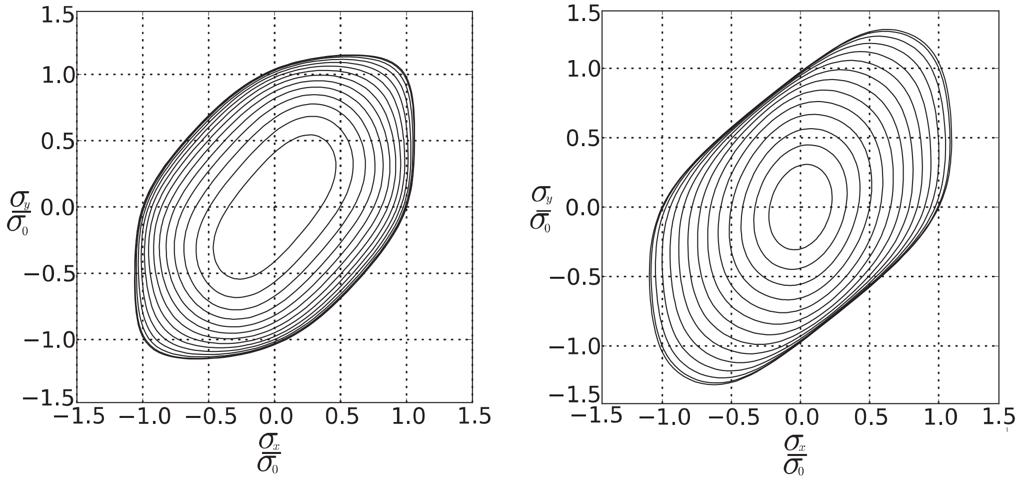

Figure 5: Yield surfaces obtained with the full-constraint Taylor CP model for the cast and homogenized (left) and extruded (right) materials

Table 1: Parameters of the CP model taken from the literature [50] [51] and used in all simulations.

c_{11}, MPa	c_{12}, MPa	c_{44}, MPa	$\dot{\gamma}_0$, s^{-1}	m	$q_{\alpha\beta}$
106430	60350	28210	0.010	0.005	1.40, if $\alpha \neq \beta$ 1.00, if $\alpha = \beta$

Table 2: Parameters of the two-term Voce hardening rules used in the CP calculations to determine the yield surface.

τ_{c0}^{α}, MPa	τ_1, MPa	θ_1, MPa	τ_2, MPa	θ_2, MPa
27.00	24.85	183.81	29.17	40.95

Table 3: Components of the Yld2004-18p transformation tensors.

Coefficients	Cast and homogenized	Extruded
c'_{12}	1.0000	0.2015
c'_{13}	1.0000	0.7199
c'_{21}	1.0000	-0.2025
c'_{23}	1.0000	0.5182
c'_{31}	1.0000	-0.4494
c'_{32}	1.0000	0.5750
c'_{44}	1.0000	1.0296
c'_{55}	1.0000	1.0000
c'_{66}	1.0000	1.0000
c''_{12}	1.0000	1.0346
c''_{13}	1.0000	-0.1664
c''_{21}	1.0000	1.0885
c''_{23}	1.0000	0.8119
c''_{31}	1.0000	1.2441
c''_{32}	1.0000	0.6630
c''_{44}	1.0000	0.0001
c''_{55}	1.0000	1.0000
c''_{66}	1.0000	1.0000

Thus, the remaining parameters to be found for the phenomenological model were the yield stress κ_0 and the hardening constants Q_i and θ_i, $i = 1, 2$. To find these parameters, the FEM model of the tensile test was run with LS-DYNA and the nonlinear optimisation tool LS-OPT [52]. The free variables were the hardening constants while the yield stress was found directly from the tensile test data. In the optimisation process, LS-OPT compares the true stress-strain curve obtained with the FEM model with the prescribed experimental true stress-strain curve and varies Q_i and θ_i, $i = 1, 2$, using an optimization algorithm, so that the difference between the two curves (mean squared error) is minimum. 15-20 iterations, consisting of 8 simulation runs each were necessary to minimize the mean squared error. As a result, a set of hardening parameters was obtained, which produces a response of the FEM model similar to the response of the real specimen. The parameters thus obtained are given in Table 4. The resulting true stress-strain curves from the FEM model are compared to the experimental ones in Figure 6. The equivalent stress-strain curves for the materials in the reference direction are then found directly from the hardening parameters. These curves are shown in Figure 7.

4.2. Slip system level

Some of the CP model parameters are common for a broad range of Al alloys and may be found in the literature. In particular, the parameters $\dot{\gamma}_0$ and m in Equation (9) governing rate dependence, the matrix components $q_{\alpha\beta}$ in Equation (11) governing latent hardening, and the components of the tensor of elastic moduli $\bar{\mathbf{C}}_{el}^{\bar{S}}$ in Equation (8) may be found in [50] and [51]. The values used here are given in Table 1. On the contrary, the initial slip resistance τ_{c0}^{α} and the hardening parameters θ_k and τ_k, $k = 1, 2$, in Equation (13) are material dependent and have to be fitted to the experimental data.

The material was modelled by a representative volume element (RVE) – a $10\times10\times10$ element cube with periodic boundary conditions applied to the nodes on the facets (Figure 8). To represent the texture, sets of 1000 orientations were chosen randomly from the measured set of grain orientations for each material. Then each orientation was assigned to a grain, represented by an element. The RVE was subjected to uniaxial tension in the reference direction. The optimization software LS-OPT was used again in a similar manner as above.

Table 4: Parameters of the two-term Voce hardening rule used in the phenomenological plasticity model.

Material	κ_0, MPa	Q_1, MPa	θ_1, MPa	Q_2, MPa	θ_2, MPa
Cast and homogenized	70.00	82.93	1820.17	129.96	299.04
Extruded	70.00	122.81	2151.39	51.35	84.99

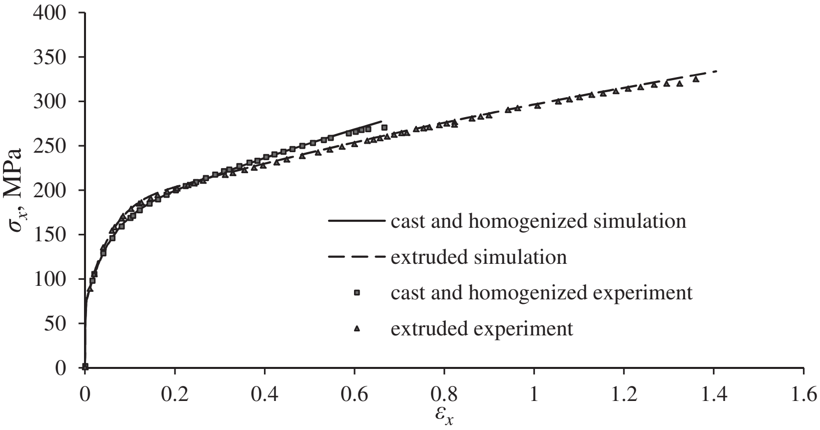

Figure 6: True stress-strain curves from the experiment and the simulations used in the material model calibration for the cast and homogenized and the extruded materials.

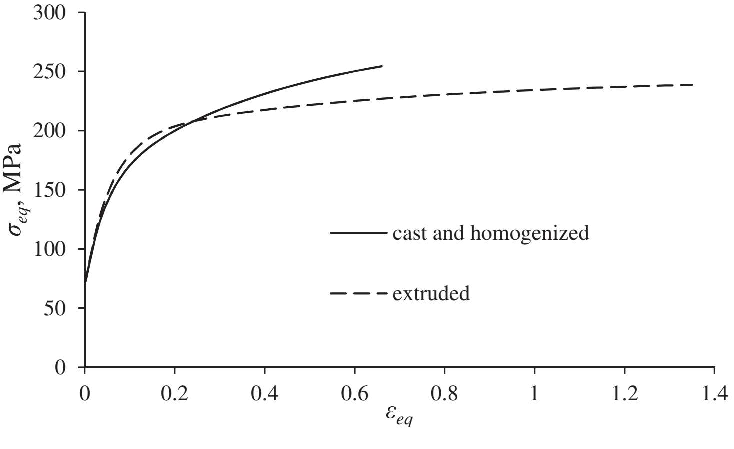

Figure 7: Equivalent stress-strain curves obtained after a numerical fitting procedure for the cast and homogenized and the extruded materials.

The equivalent stress-strain curve determined with the CP-FEM model was compared to the equivalent stress-strain curve obtained in the previous section. The free variables were the initial slip resistance τ_{c0}^{α} and the hardening parameters θ_k and τ_k, $k = 1, 2$. By changing them in every run of LS-DYNA according to an optimization algorithm, the equivalent stress-strain curve from the numerical model was fitted to the equivalent stress-strain curve obtained for the material. The results of this procedure are shown in Figure 9. The parameters obtained for the CP model are given in Table 5.

Table 5: Parameters of the two-term Voce hardening rule used in the CP model.

Material	τ_{c0}^{α}, MPa	τ_1, MPa	θ_1, MPa	τ_2, MPa	θ_2, MPa
Cast and homogenized	23.00	18.99	151.19	23.61	33.88
Extruded	28.00	40.17	292.75	12.72	6.40

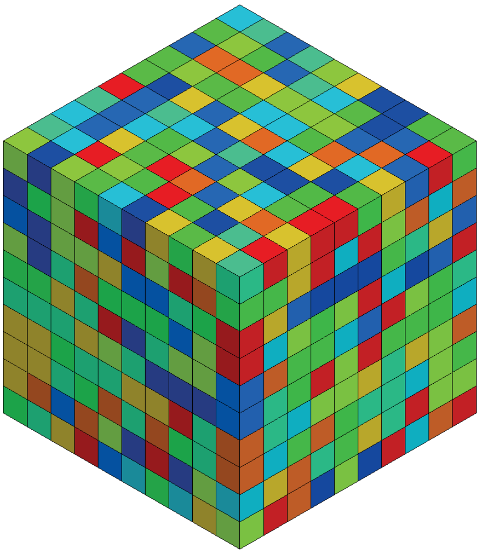

Figure 8: RVE used for calibration of the crystal plasticity two-term Voce hardening rule.

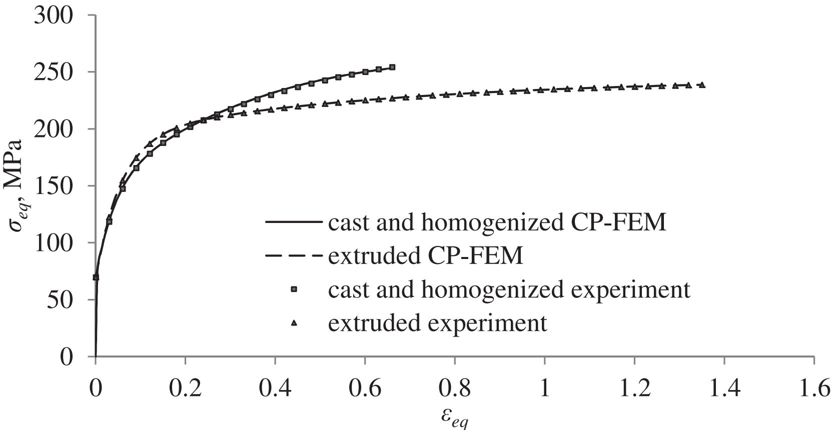

Figure 9: Calibration of the CP model for the cast and homogenized and the extruded materials based on the experimentally obtained equivalent stress-strain curves.

5. Finite element modelling

For the purpose of identifying material parameters, quite simple FEM models were used for both the phenomenological and CP material modelling. The proper study of the post-necking behaviour of the specimens requires a much more detailed specimen description.

However, a representation of the specimen as a polycrystalline body with each 60-100 µm sized grains modelled by at least one element would require a CP-FEM model consisting of many millions of elements. To reduce the computation time some simplifications and reductions had to be made. Most part of the specimen in case of both smooth and notched geometry undergoes relatively small strains compared to the neck region. Therefore the meshes of the specimens were divided into two parts: a part encompassing the necking region and a part adjacent to the fixed end of the specimen. The part undergoing large strains is assigned either a CP material model or the Yld2004-18p material model. The part with lower strains is assigned a simple isotropic J_2 plasticity model with two-term Voce hardening. For the notched specimens the notch area contains the vast majority of plastic deformation, so the rest of the specimen is not modelled fully as for the smooth specimen, where the highly strained regions are more extensive.

The size of the elements also varies for the two parts. In the necking area, the average dimension of an element is 100-120 µm in the thickness and width directions. In the reference direction, the elements are shorter the closer they are to the symmetry plane of the mesh in the middle of the gauge area. During necking the edge elements undergo very large strains, which may lead to numerical problems. To keep the element aspect ratio within reasonable limits during the whole deformation process, the elements are initially shorter in this direction, with a length of about 25 µm. The size of the elements is therefore not the same as the size of the grains in some directions. This was done for the practical reasons of keeping the model size within reasonable limits of around a hundred thousand elements, while still being very close to the physical dimensions of the grains. On the other hand even when the element size was increased to around 150-200 µm, the response of the model (forces and deformation patterns) was still very similar. The number of elements in the meshes used for the localisation simulations is shown in Table 6. All simulations were run on a node of the Vilje supercomputer at Norwegian University of Science and Technology [53], with the node consisting of 2 eight-core processors. The typical total CPU time for each simulation was 100-200 hours for the CP-FEM and 50-150 hours for the Yld2004-18p plasticity model, depending on the number of elements in the model, while the simulation time, due to parallel computing, was around 10 times shorter.

Table 6: Parameters of the numerical models

Specimen geometry	Number of elements in the anisotropic plasticity part	Number of elements in the J_2 plasticity part
Smooth	149472	41520
Smooth 1/8th	103054	9526
Notch 2 mm	56592	30136
Notch 0.8 mm	85788	23080

The meshes of the smooth and notched specimens are presented in Figure 10. Symmetry boundary conditions were applied at the middle cross-section of the specimen, while the clamped end was subjected to a velocity ramped smoothly to a constant value. The specimen was also prevented from rigid body motions. Eight-node brick elements with reduced integration and Flanagan-Belytschko stiffness form hourglass control [54] were used to discretize the specimens. Explicit time integration of the momentum equations was applied, with mass scaling to decrease computation time. It was carefully checked in all simulations that the kinetic energy remained very small compared with the internal energy to ensure that the numerical solution could be considered quasi-static.

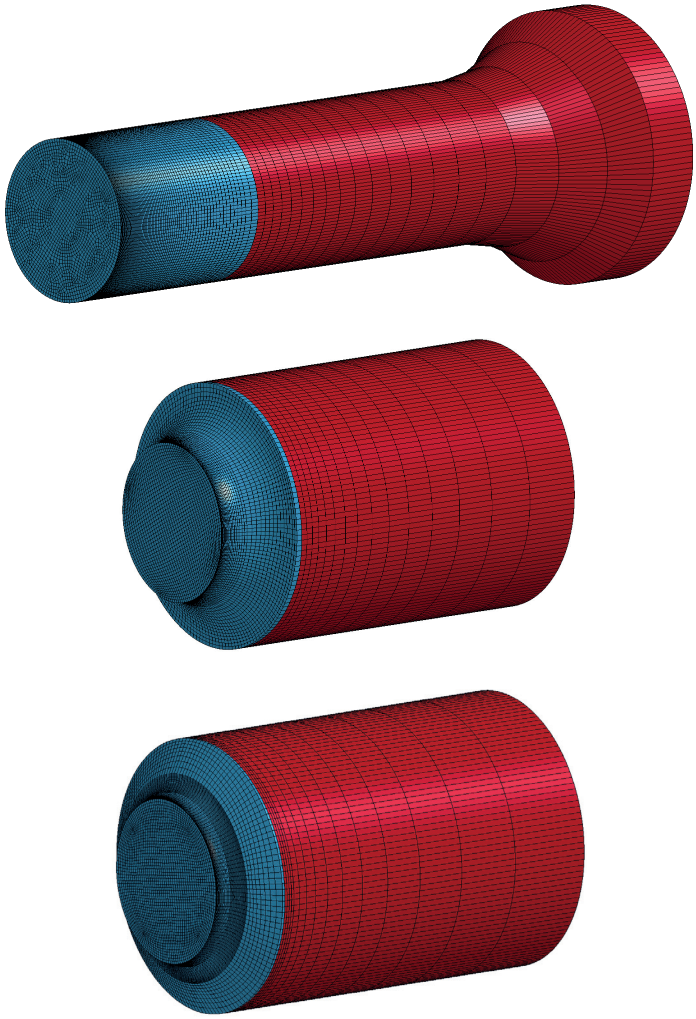

Figure 10: Finite element meshes used in the tensile test simulations: smooth (top), 2 mm notch (middle) and 0.8 mm notch (bottom). Red colour is used for the phenomenological plasticity model parts and blue for the CP model parts.

6. Results and discussion

The true stress-strain curves from the experiments for the cast and homogenized and the extruded materials for smooth and notched specimens, as calculated from Equation (1), are shown in Figure 11. The results from all 3 parallel tests are shown. The parallel tests are found to give consistent results, except for one of the parallel tests on the specimens with 2 mm and 0.8 mm notch of the extruded material.

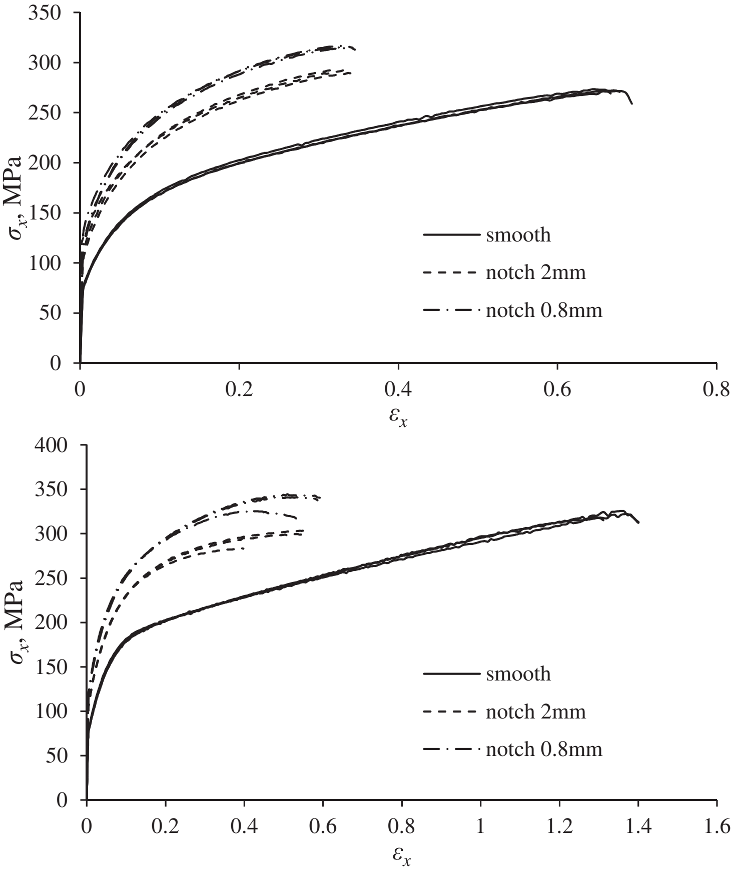

Figure 11: Experimental average Cauchy stress vs. logarithmic strain for the cast and homogenized (top) and extruded materials (bottom) obtained for smooth and notched specimens.

The smooth specimens deform until much larger strain and unlike the notched specimens they have a long linear part of the stress-strain curve after necking. The notched specimens on the other hand demonstrate a higher initial slope of the stress-strain curve and, in case of the cast and homogenized material, a higher maximum stress. The reason for this difference is obviously the difference in the specimen geometry and, in particular, the superimposed triaxial stress field within the pre-machined notch. Accordingly, the response of the specimen is governed both by the work-hardening of the material and the contribution of the constraint imposed by the neck or notch, as discussed in Section 4.1. In contrast, the yield stress is approximately the same for all specimens.

The results obtained for the extruded material should be used with caution, because the assumption of an elliptical shape of the cross-section at all times during deformation seems not to hold. The cross-sections of the specimens after fracture are presented in Figure 12. While the cast and homogenized material exhibits the expected circular cross-sections, the shapes of the extruded material specimens are either rhomboid for the notched specimens or approximately rectangular for the smooth specimens. Therefore, the calculated cross-sectional areas and consequently the strains and stresses will deviate from the real ones as the deformation progresses closer to failure. The exact deviation is difficult to calculate because the qualitative change in the shape of the specimen during deformation is impossible to capture with the present setup.

Consequently, in the following, to present the results of the simulations, the force as a function of the minimum specimen diameter in the thickness direction was used. The results of the simulations, using the phenomenological plasticity model with anisotropic yield criterion and the CP-FEM model, are presented in Figure 13, Figure 14 and Figure 15. Both plasticity models worked well for the cast and homogenized material. The phenomenological plasticity model tends to slightly underestimate the yield stress for the notched specimens. In the case of the notched geometry, both numerical models overestimate the force after necking, while for the smooth geometry the CP-FEM underestimates it. On the other hand, the results for the extruded material are less consistent with the experiment. The results for the smooth specimen are similar to the corresponding results for the cast and homogenized material, with CP-FEM underestimating the force after necking. The response of the notched specimens was not predicted well. For both 2 mm and 0.8 mm notch radii the trend is the same, namely that both the phenomenological and crystal plasticity models overestimate the maximum force.

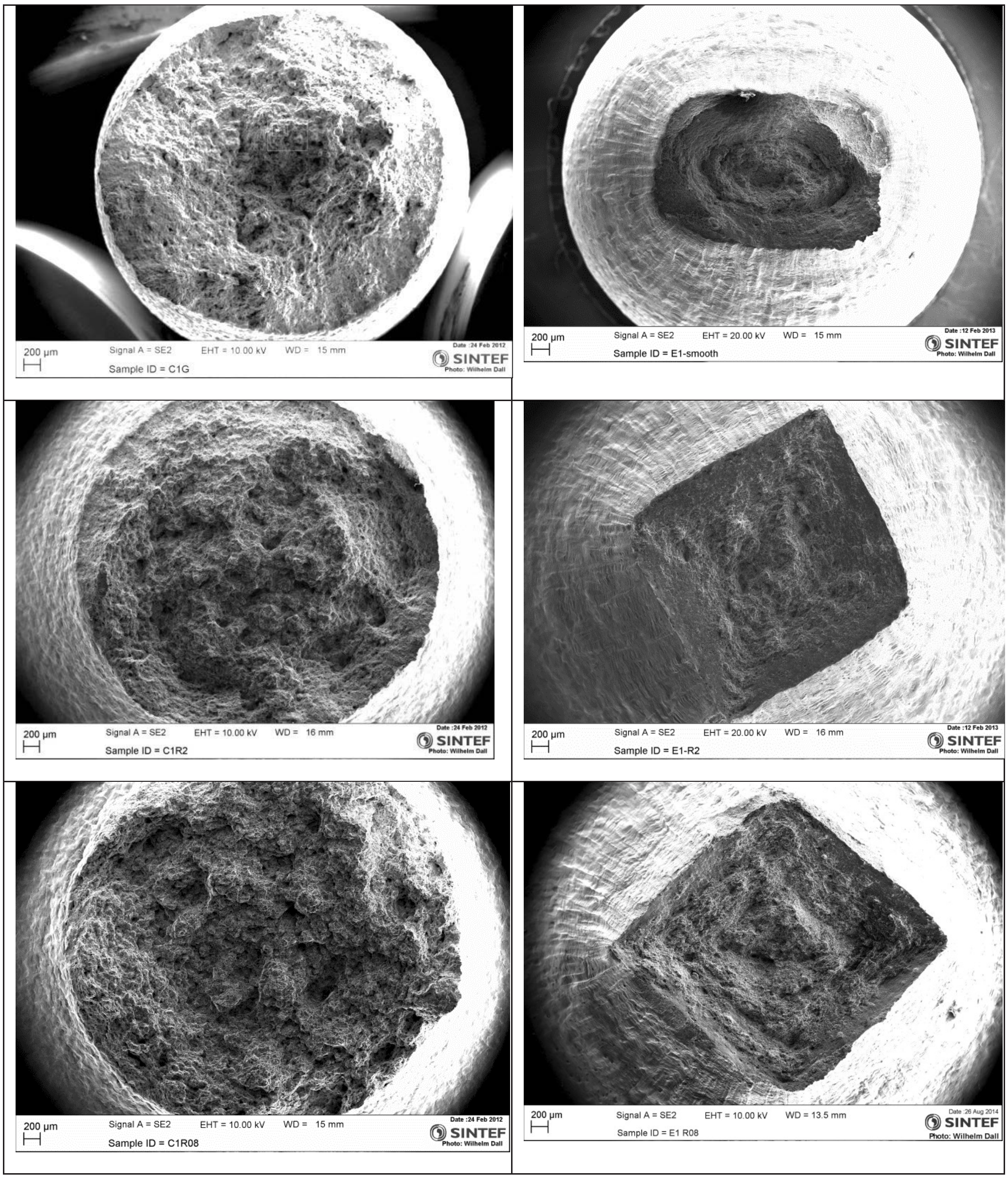

Figure 12: Geometry of fracture surface for the cast and homogenized material (left) and the extruded material (right): smooth specimens (top), 2 mm notch specimens (middle) and 0.8 mm notch specimens (bottom).

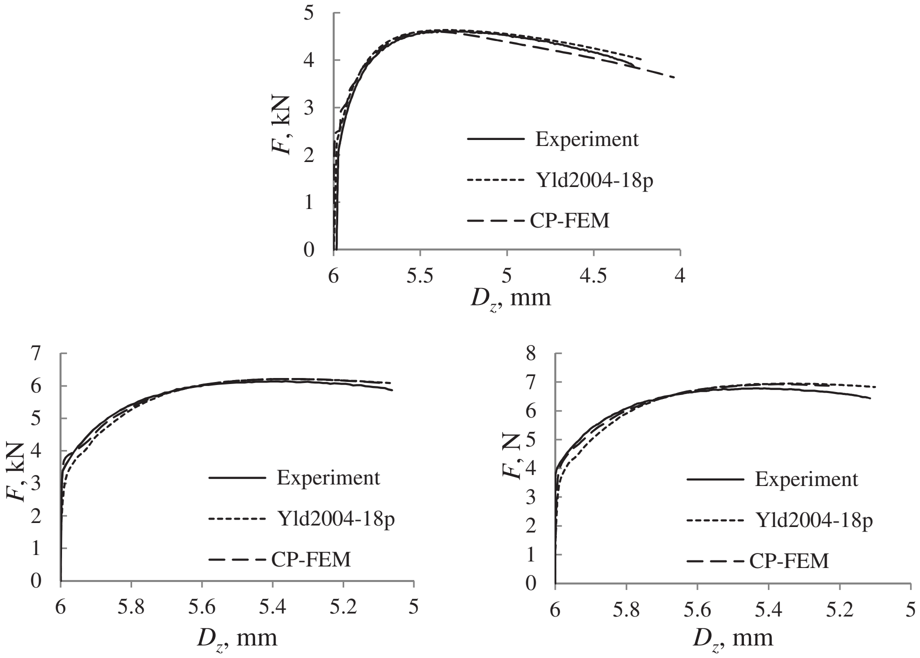

Figure 13: Force-diameter diagrams for the cast and homogenized material: smooth specimens (top) and notched specimens (bottom) with 2 mm (left) and 0.8 mm (right) notch radius in experiment and simulations using the phenomenological and crystal plasticity models.

The phenomenological model also gives a faster force reduction after necking than the CP-FEM model, which has a slope closer to the experimental one. The explanation for this behaviour lies probably in the evolution of the cross-section shape and the resulting difference in local stress and strain fields. It is important to recall here that the identification of the parameters of the two plasticity models relies on the measured true stress-strain curve which is less accurate for the extruded material because of the non-elliptical shape of the minimum cross-section of the specimens.

The deformed shapes produced by the phenomenological and CP-FEM models are shown in Figure 16 and Figure 17. As expected, the cast and homogenized material behaves isotropically and the cross-sections remain circular in all simulations; although with CP-FEM the grains deform differently, depending on their orientation, and create a rough, uneven surface, as in the experiments. Noticeably for the extruded material the surface roughness is much less pronounced for the CP-FEM simulations results. For the extruded material the phenomenological plasticity model produced elliptic cross-sections in all cases, though the curvature of the ellipses is different for the smooth and notched specimen geometries, and for the smooth geometry it is almost rectangular. The CP-FEM model produced a more circular shape of the cross-section for the smooth geometry and a distinct rhomboid shape for both notched geometries. The comparison with the cross-sections of the real specimens shows that in this case the CP-FEM model of the notched specimens was much closer to the qualitative behaviour observed experimentally. The stress and strain fields and the plastic anisotropy predicted by the Yld2004-18p function are quite different from the experimental. This is also apparent from the strain ratio diagrams for the extruded material shown in Figure 15. The strain ratio predicted by the CP-FEM model is closer to the experiment and to unity for the notched specimens, while Yld2004-18p yield surface overestimates it; for the smooth specimen, the opposite trend is observed.

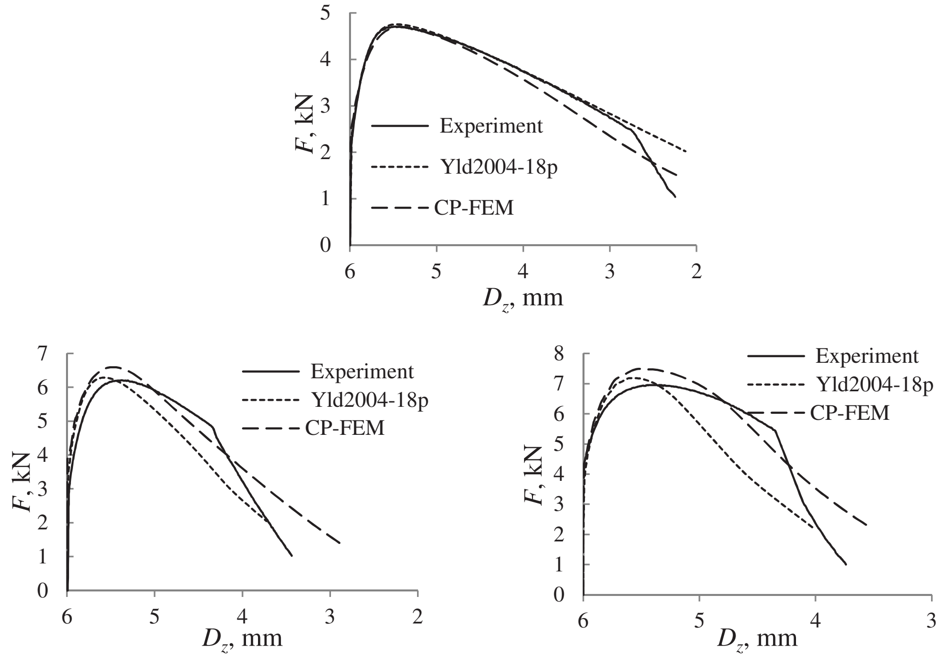

Figure 14: Force-diameter diagrams for the extruded material: smooth specimens (top) and notched specimens (bottom) with 2 mm (left) and 0.8 mm (right) notch radius in experiment and simulations using the phenomenological and crystal plasticity models.

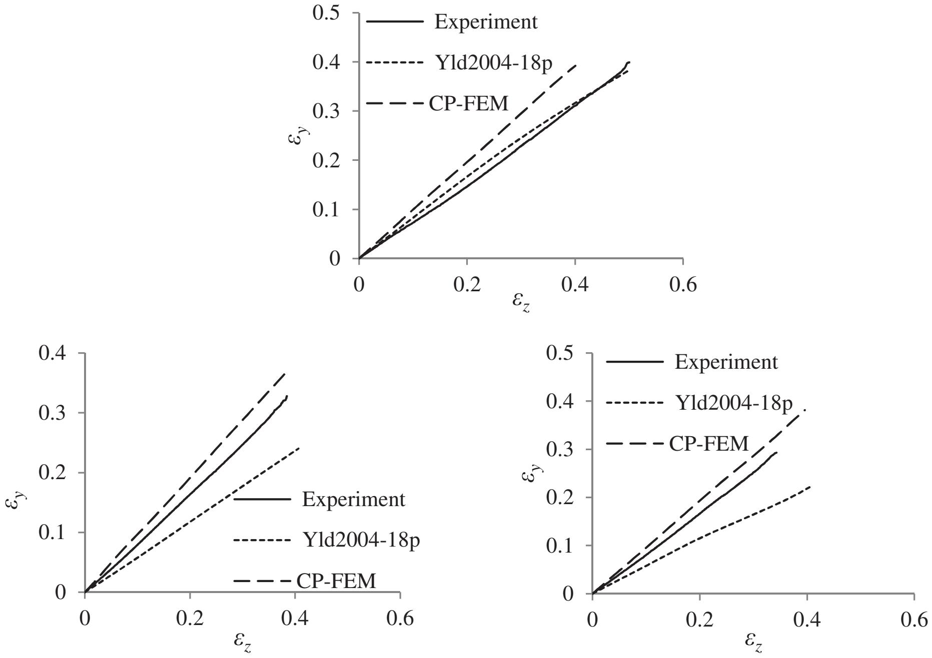

Figure 15: Smooth specimens (top) and notched specimens (bottom) with 2 mm (left) and 0.8 mm (right) notch radius in experiment and simulations using the phenomenological and crystal plasticity models: logarithmic strains in thickness vs. width directions for the experiment and simulations on the extruded material.

The rhomboid shape of a deformed cross-section is not often observed for Al alloys and is most likely a result of the extremely sharp cube texture. The CP-FEM model managed to capture the collective behaviour of the grains, by accounting for their real physical modes of deformation by slip on slip systems. The phenomenological model naturally lacks such capability. The extremely sharp texture though leads to some complications for the smooth specimen. When the same mesh was used for the CP-FEM model of the extruded material as for the cast and homogenized material, the model tended to predict necking in combination with a shear localization mode, producing a very different cross section and too soft response compared to the experiment and the phenomenological plasticity model. A large number of grains with almost perfect Cube orientation were situated in close neighbourhood to each other because of the sharp texture of the material. These grains, in form of their representative elements, tend to fall into a shear mode of deformation easily and disrupt the normal necking process. This does not happen when the random texture of the cast homogenised material is used, neither is such phenomenon observed in experiment. Thus it is a numerical problem of this particular texture and mesh combination. To stabilize the deformation behaviour, only a quarter of the mesh presented in Figure 10 was used with applied symmetry boundary conditions. The notched specimens' simulations showed that the material modelled with CP-FEM retained the orthotropic behaviour and the *xz* and *yz* planes indeed were its symmetry planes. Consequently, the introduction of these symmetry planes as boundary conditions into the smooth specimen model should not distort the results. The additional symmetry planes allowed for a stable neck forming.

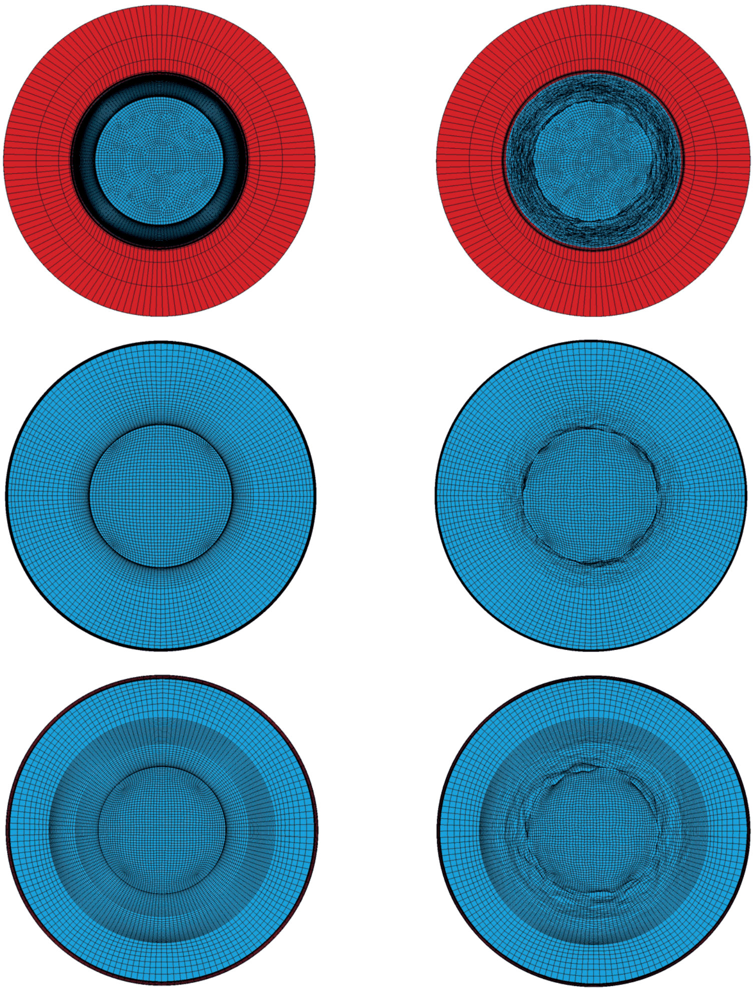

Figure 16: Cross-sections of the uniaxial tension (top), 2 mm notch (middle) and 0.8 mm notch (bottom) specimens from FEM simulations at strains approximately corresponding to fracture with phenomenological plasticity (left) and crystal plasticity (right) for the cast and homogenized material.

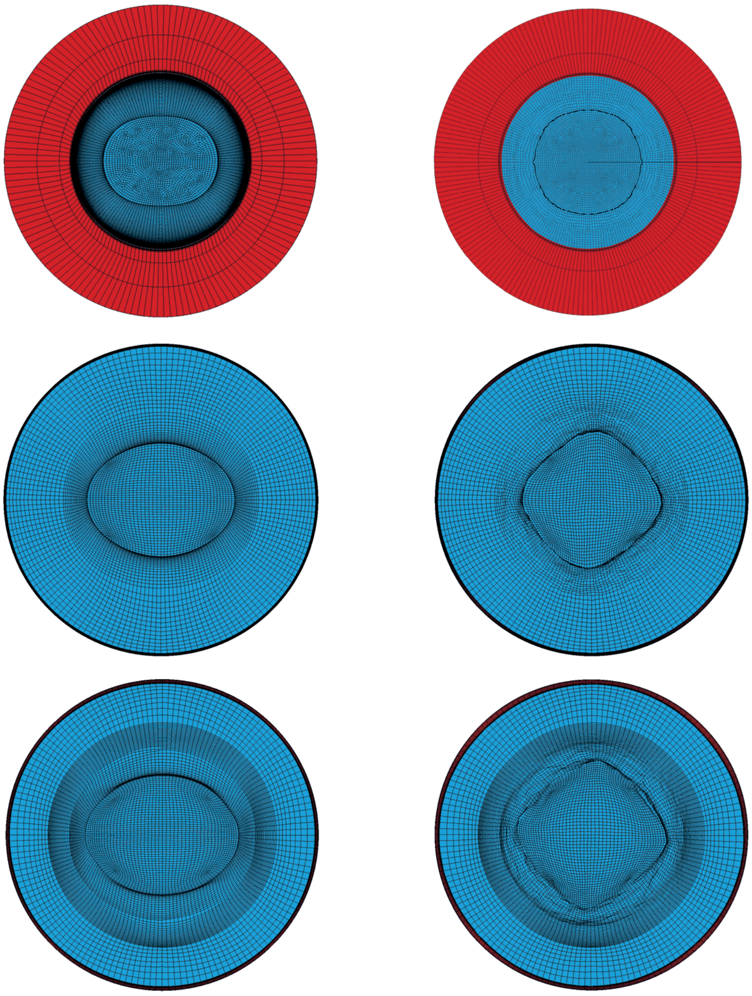

Figure 17: Cross-sections of the uniaxial tension (top), 2 mm notch (middle) and 0.8 mm notch (bottom) specimens from FEM simulations at strains approximately corresponding to fracture with phenomenological plasticity (left) and crystal plasticity (right) for the extruded material.

The most obvious weakness of the methodology used is the material parameter identification. The identification of the equivalent stress-strain curve relies on the assumption of an elliptical specimen cross-section, while the real cross-section deviates from it, introducing the first source of error. It also relies on a yield surface found with a CP model and representative set of grain orientations, which has its own difficulties [55, 56]. The CP-FEM model with one element representing one grain is also not ideal, allowing only for limited strain compatibility and stress relaxation between the grains. Although this should not affect the global response considerably, the local stress and strain fields and the resulting localized deformation may be more affected.

The Al alloys with strong textures may, as it was shown, demonstrate unusual plastic behaviour after necking. The phenomenological models fail to capture this behaviour, but the use of CP-FEM may provide a means to describe it. In modelling ductile fracture of Al alloys, a correct description of the local stress and strain fields is crucial for successful predictions. The CP-FEM model may therefore give the edge that the phenomenological plasticity models lack.

Acknowledgements

We want to thank Norsk Hydro ASA for the material used to produce the specimens. This research was supported in part with computational resources at NTNU provided by NOTUR, http://www.notur.no.

References

[1] M. Considère, *Memoire sur l'emploi du fer et de l'acier dans les constructions*: Dunod, 1885.

[2] J. Hutchinson and J. Miles, "Bifurcation analysis of the onset of necking in an elastic/plastic cylinder under uniaxial tension," *Journal of the Mechanics and Physics of Solids,* vol. 22, pp. 61-71, 1974.

[3] H. Noguchi, S. Okazawa, and F. Fujii, "Scaled corrector and branch-switching in necking problems," *Computational Mechanics,* vol. 26, pp. 236-242, 2000.

[4] P. Bridgman, "The stress distribution at the neck of a tension specimen," *Transactions of American Society for Metals,* vol. 32, pp. 553-574, 1944.

[5] J. Aronofsky, "Evaluation of stress distribution in the symmetrical neck of flat tensile bars," *Journal of Applied Mechanics,* pp. 75-84, 1951.

[6] N. Davidenkov and N. Spiridonova, "Analysis of the state of stress in the neck of a tension test specimen," in *Proceedings of American Society of Testing Materials*, 1946, pp. 1147-1158.

[7] A. Argon, J. Im, and A. Needleman, "Distribution of plastic strain and negative pressure in necked steel and copper bars," *Metallurgical Transactions A,* vol. 6, pp. 815-824, 1975.

[8] G. Le Roy, J. Embury, G. Edwards, and M. Ashby, "A model of ductile fracture based on the nucleation and growth of voids," *Acta Metallurgica,* vol. 29, pp. 1509-1522, 1981.

[9] A. Ostsemin, "Stress in the least cross section of round and plane specimens in tension," *Strength of Materials,* vol. 24, pp. 298-301, 1992.

[10] M. Gromada, G. Mishuris, and A. Ochsner, "Necking in the tensile test. Correction formulae and related error estimation," *Archives of Metallurgy and Materials,* vol. 52, p. 231, 2007.

[11] A. Needleman, "A numerical study of necking in circular cylindrical bar," *Journal of the Mechanics and Physics of Solids,* vol. 20, pp. 111-127, 1972.

[12] D. Norris Jr, B. Moran, J. Scudder, and D. Quinones, "A computer simulation of the tension test," *Journal of the Mechanics and Physics of Solids,* vol. 26, pp. 1-19, 1978.

[13] V. Tvergaard and A. Needleman, "Analysis of the cup-cone fracture in a round tensile bar," *Acta Metallurgica,* vol. 32, pp. 157-169, 1984.

[14] M. Brünig, "Numerical analysis and modeling of large deformation and necking behavior of tensile specimens," *Finite Elements in Analysis and Design,* vol. 28, pp. 303-319, 1998.

[15] T. Datta and D. Banerjee, "A numerical analysis of neck formation in tensile specimens," *Journal of Materials Processing Technology,* vol. 54, pp. 309-313, 1995.

[16] C. García-Garino, F. Gabaldón, and J. M. Goicolea, "Finite element simulation of the simple tension test in metals," *Finite Elements in Analysis and Design,* vol. 42, pp. 1187-1197, 2006.

[17] V. Tvergaard, "Necking in tensile bars with rectangular cross-section," *Computer Methods in Applied Mechanics and Engineering,* vol. 103, pp. 273-290, 1993.

[18] V. Tvergaard, A. Needleman, and K. K. Lo, "Flow localization in the plane strain tensile test," *Journal of the Mechanics and Physics of Solids,* vol. 29, pp. 115-142, 1981.

[19] A. K. Ghosh, "A numerical analysis of the tensile test for sheet metals," *Metallurgical Transactions A,* vol. 8, pp. 1221-1232, 1977.

[20] A. Bacha, D. Daniel, and H. Klocker, "On the determination of true stress triaxiality in sheet metal," *Journal of Materials Processing Technology,* vol. 184, pp. 272-287, 2007.

[21] L. P. Mikkelsen, "Post-necking behaviour modelled by a gradient dependent plasticity theory," *International Journal of Solids and structures,* vol. 34, pp. 4531-4546, 1997.

[22] J. M. Gerken and P. R. Dawson, "A crystal plasticity model that incorporates stresses and strains due to slip gradients," *Journal of the Mechanics and Physics of Solids,* vol. 56, pp. 1651-1672, 2008.

[23] M. Brünig, S. Ricci, and H. Obrecht, "Nonlocal large deformation and localization behavior of metals," *Computers & Structures,* vol. 79, pp. 2063-2074, 2001.

[24] R. Hill, "A theory of the yielding and plastic flow of anisotropic metals," *Proceedings of the Royal Society of London. Series A. Mathematical and Physical Sciences,* vol. 193, pp. 281-297, 1948.

[25] W. Hosford, "A generalized isotropic yield criterion," *Journal of Applied Mechanics,* vol. 39, p. 607, 1972.

[26] F. Bron and J. Besson, "A yield function for anisotropic materials application to aluminum alloys," *International Journal of Plasticity,* vol. 20, pp. 937-963, 2004.

[27] F. Barlat, Y. Maeda, K. Chung, M. Yanagawa, J. Brem, Y. Hayashida, D. Lege, K. Matsui, S. Murtha, and S. Hattori, "Yield function development for aluminum alloy sheets," *Journal of the Mechanics and Physics of Solids,* vol. 45, pp. 1727-1763, 1997.

[28] H. Aretz and F. Barlat, "General orthotropic yield functions based on linear stress deviator transformations," in *AIP Conference Proceedings*, 2004, p. 147.

[29] F. Barlat, H. Aretz, J. Yoon, M. Karabin, J. Brem, and R. Dick, "Linear transfomation-based anisotropic yield functions," *International Journal of Plasticity,* vol. 21, pp. 1009-1039, 2005.

[30] P. Wu, K. Neale, and E. Van der Giessen, "On crystal plasticity FLD analysis," *Proceedings of the Royal Society of London. Series A: Mathematical, Physical and Engineering Sciences,* vol. 453, pp. 1831-1848, 1997.

[31] E. Viatkina, W. Brekelmans, and M. Geers, "A crystal plasticity based estimate for forming limit diagrams from textural inhomogeneities," *Journal of Materials Processing Technology,* vol. 168, pp. 211-218, 2005.

[32] N. Boudeau, J. Gelin, and S. Salhi, "Computational prediction of the localized necking in sheet forming based on microstructural material aspects," *Computational Materials Science,* vol. 11, pp. 45-64, 1998.

[33] K. Inal, P. Wu, and K. Neale, "Instability and localized deformation in polycrystalline solids under plane-strain tension," *International Journal of Solids and structures,* vol. 39, pp. 983-1002, 2002.

[34] P. Wu, D. Lloyd, M. Jain, K. Neale, and Y. Huang, "Effects of spatial grain orientation distribution and initial surface topography on sheet metal necking," *International Journal of Plasticity,* vol. 23, pp. 1084-1104, 2007.

[35] S. Wang, W. Zhuang, D. Balint, and J. Lin, "A crystal plasticity study of the necking of micro-films under tension," *Journal of Multiscale Modelling,* vol. 1, pp. 331-345, 2009.

[36] Y. Shi, P. Wu, D. Lloyd, and J. Embury, "Crystal plasticity based analysis of localized necking in aluminum tube under internal pressure," *European Journal of Mechanics-A/Solids,* vol. 29, pp. 475-483, 2010.

[37] M. Grujicic and S. Batchu, "Crystal plasticity analysis of earing in deep-drawn OFHC copper cups," *Journal of Materials Science,* vol. 37, pp. 753-764, 2002.

[38] K. Zhang, X. Geng, J. Li, and R. Hu, "On the tension necking of copper single crystal specimen under slip deformation mechanism," *Science in China Series E: Technological Sciences,* vol. 50, pp. 308-318, 2007.

[39] F. Zhang, A. Bower, R. Mishra, and K. Boyle, "Numerical simulations of necking during tensile deformation of aluminum single crystals," *International Journal of Plasticity,* vol. 25, pp. 49-69, 2009.

[40] K. Pedersen, I. Westermann, T. Furu, T. Børvik, and O. Hopperstad, "Influence of microstructure on work-hardening and ductile fracture of aluminium alloys," *Submitted for publication,* 2014.

[41] M. Fourmeau, T. Børvik, A. Benallal, O. Lademo, and O. Hopperstad, "On the plastic anisotropy of an aluminium alloy and its influence on constrained multiaxial flow," *International Journal of Plasticity,* vol. 27, pp. 2005-2025, 2011.

[42] E. Lee and D. Liu, "Finite-Strain Elastic—Plastic Theory with Application to Plane-Wave Analysis," *Journal of Applied Physics,* vol. 38, pp. 19-27, 1967.

[43] G. I. Taylor, "The Mechanism of Plastic Deformation of Crystals. Part I. Theoretical," *Proceedings of the Royal Society of London. Series A,* vol. 145, pp. 362-387, July 2, 1934 1934.

[44] A. Hershey, "The plasticity of an isotropic aggregate of anisotropic face-centered cubic crystals," *Journal of Applied Mechanics-Transactions of the Asme,* vol. 21, pp. 241-249, 1954.

[45] J. O. Hallquist, "LS-DYNA theory manual," *Livermore software technology corporation,* vol. 3, 2006.

[46] M. Ortiz and J. Simo, "An analysis of a new class of integration algorithms for elastoplastic constitutive relations," *International Journal for Numerical Methods in Engineering,* vol. 23, pp. 353-366, 1986.

[47] R. J. Asaro, "Crystal plasticity," *Journal of Applied Mechanics,* vol. 50, pp. 921-934, 1983.

[48] D. Achani, O. S. Hopperstad, and O. G. Lademo, "Behaviour of extruded aluminium alloys under proportional and non-proportional strain paths," *Journal of Materials Processing Technology,* vol. 209, pp. 4750-4764, 2009.

[49] K. O. Pedersen, O. G. Lademo, T. Berstad, T. Furu, and O. S. Hopperstad, "Influence of texture and grain structure on strain localisation and formability for AlMgSi alloys," *Journal of Materials Processing Technology,* vol. 200, pp. 77-93, 2008.

[50] C. Teodosiu and J. L. Raphanel, "Finite element simulations of large elastoplastic deformations of multicrystals," in *Proceedings of the international seminar MECAMAT91*, 1991, pp. 153-168.

[51] S. Dumoulin, L. Tabourot, T. Gradel, M. Fivel, and J. Moreau, "Identification of constitutive laws for Al 99.5," in *Advances in Mechanical Behaviour, Plasticity and Damage: Proceedings of Euromat 2000*, 2000, p. 311.

[52] N. Stander, W. Roux, T. Goel, T. Eggleston, and K. Craig, "LS-OPT user's manual," *Livermore software technology corporation,* 2008.

[53] *https://www.hpc.ntnu.no/display/hpc/Vilje*.

[54] D. Flanagan and T. Belytschko, "A uniform strain hexahedron and quadrilateral with orthogonal hourglass control," *International Journal for Numerical Methods in Engineering,* vol. 17, pp. 679-706, 1981.

[55] M. Khadyko, S. Dumoulin, T. Børvik, and O. Hopperstad, "An experimental-numerical method to determine the work-hardening of anisotropic ductile materials at large strains," *International Journal of Mechanical Sciences,* vol. 88, pp. 25-36, 2014.

[56] S. Dumoulin, O. Engler, O. Hopperstad, and O. Lademo, "Description of plastic anisotropy in AA6063-T6 using the crystal plasticity finite element method," *Modelling and Simulation in Materials Science and Engineering,* vol. 20, p. 055008, 2012.

Appendix

Article 5

M. Khadyko, S. Dumoulin, O.S. Hopperstad

Slip system interaction matrix and its influence on the macroscopic response of Al alloys.

Materials Science Forum 794-796 (2014) 566-571

Is not included due to copyright

DEPARTMENT OF STRUCTURAL ENGINEERING
NORWEGIAN UNIVERSITY OF SCIENCE AND TECHNOLOGY

N–7491 TRONDHEIM, NORWAY
Telephone: +47 73 59 47 00   Telefax: +47 73 59 47 01

"Reliability Analysis of Structural Systems using Nonlinear Finite Element Methods",
C. A. Holm, 1990:23, ISBN 82-7119-178-0.

"Uniform Stratified Flow Interaction with a Submerged Horizontal Cylinder",
Ø. Arntsen, 1990:32, ISBN 82-7119-188-8.

"Large Displacement Analysis of Flexible and Rigid Systems Considering
Displacement-Dependent Loads and Nonlinear Constraints",
K. M. Mathisen, 1990:33, ISBN 82-7119-189-6.

"Solid Mechanics and Material Models including Large Deformations",
E. Levold, 1990:56, ISBN 82-7119-214-0, ISSN 0802-3271.

"Inelastic Deformation Capacity of Flexurally-Loaded Aluminium Alloy Structures",
T. Welo, 1990:62, ISBN 82-7119-220-5, ISSN 0802-3271.

"Visualization of Results from Mechanical Engineering Analysis",
K. Aamnes, 1990:63, ISBN 82-7119-221-3, ISSN 0802-3271.

"Object-Oriented Product Modeling for Structural Design",
S. I. Dale, 1991:6, ISBN 82-7119-258-2, ISSN 0802-3271.

"Parallel Techniques for Solving Finite Element Problems on Transputer Networks",
T. H. Hansen, 1991:19, ISBN 82-7119-273-6, ISSN 0802-3271.

"Statistical Description and Estimation of Ocean Drift Ice Environments",
R. Korsnes, 1991:24, ISBN 82-7119-278-7, ISSN 0802-3271.

“Properties of concrete related to fatigue damage: with emphasis on high strength concrete”,
G. Petkovic, 1991:35, ISBN 82-7119-290-6, ISSN 0802-3271.

"Turbidity Current Modelling",
B. Brørs, 1991:38, ISBN 82-7119-293-0, ISSN 0802-3271.

"Zero-Slump Concrete: Rheology, Degree of Compaction and Strength. Effects of Fillers as Part Cement-Replacement",
C. Sørensen, 1992:8, ISBN 82-7119-357-0, ISSN 0802-3271.

"Nonlinear Analysis of Reinforced Concrete Structures Exposed to Transient Loading",
K. V. Høiseth, 1992:15, ISBN 82-7119-364-3, ISSN 0802-3271.

"Finite Element Formulations and Solution Algorithms for Buckling and Collapse Analysis of Thin Shells",
R. O. Bjærum, 1992:30, ISBN 82-7119-380-5, ISSN 0802-3271.

"Response Statistics of Nonlinear Dynamic Systems",
J. M. Johnsen, 1992:42, ISBN 82-7119-393-7, ISSN 0802-3271.

"Digital Models in Engineering. A Study on why and how engineers build and operate digital models for decisison support",
J. Høyte, 1992:75, ISBN 82-7119-429-1, ISSN 0802-3271.

"Sparse Solution of Finite Element Equations",
A. C. Damhaug, 1992:76, ISBN 82-7119-430-5, ISSN 0802-3271.

"Some Aspects of Floating Ice Related to Sea Surface Operations in the Barents Sea",
S. Løset, 1992:95, ISBN 82-7119-452-6, ISSN 0802-3271.

"Modelling of Cyclic Plasticity with Application to Steel and Aluminium Structures",
O. S. Hopperstad, 1993:7, ISBN 82-7119-461-5, ISSN 0802-3271.

"The Free Formulation: Linear Theory and Extensions with Applications to Tetrahedral Elements
with Rotational Freedoms",
G. Skeie, 1993:17, ISBN 82-7119-472-0, ISSN 0802-3271.

"Høyfast betongs motstand mot piggdekkslitasje. Analyse av resultater fra prøving i Veisliter'n",
T. Tveter, 1993:62, ISBN 82-7119-522-0, ISSN 0802-3271.

"A Nonlinear Finite Element Based on Free Formulation Theory for Analysis of Sandwich Structures",
O. Aamlid, 1993:72, ISBN 82-7119-534-4, ISSN 0802-3271.

"The Effect of Curing Temperature and Silica Fume on Chloride Migration and Pore Structure of High Strength Concrete",
C. J. Hauck, 1993:90, ISBN 82-7119-553-0, ISSN 0802-3271.

"Failure of Concrete under Compressive Strain Gradients",
G. Markeset, 1993:110, ISBN 82-7119-575-1, ISSN 0802-3271.

"An experimental study of internal tidal amphidromes in Vestfjorden",
J. H. Nilsen, 1994:39, ISBN 82-7119-640-5, ISSN 0802-3271.

"Structural analysis of oil wells with emphasis on conductor design",
H. Larsen, 1994:46, ISBN 82-7119-648-0, ISSN 0802-3271.

"Adaptive methods for non-linear finite element analysis of shell structures",
K. M. Okstad, 1994:66, ISBN 82-7119-670-7, ISSN 0802-3271.

"On constitutive modelling in nonlinear analysis of concrete structures",
O. Fyrileiv, 1994:115, ISBN 82-7119-725-8, ISSN 0802-3271.

"Fluctuating wind load and response of a line-like engineering structure with emphasis on motion-induced wind forces",
J. Bogunovic Jakobsen, 1995:62, ISBN 82-7119-809-2, ISSN 0802-3271.

"An experimental study of beam-columns subjected to combined torsion, bending and axial actions",
A. Aalberg, 1995:66, ISBN 82-7119-813-0, ISSN 0802-3271.

"Scaling and cracking in unsealed freeze/thaw testing of Portland cement and silica fume concretes",
S. Jacobsen, 1995:101, ISBN 82-7119-851-3, ISSN 0802-3271.

"Damping of water waves by submerged vegetation. A case study of laminaria hyperborea",
A. M. Dubi, 1995:108, ISBN 82-7119-859-9, ISSN 0802-3271.

"The dynamics of a slope current in the Barents Sea",
Sheng Li, 1995:109, ISBN 82-7119-860-2, ISSN 0802-3271.

"Modellering av delmaterialenes betydning for betongens konsistens",
Ernst Mørtsell, 1996:12, ISBN 82-7119-894-7, ISSN 0802-3271.

"Bending of thin-walled aluminium extrusions",
Birgit Søvik Opheim, 1996:60, ISBN 82-7119-947-1, ISSN 0802-3271.

"Material modelling of aluminium for crashworthiness analysis",
Torodd Berstad, 1996:89, ISBN 82-7119-980-3, ISSN 0802-3271.

"Estimation of structural parameters from response measurements on submerged floating tunnels",
Rolf Magne Larssen, 1996:119, ISBN 82-471-0014-2, ISSN 0802-3271.

“Numerical modelling of plain and reinforced concrete by damage mechanics”,
Mario A. Polanco-Loria, 1997:20, ISBN 82-471-0049-5, ISSN 0802-3271.

“Nonlinear random vibrations - numerical analysis by path integration methods”,
Vibeke Moe, 1997:26, ISBN 82-471-0056-8, ISSN 0802-3271.

“Numerical prediction of vortex-induced vibration by the finite element method”,
Joar Martin Dalheim, 1997:63, ISBN 82-471-0096-7, ISSN 0802-3271.

“Time domain calculations of buffeting response for wind sensitive structures”,
Ketil Aas-Jakobsen, 1997:148, ISBN 82-471-0189-0, ISSN 0802-3271.

"A numerical study of flow about fixed and flexibly mounted circular cylinders",
Trond Stokka Meling, 1998:48, ISBN 82-471-0244-7, ISSN 0802-3271.

“Estimation of chloride penetration into concrete bridges in coastal areas”,
Per Egil Steen, 1998:89, ISBN 82-471-0290-0, ISSN 0802-3271.

“Stress-resultant material models for reinforced concrete plates and shells”,
Jan Arve Øverli, 1998:95, ISBN 82-471-0297-8, ISSN 0802-3271.

“Chloride binding in concrete. Effect of surrounding environment and concrete composition”,
Claus Kenneth Larsen, 1998:101, ISBN 82-471-0337-0, ISSN 0802-3271.

“Rotational capacity of aluminium alloy beams”,
Lars A. Moen, 1999:1, ISBN 82-471-0365-6, ISSN 0802-3271.

“Stretch Bending of Aluminium Extrusions”,
Arild H. Clausen, 1999:29, ISBN 82-471-0396-6, ISSN 0802-3271.

“Aluminium and Steel Beams under Concentrated Loading”,
Tore Tryland, 1999:30, ISBN 82-471-0397-4, ISSN 0802-3271.

"Engineering Models of Elastoplasticity and Fracture for Aluminium Alloys",
Odd-Geir Lademo, 1999:39, ISBN 82-471-0406-7, ISSN 0802-3271.

"Kapasitet og duktilitet av dybelforbindelser i trekonstruksjoner",
Jan Siem, 1999:46, ISBN 82-471-0414-8, ISSN 0802-3271.

“Etablering av distribuert ingeniørarbeid; Teknologiske og organisatoriske erfaringer fra en norsk ingeniørbedrift”,
Lars Line, 1999:52, ISBN 82-471-0420-2, ISSN 0802-3271.

“Estimation of Earthquake-Induced Response”,
Símon Ólafsson, 1999:73, ISBN 82-471-0443-1, ISSN 0802-3271.

“Coastal Concrete Bridges: Moisture State, Chloride Permeability and Aging Effects”
Ragnhild Holen Relling, 1999:74, ISBN 82-471-0445-8, ISSN 0802-3271.

”Capacity Assessment of Titanium Pipes Subjected to Bending and External Pressure”,
Arve Bjørset, 1999:100, ISBN 82-471-0473-3, ISSN 0802-3271.

“Validation of Numerical Collapse Behaviour of Thin-Walled Corrugated Panels”,
Håvar Ilstad, 1999:101, ISBN 82-471-0474-1, ISSN 0802-3271.

“Strength and Ductility of Welded Structures in Aluminium Alloys”,
Miroslaw Matusiak, 1999:113, ISBN 82-471-0487-3, ISSN 0802-3271.

“Thermal Dilation and Autogenous Deformation as Driving Forces to Self-Induced Stresses in High Performance Concrete”,
Øyvind Bjøntegaard, 1999:121, ISBN 82-7984-002-8, ISSN 0802-3271.

“Some Aspects of Ski Base Sliding Friction and Ski Base Structure”,
Dag Anders Moldestad, 1999:137, ISBN 82-7984-019-2, ISSN 0802-3271.

"Electrode reactions and corrosion resistance for steel in mortar and concrete",
Roy Antonsen, 2000:10, ISBN 82-7984-030-3, ISSN 0802-3271.

"Hydro-Physical Conditions in Kelp Forests and the Effect on Wave Damping and Dune Erosion. A case study on Laminaria Hyperborea",
Stig Magnar Løvås, 2000:28, ISBN 82-7984-050-8, ISSN 0802-3271.

"Random Vibration and the Path Integral Method",
Christian Skaug, 2000:39, ISBN 82-7984-061-3, ISSN 0802-3271.

"Buckling and geometrical nonlinear beam-type analyses of timber structures",
Trond Even Eggen, 2000:56, ISBN 82-7984-081-8, ISSN 0802-3271.

”Structural Crashworthiness of Aluminium Foam-Based Components”,
Arve Grønsund Hanssen, 2000:76, ISBN 82-7984-102-4, ISSN 0809-103X.

“Measurements and simulations of the consolidation in first-year sea ice ridges, and some aspects of mechanical behaviour”,
Knut V. Høyland, 2000:94, ISBN 82-7984-121-0, ISSN 0809-103X.

”Kinematics in Regular and Irregular Waves based on a Lagrangian Formulation”,
Svein Helge Gjøsund, 2000-86, ISBN 82-7984-112-1, ISSN 0809-103X.

”Self-Induced Cracking Problems in Hardening Concrete Structures”,
Daniela Bosnjak, 2000-121, ISBN 82-7984-151-2, ISSN 0809-103X.

"Ballistic Penetration and Perforation of Steel Plates",
Tore Børvik, 2000:124, ISBN 82-7984-154-7, ISSN 0809-103X.

"Freeze-Thaw resistance of Concrete. Effect of: Curing Conditions, Moisture Exchange and Materials",
Terje Finnerup Rønning, 2001:14, ISBN 82-7984-165-2, ISSN 0809-103X

"Structural behaviour of post tensioned concrete structures. Flat slab. Slabs on ground",
Steinar Trygstad, 2001:52, ISBN 82-471-5314-9, ISSN 0809-103X.

"Slipforming of Vertical Concrete Structures. Friction between concrete and slipform panel",
Kjell Tore Fosså, 2001:61, ISBN 82-471-5325-4, ISSN 0809-103X.

"Some numerical methods for the simulation of laminar and turbulent incompressible flows",
Jens Holmen, 2002:6, ISBN 82-471-5396-3, ISSN 0809-103X.

“Improved Fatigue Performance of Threaded Drillstring Connections by Cold Rolling”,
Steinar Kristoffersen, 2002:11, ISBN: 82-421-5402-1, ISSN 0809-103X.

"Deformations in Concrete Cantilever Bridges: Observations and Theoretical Modelling",
Peter F. Takâcs, 2002:23, ISBN 82-471-5415-3, ISSN 0809-103X.

"Stiffened aluminium plates subjected to impact loading",
Hilde Giæver Hildrum, 2002:69, ISBN 82-471-5467-6, ISSN 0809-103X.

"Full- and model scale study of wind effects on a medium-rise building in a built up area",
Jónas Thór Snæbjørnsson, 2002:95, ISBN82-471-5495-1, ISSN 0809-103X.

“Evaluation of Concepts for Loading of Hydrocarbons in Ice-infested water”,
Arnor Jensen, 2002:114, ISBN 82-417-5506-0, ISSN 0809-103X.

”Numerical and Physical Modelling of Oil Spreading in Broken Ice”,
Janne K. Økland Gjøsteen, 2002:130, ISBN 82-471-5523-0, ISSN 0809-103X.

”Diagnosis and protection of corroding steel in concrete”,
Franz Pruckner, 20002:140, ISBN 82-471-5555-4, ISSN 0809-103X.

“Tensile and Compressive Creep of Young Concrete: Testing and Modelling”,
Dawood Atrushi, 2003:17, ISBN 82-471-5565-6, ISSN 0809-103X.

“Rheology of Particle Suspensions. Fresh Concrete, Mortar and Cement Paste with Various Types of Lignosulfonates”,
Jon Elvar Wallevik, 2003:18, ISBN 82-471-5566-4, ISSN 0809-103X.

“Oblique Loading of Aluminium Crash Components”,
Aase Reyes, 2003:15, ISBN 82-471-5562-1, ISSN 0809-103X.

“Utilization of Ethiopian Natural Pozzolans”,
Surafel Ketema Desta, 2003:26, ISSN 82-471-5574-5, ISSN:0809-103X.

“Behaviour and strength prediction of reinforced concrete structures with discontinuity regions”, Helge Brå, 2004:11, ISBN 82-471-6222-9, ISSN 1503-8181.

“High-strength steel plates subjected to projectile impact. An experimental and numerical study”, Sumita Dey, 2004:38, ISBN 82-471-6282-2 (printed version), ISBN 82-471-6281-4 (electronic version), ISSN 1503-8181.

“Alkali-reactive and inert fillers in concrete. Rheology of fresh mixtures and expansive reactions.”
Bård M. Pedersen, 2004:92, ISBN 82-471-6401-9 (printed version), ISBN 82-471-6400-0 (electronic version), ISSN 1503-8181.

“On the Shear Capacity of Steel Girders with Large Web Openings”.
Nils Christian Hagen, 2005:9 ISBN 82-471-6878-2 (printed version), ISBN 82-471-6877-4 (electronic version), ISSN 1503-8181.

”Behaviour of aluminium extrusions subjected to axial loading”.
Østen Jensen, 2005:7, ISBN 82-471-6873-1 (printed version), ISBN 82-471-6872-3 (electronic version), ISSN 1503-8181.

”Thermal Aspects of corrosion of Steel in Concrete”.
Jan-Magnus Østvik, 2005:5, ISBN 82-471-6869-3 (printed version), ISBN 82-471-6868 (electronic version), ISSN 1503-8181.

”Mechanical and adaptive behaviour of bone in relation to hip replacement.” A study of bone remodelling and bone grafting.
Sébastien Muller, 2005:34, ISBN 82-471-6933-9 (printed version), ISBN 82-471-6932-0 (electronic version), ISSN 1503-8181.

“Analysis of geometrical nonlinearities with applications to timber structures”.
Lars Wollebæk, 2005:74, ISBN 82-471-7050-5 (printed version), ISBN 82-471-7019-1 (electronic version), ISSN 1503-8181.

“Pedestrian induced lateral vibrations of slender footbridges”,
Anders Rönnquist, 2005:102, ISBN 82-471-7082-5 (printed version), ISBN 82-471-7081-7 (electronic version), ISSN 1503-8181.

“Initial Strength Development of Fly Ash and Limestone Blended Cements at Various Temperatures Predicted by Ultrasonic Pulse Velocity”,
Tom Ivar Fredvik, 2005:112, ISBN 82-471-7105-8 (printed version), ISBN 82-471-7103-1 (electronic version), ISSN 1503-8181.

“Behaviour and modelling of thin-walled cast components”,
Cato Dørum, 2005:128, ISBN 82-471-7140-6 (printed version), ISBN 82-471-7139-2 (electronic version), ISSN 1503-8181.

“Behaviour and modelling of selfpiercing riveted connections”,
Raffaele Porcaro, 2005:165, ISBN 82-471-7219-4 (printed version), ISBN 82-471-7218-6 (electronic version), ISSN 1503-8181.

”Behaviour and Modelling og Aluminium Plates subjected to Compressive Load”,
Lars Rønning, 2005:154, ISBN 82-471-7169-1 (printed version), ISBN 82-471-7195-3 (electronic version), ISSN 1503-8181.

”Bumper beam-longitudinal system subjected to offset impact loading”,
Satyanarayana Kokkula, 2005:193, ISBN 82-471-7280-1 (printed version), ISBN 82-471-7279-8 (electronic version), ISSN 1503-8181.

“Control of Chloride Penetration into Concrete Structures at Early Age”,
Guofei Liu, 2006:46, ISBN 82-471-7838-9 (printed version), ISBN 82-471-7837-0 (electronic version), ISSN 1503-8181.

“Modelling of Welded Thin-Walled Aluminium Structures”,
Ting Wang, 2006:78, ISBN 82-471-7907-5 (printed version), ISBN 82-471-7906-7 (electronic version), ISSN 1503-8181.

”Time-variant reliability of dynamic systems by importance sampling and probabilistic analysis of ice loads”,
Anna Ivanova Olsen, 2006:139, ISBN 82-471-8041-3 (printed version), ISBN 82-471-8040-5 (electronic version), ISSN 1503-8181.

“Fatigue life prediction of an aluminium alloy automotive component using finite element analysis of surface topography”.
Sigmund Kyrre Ås, 2006:25, ISBN 82-471-7791-9 (printed version), ISBN 82-471-7791-9 (electronic version), ISSN 1503-8181.

”Constitutive models of elastoplasticity and fracture for aluminium alloys under strain path change”,
Dasharatha Achani, 2006:76, ISBN 82-471-7903-2 (printed version), ISBN 82-471-7902-4 (electronic version), ISSN 1503-8181.

“Simulations of 2D dynamic brittle fracture by the Element-free Galerkin method and linear fracture mechanics”,
Tommy Karlsson, 2006:125, ISBN 82-471-8011-1 (printed version), ISBN 82-471-8010-3 (electronic version), ISSN 1503-8181.

“Penetration and Perforation of Granite Targets by Hard Projectiles”,
Chong Chiang Seah, 2006:188, ISBN 82-471-8150-9 (printed version), ISBN 82-471-8149-5 (electronic version), ISSN 1503-8181.

“Deformations, strain capacity and cracking of concrete in plastic and early hardening phases”,
Tor Arne Hammer, 2007:234, ISBN 978-82-471-5191-4 (printed version), ISBN 978-82-471-5207-2 (electronic version), ISSN 1503-8181.

“Crashworthiness of dual-phase high-strength steel: Material and Component behaviour”, Venkatapathi Tarigopula, 2007:230, ISBN 82-471-5076-4 (printed version), ISBN 82-471-5093-1 (electronic version), ISSN 1503-8181.

“Fibre reinforcement in load carrying concrete structures”,
Åse Lyslo Døssland, 2008:50, ISBN 978-82-471-6910-0 (printed version), ISBN 978-82-471-6924-7 (electronic version), ISSN 1503-8181.

“Low-velocity penetration of aluminium plates”,
Frode Grytten, 2008:46, ISBN 978-82-471-6826-4 (printed version), ISBN 978-82-471-6843-1 (electronic version), ISSN 1503-8181.

“Robustness studies of structures subjected to large deformations”,
Ørjan Fyllingen, 2008:24, ISBN 978-82-471-6339-9 (printed version), ISBN 978-82-471-6342-9 (electronic version), ISSN 1503-8181.

“Constitutive modelling of morsellised bone”,
Knut Birger Lunde, 2008:92, ISBN 978-82-471-7829-4 (printed version), ISBN 978-82-471-7832-4 (electronic version), ISSN 1503-8181.

“Experimental Investigations of Wind Loading on a Suspension Bridge Girder”,
Bjørn Isaksen, 2008:131, ISBN 978-82-471-8656-5 (printed version), ISBN 978-82-471-8673-2 (electronic version), ISSN 1503-8181.

“Cracking Risk of Concrete Structures in The Hardening Phase”,
Guomin Ji, 2008:198, ISBN 978-82-471-1079-9 (printed version), ISBN 978-82-471-1080-5 (electronic version), ISSN 1503-8181.

“Modelling and numerical analysis of the porcine and human mitral apparatus”,
Victorien Emile Prot, 2008:249, ISBN 978-82-471-1192-5 (printed version), ISBN 978-82-471-1193-2 (electronic version), ISSN 1503-8181.

“Strength analysis of net structures”,
Heidi Moe, 2009:48, ISBN 978-82-471-1468-1 (printed version), ISBN 978-82-471-1469-8 (electronic version), ISSN1503-8181.

“Numerical analysis of ductile fracture in surface cracked shells”,
Espen Berg, 2009:80, ISBN 978-82-471-1537-4 (printed version), ISBN 978-82-471-1538-1 (electronic version), ISSN 1503-8181.

"Subject specific finite element analysis of bone – for evaluation of the healing of a leg lengthening and evaluation of femoral stem design",
Sune Hansborg Pettersen, 2009:99, ISBN 978-82-471-1579-4 (printed version), ISBN 978-82-471-1580-0 (electronic version), ISSN 1503-8181.

"Evaluation of fracture parameters for notched multi-layered structures",
Lingyun Shang, 2009:137, ISBN 978-82-471-1662-3 (printed version), ISBN 978-82-471-1663-0 (electronic version), ISSN 1503-8181.

"Modelling of Dynamic Material Behaviour and Fracture of Aluminium Alloys for Structural Applications"
Yan Chen, 2009:69, ISBN 978-82-471-1515-2 (printed version), ISBN 978-82 471-1516-9 (electronic version), ISSN 1503-8181.

"Nanomechanics of polymer and composite particles"
Jianying He 2009:213, ISBN 978-82-471-1828-3 (printed version), ISBN 978-82-471-1829-0 (electronic version), ISSN 1503-8181.

"Mechanical properties of clear wood from Norway spruce"
Kristian Berbom Dahl 2009:250, ISBN 978-82-471-1911-2 (printed version) ISBN 978-82-471-1912-9 (electronic version), ISSN 1503-8181.

"Modeling of the degradation of TiB_2 mechanical properties by residual stresses and liquid Al penetration along grain boundaries"
Micol Pezzotta 2009:254, ISBN 978-82-471-1923-5 (printed version) ISBN 978-82-471-1924-2 (electronic version) ISSN 1503-8181.

"Effect of welding residual stress on fracture"
Xiabo Ren 2010:77, ISBN 978-82-471-2115-3 (printed version) ISBN 978-82-471-2116-0 (electronic version), ISSN 1503-8181.

"Pan-based carbon fiber as anode material in cathodic protection system for concrete structures"
Mahdi Chini 2010:122, ISBN 978-82-471-2210-5 (printed version) ISBN 978-82-471-2213-6 (electronic version), ISSN 1503-8181.

"Structural Behaviour of deteriorated and retrofitted concrete structures"
Irina Vasililjeva Sæther 2010:171, ISBN 978-82-471-2315-7 (printed version) ISBN 978-82-471-2316-4 (electronic version) ISSN 1503-8181.

"Prediction of local snow loads on roofs"
Vivian Meløysund 2010:247, ISBN 978-82-471-2490-1 (printed version) ISBN 978-82-471-2491-8 (electronic version) ISSN 1503-8181.

"Behaviour and modelling of polymers for crash applications"
Virgile Delhaye 2010:251, ISBN 978-82-471-2501-4 (printed version) ISBN 978-82-471-2502-1 (electronic version) ISSN 1503-8181.

“Blended cement with reducted CO_2 emission – Utilizing the Fly Ash-Limestone Synergy”,
Klaartje De Weerdt 2011:32, ISBN 978-82-471-2584-7 (printed version) ISBN 978-82-471-2584-4 (electronic version) ISSN 1503-8181.

“Chloride induced reinforcement corrosion in concrete” Concept of critical chloride content – methods and mechanisms.
Ueli Angst 2011:113, ISBN 978-82-471-2769-9 (printed version) ISBN 978-82-471-2763-6 (electronic version) ISSN 1503-8181.

“A thermo-electric-Mechanical study of the carbon anode and contact interface for Energy savings in the production of aluminium”.
Dag Herman Andersen 2011:157, ISBN 978-82-471-2859-6 (printed version) ISBN 978-82-471-2860-2 (electronic version) ISSN 1503-8181.

“Structural Capacity of Anchorage Ties in Masonry Veneer Walls Subjected to Earthquake”. The implications of Eurocode 8 and Eurocode 6 on a typical Norwegain veneer wall.
Ahmed Mohamed Yousry Hamed 2011:181, ISBN 978-82-471-2911-1 (printed version) ISBN 978-82-471-2912-8 (electronic ver.) ISSN 1503-8181.

“Work-hardening behaviour in age-hardenable Al-Zn-Mg(-Cu) alloys”.
Ida Westermann , 2011:247, ISBN 978-82-471-3056-8 (printed ver.) ISBN 978-82-471-3057-5 (electronic ver.) ISSN 1503-8181.

“Behaviour and modelling of selfpiercing riveted connections using aluminium rivets”.
Nguyen-Hieu Hoang, 2011:266, ISBN 978-82-471-3097-1 (printed ver.) ISBN 978-82-471-3099-5 (electronic ver.) ISSN 1503-8181.

“Fibre reinforced concrete”.
Sindre Sandbakk, 2011:297, ISBN 978-82-471-3167-1 (printed ver.) ISBN 978-82-471-3168-8 (electronic ver) ISSN 1503:8181.

“Dynamic behaviour of cablesupported bridges subjected to strong natural wind”.
Ole Andre Øiseth, 2011:315, ISBN 978-82-471-3209-8 (printed ver.) ISBN 978-82-471-3210-4 (electronic ver.) ISSN 1503-8181.

“Constitutive modeling of solargrade silicon materials”
Julien Cochard, 2011:307, ISBN 978-82-471-3189-3 (printed ver). ISBN 978-82-471-3190-9 (electronic ver.) ISSN 1503-8181.

“Constitutive behavior and fracture of shape memory alloys”
Jim Stian Olsen, 2012:57, ISBN 978-82-471-3382-8 (printed ver.) ISBN 978-82-471-3383-5 (electronic ver.) ISSN 1503-8181.

“Field measurements in mechanical testing using close-range photogrammetry and digital image analysis”
Egil Fagerholt, 2012:95, ISBN 978-82-471-3466-5 (printed ver.) ISBN 978-82-471-3467-2 (electronic ver.) ISSN 1503-8181.

“Towards a better under standing of the ultimate behaviour of lightweight aggregate concrete in compression and bending”,
Håvard Nedrelid, 2012:123, ISBN 978-82-471-3527-3 (printed ver.) ISBN 978-82-471-3528-0 (electronic ver.) ISSN 1503-8181.

“Numerical simulations of blood flow in the left side of the heart”
Sigrid Kaarstad Dahl, 2012:135, ISBN 978-82-471-3553-2 (printed ver.) ISBN 978-82-471-3555-6 (electronic ver.) ISSN 1503-8181.

“Moisture induced stresses in glulam”
Vanessa Angst-Nicollier, 2012:139, ISBN 978-82-471-3562-4 (printed ver.) ISBN 978-82-471-3563-1 (electronic ver.) ISSN 1503-8181.

“Biomechanical aspects of distraction osteogensis”
Valentina La Russa, 2012:250, ISBN 978-82-471-3807-6 (printed ver.) ISBN 978-82-471-3808-3 (electronic ver.) ISSN 1503-8181.

“Ductile fracture in dual-phase steel. Theoretical, experimental and numerical study”
Gaute Gruben, 2012:257, ISBN 978-82-471-3822-9 (printed ver.) ISBN 978-82-471-3823-6 (electronic ver.) ISSN 1503-8181.

“Damping in Timber Structures”
Nathalie Labonnote, 2012:263, ISBN 978-82-471-3836-6 (printed ver.) ISBN 978-82-471-3837-3 (electronic ver.) ISSN 1503-8181.

“Biomechanical modeling of fetal veins: The umbilical vein and ductus venosus bifurcation”
Paul Roger Leinan, 2012:299, ISBN 978-82-471-3915-8 (printed ver.) ISBN 978-82-471-3916-5 (electronic ver.) ISSN 1503-8181.

“Large-Deformation behaviour of thermoplastics at various stress states”
Anne Serine Ognedal, 2012:298, ISBN 978-82-471-3913-4 (printed ver.) ISBN 978-82-471-3914-1 (electronic ver.) ISSN 1503-8181.

“Hardening accelerator for fly ash blended cement”
Kien Dinh Hoang, 2012:366, ISBN 978-82-471-4063-5 (printed ver.) ISBN 978-82-471-4064-2 (electronic ver.) ISSN 1503-8181.

“From molecular structure to mechanical properties”
Jianyang Wu, 2013:186, ISBN 978-82-471-4485-5 (printed ver.) ISBN 978-82-471-4486-2 (electronic ver.) ISSN 1503-8181.

“Experimental and numerical study of hybrid concrete structures”
Linn Grepstad Nes, 2013:259, ISBN 978-82-471-4644-6 (printed ver.) ISBN 978-82-471-4645-3 (electronic ver.) ISSN 1503-8181.

“Mechanics of ultra-thin multi crystalline silicon wafers”
Saber Saffar, 2013:199, ISBN 978-82-471-4511-1 (printed ver.) ISBN 978-82-471-4513-5 (electronic ver). ISSN 1503-8181.

“Through process modelling of welded aluminium structures”
Anizahyati Alisibramulisi, 2013:325, ISBN 978-82-471-4788-7 (printed ver.) ISBN 978-82-471-4789-4 (electronic ver.) ISSN 1503-8181.

“Combined blast and fragment loading on steel plates”
Knut Gaarder Rakvåg, 2013:361, ISBN978-82-471-4872-3 (printed ver.) ISBN 978-82-4873-0 (electronic ver.). ISSN 1503-8181.

“Characterization and modelling of the anisotropic behaviour of high-strength aluminium alloy”
Marion Fourmeau, 2014:37, ISBN 978-82-326-0008-3 (printed ver.) ISBN 978-82-326-0009-0 (electronic ver.) ISSN 1503-8181.

“Behaviour of threated steel fasteners at elevated deformation rates”
Henning Fransplass, 2014:65, ISBN 978-82-326-0054-0 (printed ver.) ISBN 978-82-326-0055-7 (electronic ver.) ISSN 1503-8181.

“Sedimentation and Bleeding”
Ya Peng, 2014:89, ISBN 978-82-326-0102-8 (printed ver.) ISBN 978-82-326-0103-5 (electric ver.) ISSN 1503-8181.

“Impact against X65 offshore pipelines”
Martin Kristoffersen, 2014:362, ISBN 978-82-326-0636-8 (printed ver.) ISBN 978-82-326-0637-5 (electronic ver.) ISSN 1503-8181.

“Formability of aluminium alloy subjected to prestrain by rolling”
Dmitry Vysochinskiy, 2014:363, , ISBN 978-82-326-0638-2 (printed ver.) ISBN 978-82-326-0639-9 (electronic ver) ISSN 1503-8181.